Crystal Fields and Spin Dynamics in Frustrated Quantum Materials

Chien Hung Wu

Wadham College

University of Oxford

A thesis submitted for the degree of

Doctor of Philosophy

Hilary 2024

Acknowledgements

My deepest gratitude goes to **Stephen J. Blundell**, whom I am fortunate to have as my supervisor for the past three and a half years. His invaluable guidance, unwavering encouragement, and insightful feedback have been instrumental in shaping this DPhil. Without him, this thesis would not have been possible. The advice he gave me in our very first meeting – to keep up with cutting-edge research, sparked many new ideas that are explored in this thesis.

I would also like to posthumously acknowledge **Pabitra Biswas** who supervised my summer internship in 2018. I will always remember his kindness, warm compassion, and guidance on μSR. I am especially grateful to several people who have played a significant role in my DPhil journey: **John Wilkinson** and **George Gill**, for teaching me everything since I started, guiding me through data analysis, and being great friends throughout. **Dharmalingam Prabhakaran** for synthesising the high-quality samples that underpinned many of the results presented in this thesis. **Benjamin Huddart** and **Dipranjan Chatterjee** for the laughter, the joy, and for keeping the coffee machine running in 106. At Colleges, I thank all my students at Exeter, St Hugh's, and Wadham for the insightful discussions, and the Physics Fellows at Wadham, **Seamus Davis** and **Martin Bureau**, for their kind and thoughtful support. I am immensely grateful to the **Croucher Foundation** and the **University of Oxford** for generously funding the Oxford-Croucher Scholarship, and to the **STFC** and the **Max Planck GCQM** for supporting my travels to conduct experiments and attend workshops.

Across the wider Oxford Physics community, I am deeply thankful to **Hiroto Takahashi** for being my "partner in crime" in the department. The "nearest-neighbours" **Leonie Woodland** and **Viviane Pecanha Antonio** for the relaxing conversations. **Emily Archer** for the amazing friendship and support, especailly during the writing of this thesis. I am also grateful to others who have helped and inspired me along the way: **Andrew Boothroyd**, **Jordan Thompson**, **Moovendaran Kalimuthu**, **Pam Triggs**, and **Cristina Bormio-Nunes**.

To all the staff and beamline scientists at ISIS and at PSI – some of whom have shaped my research career path, thank you for your dedication to maintaining the

instruments and enabling the science: **Francis Pratt, Chennan Wang, Zurab Guguchia, Thomas Hickens, Russell Ewings, Gøran Nielsen, Andrew Princep, Peter Baker**, and the engineers.

To all the incredible flatmates and friends at Merifield over the past five years – thank you for filling my life with laughter and unforgettable memories. I am forever indebted to you: **Beverly Adrian**, **Scott Cameron**, **Guadalupe Chavez**, **Joseph Hettrick**, **Joseph Khaw**, **Lindsay Kennedy**, **Kris Lambert**, **Gwenafaye McCormick**, **Cheng Qian**, **Michaela Rychetska**, **Marek Rychetsky**, **Atchuta Surampudi**, **Cheng Yuan Tham** (a.k.a. Chef), **Ha-Neul Yu**, and finally, **Socks** – the cat, whose mood is often in a quantum superposition, like Schrödinger's.

To my friends in Oxford and around the world, thank you for your unwavering support throughout this journey: **Antony Au**, **Brian Chan**, **Aswin Chow**, **Chris Chung**, **Gabriel Dalboozi**, **Jeffery Ip**, **Renat Karimov**, **Allan Lee**, **Ernest Leung**, **Julián Mena**, **Jason Ng**, **Soyoung Oh**, **Andrea Rodríguez**, **Petra Stankovic**, **Mikhail Vaganov**, **Vivian Yeung**, and **Angus Yuen**.

And finally, to my family: **Mum**, **Dad**, and **Charwin**. Thank you.

Hank C. H. Wu
May 2025

Abstract

This thesis presents studies of the magnetism in a number of frustrated quantum materials including 1D spin chain compounds, 2D honeycomb and triangular lattice materials, as well as 3D pyrochlores and Weyl semimetals. First, it reveals the tunable magnetic frustration in the family of $PbM_2Ni_6Te_3O_{18}$ spin chain compounds through experimental methods such as μSR and magnetometry, combined with computational simulations including dipolar field calculations and DFT+μ muon site determination. This demonstrates how one can use a suite of techniques to investigate the various aspects of novel frustrated materials.

The main focus of this thesis is to study the spin dynamics and the underlying magnetism in frustrated magnets using the μSR technique. Starting from the fundamental principles of μSR, this thesis provides a brief mathematical treatment of how various magnetic structures and dynamics result in a number of signature muon polarisation asymmetries. Furthermore, through zero-, transverse-, and longitudinal-field μSR experiments, the studies on α-RuI_3 and $DyTa_7O_{19}$ illustrate strong evidence for persistent spin dynamics at base temperature and the mode of spin diffusion.

Finally, through the analysis of the rare-earth oxides, the thesis outlines how the CEF environments determine the magnetic anisotropy, and together with exchange interactions and crystal geometry, they can lead to the spin dynamics commonly observed in frustrated spin liquid materials. This thesis sets out the differences between the Kramers and non-Kramers rare earth ions and how the magnetic behaviour might change in each scenario as a result of chemical disorder or the injection of muons in μ^+SR experiments. Therefore, this thesis provides insight into future developments on how new materials can be designed to strengthen the effect of magnetic frustration.

Contents

x

List of Figures

1 Introduction

Quantum materials are fascinating objects in modern physics. They offer a glimpse into a world where, similar to how human interactions give rise to culture and societal order, electrons come together to exhibit emergent behaviours – behaviours that would not have occurred had each electron acted alone, unlocking new collective properties such as superconductivity, spin dynamics, quantum entanglement, and novel electronic states with topological features [1–4].

This thesis, in particular, aims to unveil the magnetic behaviours in materials where a high density of electronic spins can interact with each other. When such a material cools and crosses its critical temperature, its spins begin to form alignments with their neighbours, an effect known as magnetic ordering, which is driven by the need to minimise energy. While conventional magnetic orders stem from nearest-neighbour ferromagnetic (FM) and anti-ferromagnetic (AFM) interactions, when they are combined with additional terms such as the Dzyaloshinskii-Moriya interaction or when there are competing exchange pathways, more exotic forms of magnetic structures can appear such as the helical or the chiral orders, notably including the skyrmion phase [5].

What makes these magnetic phases particularly interesting is when the spins are arranged in certain geometries, where their tendency to order can be suppressed – this is referred to as geometrical frustration. To illustrate this one can imagine

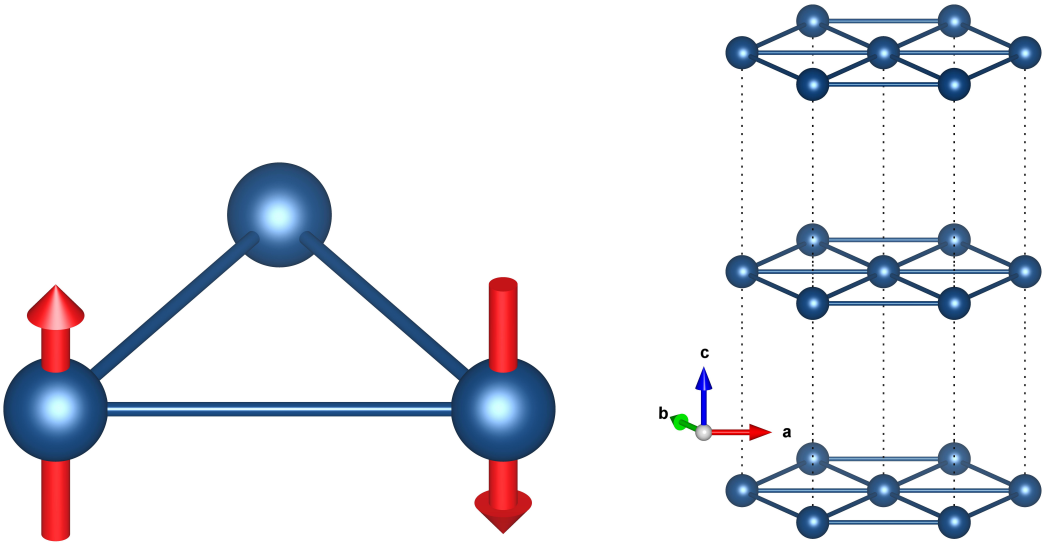

Figure 1.1: (Left) Three spins on a triangular lattice with AFM bonds. (Right) Layers of triangular lattice with AFM bonds stacked along c, giving rise to 2D frustrated magnetism.

three spins at the vertices of an equilateral triangular where they are connected by AFM bonds, as shown in Fig. 1.1. It is clear that the three AFM links would never be fulfilled simultaneously regardless of the choice of the third spin. As a result, geometrical frustration can be readily found in materials containing triangular plaquettes of nearest-neighbour AFM bonds. For quantum spins, this idea gave rise to the resonating valence bond (RVB) model in which pairs of spin form singlets and the magnetic system can break and form new pairings over time [6]. The development of these ideas has led to the quest for the so-called quantum spin liquid (QSL) state, which could be characterised by a superposition of the extensively degenerate, RVB-like ground states, though different types of QSL are possible [7, 8].

Materials that have layers of magnetic atoms well-separated along the vertical c-axis are ideal platforms to explore geometrically frustrated magnetism because of the weaker exchange pathways along this c-axis, and therefore, they are usually referred to as 2D (or quasi-2D) materials. Examples include the delafossite minerals ABO_2 which contain triangular layers [9–11] (as illustrated in Fig. 1.1), the herbersmithite compound $ZnCu_3(OH)_6Cl_2$ which has Cu^{2+} ions arranged in a kagome structure [12, 13], and the honeycomb lattice α-RuX_3 materials (X = Cl, Br, or I) which has the potential to realise the Kiteav model and will be discussed in Chapter 5. For

3D materials, geometrical frustration manifests in structures like the face-centred cubic (FCC) and the pyrochlore lattices which contain a network of edge/corner-sharing tetrahedra. The latter, in particular, is known for hosting intriguing phenomena such as the finite zero-point entropy, the 'magnetic monopole' and magnetic spin noise (see Chapter 7). The degree of frustration of these materials can be represented by the frustration parameter

$$f = \frac{|\theta_{\mathrm{CW}}|}{T_{\mathrm{N}}}, \tag{1.1}$$

representing the ratio of the Curie-Weiss temperature θ_{CW} to the ordering Néel temperature T_{N}. The larger the value f, the greater the frustration and the more likely it is to realise a real QSL state of which $f \to \infty$ [14, 15].

Searching for a quantum spin liquid (QSL) material is no simple task; an ideal QSL material exhibits no long-range order or symmetry breaking, while simultaneously displaying signatures of quantum entanglement and persistent spin dynamics at absolute zero. Despite the advances in theoretical models, experimental realisations of these systems remain challenging due to imperfections in real materials. Common examples include the next-nearest neighbour interactions which can destabilise the fragile ground states, while additional factors such as chemical disorder and magnetic anisotropy within the material can also cause deviation from the idealised model. That said, by strategically engineering magnetic structures with features such as having a low dimensionality and a reduced spin S, it is possible to enhance quantum fluctuations, thereby impeding the formation of a magnetic order [16, 17].

The remaining chapters of this thesis explore a vast array of materials through a combination of experimental techniques and detailed analysis. By investigating the interplay between the crystal geometry and interactions, this thesis aims to unravel the fundamental mechanisms that govern the spin dynamics within frustrated quantum materials.

Thesis outline

The structure of this thesis is as follows:

Chapter 2 provides a brief account of the origin of electronic moments in magnetic atoms. I outline the typical interactions that occur in a frustrated magnet and present the basics of the Kramers theorem.

Chapter 3 introduces the experimental and computational techniques that were used to carry out the studies in this thesis, including magnetometric measurements, μSR spectroscopy, DFT+μ simulations, and Crystal Electric Field (CEF) calculations. Additionally, it provides the derivation for some of the most commonly used polarisation functions in μSR studies.

Chapter 4 presents new μSR results of a family of quasi-1D spin chain compounds $PbM_2Ni_6Te_3O_{18}$. With DFT+μ and dipolar field calculations, I show that the substitution of the transition metal ion allows one to adjust the degree of magnetic frustration due to the competition between exchange interactions.

Chapter 5 is a μSR study on a 2D honeycomb layered compound α-RuI_3, a quantum spin liquid candidate. I provide evidence that the electronic moments remain dynamic down to the lowest achievable temperature of 40 mK and demonstrate that the LF-μSR results show signatures of a 2D spin diffusion system in α-RuI_3.

Chapter 6 presents results on a new 2D triangular lattice material $DyTa_7O_{19}$. I illustrate the persistent spin dynamics at 40 mK using μSR, provide additional results on related compounds, and discuss the difference between Kramers and non-Kramers ions from the point of view of μSR studies.

Chapter 7 investigates the magnetic properties of the B-site substituted pyrochlore compounds Pr_2ScTaO_7 and Pr_2ScNbO_7. I show the effect of chemical substitution of the non-magnetic site on the non-Kramers Pr^{3+} ions, present high-field magnetisation and μSR measurements on these materials, and explore the effect of hyperfine interaction on the low-lying singlet states.

Chapter 8 presents μSR studies on two Weyl semimetals compounds CeAlSi and NdAlSi. I show results on the muon site calculations and findings on the magnetic structure and explore the formation of domains and magnetic disorder in

both compounds. In addition, I give evidence for a link between bulk magnetisation and peaks in the TF-μSR frequency spectrum.

Chapter 9 provides the summary of this thesis and outlines some of the future work that could be carried out.

Appendix A includes the derivations of the Larmor diamagnetism, the Van Vleck paramagnetism, and the Van Vleck susceptibility.

Appendix B includes the derivation of the Landé g-factor.

2

Theoretical Background

Contents

2.1 Magnetic Moments

Consider an atom with Z electrons, each with charge $-e$, the Hamiltonian in the absence of the field can be written as the sum of the kinetic energy and potential energy of all electrons so that

$$H_0 = \sum_{i=1}^{Z} \left(\frac{\hat{\mathbf{p}}_i^2}{2m_e} + \hat{V}_i \right), \tag{2.1}$$

where $\hat{\mathbf{p}}_i$ is the momentum operator of the i-th electron. In the presence of a magnetic field $\mathbf{B} = \boldsymbol{\nabla} \times \mathbf{A}$, where the gauge for the magnetic potential $\mathbf{A}$ is chosen to be $\mathbf{A}(\mathbf{r}) = \frac{1}{2}\mathbf{B} \times \mathbf{r}$, the momentum operator becomes $\hat{\mathbf{p}}' = \hat{\mathbf{p}} - q\mathbf{A}(\mathbf{r}) = \hat{\mathbf{p}} + e\mathbf{A}(\mathbf{r})$

and the Hamiltonian in Eqn. 2.1 is modified to be

$$H = \sum_{i=1}^{Z} \left(\frac{\hat{\mathbf{p}}_i'^2}{2m_e} + \hat{V}_i \right) + g\mu_{\mathrm{B}} \mathbf{B} \cdot \hat{\mathbf{S}}, \tag{2.2}$$

$$= \sum_{i=1}^{Z} \left(\frac{\hat{\mathbf{p}}_i^2}{2m_e} + \hat{V}_i + \frac{e}{2m_e} \hat{\mathbf{p}}_i \cdot [\mathbf{B} \times \mathbf{r}_i] + \frac{e^2}{2m_e} \mathbf{A}(\mathbf{r_i})^2 \right) + g\mu_{\mathrm{B}} \mathbf{B} \cdot \hat{\mathbf{S}}, \tag{2.3}$$

$$= H_0 + \underbrace{\mu_{\mathrm{B}} \left(\hat{\mathbf{L}} + g_S \hat{\mathbf{S}} \right) \cdot \mathbf{B}}_{\text{paramagnetism}} + \underbrace{\sum_{i=1}^{Z} \frac{e^2}{8m_e} (\mathbf{B} \times \mathbf{r}_i)^2}_{\text{diamagnetism}}. \tag{2.4}$$

where the Zeeman term for the total spin angular moment $\mathbf{S}$ has been included, and that $\sum_i \hat{\mathbf{p}}_i \cdot (\mathbf{B} \times \mathbf{r}_i) = \sum_i \mathbf{B} \cdot (\mathbf{r}_i \times \hat{\mathbf{p}}_i) = \mathbf{B} \cdot \hat{\mathbf{L}}$ [18].

The paramagnetic part of Eqn. 2.4 is the essence of magnetism; an atom that has a total spin $\mathbf{S}$ or a partially-filled orbital (and hence non-zero $\mathbf{L}$) will have a magnetic moment.

We can re-write Eqn. 2.4 as $H = H_0 + H'$ and apply the (non-degenerate) perturbation theory on the ground state $|\Psi_0\rangle$. We obtain the first-order correction in energy

$$\Delta E^{(1)} = \mu_{\mathrm{B}} \left\langle \Psi_0 \middle| \left(\hat{\mathbf{L}} + g_S \hat{\mathbf{S}} \right) \cdot \mathbf{B} \middle| \Psi_0 \right\rangle + \frac{e^2}{8m_e} \sum_i \left\langle \Psi_0 \middle| (\mathbf{B} \times \mathbf{r}_i)^2 \middle| \Psi_0 \right\rangle, \tag{2.5}$$

which gives the paramagnetic and diamagnetic responses as expected. In addition, the second-order correction in energy (keeping only the B^2 terms) is given by

$$\Delta E^{(2)} = \mu_{\mathrm{B}}^2 \sum_{j>0} \frac{\left| \left\langle \Psi_0 \middle| \left(\hat{\mathbf{L}} + g_S \hat{\mathbf{S}} \right) \cdot \mathbf{B} \middle| \Psi_0 \right\rangle \right|^2}{E_0 - E_j}, \tag{2.6}$$

which is known as the Van Vleck paramagnetism. The full derivation of the diamagnetism and the Van Vleck paramagnetism contributions to the magnetic susceptibility are presented in Appendix A.

2.2 Interactions

Magnetic moments in solid-state materials can interact in a number of ways and identifying the dominant interaction(s) provides us deeper insight into the nature of the underlying magnetism in a material. These interactions, together with the geometry, crystal field, and spin-orbit coupling, collectively shape the resulting

magnetic structure and spin dynamics. For example, the balance between the nearest-neighbour exchange interaction and the dipolar coupling of the rare-earth moments in pyrochlore compounds $RE_2Ti_2O_7$ is known to produce complex spin arrangements and magnetic behaviours (also see Chapter 7). In this Section, I will outline the most common interactions discussed in this thesis: the magnetic dipolar interaction and the exchange interaction, the former is of significant importance to the muon spin rotation spectroscopy and when the rare-earth moments are relatively large. Other coupling schemes, such as the hyperfine interaction that can be play a role in metallic compounds, will be addressed in relevant Chapters.

2.2.1 Magnetic dipolar coupling

The magnetic dipolar coupling (or dipole-dipole coupling) refers to the interaction between two magnetic moments. A dipole moment generates a magnetic field which couples to another dipole moment and this can be mathematically expressed using the Hamiltonian

$$H = \frac{\mu_0}{4\pi|\mathbf{r}|^3}\left[\boldsymbol{\mu}_1 \cdot \boldsymbol{\mu}_2 - 3(\boldsymbol{\mu}_1 \cdot \hat{\mathbf{r}})(\boldsymbol{\mu}_2 \cdot \hat{\mathbf{r}})\right] \tag{2.7}$$

where $\hat{\mathbf{r}}$ is the unit vector between two magnetic dipole moments $\boldsymbol{\mu}_1$ and $\boldsymbol{\mu}_2$.

In terms of the muon spin rotation (μSR) spectroscopy (see Chapter 3), each muon, which is a spin-$\frac{1}{2}$ particle, carries a magnetic dipole moment. When they are placed in a crystal, the muon is exposed to a collective sum of magnetic fields generated by all nearby magnetic ions via the magnetic dipole-dipole interaction, so using Eqn. 2.7, the local field at the position of the muon is given as

$$B^{\alpha}_{\mathrm{dip}}(\mathsf{r}_\mu) = \sum_i D_i^{\alpha\beta}(\mathsf{r}_\mu) m_i^{\beta}, \tag{2.8}$$

where the dipolar tensor $D_i^{\alpha\beta}$ is given by

$$D_i^{\alpha\beta}(\mathsf{r}_\mu) = \frac{\mu_0}{4\pi|\mathbf{R}_i|^3}\left(\frac{3R_i^{\alpha}R_i^{\beta}}{\mathbf{R}_i^2} - \delta^{\alpha\beta}\right), \tag{2.9}$$

where R_i^{α} refers to the component of the displacement vector ($\mathbf{R}_i = \mathsf{r}_\mu - \mathsf{r}_i$) between the muon and the i-th magnetic moment m_i [19].

2.2.2 Exchange interaction

In quantum mechanics, indistinguishable fermions have to satisfy the exchange symmetry given by $\Psi(\mathbf{r}_1, \mathbf{r}_2) = -\Psi(\mathbf{r}_1, \mathbf{r}_2)$, and therefore, one has to construct an overall antisymmetric wavefunction for a system of electrons. When the Hamiltonian is evaluated with such a state for two electrons, a quantity known as the exchange integral appears, which is half the energy difference between the singlet and the triplet state. While the full description of different types of exchange interactions is out of the scope of this thesis, in most oxide compounds we are dealing with the *superexchange interaction* – an exchange interaction mediated via non-magnetic anions' orbitals and favours antiferromagnetism [18].

Consider a system that contains only the nearest neighbour exchange interactions, the Hamiltonian is given by

$$H = -\sum_{\langle ij \rangle} S_i^{\mu} J_{ij}^{\mu\nu} S_j^{\nu}, \tag{2.10}$$

where $J_{ij}^{\mu\nu}$ is the exchange tensor that connects spin S_i at site-i and spin S_j at site-j, and μ, ν can be x, y, or z. For $J^{\mu\nu} = J\delta^{\mu\nu}$, this is known as the Heisenberg model where $H_{\text{Heisenberg}} = -J \sum_{\langle ij \rangle} \mathbf{S}_i \cdot \mathbf{S}_j$. The values of the exchange tensor $J_{ij}^{\mu\nu}$ depend on the geometry of the crystal and the arrangement of the electron orbitals.

Magnetic anisotropy exists for magnetic ions in many materials and it could be caused by the orbital interactions or the crystal electric fields (see Section 2.3). In this case, the exchange couplings between magnetic moments can be more significant in some directions than others. For example, when there is an easy-axis anisotropy along $\mathbf{z}$, the interaction of the z-component of the spin becomes the most important and consequently Eqn. 2.10 can be simplified to become

$$H_{\text{Ising}} = -J \sum_{\langle ij \rangle} S_i^z S_j^z, \tag{2.11}$$

which is known as the Ising model. On the other hand, when a magnetic ion exhibits an easy-plane anisotropy, its spin lies in the local XY plane and Eqn. 2.10 becomes what is known as the XY model

$$H_{\text{XY}} = -J \sum_{\langle ij \rangle} (S_i^x S_j^x + S_i^y S_j^y), \tag{2.12}$$

assuming isotropic exchange along the XY plane ($J = J^x = J^y$), and H_{XY} has a continuous O(2) rotation symmetry. Equivalently, one can express Eqn. 2.12 in terms of raising and lowering spin operators S^- and S^+ so that

$$H_{\mathrm{XY}} = -\frac{J}{2}\sum_{\langle ij\rangle}(S_i^+ S_j^- + S_i^- S_j^+), \tag{2.13}$$

which demonstrates the transverse (XY) components of the Heisenberg Hamiltonian in Eqn. 2.10 encourage spin-flipping. This is important in a wide range of frustrated systems in which easy-axis anisotropy stems from the crystal field environments; the small but non-vanishing transverse exchange interaction, together with geometric frustration, can engineer a highly frustrated magnetic spin system which comprises strong quantum fluctuation in the effective $J = \frac{1}{2}$ Ising-like ground state. Examples of this include the 2D triangular lattice material in Chapter 6 and 3D pyrochlore oxides in Chapter 7.

2.3 Crystalline Electric Fields

Crystalline Electric Fields (CEF), or simply Crystal Fields, refer to the static electric fields experienced by a magnetic ion when it is placed inside a crystal. The crystal field theory describes how the free-ion degenerate energy is split into a number of energy states due to the surrounding ligands. This effect is prominent in many materials, especially in many oxide compounds when oxide anions (O^{2-}) are located around the transition metal cations.

3d transition metal ions

Transition metal ions contain 3d orbitals where the radial wavefunctions are more spread out than those in 4f orbitals and they can directly interact with the 2p orbitals of the O^{2-} ions, or other relevant orbitals for other ligands, therefore, the CEF interaction is much stronger than the spin-orbit coupling (or LS-coupling) so that

$$\mathbf{H}_{\mathrm{free}} \overset{\mathrm{crystal}}{\rightarrow} \gg \mathbf{H}_{\mathrm{CEF}} \gg \mathbf{H}_{\mathrm{SO}}, \tag{2.14}$$

where $\mathbf{H}_{\text{free}}$ refers to the Hamiltonian of the free transition metal ion. In such as case, one should first consider the CEF splitting of the five degenerate 3d states in $\mathbf{H}_{\text{free}}$. Using an octahedral ligand environment as an example, the five 3d states split into three lower energy t_{2g} states and two excited e_g states.

Generally, it is found that the 3d ions are better represented by a $J = S$ state instead of a $J = L + S$ state [18]. This is an effect called orbital quenching, where the 3d ions have zero orbital angular momentum ($L = 0$). The total spin S of a 3d ion depends on the pairing energy (the energy cost for two 3d electrons with opposite spins occupying the same orbital) and can be classified as the Low Spin and High Spin cases; for the Low Spin case, the spin fills the lowest energy state (e.g. t_{2g}) before filling any upper e_g state so that some spins can cancel each other and hence Low Spin. In contrast, when the pairing energy cost is high, the spins avoid occupying the same states, and therefore, produce a higher overall spin S. Because $L \approx 0$ for 3d ions, the $\mathbf{H}_{\text{SO}}$ term is generally very small and is treated as a weak perturbation.

4f rare earth ions

The 4f orbitals have radial wavefunctions that are more localised than the 3d orbitals, as a result, the overlap with the ligands' orbitals are smaller for a 4f ion and the interaction is mainly an electrostatic one which means that the CEF effect is much weaker than in 3d ions. The energy hierarchy in a 4f ion in a crystal is given by

$$\mathbf{H}_{\text{free}} \gg \mathbf{H}_{\text{SO}} \overset{\text{crystal}}{\gg} \mathbf{H}_{\text{CEF}}, \tag{2.15}$$

where the LS-coupling is considered first and the CEF effect becomes a perturbation of the system.

In these systems, the magnetic moments $\mathbf{L}$ and $\mathbf{S}$ are given by the sum of orbital and spin angular momentum of individual electrons, i.e.

$$\mathbf{L} = \sum_i \mathbf{l}_i \text{ and } \mathbf{S} = \sum_i \mathbf{s}_i, \tag{2.16}$$

and that $\boldsymbol{\mu}_L = \mu_{\text{B}}\mathbf{L}$ and $\boldsymbol{\mu}_S = g_S\mu_{\text{B}}\mathbf{S}$.

A classical way of describing the spin-orbit coupling H_{SO} is to treat the orbital $\mathbf{L}$ as a current that generates a magnetic field $\mathbf{B}$, and therefore, with a spin $\mathbf{S}$,

the system gets an additional energy contribution $E = -\boldsymbol{\mu_S} \cdot \mathbf{B}$. If we assume that $\mathbf{B}$ is proportional to $\mathbf{L}$, one can write this as

$$\mathbf{H}_{\mathrm{SO}} \propto \mathbf{L} \cdot \mathbf{S}. \tag{2.17}$$

As a result, the basis $\{|m_L\rangle \otimes |m_S\rangle\}$ can no longer be the eigenstates of the system but the total angular momentum eigenstates $|J, m_J\rangle$ are, and that $\mathbf{J} = \mathbf{L} + \mathbf{S}$. With a total angular momentum of $\mathbf{J}$, a free 4f ion has $2J + 1$ degenerate states, and the states $|m_J\rangle$ spam from $|m_J = -J\rangle$ to $|m_J = +J\rangle$.

Similar to the electron orbitals in a hydrogen atom, the eigenstates of the free ion of momentum $\mathbf{J}$ can be expressed as spherical harmonics

$$Y_k^q(\theta, \phi) = N e^{iq\phi} P_k^q(\cos\theta), \tag{2.18}$$

where $P_k^q(x)$ is the associated Legendre polynomial with $0 \leq k$ and $-k \leq m \leq k$. Therefore, it is usually convenient to express the CEF perturbation H_{CEF} in Eqn. 2.15 as a linear combination of these spherical harmonics of J so that

$$H_{\mathrm{CEF}} = \sum_{k,q} B_q^k O_q^k, \quad \text{where} \quad O_q^k \propto Y_k^q(\theta, \phi), \tag{2.19}$$

where C_q^k are the Stevens operators and B_q^k are the CEF parameters (the coefficient for each operator O_q^k) [20]. In general, k and q are similar to l and m_l for the orbital angular momentum of an electron; k can take any value from 0 to $2l$, and when the electrons are solely equivalent, odd k vanishes and hence $k = 0, 2, 4$ or 6 for rare earth materials. Meanwhile, the value for q is restricted between $-k$ and k, and it must match the CEF symmetry around the central ion.

Using Pr^{3+} ions of a pyrochlore structure as an example (also see Chapter 7); Pr^{3+} ($4f^2$, $L = 5$, $S = 1$, $J = 4$) ion contains two 4f electrons ($l = 3$), therefore, $k = 0$, 2, 4, or 6. In terms of the CEF environment, it has a D_{3d} point group symmetry, which includes symmetries operations C_3 and S_6, therefore the possible values for q are $0, 3,$ and 6. Explicitly, the H_{CEF} is given by

$$H_{\mathrm{CEF}} = \underbrace{B_0^2 C_0^2}_{k=2} + \underbrace{B_0^4 O_0^4 + B_3^4 O_3^4}_{k=4} + \underbrace{B_0^6 O_0^6 + B_3^6 O_3^6 + B_6^6 O_6^6}_{k=6}. \tag{2.20}$$

The Stevens operators can be expressed in terms of angular momentum operators J, i.e. $O_q^k = O_q^k(\mathbf{J})$, and for example, $O_6^6 = \frac{1}{2}\left[J_+^6 + J_-^6\right]$. Therefore, the effect of the CEF perturbation H_{CEF} is to select and form eigenstates with distinct energy levels from the otherwise degenerate $|J, m_J\rangle$ eigenbasis.

4d & 5d transition metal ions

In materials containing 4d and 5d ions, the electronic wavefunctions are more spatially spread out than the 3d orbitals, thus increasing the chance of metallicity [21]. Meanwhile, the effect of orbital quenching is less effective in 4d and 5d orbitals, giving a non-zero orbital angular momentum L, which means that the magnitude of the CEF term and the spin-orbit coupling term are now comparable, i.e.

$$\mathbf{H}_{\text{free}} \overset{\text{crystal}}{\gg} \mathbf{H}_{\text{CEF}} \approx \mathbf{H}_{\text{SO}}, \tag{2.21}$$

and as a result, one has to examine the underlying interactions case-by-case in order to write down the effective ground state.

2.4 Kramers Theorem

The Kramers theorem states that for a system with an odd number of (identical) electrons, the energy levels are always at least doubly degenerate [22, 23]. A formal derivation of Kramers theorem is set out by considering the time-reversal symmetry of a pair of half-integer states $\left|m_J = \pm\frac{n}{2}\right\rangle$ [24]. The matrix element of the crystalline electric fields, which can be represented by a potential $H_{\text{CEF}} = \sum_{k,q} V_q^k$, is transformed under the time-reversal symmetry by

$$M \propto \left\langle \frac{n}{2}\middle|\sum_{k,q} V_q^k\middle|-\frac{n}{2}\right\rangle = (-1)^n \left\langle -\frac{n}{2}\middle|\sum_{k,q} V_q^{k*}\middle|\frac{n}{2}\right\rangle, \tag{2.22}$$

where V_q^k is a function of the Stevens operators O_q^k. And because O_q^k for even k is always Hermitian, so that $V_q^k = V_q^{k*}$, the matrix element M for a system with an odd number of 4f electrons (i.e. odd n and even k) vanishes. As a result, with no off-diagonal matrix element within the doublet states $\left|\pm\frac{g}{2}\right\rangle$, the degeneracy of a Kramers ion is always protected against CEF distortion [24].

In the context of μSR spectroscopy, which will be thoroughly explained in Chapter 3, positively charged muons (μ^+) are sent into a crystal. Because of the Coulomb interaction between the muon and the nearby ions, the implanted muon can distort the CEF environment and symmetry around a magnetic ion. This is where the Kramers theorem becomes important in understanding the effect of the muon on the CEF energy levels of the magnetic ions.

As we shall see in Chapters 6 and 7, rare-earth ions with even number of electrons and hence integer spin S, such as the Pr^{3+} and Tb^{3+} ions, can have an effective $J = \frac{1}{2}$ ground state which is split by the CEF distortion. On the other hand, with an odd number of 4f electrons, the ground states in the Nd^{3+} and Yb^{3+} ions are always protected against any distortion in the electric field. However, one should note that the degenerate $\pm m_J$ states are not protected under an applied magnetic field because $\mathbf{B}$ changes sign upon time-reversal $t \rightarrow -t$.

Kramers theorem is therefore a powerful tool to predict the magnetic properties of a material based on its CEF symmetry and structural properties. It also reflects that non-Kramers ions are much more susceptible to structural or chemical disorder as the magnetic moment of the effective $J = \frac{1}{2}$ ground state can vanish at very low temperatures when the atom occupies only the lowest singlet state and becomes $J = 0$.

3
Methods

Contents

This chapter lays the foundation by introducing the essential experimental and computational methods applied throughout this thesis. These techniques encompass SQUID magnetometry, moun spin rotation spectroscopy (μSR), density functional theory (DFT) and crystal field calculations. Notably, this chapter focuses on the most widely used methods and excludes other techniques, such as AC susceptibility and heat capacity measurements, which will be discussed in dedicated chapters where they have specific relevance.

3.1 Magnetometry

Magnetometric measurements presented in this thesis are performed using a Quantum Design Magnetic Property Measurement System (MPMS3) which operates with a superconducting quantum interference device (SQUID) sensor that monitors the change in magnetic flux as the sample undergoes a sinusoidal movement within a superconducting pick-up coil [25, 26]. The MPMS3 system offers an operating temperature range from 1.8 K to 300 K (extendable to 500 mK with the additional Helium-3 module) and can apply an external magnetic field up to 7 T. Therefore, it is an extremely powerful machine for researchers to characterise and investigate the magnetic properties of their samples within a range of conditions.

In this section, I present the key magnetometry techniques that are repeatedly employed in the following chapters: (1) magnetisation as a function of field M(H) and (2) magnetic susceptibility as a function of temperature $\chi(T)$, while holding other parameters constant whenever possible.

3.1.1 Magnetisation

Magnetisation refers to the sum of magnetic moments per unit volume and, by studying its changes as a function of field and temperature, one can extract information about the magnetic state of the material.

The magnetisation of a material in the paramagnetic state can be written as

$$M(H) = Ng\mu_{\mathrm{B}}B_J(H), \tag{3.1}$$

where N is the density of magnetic ion per unit volume, g is the g-factor of the system, and $B_J(H)$ is the Brillouin function given by

$$B_J(x) = \frac{2J+1}{2J}\coth\left(\frac{2J+1}{2J}x\right) - \frac{1}{2J}\coth\left(\frac{1}{2J}x\right), \tag{3.2}$$

where J refers total angular momentum quantum number of the system and $x = \frac{\mu_0 g J \mu_{\mathrm{B}} H}{k_{\mathrm{B}} T}$ is the ratio of the magnetic moment in an external field to the thermal energy.

At a high magnetic field, the magnetisation curve approaches a saturation value $M_{\text{sat}} = Ng\mu_{\text{B}}$ where the material becomes fully magnetized. This refers to the situation in which all the moments are aligned along the applied field and one can compare the measured magnetic moment per ion with the theoretical predictions to verify the magnetic properties of the material.

In general, examples of magnetic behaviours that magnetisation curves can reveal include, but are not limited to, hysteresis loops in ferromagnetic materials, domain wall formations, 1/3-plateau in antiferromagnetic magnets, and magnetic anisotropy by applying H along different axes. Therefore, magnetisation measurements can give us valuable insights into the properties exhibited by different materials, especially at temperatures below their transition temperature.

3.1.2 Magnetic susceptibility

Magnetic susceptibility χ is the response of the system's magnetisation M in a small applied field H, in the limit where H goes to 0. Mathematically, one can express the quantity χ as

$$\chi(T) = \lim_{H \to 0} \frac{M(H,T)}{H}. \tag{3.3}$$

Ideally, the applied field H used for magnetic susceptibility measurements should be as small as possible, but it cannot be zero because it would lead to a zero signal. In practice, the minimum applied field B is of the order of 100 G (or equivalently 10 mT) to prompt a sizeable response and reduce uncertainty against other background signals and noise.

The magnetic susceptibility of a magnetic material usually comprises two main terms: the Curie-Weiss paramagnetism χ and the Larmor diamagnetism χ_{D}. The former is significantly stronger and originates from unpaired electrons in the outermost orbital of an atom, where there orbital and spin angular momenta magnetic moments add up to give a magnetic moment.

Paramagnetism

The Curie-Weiss law outlines how magnetic susceptibility χ behaves as a function of temperature T for an ideal paramagnet according to

$$\chi = \frac{C}{T}, \tag{3.4}$$

where C is the Curie constant. However, there might be additional interactions that would prefer a certain alignment between the magnetic moments. One such interaction is the exchange interaction which is observed in most oxide compounds and connects one spin to another via an oxygen atom. In this case, competition exists between the thermal paramagnetic fluctuations and the ordering forces. The Curie-Weiss law is then modified to

$$\chi = \frac{C}{T - \theta_{\mathrm{CW}}}, \tag{3.5}$$

where θ_{CW} is called the Curie-Weiss temperature which represents the tipping point between the paramagnetic state and the ordered state [18]. One should note that θ_{CW} is only a theoretical value which is often used to quantify the strength of the alignment forces; for ferromagnetic compounds, θ_{CW} is positive, and negative for antiferromagnetic compounds. The measurement of $\chi(T)$ can be particularly impactful in identifying magnetic transitions across critical regimes where the material's behaviour is expected to change.

By performing a fit to the susceptibility data according to Eqn. 3.5 in the high-temperature regime, where paramagnetic behaviour dominates, the extracted Curie constant C is linked to the effective magnetic moment μ_{eff}, in CGS units, by

$$\mu_{\mathrm{eff}} \approx \sqrt{8C}\,\mu_{\mathrm{B}}. \tag{3.6}$$

From Eqn. 3.5 and Eqn. 3.6, one could infer that $\chi \propto \mu_{\mathrm{eff}}^2$. Therefore, when there are multiple magnetic species, the fitted effective moment per formula unit is linked to individual moments by

$$\mu_{\mathrm{eff}}^2 = \sum_i \mu_{\mathrm{eff,i}}^2\,, \tag{3.7}$$

where $\mu_{\mathrm{eff,i}}$ is its effective moment of the i-th magnetic atom in the formula unit.

Langevin diamagnetism

The other contribution to the magnetic susceptibility is the Langevin diamagnetism. This takes all electrons into account and the contribution from each type of atom is given by

$$\chi_{\mathrm{D}} = -\frac{ne^2}{6m_e c^2}\sum_i \left\langle r_i^2 \right\rangle \tag{3.8}$$

in CGS units, where n is the atomic density and $\langle r_i^2 \rangle$ is the mean squared radial distance evaluated for the i-th electronic wavefunction [18]. The Langevin diamagnetism is always negative as it physically represents a current induced to oppose the applied field H. In a magnetometry measurement, it is important that one also checks for the diamagnetic signal of the sample holder as it could be significant when the sample mass is small or when the signal is relatively weak.

To summarise, we can write the overall magnetic susceptibility as

$$\chi(T) = \frac{C}{T - \theta_{\mathrm{CW}}} + \chi_0, \tag{3.9}$$

where χ_0 includes the temperature-independent terms such as the Langevin diamagnetism χ_{D}.

4f Rare earth moments

For 4f rare earth elements, where the $2J+1$ degenerate levels are split by the crystal electric field (CEF) environment, the energy states become a superposition of orbital angular momentum states, for example in pyrochlores (which will be discussed in Chapter 7), the ground state is given by $|\mathrm{GS}_{\pm}\rangle = |m_J = \pm 4\rangle$ for Pr^{3+} moments in an octahedral CEF environment. Because of spin-orbit coupling (also called LS-coupling), the Landé g-factor of the quantum number **J** is given by

$$g_J = \frac{3}{2} + \frac{S(S+1) - L(L+1)}{2J(J+1)} \tag{3.10}$$

of which the derivation is provided in Appendix B. The magnetic moment in the doublet ground state is given by

$$\mu_{\mathrm{GS}} = \left\langle \mathrm{GS}_{\pm} \middle| g_J \hat{J}_z \middle| \mathrm{GS}_{\pm} \right\rangle \ \mu_{\mathrm{B}} = 3.2\ \mu_{\mathrm{B}}, \tag{3.11}$$

where $g_J = 0.8$ for Pr^{3+} ($4f^2$, $L = 5$, $S = 1$, and $J = 4$) in the $^3H_4$ multiplet.

The magnetic susceptibility of a rare earth ion is often found to deviate from the Curie-Weiss law at low temperatures. This is because the system slowly de-occupies the upper levels and populates the ground state as it is cooled and the $|m_J\rangle$ composition for each energy eigenstate varies. To account for this, we can express the Boltzmann-weighted effective moment at temperature T as

$$\mu_{\text{eff}}^2(T) = \frac{\mu_0^2 + \sum_{\text{i}} \mu_{\text{i}}^2 e^{-\beta\Delta_i}}{1 + \sum_{\text{i}} e^{-\beta\Delta_{\text{i}}}}\,, \tag{3.12}$$

where μ_{i} and Δ_i refer to the effective moment and the energy of the i-th excited state (relative to the ground state) respectively [21].

Additionally, the temperature-independent Van Vleck paramagnetism, as shown in Eqn. 2.6, contributes to the magnetic susceptibility χ_{VV} and it could become significant effect when the system occupies many energy states at room temperature, especially for Sm^{3+} and Eu^{3+} ions. Therefore, the magnetic susceptibility for 4f rare earth systems can be written as

$$\chi(T) = \frac{\mu_0^2 + \sum_{\text{i}} \mu_{\text{i}}^2 e^{-\beta\Delta_i}}{8(T - \theta_{\text{CW}})(1 + \sum_{\text{i}} e^{-\beta\Delta_{\text{i}}})} + \chi_0\,, \tag{3.13}$$

where $\beta = 1/k_{\text{B}}T$, and χ_0 is a constant term that includes all temperature-independent contributions such as χ_{D} and χ_{VV}.

3.2 Muon Spin Rotation Spectroscopy (μSR)

A muon is a fundamental particle that forms part of the building block of our universe. It belongs to the family of elementary particles called leptons and behaves very much like an electron, its lighter family member. In fact, muons are everywhere – when the cosmic radiation [27] that comes from outer space collides with the Earth's atmosphere, a shower of secondary particles, which includes muons, is created and hits the surface of Earth. These muons, however, are not fit for experimental purposes. First of all, the flux rate of cosmic muons at sea level is about 1 per cm^2 per minute [28], meaning that one would have to wait for an incredibly long time to collect any meaningful data. Second, they are too energetic. Their energy

of 4 GeV [28] would penetrate through the samples without any difficulty. But perhaps most importantly, cosmic muons are unpolarised and the isotropic setting makes it impossible for us to track the spin precession.

In spite of that, high-intensity muon beams can be produced at large facilities where cyclotrons are used to accelerate proton beams to energies between 500 MeV and 3 MeV which make a head-on collision with a graphite target to produce positive and negative pions $\pi^{\pm}$ at rest on the surface of the target. A pion is a hadronic meson particle that has a short lifetime of 26 ns, and it subsequently decays into a muon and a muon neutrino via a weak boson W, so that for a position pion,

$$\pi^{+} \xrightarrow{\mathrm{W}^{+}} \mu^{+} + \nu_{\mu}, \tag{3.14}$$

where the muon produced is 100% spin-polarised and has an energy of around 4 MeV [29]. These muons are then sent through the beamlines with their spins antiparallel to their direction of travel.

The ability to produce a high flux of spin-polarised muons leads to the possibility of using positive muons to study a wide range of materials by an experimental technique called the Muon Spin Rotation (μSR) spectroscopy [19, 29, 30]. In μSR experiments, the sample is placed in a cryostat and is bombarded with the incoming muon flux. As a muon enters the sample, it loses kinetic energy through collisions with other atoms, slows down gradually, and stops at a position which has the lowest potential energy called the muon stopping site [31] (also see Section 3.3.3). At this position, the muon is exposed to the local magnetic field generated by nearby magnetic ions (and also any externally applied field). As a spin-$\frac{1}{2}$ particle, a muon has a magnetic moment and it precesses around the local magnetic field according to the gyromagnetic ratio of 135 MHz T^{-1}.

The muon does not live in the sample forever. Being an unstable particle, with an average lifetime of 2.2 μs, it decays into a positron and two neutrinos via a weak interaction process

$$\mu^{+} \rightarrow e^{+} + \bar{\nu}_{\mu} + \nu_{e}, \tag{3.15}$$

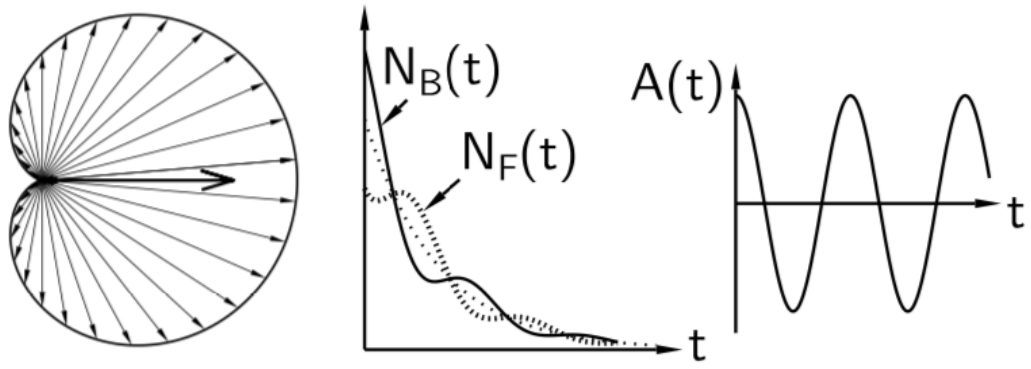

(a) (b)

Figure 3.1: (a) Probability distribution of positron emission with respect to muon spin (represented by the arrow). (b) Forward and backward count rates N_{F} and N_{B} and the resulting asymmetry function given by Eqn. 3.16 when all muons precess in a uniform magnetic field. These figures are extracted from [19].

where parity violation means that the positron is preferentially emitted into the direction of the muon spin (see Fig. 3.1(a)) [32, 33]. With a rest mass of approximately 200 m_{e}, the muon is significantly heavier than the positron, and therefore, the positron acquires a substantial amount of kinetic energy, leaves the sample, and is ultimately picked up by the surrounding detectors.

The nature of the probabilistic emission is the reason why many millions of muons are normally used to collect enough statistics to resolve the muon spin direction. (In other words, only if we had enough positron emission events could we have assembled the distribution in Fig. 3.1(a), and hence, found the direction of the arrow.)

Due to the initial backward polarization of the muons, the group of backward detectors initially measures a higher positron count N_{B} as compared to the forward detectors N_{B}. As the muon spins precess over time, the forward and backward (F-B) counts oscillate around an exponential decay curve reflecting the overall muon decay rate, as illustrated in Fig. 3.1(b). These oscillations originate from the changing probability of positrons being emitted in the forward or backward directions. This information is then captured in the muon asymmetry $A(t)$, defined as the difference between the F-B counts,

$$A(t) = A_0 P(t) = \frac{N_{\mathrm{B}} - \alpha N_{\mathrm{F}}}{N_{\mathrm{B}} + \alpha N_{\mathrm{F}}} \tag{3.16}$$

as a function of time and normalized by their sum, where $P(t)$ is the muon polarisation, A_0 is the initial asymmetry, and α is the detector efficiency, of the order of unity, that depends on the F-B detector geometry and the exact sample location [34].

Interpreting the muon asymmetry plot can occasionally be challenging. However, a Fast Fourier Transform (FFT) [35] of the asymmetry can provide a better visual representation and inform us about the internal field distribution at the muon site(s). The FFT of the asymmetry is written as

$$I(\omega) \propto \int_0^{t_1} A(t) e^{-i\omega t}\, dt, \tag{3.17}$$

where t_1 is the time window of $A(t)$ used in the FFT and $I(\omega)$ is the Fourier intensity spectrum against ω. This is a particularly useful method when the data involves fast oscillations [36], multiple oscillations [37], or when there is a broad distribution of local field that leads to fast damping, as shown in the μSR data in Chapters 4 and 8. The μSR data presented in this data are analysed using the WIMDA software [38] which also comes with the capabilities to perform fitting and to extract key parameters.

μSR facilities are currently available at five large-scale facilities around the world, these are at the

1. ISIS Neutron and Muon Source, UK,
2. Paul Scherrer Institute, Switzerland,
3. Japan Proton Accelerator Research Complex, Japan,
4. MuSIC muon centre, Japan, and
5. TRIUMF, Canada.

μSR has become one of the key spectroscopy methods in magnetism research and it allows researchers to study the underlying magnetic properties over a wide range of conditions (temperature, applied field, pressure, etc) in different magnetic phases. Over the course of years, many μSR-specific techniques have been developed to study

a variety of quantum materials, including the zero, longitudinal, and transverse field methods that are outlined in the following sections. Other advanced techniques include, but are not limited to, muon spin echo [39], RF resonance [40], and electric field μSR [41].

The sample mounting process for μSR experiments are straightforward, one typically load powder samples or single crystals into a silver packet which is then taped to the sample holder, this could either be a copper fork or a silver plate (the latter is usually used for measurements involving dilution refrigerator and in which case one should apply suitable cryogenic vacuum grease to enhance the thermal contact between the sample and the sample plate).

3.2.1 Zero Field μSR

Zero Field (ZF-)μSR measurement is the most widely used technique used in μSR experiments. With zero applied field, the implanted muons experience only the intrinsic magnetic environment within the sample. This method acts as the initial probe to explore the spin dynamics and to identify potential magnetic transitions in a material before subsequent measurements with externally applied fields. Here, I will delve into the connection between the muon precession and some frequently observed asymmetry curves by reviewing various scenarios of local field distribution that muons might encounter within a magnetic material.

The Hamiltonian of a quantum spin $\mathbf{S}$ in a magnetic field $\mathbf{B}$ can be written as

$$\hat{\mathbf{H}} = -\hat{\boldsymbol{\mu}} \cdot \mathbf{B} = -\gamma \hat{\mathbf{S}} \cdot \mathbf{B}, \tag{3.18}$$

where μ and γ are the magnetic moment and the gyromagnetic ratio of the spin respectively (for muons, $\gamma_\mu = 135.53$ MHz T^{-1}), and $\hat{\mathbf{S}}$ is the spin operator. If we imagine a muon polarised in $\hat{\mathbf{z}}$ with a field applied in a general $\hat{\mathbf{n}}$ direction system, where $\hat{\mathbf{n}} = (\sin\theta\cos\phi, \sin\theta\sin\phi, \cos\theta)$ in spherical coordinates. The Hamiltonian of the setup is given by

$$\hat{\mathbf{H}} = \frac{1}{2}\hbar\gamma B \hat{\mathbf{n}} \cdot \hat{\boldsymbol{\sigma}}, \tag{3.19}$$

where the spin operator $\hat{\mathbf{S}}$ in Eqn 3.18 has been replaced by $\frac{\hbar}{2}\hat{\boldsymbol{\sigma}}$. This represents that the polarised muon implanted in the material sees a local magnetic field of $\mathbf{B}_{\text{loc}}$ which points in $\hat{\mathbf{n}}$. The energy eigenstates of Eqn 3.19 are

$$|+,\hat{\mathbf{n}}\rangle = \begin{pmatrix} e^{-i\frac{\phi}{2}}\cos\frac{\theta}{2} \\ e^{i\frac{\phi}{2}}\sin\frac{\theta}{2} \end{pmatrix} \text{ and } |-,\hat{\mathbf{n}}\rangle = \begin{pmatrix} e^{-i\frac{\phi}{2}}\sin\frac{\theta}{2} \\ -e^{i\frac{\phi}{2}}\cos\frac{\theta}{2} \end{pmatrix} \tag{3.20}$$

which represent the spin-up and spin-down states respectively along $\hat{\mathbf{n}}$ in the basis of the conventional spin-$\frac{1}{2}$ states along $\hat{\mathbf{z}}$. The energies of these states are given by $E_{\pm} = \mp\frac{\hbar}{2}\gamma_\mu B = \mp\frac{1}{2}\hbar\omega$, where B is the magnitude of the field $\mathbf{B}$ and ω is the muon precession frequency in the unit of radian per second.

The spin state of the muon at $t = 0$ is given by $|\Psi(t=0)\rangle = \begin{pmatrix} 1 \\ 0 \end{pmatrix}$ and hence

$$|\Psi(t=0)\rangle = \cos\frac{\theta}{2}\,|+,\hat{\mathbf{n}}\rangle + \sin\frac{\theta}{2}\,|-,\hat{\mathbf{n}}\rangle\,, \tag{3.21}$$

and at times t by

$$|\Psi(t)\rangle = e^{i\frac{\omega t}{2}}\cos\frac{\theta}{2}\,|+,\hat{\mathbf{n}}\rangle + e^{-i\frac{\omega t}{2}}\sin\frac{\theta}{2}\,|-,\hat{\mathbf{n}}\rangle\,. \tag{3.22}$$

To connect the muon's state to the polarisation function, we can use Eqns 3.20 and 3.22 and obtain the polarisation $P(t)$ at time t of the muon spin, which is given by the expectation value of $\sigma_z(t)$ (i.e. measuring the muon spin along $\hat{\mathbf{z}}$), as

$$P_z(t) = \langle\hat{\boldsymbol{\sigma}}_z(t)\rangle = \cos^2\theta + \sin^2\theta\cos\left(\gamma_\mu B t\right) \tag{3.23}$$

by setting the azimuthal angle $\phi = 0$.

A large number of positive muon particles are being used during μSR experiments and the local magnetic environment of each muon may not be identical, therefore, a more general expression to calculate the averaged polarisation is given by

$$P_z(t) = \int p(\mathbf{B})\,\langle\hat{\boldsymbol{\sigma}}_z(t)\rangle\,d^3\mathbf{B}, \tag{3.24}$$

where p($\mathbf{B}$) is the probability density of the local magnetic field $\mathbf{B}$, to account for the varying precession frequencies in a range of local fields.

Identical magnetic field

In the simple case where the local magnetic field only takes one value B_0 and is transverse to the polarised muon spin direction, i.e. $\theta = 90°$ and $\mathbf{B} = \delta(B - B_0)\hat{\mathbf{x}}$, we obtain the polarisation over time

$$P(t) = \cos(\gamma_\mu B t), \tag{3.25}$$

which physically represents the precession of the muon spin along the local field at a perpendicular angle.

Isotropic magnetic field

When the local magnetic field is isotropic, one could average the polarisation function over all θ directions using Eqn 3.23 and Eqn 3.24 and obtain

$$P(t) = \frac{1}{3} + \frac{2}{3}\int_0^\infty p(\mathbf{B})\cos(\gamma_\mu B t)\, d^3\mathbf{B}. \tag{3.26}$$

an equivalent statement of Eqn 3.26 is that, on average, one-third of the muons experience only a field along their spin polarisation and hence do not precess [42].

Isotropic and Gaussian distribution of fields

In materials where the electronic and nuclear moments are randomly oriented, the local magnetic fields $\mathbf{B}$ at the muon sites become isotropic and the distribution becomes Gaussian-like. The probability distribution of the field strength $p(B)$ could be written as the Maxwell-Boltzmann distribution

$$p(B) = \left(\frac{\gamma_\mu^2}{2\pi\Delta^2}\right)^{\frac{3}{2}} (4\pi B^2) e^{-\frac{\gamma_\mu^2 B^2}{2\Delta^2}} \tag{3.27}$$

where Δ/γ_μ is the Gaussian width of the distribution in B_x, B_y and B_z. Using Eqn 3.26 and Eqn 3.27, we obtain the Kubo-Toyabe function [43]

$$P(t) = \frac{1}{3} + \frac{2}{3}\left(1 - \Delta^2 t^2\right) e^{-\frac{\Delta^2 t^2}{2}}, \tag{3.28}$$

which falls at the beginning and recovers to a characteristic one-third static tail at large time t that represents, once again, the $\frac{1}{3}$ of the muons that do not precess.

Incommensurate magnetic structure

Muons in μSR probe a large number of unit cells at roughly the same positions which are known as the muon sites. When a material possesses a commensurate magnetic structure, the magnetic ordering repeats itself after propagating through a number of unit cells, and there are a finite number of muon precession frequencies. In general, the number of precession frequencies, or equivalently peaks in the Fourier spectrum, is the number of distinct local magnetic environments across all unit cells.

In the case where the material hosts an incommensurate magnetic structure so that the magnetic **k** vector has an irrational component (or mathematically, $k_i \cdot n a_i \neq 2\pi \ \forall \ n \in \mathbb{Z}$ where a_i is the lattice parameter in the i-th direction), there exists a large number of local magnetic environments across unit cells. If one could write down the field distribution $p(B)$, the form of the polarisation could be numerically evaluated using Eqn. 3.23 and Eqn. 3.24 [44].

In the simple case where the local magnetic field oscillates as a cosine function, such as the modulus of the field $|\mathbf{B}|$ is between $-B_0$ and $+B_0$, the field distribution across all muon sites can be written as

$$p(B) = \begin{cases} \frac{1}{\pi} \frac{B}{\sqrt{(B_0^2) - B^2}}, & \text{if } -B_0 \leq B \leq B_0, \\ 0, & \text{otherwise.} \end{cases} \tag{3.29}$$

By setting $\theta = 0$ in Eqn. 3.23, we consider a case where all local fields are transverse to the muon spin. Performing the integral in Eqn. 3.24 with $p(B)$ in Eqn. 3.29, one obtains the zero-order Bessel function of the first kind $J_0(B_0 t)$ given in the form

$$P_z(t) = J_0(B_0 t) \approx \begin{cases} 1 - \frac{1}{4}(\gamma_\mu B_0 t)^2, & \text{for small } t, \text{ and} \\ \sqrt{\frac{2}{\pi \gamma_\mu B_0 t}} \cos\left(\gamma_\mu B_0 t - \frac{\pi}{4}\right) & \text{for large } t. \end{cases} \tag{3.30}$$

In other words, the muon asymmetry is strongly damped at the beginning and transforms into a persisting oscillation that has a characteristic $\frac{\pi}{4}$ phase shift [42, 44]. Equation 3.30 is particularly useful when one studies materials that contain spin density waves, such as the Weyl semimetal compounds that will be discussed in Chapter 8 [45–47].

Dynamical fields

Up until now, we have considered magnetic structures that are static, such that the local field remains constant over time. However, many frustrated materials show spin dynamics and the absence of magnetic order at very low temperatures. Therefore, we require a different approach to account for the time dependence of the local magnetic field $B(t)$.

On the other hand, thermal fluctuation also plays a role in the spin dynamics. One common observation in many materials studied is that the muon relaxation rate gradually slows down as the temperature increases and when the thermal fluctuation rate is expected to rise. Figures plotting the muon relaxation rate against temperature in Chapters 6, 7 and 8 demonstrate this effect.

One could write down the correlation between the local field at time t_0 and t_0+t as

$$\langle B(t_0)B(t_0+t)\rangle = \left\langle B(t_0)^2\right\rangle e^{-\nu t} \tag{3.31}$$

which describes how the local field connects over time t with ν being the rate at which it fluctuates [42, 44]. The outcome of this is that, in the zero field limit, the polarisation becomes

$$P_z(t) = \exp\left\{-\frac{2\Delta^2}{\nu^2}\left(e^{-\nu t} - 1 + \nu t\right)\right\} \tag{3.32}$$

[48, 49]. We notice that when the fluctuation is small, i.e. $\nu t \ll 1$, the relaxation becomes Gaussian-like $P_z(t) = e^{-\Delta^2 t^2}$ which is expected for a static case. And in the limit where the fluctuation is fast, $\nu t \gg 1$, Eqn 3.32 simplifies to

$$P_z(t) = e^{-\lambda t}, \quad \text{where} \quad \lambda = \frac{2\Delta^2}{\nu} \tag{3.33}$$

and is known as the dynamical relaxation rate. This is referred to as the motional narrowing effect [50] where, by introducing dynamics, the field distribution at the muon site is narrowed (as compared to the static case). In some literature, a term called the correlation time τ_c is mentioned; this quantity gives the characteristic timescale to which a state is still 'correlated' to its past, and it is simply the inverse of the fluctuation rate ν so that $\nu = \tau_c^{-1}$ [44].

Equation 3.33 constitutes one of the key polarisation functions in the studies of spin liquid candidate materials where spin dynamics persist down to very low temperatures and will be frequently referred to in Chapters 5 and 6.

Nuclear moments

Many frustrated magnets rely on having interesting mechanisms of interactions between electronic moments and the relatively weak nuclear moments are often neglected. The reason is simple – the magnetic moment μ scales with the gyromagnetic ratio $\gamma = g\frac{q}{2m}$ where g is the g-factor, and q and m are the charge and the mass of the particle, respectively. For an electronic moment, γ can be written as $g\frac{\mu_\mathrm{B}}{\hbar}$ where μ_B is the Bohr magneton. For a nuclear moment, the corresponding expression is $g\frac{\mu_\mathrm{N}}{\hbar}$ with μ_N being the nuclear magneton. The ratio between μ_B and μ_N is given by the ratio between the mass of a proton and an electron $\frac{m_\mathrm{p}}{m_\mathrm{e}}$. In other words, a nuclear moment is of the order of 1800 times smaller than an electronic moment (although this ratio would vary depending on the exact g-factors of the particular atom's electronic and nuclear moments).

That being said, nuclear moments are still considerably important in μSR studies for several reasons; first, the muon has a large gyromagnetic ratio γ_μ and is therefore very sensitive to small fields such as those coming from a nuclear moment. Second, some materials do not contain electronic moments, for example, when they do not have any transition or rare earth atoms. Or if they do, the d or f orbitals could be empty or fully filled giving a net zero moment according to Hund's rules. On the other hand, every nucleus has a nuclear moment $\mathbf{I}$ (although for some isotopes $\mathbf{I} = 0$) and the studies of its interaction with the muon have led to important work such as the F-μ-F interactions [51] and muon diffusion in copper [52], where in both cases there is no electronic moment.

In frustrated magnets with Kramers ions, electronic moments can vanish because of their fluctuation in the Kramers doublet ground state [53]. When the fluctuation rate is too fast (from the muon's point of view), i.e. when $\nu t \gg 1$, the moment may not be detectable by the muon. As for a non-Kramers ion, the ground state

could either be a singlet or a doublet state depending on the CEF environment. In the latter case, the arrival of a muon could distort the local structure and split the doublet state into two singlet states; each of the singlet states has no moment, $\langle\mu\rangle \propto \left\langle\hat{\mathbf{J}}\right\rangle = 0$, because it always has an equal proportion of probability amplitudes between the opposite angular momentum eigenstates $|\pm m_J\rangle$.

Because nuclear moments are rather small in magnitude, they do not form magnetic structures in the way the electronic moments do. We can therefore assume that, with no applied field, nuclear moments are randomly oriented and paramagnetic-like, and because of their static nature the local field distribution at the muon site has a Gaussian form. In this case, the muon asymmetry can be represented by a Kubo-Toyabe function (also Eqn. 3.28)

$$P(t) = \frac{1}{3} + \frac{2}{3}\left(1 - \sigma^2 t^2\right) e^{-\frac{\sigma^2 t^2}{2}}, \tag{3.34}$$

where σ is the spin-lattice relaxation rate (sometimes referred to as the second moment of the field distribution) given by

$$\sigma^2 = \frac{2}{3}\left(\frac{\mu_0}{4\pi}\right)^2 \hbar^2 \gamma_\mu^2 \sum_i \gamma_{\mathrm{N},i}^2 I_{\mathrm{N},i}(I_{\mathrm{N},i}+1)\frac{1}{r_i^6}, \tag{3.35}$$

where $\gamma_{\mathrm{N},i}$ and $I_{\mathrm{N},i}$ are the gyromagnetic ratio and the total angular momentum of the i-th nuclear spin [54].

For atoms that have a number of nuclear isotopes, the natural abundance of each should be taken into account. Therefore, we can replace the expectation value $\left\langle\gamma_{\mathrm{N},i}^2 I_{\mathrm{N},i}(I_{\mathrm{N},i}+1)\right\rangle$ in Eqn. 3.35 with an effective nuclear moment μ_{eff}^2 such that

$$\sigma^2 = \frac{2}{3}\left(\frac{\mu_0}{4\pi}\right)^2 \hbar^2 \gamma_\mu^2 \sum_i \mu_{\mathrm{eff},i}^2 \frac{1}{r_i^6}. \tag{3.36}$$

The sum in Eqn. 3.36 converges as $\frac{1}{r_i^6}$ and, therefore, the closest nuclear spins dominate the sum.

3.2.2 Longitudinal Field μSR

Longitudinal Field (LF) refers to an applied magnetic field along the muon polarisation and LF-μSR is an important technique in studies of frustrated magnets to

understand the ground state dynamics. When a longitudinal field $\mathbf{B}_{\mathrm{LF}}$ is applied, the muon experiences both the intrinsic field $\mathbf{B}_{\mathrm{loc}}$ and the applied field so that

$$\mathbf{B}_{\mathrm{tot}} = \mathbf{B}_{\mathrm{loc}} + \mathbf{B}_{\mathrm{LF}}, \tag{3.37}$$

where $\mathbf{B}_{\mathrm{tot}}$ is the total resultant field at the muon site. In the extreme limit where a large field is applied, i.e. $\mathbf{B}_{\mathrm{LF}} \gg \mathbf{B}_{\mathrm{loc}}$, the resultant field is effectively $\mathbf{B}_{\mathrm{LF}}$. In this case, substitute $\theta = 0$ in Eqn 3.23, the muon polarisation $P(t) = 1$ and remains constant at all times.

With this concept in mind, LF-μSR has routinely been used as a technique to determine the nature of the ground state in quantum spin liquid (QSL) compounds [55, 56]. A typical muon asymmetry of QSL compounds decays exponentially due to fluctuations of the electronic moment that can be modelled as an exponential function $e^{-\lambda t}$, as discussed above. However, this asymmetry lineshape could occasionally be reproduced by a combination of randomly orientated nuclear moments and thermal fluctuation, so that

$$P(t) = \left(\frac{1}{3} + \frac{2}{3}\left(1 - \sigma^2 t^2\right) e^{-\frac{\sigma^2 t^2}{2}}\right) e^{-\lambda t}, \tag{3.38}$$

which is the same as the nuclear Kudo-Toyabe function in Eqn. 3.34 multiplied by an exponential decay function that represents the fluctuating dynamics (see Eqn. 3.33).

If the exponential-like decay of the muon asymmetry is caused by nuclear moments, a small applied LF (of the order of 50 G) should be able to quench the nuclear contributions and recover the full asymmetry $P_z(t) = 1$. However, if the nature of the ground state is made of fast fluctuating electronic moments, as it does in QSL candidates, it would be more robust and a much stronger LF would be needed to recover the full polarisation (usually of the order of 5000 G). As a result, LF-μSR is a crucial technique to study persistent dynamics at low temperatures.

Equation 3.33 (an exponential decay function) is frequently used to fit the muon asymmetry data for compounds with fluctuating dynamics. When an external LF of B is applied, the relaxation rate λ is derived to be

$$\lambda(t)t = 2\Delta^2\tau_{\mathrm{c}}^2 \frac{\left(e^{-\frac{t}{\tau_{\mathrm{c}}}}\cos\omega_0 t - 1\right)\left(1 - \omega_0^2\tau_{\mathrm{c}}^2\right) + \frac{t}{\tau_{\mathrm{c}}}\left(1 + \omega_0^2\tau_{\mathrm{c}}^2\right) - 2\omega_0\tau_{\mathrm{c}}e^{-\frac{t}{\tau_{\mathrm{c}}}}\sin\omega_0 t}{\left(1 + \omega_0^2\tau_{\mathrm{c}}^2\right)^2}, \tag{3.39}$$

where $\tau_c = \frac{1}{\nu}$ is the correlation time and Eqn. 3.39 is known as the Keren function [57]. In the fast fluctuation limit, i.e. $\nu t = \frac{t}{\tau_c} \gg 1$, Eqn. 3.39 can be simplified to give

$$\lambda = \frac{2\Delta^2\tau}{1+\omega_0^2\tau^2} \qquad \text{or equivalently, } \frac{2\Delta^2\nu}{\nu^2+\gamma_\mu^2 B_0^2}, \tag{3.40}$$

and is known as the Redfield formula or the BPP model [50]. Therefore, from LF-μSR measurements, one could extract the relaxation rate λ as a function of the applied LF $|\mathbf{B}_{\text{LF}}|$ at temperature T and find information on the spin correlation using different spin diffusion models [55, 56].

In Chapters 5 and 6, LF-μSR has been regularly deployed as the main technique to understand the ground state dynamics of several 2D QSL candidates, such as the $DyTa_7O_{19}$ and α-RuI_3 compounds.

3.2.3 Transverse Field μSR

Similar to the LF-μSR, one can set the orientation of the applied field to the transverse direction to perform Transverse Field (TF) μSR measurements. In this configuration, muons can be considered to be initially polarized along $\hat{\mathbf{x}}$ and experience a total resultant magnetic field of

$$\mathbf{B}_{\text{tot}} = B_{\text{ext}}\hat{\mathbf{z}} + \mathbf{B}_{\text{int}} \tag{3.41}$$

where $\mathbf{B}_{\text{int}}$ refers to the intrinsic field from the sample and B_{ext} is the external field applied along $\hat{\mathbf{z}}$. In TF-μSR measurements, detectors surround the sample in the x-y directions which are then sorted into the forward and backward groups to find the muon polarisation asymmetry.

A routine procedure of any μSR measurements is to perform a TF measurement with a small 50 G (or equivalently 5 mT) in the paramagnetic state at room temperature to find and calibrate the parameter α in Eqn 3.16 which varies based on the position of the mounted sample and detector coverage. This allows one to find the maximum initial asymmetry $A(t=0)$ as the muon asymmetry should simply follow an oscillating cosine function. When the same measurement is performed below the transition temperature, one expects the sample's intrinsic magnetism to

play a role – this is known as a weak transverse field measurement (or sometimes referred to as wTF-μSR) which could provide also meaningful information about the nature of the ground state magnetism (see Chapter 5 and Chapter 6).

TF-μSR measurements with a higher field are usually performed using the HAL-9500 instrument at the Paul Scherrer Institute in Switzerland which allows users to apply an external field B_{ext} of up to 9 T. Based on the precession frequency in many ZF-μSR experiments, the intrinsic field B_{int} at the muon site is normally of order below 1 T, and therefore, with a large applied transverse field, B_{ext} dominates over B_{int}, and Eqn. 3.41 can be approximated to be

$$\mathbf{B}_{\text{tot}} \approx B_{\text{ext}}\hat{\mathbf{z}} + B_{\text{int,z}}\hat{\mathbf{z}}, \tag{3.42}$$

which means that any deviation of the muon precession rate from $\gamma_\mu B_{\text{ext}}$ is caused by $B_{\text{int,z}}$, the z-component of the intrinsic field $\mathbf{B}_{\text{int}}$.

A common technique used in the analysis of TF-μSR data is to plot the Fourier spectrum and look for observable peaks [36]. In the case where there is no intrinsic field, or at least when $B_{\text{int,z}}$ is 0, the muon simply rotates along the applied external field and therefore $\mathbf{B}_{\text{tot}} = B_{\text{ext}}\hat{\mathbf{z}}$. This shows up as a Gaussian peak in the Fourier spectrum and is known as the silver peak – the (unfortunate) muons that missed the sample and instead landed on the silver sample plate see only B_{ext}. However, the muons that stopped inside the sample experience a resultant field (see Eqn. 3.42) and are reflected by peaks that are centred at $|\mathbf{B}| = B_{\text{ext}} \pm \delta B_{\text{int}}$ in the Fourier spectrum.

Interpreting data from TF-μSR experiments involves careful consideration of both the crystal and magnetic structure symmetries. A muon site in a unit cell is not a unique position and there are usually several crystal-equivalent sites, as indicated by the Wyckoff symbol. These equivalent sites can be categorised into sub-groups of magnetically equivalent sites when the crystal and magnetic structure symmetries do not perfectly align; the magnitude of $\mathbf{B}_{\text{int}}$ at these sites are very often the same but the sign of individual components can change, as determined by the dipolar tensor. Most importantly, a sign change in the z-component translates to

two observable peaks with comparable intensities in the Fourier Spectrum, centred at $B_{\text{ext}} + \delta B_{\text{int}}$ and $B_{\text{ext}} - \delta B_{\text{int}}$ according to Eqn. 3.42.

The application of TF-μSR to study a series of Weyl semimetal compounds REAlSi (where RE represents La, Nd, and Sm) will be explored in Chapter 8, which effectively showcases both the strengths and complexities involved in studying a new magnetic material using the TF-μSR technique.

3.3 Density Functional Theory (DFT)

One of the research questions in Condensed Matter Physics is to understand the key properties of a material by modelling its crystal structure and calculating its physical and magnetic behaviours, and density functional theory (DFT) calculation programs such as QuantumEspresso [58, 59], are widely used by researchers for these purposes. It is an efficient quantum mechanical modelling method that considers the functional of a many-body electronic system to calculate many of the intrinsic properties from first principle [60, 61].

3.3.1 Key concepts

An intuitive way to describe a system with N electrons is to use the many-body wavefunction $\Psi(\mathbf{r}_1, \cdots, \mathbf{r}_N)$. This, however, is a function of $3N$ variables and it would be extremely time-consuming and memory-intensive to perform any calculation. The main advantage of DFT is that it instead writes the energy of the ground state E as a functional of the electron density $n(\mathbf{r})$ [42, 60], i.e.

$$E = F[n(\mathbf{r})]. \tag{3.43}$$

This effectively reduces the dimension of the system from $3N$ to 3, making it much faster to solve on a modern computer. The exact form of the functional is not known, but numerous attempts have been made to introduce useful approximations of $F[n(\mathbf{r})]$. In 1965, Kohn and Sham set out $F[n(\mathbf{r})]$ in terms of kinetic and Coulomb energy of independent electrons such that

$$F[n(\mathbf{r})] = \underbrace{\int n(\mathbf{r})V_n(\mathbf{r})d\mathbf{r}}_{\text{Potential energy}} - \underbrace{\sum_i \int \phi_i^*(\mathbf{r})\frac{\nabla^2}{2}\phi_i(\mathbf{r})d\mathbf{r}}_{\text{Kinetic energy}} + \underbrace{\frac{1}{2}\int\int \frac{n(\mathbf{r})n(\mathbf{r}')}{|\mathbf{r}-\mathbf{r}'|}d\mathbf{r}d\mathbf{r}'}_{\text{Hartree energy}} + E_{xc}[n], \tag{3.44}$$

where V_n is the Coulomb potential between nuclei and the electronic distribution $n(\mathbf{r})$, and $E_{xc}[n]$ is the exchange-correlation energy that accounts for the differences between the first three terms and the actual energy [62, 63]. The ground state lies at a global minimum $F[n_0]$ that satisfies the relation $\frac{\delta F}{\delta n}\Big|_{n_0} = 0$ and hence we have

$$\left[-\frac{1}{2}\nabla^2 + V_n(\mathbf{r}) + V_{\mathrm{H}}(n(\mathbf{r})) + V_{xc}\right]\phi_i(\mathbf{r}) = \epsilon_i\phi_i(\mathbf{r}), \tag{3.45}$$

where $\phi_i(\mathbf{r})$ is a single particle wavefunction of the i-th eigenstates and that $n(\mathbf{r}) = \sum_i |\phi_i|^2$ for all occupied i-th states, $V_{\mathrm{H}}(\mathbf{r})$ and V_{xc} are the Hartree and exchange-correlation potential terms respectively [60, 64].

With these equations in place, one can start the self-consistent calculation by performing the following iteration:

1. Make an initial guess of $n(\mathbf{r})$ based on atomic positions,
2. calculate $\nabla^2 V_{\mathrm{H}}(\mathbf{r}) = -4\pi n(\mathbf{r})$ and $V_{xc}(\mathbf{r}) = \frac{\delta E_{xc}[n]}{\delta n}(\mathbf{r})$,
3. solve for the single-particle Schrödinger equation in Eqn. 3.45 and find eigenfunctions $\phi_i(\mathbf{r})$,
4. calculate the new electron density $n'(\mathbf{r}) = \sum_i |\phi_i(\mathbf{r})|^2$,
5. if $n'(\mathbf{r}) \neq n(\mathbf{r})$, repeat the steps 2-4 until a consistent solution is reached.

Obtaining accurate results in DFT calculations requires a good estimate of the unknown exchange-correlation term $E_{xc}[n]$ [42, 60], and there are several schemes that provide good approximation to this term, including the local density approximation (LDA) [65, 66] and the generalized gradient approximation (GGA) methods [64].

3.3.2 DFT relaxation and atomic forces

We discussed how the ground state energy is calculated under the assumption that we fully understood the crystal structure and the atomic positions. In cases where the positions are not precisely known, DFT force calculations and relaxation on a set of initial atomic positions can be used to optimize the geometry and find the equilibrium state.

We describe the Hamiltonian of the set of N nuclei by

$$\hat{H}_n = -\sum_I \frac{\nabla^2}{2M_I} + U(\mathbf{R}_1, \cdots, \mathbf{R}_M) \tag{3.46}$$

and the force acting on the I-th nucleus is given by

$$\mathbf{F}_I = -\frac{\partial \left\langle \hat{H}_n \right\rangle}{\partial \mathbf{R}_I} = -\left\langle \Psi \middle| \frac{\partial \hat{H}_n}{\partial \mathbf{R}_I} \middle| \Psi \right\rangle, \tag{3.47}$$

based on the Hellmann-Feynman theorem [67] and Ψ is the wavefunction of the I-th nucleus. If the initial atomic positions are not at equilibrium, one expects non-zero forces $\mathbf{F}_I$ and atoms would eventually move towards the equilibrium position in order to reach the lowest energy state. Force relaxation calculation in DFT adds an outer loop to the existing self-consistent iterations because information about the nuclear positions is required in order to calculate the electron density $n(\mathbf{r})$ and to solve the Kohn-Sham equation in Eqn. 3.45, and the whole calculation ends only when all $\mathbf{F}_I = 0$ (or close to zero and below a pre-defined threshold value) [60].

3.3.3 DFT+μ

A long-standing question in μSR studies is the nature of the muon-stopping site. It is only with information of this site that we could extract key information such as the local dipolar fields or the entanglement between the muon and the nearby nuclear moments. Progress has been made in the last decade on this front, which has taken advantage of DFT's capability to perform structural relaxation calculations – but with the addition of a positive muon. This is known as the DFT+μ method (DFT with an implanted muon μ) [54, 68, 69].

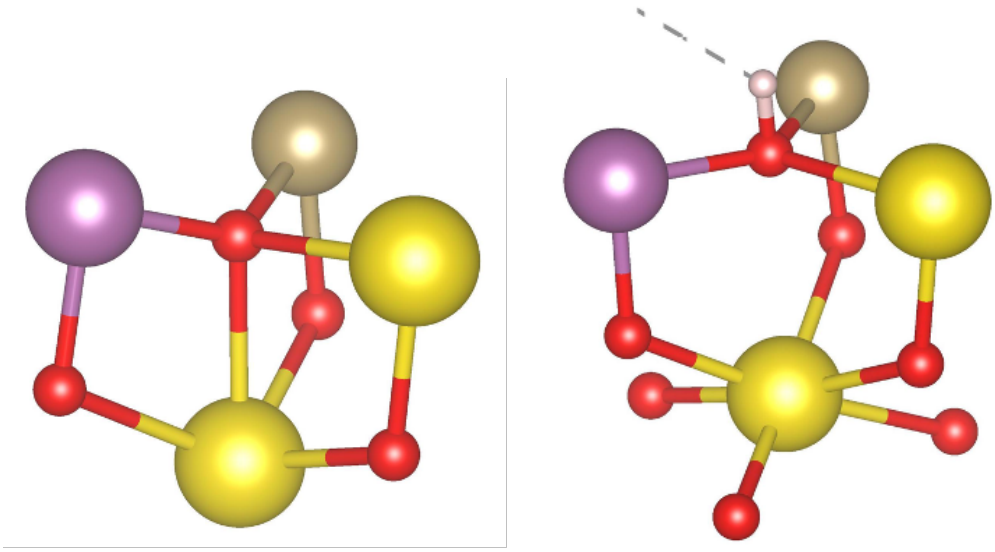

Figure 3.2: The atomic positions of Pr_2ScTaO_7 before and after the muon-induced distortion calculated using the DFT+μ method. Colour scheme: Muon (white), Oxygen (Red), Pr (Yellow), Sc (Purple) and Ta (Yellow). The compound Pr_2ScTaO_7 will be discussed in Chapter 7.

To set up a calculation, we follow the same procedure described in Section 3.3.2 with the addition of a positive muon (practically this is represented by a hydrogen atom with a lighter mass of 0.113u in the QuantumEspresso input files). The initial guess of the muon site is important to DFT+μ calculations because the muon is usually attracted towards a nearby local minimum. Therefore, a number of DFT+μ relaxations, each with a different initial position, is usually performed to thoroughly map the entire unit cell and to find the most probable site (i.e. the global minimum) by comparing the final energies of all calculations.

The benefits of DFT+μ calculations extend beyond the search of muon sites, it allows us to investigate how the added μ^+ causes electrostatic distortion to the positions of nearby atoms (see Fig. 3.2), and the implications on single-ion and crystal field properties. This is particularly advantageous when the magnetic structure is also known so that one can perform a dipolar field calculation at the muon site using information about the local distortion, as shown in Fig. 3.3.

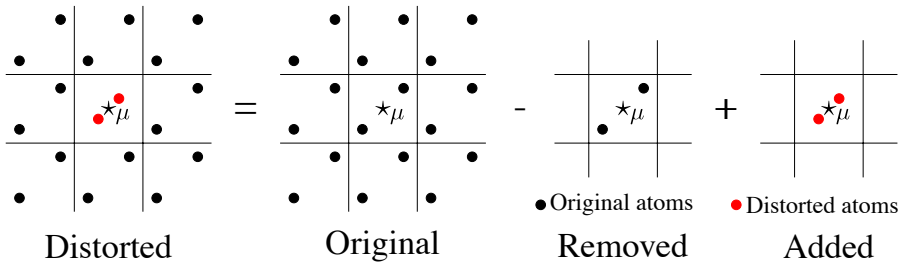

Figure 3.3: Schematic diagram on the basic principle of dipolar field calculation supplemented by DFT+μ calculations.Each square represents a unit cell.

3.4 Crystal Fields Calculation

PyCrystalField is a Python library designed to calculate and fit crystal field parameters from the CEF Hamiltonian H_{CEF} [70]. The program reads a Crystallography Information File (CIF) [71] and loads the structural properties and atomic positions. It uses the point charge model [72], which treats the electron distribution of nearby ligands to be point charges at their nuclei, to calculate the CEF properties of 3d and 4f magnetic ions such as energy splitting of the $2J + 1$ degenerate states, and express the energy states as a composition of angular momentum eigenstates $|m_J\rangle$ (or equivalently states in the LS-basis).

Alternative software that also calculate CEF properties using the point charge model includes SIMPRE [73] and SPECTRE [74], which I have tested and have produced identical energy levels and energy states. However, PyCrystalField is preferred for most of the work carried out in this thesis because it could be conveniently imported as a Python library into the wider part of the project, and it has the ability to turn a CIF into a crystal field calculation seamlessly (see Fig. 3.4).

It should be noted that these calculations only serve as a first-order approximation to the real CEF effect, as the point charge model neglects the electronic distribution and overlapping wavefunctions between the ligands and the central magnetic ion [72]. Notably, one should exercise caution with calculations that involve larger atoms such as Si or As because the 3p orbitals are far more delocalised than the 2p orbitals in O^{2-}, and therefore, the point charge approximation may not be applicable.

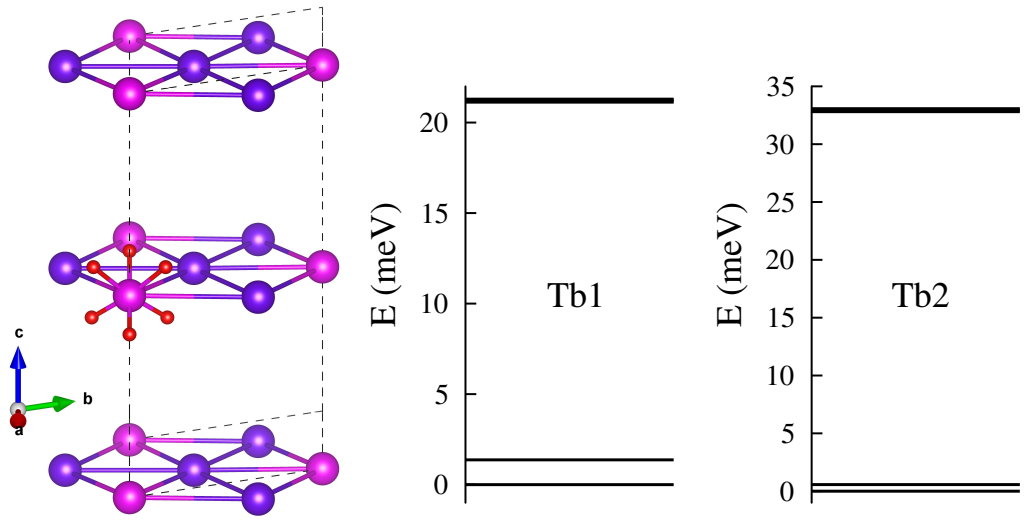

Figure 3.4: Structure of $Ba_3TaB_3O_9$ which contains magnetic Tb^{3+} ions at two sites Tb1 (violet) and Tb2 (magenta). The crystal field levels of Tb1 and Tb2 ions are calculated using PyCrystalField and show low-lying singlet states at both sites. Further details of this compound will be discussed in Section 6.9.3.

4

1D Spin Chains: $PbM_2Ni_6Te_3O_{18}$ (M = Mn, Fe, Co, and Zn)

Contents

In this chapter, I present new results on the μSR measurements, muon site analysis, and dipolar field calculations on a family of pentanary oxide compounds $PbM_2Ni_6Te_3O_{18}$ (M = Mn, Fe, Co, Zn). I demonstrate the effect of substituting the transition metal M ion and explain how this allows the level of magnetic frustration to be tuned as a result of the weakening exchange interaction between the M^{2+} ions and the Ni-chains.

The work in this chapter has been presented orally at the International Conference for Highly Frustrated Magnetism 2024 in Chennai, India. Stephen Blundell helped with the interpretation of the results. Dharmalingam Prabhakaran synthesised the four $PbM_2Ni_6Te_3O_{18}$ (M = Mn, Fe, Co, and Zn) samples. George

Gill, John Wilkinson, Tom Lancaster and Stephen Blundell assisted with the μSR measurements which were carried out on the GPS spectrometer at the Paul Scherrer Institut, Switzerland with technical support provided by Chennan Wang. All computational work was run on the SCARF cluster supported by the Scientific Computing Research Infrastructures Group at the Rutherford Appleton Laboratory and on the Redwood cluster hosted at the Department of Physics, University of Oxford.

4.1 Background

Quantum spin chains have captivated physicists for over a century. These chains are made of spins aligned linearly which are connected by exchange interactions. A 1D spin chain is regarded as a frustrated system because it evades long-range magnetic order at any finite temperature due to quantum fluctuations [75, 76]. The first exact solution for an $S = \frac{1}{2}$ Heisenberg model was introduced by H. Bethe in 1931 [77], and its interesting properties have led to discoveries such as spin wave theory showing that there is a gapless excitation spectrum which has been found in various spin chain compounds [78–80]. While theoretical studies have fueled excitements in this field, in reality, most 1D spin chain compounds synthesized are not truly one-dimensional; this is because individual spin chains can interact subtly with neighbouring chains and are, therefore, quasi-1D.

In 1983, the idea of a Haldane gap, i.e. an energy gap between the ground and excited states, was proposed for antiferromagnetic (AFM) spin chains with integer spins [81]. Ever since, this has attracted wide interest from researchers who have been attempting to design and search for new materials that would potentially realise the Haldane gap physics [82–84]. The $PbM_2Ni_6Te_3O_{18}$ family of compounds is interesting in this respect because they contain Ni^{2+} ($S = 1$) zigzag AFM spin chains that lie along the c-axis but are arrayed in a kagome-like pattern in the a-b plane. Despite the absence of the Haldane phase, the compounds still show the intriguing interplay between magnetic order and exchange interactions within quasi-1D spin chains [85–88]. The exchange interactions between Ni atoms from

different chain along the *ab*-plane are geometrical frustrated and the following section outlines how such frustration leads to the absence of long-range order and provides experimental evidence for this phenomenon.

4.2 Structural Properties

The family of pentanary oxides compounds $Pb^{2+}M_2^{2+}Ni_6^{2+}Te_3^{6+}O_{18}^{2-}$ contains transition metal atom M and crystallises in a hexagonal unit cell with space group $P6_3/m$. The lattice parameters are $a = b = 9.28$ Å and $c = 8.81$ Å [86, 88]. The M ions are located at the 4f Wyckoff site and are in an M_2O_9 dimeric unit aligned along the c-axis. Meanwhile, the Ni^{2+} ions are located at the 12i site with their edge-sharing NiO_6 octahedra forming a double-chain structure along the *c*-axis (see Fig. 4.1 (a) & (b)). For $PbMn_2Ni_6Te_3O_{18}$ (M = Mn), the Mn and Ni ions are positioned at (1/3, 2/3, 0.062) and (0.9887, 0.3483, 0.9111) respectively, and these positions are similar for other members of this family of compounds [85–88].

The double-chain structure of the NiO_6 edge-sharing octahedra allows the Ni^{2+} ions to form quasi-1D zigzag chains with spin $S = 1$ which extend along the *c*-axis. For $PbMn_2Ni_6Te_3O_{18}$, the transition temperature is reported to be 84.7 K, where the intra-chain Ni-Ni exchange interactions J_1 & J_2 (see Fig. 4.1(a) & (b)) form an AFM order with spins aligned along the **c**-axis [86]. In addition, every three nearest Ni-chains form a trigonal tunnel in which the M_2O_9 dimeric units are placed (see Fig. 4.1(d)), and when the structure extends in the *a*-*b* plane and it resembles a kagome-like pattern (this can be visualised by shrinking each Ni-Ni bond in Fig. 4.1(d) into a single point). These Mn-Mn intra-dimer exchanges J_4 are reported to have AFM order [86] with their spins also aligned along $\hat{\mathbf{c}}$ (see Fig. 4.2). Because of the proximity of the Ni-chains and M-dimers, there are additional exchange pathways exchange couplings J_3 and J_5 (see Fig. 4.1(d)) between which the competition turns out to be important in understanding the ground state magnetism in the $PbMn_2Ni_6Te_3O_{18}$ compounds.

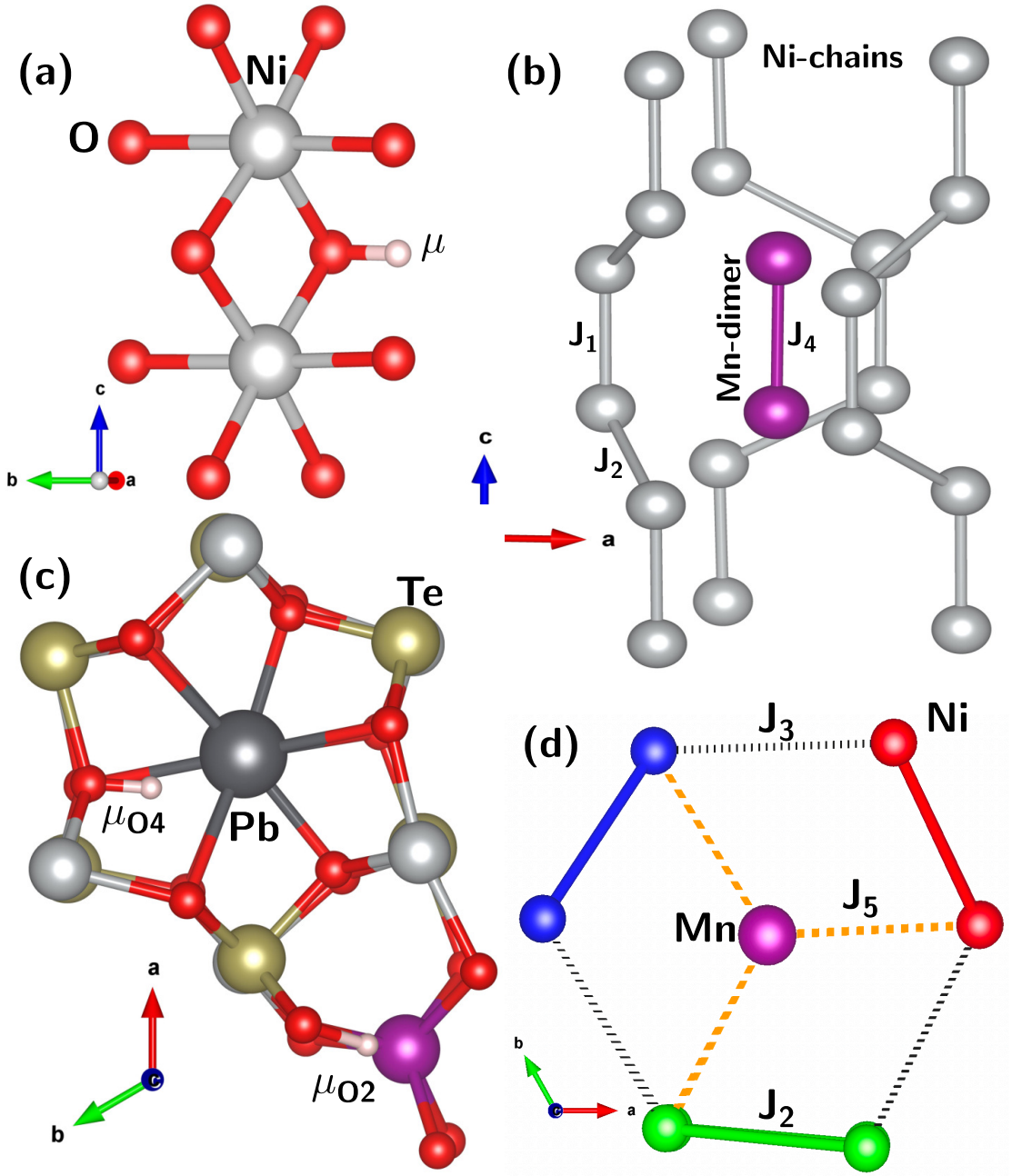

Figure 4.1: (a) Ni spin-chain in $PbMn_2Ni_6Te_3O_{18}$ with a muon attached at the bridging O4 oxygen. (b) M dimer (purple) surrounded by three Ni-chains (grey) along $\hat{\mathbf{c}}$. (c) View along $\hat{\mathbf{c}}$ showing the two muon sites. (d) View along $\hat{\mathbf{c}}$ showing the in-plane exchange pathways J_2, J_3 and J_5 between the three coloured Ni-chains and a Mn-dimer.

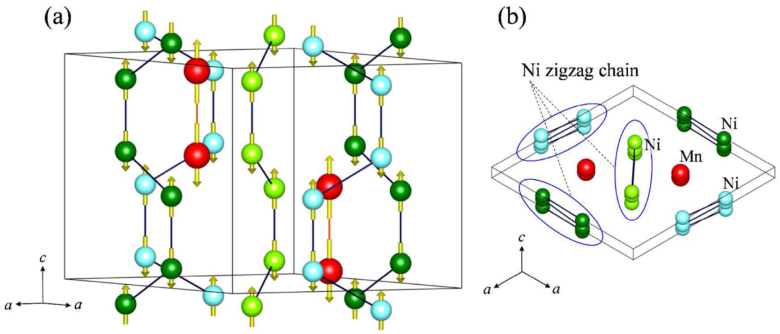

Figure 4.2: The reported magnetic structure of $PbMn_2Ni_6Te_3O_{18}$ showing that (a) the Ni and Mn spins form an AFM order and are aligned along the crystallographic c-axis, and that (b) each of the trigonal 'tunnel' formed by the Ni chain surround a Mn dimer. This Figure is extracted from [86].

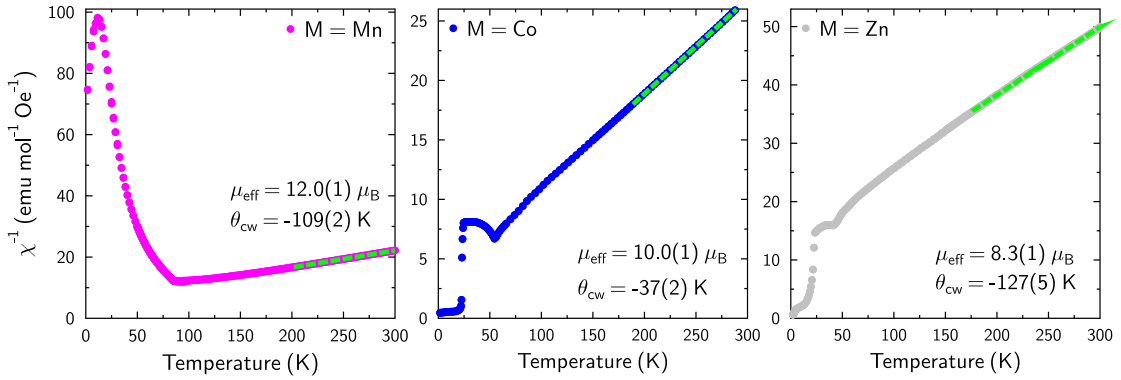

Figure 4.3: Inverse magnetic susceptibility of $PbM_2Ni_6Te_3O_{18}$, for M = Mn, Co and Zn. The effective moments are obtained by Curie Weiss fit in the high-temperature region (lime dashed line). The moment per Ni ion is therefore $\mu_{Ni} = \mu_{eff,Zn}/\sqrt{6} \approx 3.39\ \mu_B$.

As for the isostructural compounds with where M = Fe, Co, and Zn, the magnetic properties have not yet been reported, and therefore, the results in this Chapter could provide some insight to the full determination of their magnetic structures.

4.3 Magnetic Characterisation

Magnetic susceptibility measurements have been performed using a Quantum Design MPMS3 system for the M = Mn, Co, and Zn powder samples between 1.8 K and 300 K with a field of 100 G (equivalently 100 Oe), and the inverse susceptibility data χ^{-1} are plotted in Fig. 4.3 together with the fitted effective moments $\mu_{eff,M}$ per formula unit and the Curie-Weiss temperatures θ_{CW}. These values are $\mu_{eff} = 12.0(1), 10.0(1), 8.3(1)\ \mu_B$ and $\theta_{CW} = -109(2), -37(2), -127(5)$ K

for M = Mn, Co, and Zn respectively. These data suggested that there is a significant anti-ferromagnetic correlation between magnetic moments across all three compounds. Furthermore, there is a sharp feature in the magnetic susceptibility curves between 50 K and 85 K, and a further one at around 25 K for all compounds. The M = Zn compound contains only one magnetic ion species Ni^{2+} due to Zn^{2+} ion's $3d^{10}$ configuration, and therefore its fitted effective moment per formula unit $\mu_{\text{eff, Zn}}$ allows us to estimate the single ion moment of Ni^{2+} μ_{Ni} by

$$\mu^2_{\text{eff,Zn}} = 6\mu^2_{\text{Ni}}, \tag{4.1}$$

which yields $\mu_{\text{Ni}} = \mu_{\text{eff, Zn}}/\sqrt{6} \approx 3.39(4)\ \mu_{\text{B}}$. Treating the Ni^{2+} moments to be constant across the series, which is a reasonable assumption given the structural similarities, the M^{2+} ion's moment could be estimated by

$$\mu^2_{\text{eff,M}} = 2\mu^2_{\text{M}} + 6\mu^2_{\text{Zn}}, \tag{4.2}$$

which gives $\mu_{\text{Mn}} = 6.1(2)\ \mu_{\text{B}}$ and $\mu_{\text{Co}} = 3.9(3)\ \mu_{\text{B}}$ and are in good agreement with their $2\sqrt{S(S+1)}$ theoretical spin-only values shown in Table 4.1.

4.4 μSR Zero Field

Zero-field μSR measurements of $PbM_2Ni_6Te_3O_{18}$ (M = Mn, Fe, Co, and Zn) were carried out at the Paul Scherrer Institute, Switzerland, using the GPS instrument, with the powder samples of these compounds (approximately 0.5 g) packed in silver packets and held onto the sample holder using Kapton tape. The asymmetry data are plotted in Fig. 4.4 which show a clear oscillating signal below the transition

Table 4.1: Theoretical and observed magnetic moments of M^{2+} ions for M = Mn, Fe, Co, and Zn. The former represents the $\mu_{\text{eff}} = 2\sqrt{S(S+1)}\mu_{\text{B}}$ values which assume orbital quenching $L = 0$ and the latter is obtained by fitting the high-temperature region of the magnetic susceptibility data, as described in Section 4.3.

	Mn^{2+}	Fe^{2+}	Co^{2+}	Zn^{2+}	Ni^{2+}
Spin S	$\frac{5}{2}$	2	$\frac{3}{2}$	0	1
Theory (μ_{B})	5.92	4.90	3.87	0	2.83
Observed (μ_{B})	6.1(2)	—	3.9(3)	0	3.39(4)

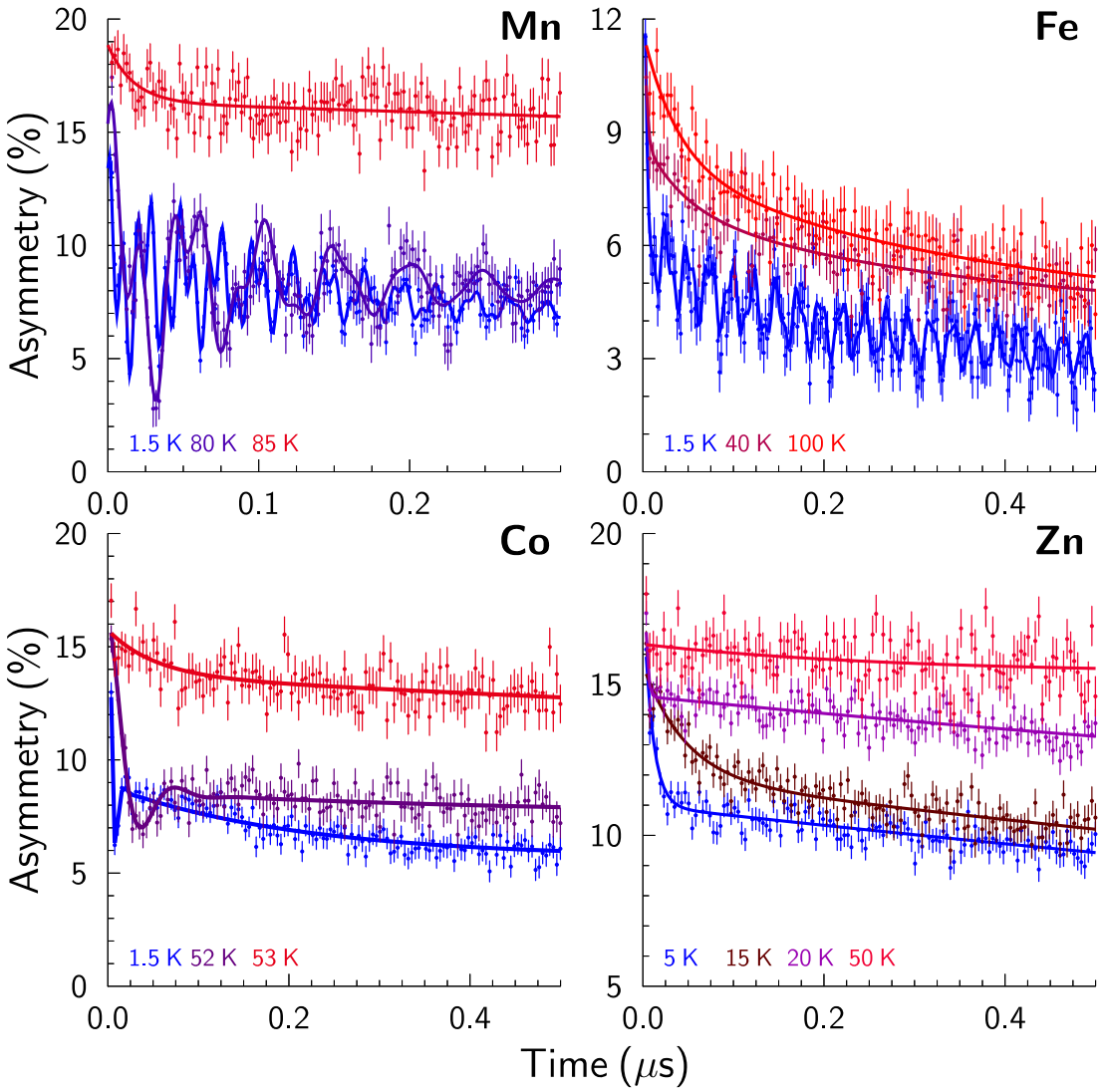

Figure 4.4: ZF-μSR asymmetry data measured at various temperatures below and above T_N for $PbM_2Ni_6Te_3O_{18}$, where M = Mn, Fe, Co, and Zn, showing a transition from clear oscillations in the M = Mn case into a monotonic decay for M = Zn when the M ion is replaced.

temperature for M = Mn, but for M = Fe and Co the oscillating signals were heavily damped and then disappeared for M = Zn. These changes are accompanied by a reduction of the spin S and the magnetic moment on the M^{2+} ion as M is substituted across the 3d-block through the series Mn $\left(S = \frac{5}{2}\right)$, Fe ($S = 2$), Co $\left(S = \frac{3}{2}\right)$ and Zn ($S = 0$).

M = Mn

For M = Mn, a muon asymmetry pattern with two clear oscillations was observed at all temperatures up to the transition temperature $T_{\mathrm{N}} = 84.7$ K. The asymmetry can be fitted according to a double-frequency function

$$A(t) = A_{\mathrm{relax}} \left(\sum_{i=1}^{2} f_i \cos(\nu_i + \phi_i) e^{-\lambda_i t} \right) + A_{\mathrm{B}} e^{-\lambda_{\mathrm{B}} t}, \tag{4.3}$$

where A_{relax} and A_{B} refer to the relaxing and baseline asymmetry respectively, and f_i and ϕ_i are the fraction and the phase of the i-th oscillatory component with frequency ν_i and dynamical relaxation rate λ_i. I found that the two oscillatory fractions f_1 and f_2 are approximately equal (≈ 0.5), with $\nu_1 = 106.2(1)$ MHz and $\nu_2 = 41.3(1)$ MHz at 1.5 K, which implies either two distinct muon sites or only one crystallographic site accompanied by two magnetically different local environments as a result of incompatibility between the crystal lattice and magnetic structure symmetries. To look into this, I have done dipolar field calculations with the reported AFM magnetic structure [86], and have confirmed that all crystal-equivalent sites produce the same magnitude of local field, and hence an identical muon precession frequency. This is because the AFM magnetic structure, where spins are aligned along the c-axis, satisfies the symmetry operations imposed by the space group $P6_3/m$. This, together with the muon site calculations discussed later, gives evidence for the case of two distinct muon sites in the family of $PbM_2Ni_6Te_3O_{18}$ compounds.

The temperature dependences of both ν_1 and ν_2 have been fitted using a phenomenological equation

$$\nu = \nu_0 \left[1 - \left(\frac{T}{T_{\mathrm{N}}} \right)^{\alpha} \right]^{\beta} \tag{4.4}$$

between 1.5 K and 85 K, and the results are plotted in Fig. 4.5. The critical temperature T_{N} was found to be 84.8 K, which is consistent with reported studies of the same compound [86, 88]. Both frequencies follow the same trend against temperature, and by expanding in the critical regime $T \to T_{\mathrm{N}}$ one could write

$$\nu = \nu_0 \left[\alpha \left(1 - \frac{T}{T_{\mathrm{N}}} \right) \right]^{\beta}, \tag{4.5}$$

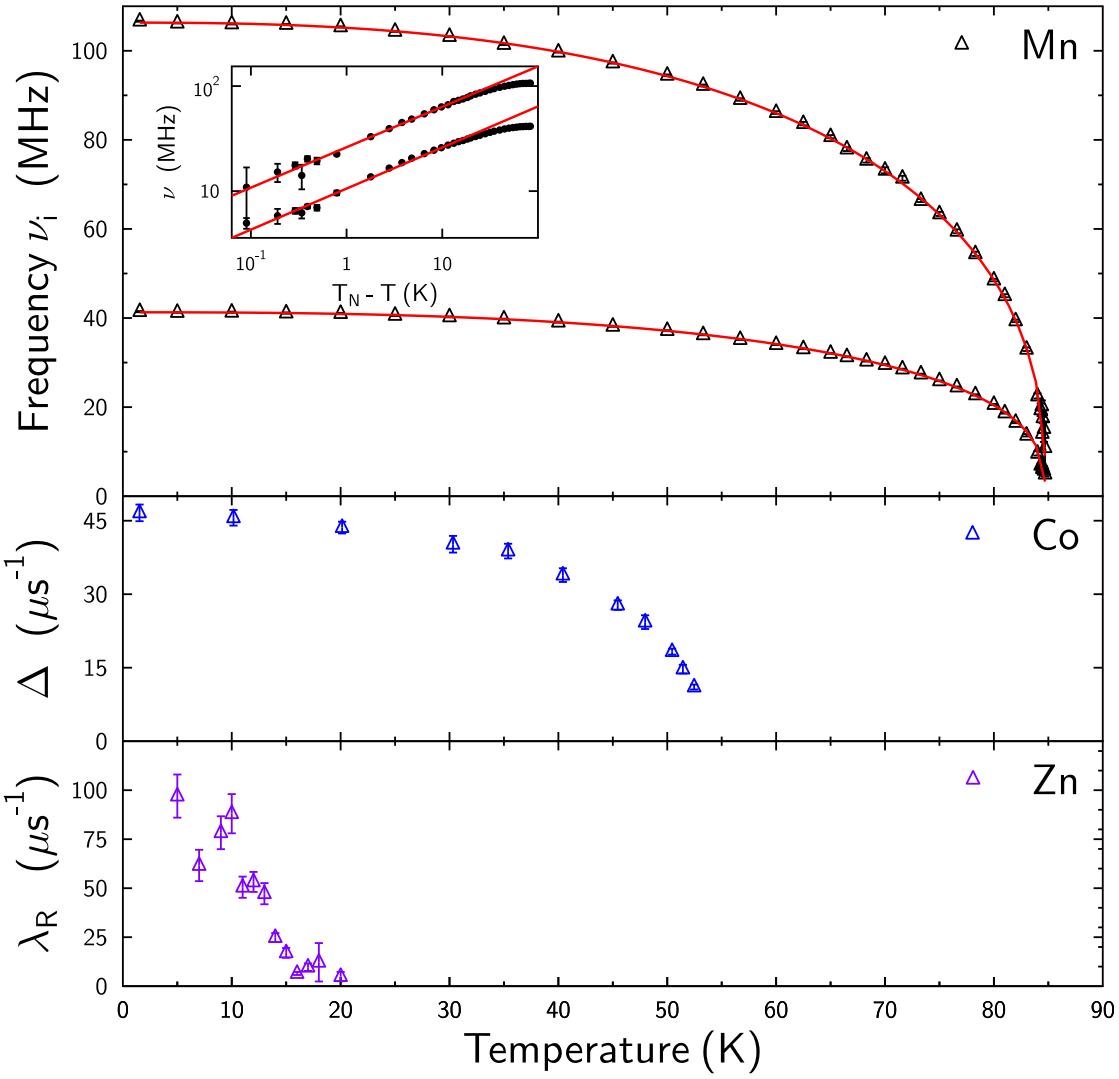

Figure 4.5: The temperature dependence of the fitted parameters in $PbM_2Ni_6Te_3O_{18}$ (M = Mn, Co, and Zn). For M = Mn, the frequencies ν_1 and ν_2 are fitted with Eqn. 4.5 which results in $\alpha = 2.54(2)$, $\beta = 0.394(3)$ and $T_N = 84.8(1)$ K). The inset shows a log-log plot of the precession frequencies in the critical regime.

so that with

$$\ln \nu \propto \beta \ln(T_N - T), \tag{4.6}$$

one could use a log-log plot of the precession frequency against $T_N - T$ to determine the exponent β (the slope in Eqn. 4.6) robustly, as shown in the inset of Fig. 4.5 that yields $\beta = 0.393(5)$ which is closest to the critical exponent of a 3D Heisenberg model than other models.

Muon site calculations

To find the muon-stopping sites and relate them to the two observed frequencies, I performed DFT+μ relaxation calculations for $PbMn_2Ni_6Te_3O_{18}$ using a single unit cell of 60 atoms and an additional μ^+. By repeating the calculations with random initial μ^+ positions and comparing the final energy values, I have identified two principal stopping sites.

The lowest energy site is at fractional coordinates (0.379, 0.745, 0.845) near an O2 oxygen atom. Dipolar field calculations at this site, with local distortion caused by the μ^+ considered, give a precession frequency of 102 MHz which matches with the experimental value ν_1 (106.2(1) MHz). The second site is found to be at (0.746, 0.031, 0.174), which is close to an O4 oxygen atom, with a frequency of 45 MHz that corresponds to ν_2. Hereafter I name them as the O2 & O4 sites (also see Fig. 4.1(c) for visualisation). The two muon sites have very different local magnetic environments; while the O2 site lies at a distance of 2.25 Å to an Mn^{2+} ion ($\mu = 4.71\ \mu_B$), the O4 site is only about 2.41 Å to its two nearest Ni^{2+} ions (1.96 μ_B). This explains the ratio $\nu_1/\nu_2 \approx 2.5$ as the local dipolar field scales as a function of the moment and the distance by μ_i/r_i^3.

Calculations for the end member M = Zn yielded the same muon sites for M = Mn, so I can conclude that the muon sites should be identical in the family of $PbM_2Ni_6Te_3O_{18}$ compounds.

M = Fe, Co and Zn

For M = Fe, the μSR data in Fig. 4.4 show evident oscillatory behaviour, albeit with a much smaller amplitude and very strong initial damping, and the precession frequencies ν_1 and ν_2 are 90.0(3) MHz and 41.0(1) MHz at 1.5 K. Note that the ν_1 value here is less than that found at the O2 site for the previous M = Mn compound, yet this is expected because the O2 site is near a M^{2+} ion and Fe^{2+} contains a smaller moment than Mn^{2+} (see Table 4.1). Meanwhile, at the O4 site, ν_2 remains mostly unchanged as the local field comes mainly from the two nearest Ni^{2+} ions. Given the similarities in the μSR asymmetry spectrum, I think that the M = Fe

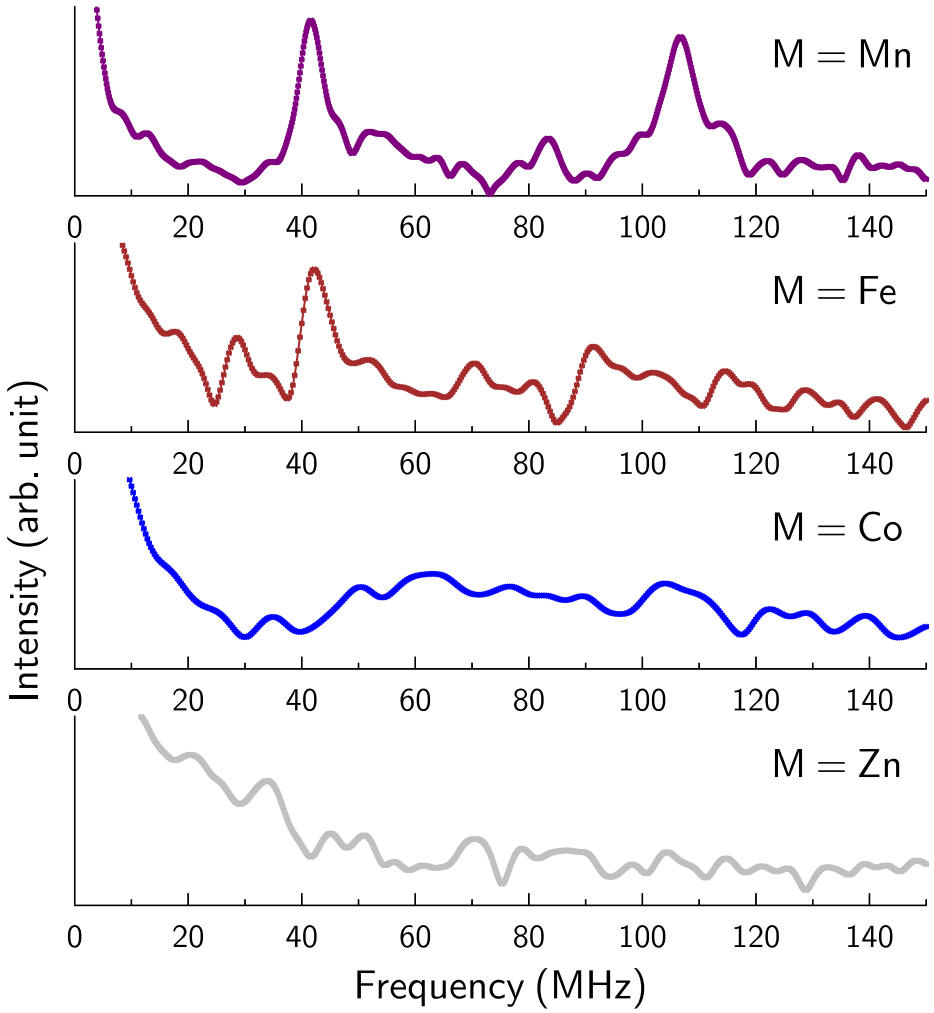

Figure 4.6: Frequency spectra of the ZF-μSR asymmetry for $PbM_2Ni_6Te_3O_{18}$ at 1.5 K (except for M = Zn which is at 5 K) showing two sharp peaks in the M = Mn which gradually turn into a broadened spectrum as the M ion is being replaced Fe, Co and Zn.

compound has a similar magnetic structure as the M = Mn case. However, it should be noted that the broadening in the frequency spectrum, as shown in Fig. 4.6, which has caused the rapid initial relaxation is an indication that the magnetic structure for M = Fe might have slightly departed from the ideal AFM order.

For the M = Co compound, there is a Kubo-Toyabe-like relaxation with a one-third tail at 1.5 K. This indicates that the implanted muon is exposed to a static but disordered magnetic environment where the local field spectrum can be described by a Gaussian distribution width of Δ/γ_μ. The temperature dependence of $\Delta(T)$ is plotted in Fig. 4.5 which shows a magnetic phase transition at 53 K.

And for M = Zn, the Ni^{2+} ions are the only magnetically active ion in the compound because Zn^{2+} has a $3d^{10}$ electronic configuration. As shown in Fig. 4.4, the ZF asymmetry at base temperature 5 K has no observable oscillating component but a monotonic decay relaxation. This can be modelled by the phenomenological function

$$A(t) = A_{\mathrm{R}} e^{-\lambda_{\mathrm{R}} t} + A_{\mathrm{B}} e^{-\lambda_{\mathrm{B}} t}, \tag{4.7}$$

where A_{R} and A_{B} refer to the initial relaxing and baseline asymmetry, and λ_{R} and λ_{B} are the respective relaxation rates. The relaxation rate λ_{R} is plotted in Fig. 4.5 against temperature and contributes to the initial damping of the muon asymmetry. The absence of oscillation usually reflects either dynamics in the system, or static fields where the frequency spectrum somewhat resembles an exponential distribution and, therefore, damps the asymmetry very effectively. Further μSR measurements on another batch of sample at 1.8 K also showed a heavily damped relaxation, although a short-lived and weak oscillation in the first 0.05 μs can be seen, hence confirming the static nature of the Ni spin-chain.

A summary of the ZF-μSR data could be made by plotting the frequency spectrum of all compounds at base temperature, as shown in Fig. 4.6. This illustrates the same behaviour I have mentioned above and will discuss in further detail: as one substitutes the M ion from Mn to Fe, Co and Zn, there is a crossover from two sharp frequency peaks ν_1 and ν_2 for M = Mn, which corresponds to the O2 and O4 muon sites, to a significantly broadened distribution for M = Zn. This phenomenon hints at the onset of magnetic frustration and local disorder, and that the system is increasingly prevented from achieving any long-range magnetic order.

4.5 Discussion

The trends observed in the μSR data could be explained by considering the exchange pathways illustrated in Fig. 4.7. The J_3 interchain exchange pathways form a kagome-like structure in the *a*-*b* plane. When $J_3 > 0$ (AFM), all Ni-chains have the same alignment and exhibit long-range three-dimensional magnetic order. However when $J_3 < 0$ (FM), Ni-chains would anti-align with their neighbouring chains which leads

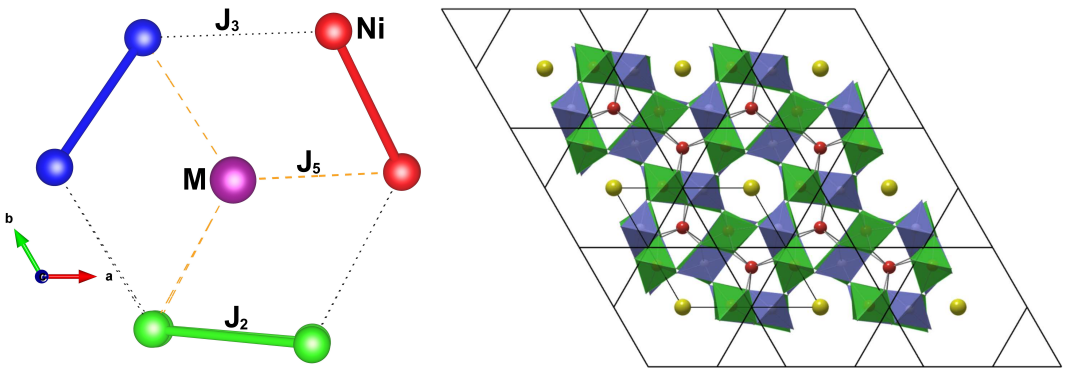

Figure 4.7: (Left) View along $\hat{\mathbf{c}}$ showing the in-plane exchange pathways J_2, J_3 and J_5 between three Ni-chains and a Mn-dimer. Same figure as Fig. 4.1(d). (Right) View along $\hat{\mathbf{c}}$ demonstrating the kagome-like structure of the arrays of Ni-Te double-chains (shown as edge-sharing polyhedra). This figure is extracted from the supplementary information of [86].

to geometric frustration similar to the classical example of AFM-coupled spins in a triangular lattice. From the M = Zn data, the broad frequency spectrum shows that the implanted muons are probing a mix of disordered local arrangements instead of two sharp peaks, and one could hence establish that J_3 is ferromagnetic in nature.

The interchain magnetic ordering is therefore a result of the competition between J_3 and J_5. In the case of M = Mn ($\mu = 4.92\ \mu_B$ [86]), the stronger moment allows J_5 to dominate over J_3 and therefore forces the Ni ions to align ferromagnetically with the dimer. But as the M ion is substituted by Fe, Co, and Zn, this M-Ni interchain J_5 pathway weakens and vanishes, and therefore, the ferromagnetic J_3 pathways lead to magnetic frustration between the Ni-chains.

Another indication of the emerging frustration is the trend of lowering T_N that decreases from 84.5 K for Mn, to around 55 K for Fe and Co, and down to about 20 K for Zn. This is a sign that the underlying magnetic ground state is becoming more unstable as the J_5 link between M^{2+} and Ni^{2+} weakens.

4.6 Dipolar Field Simulations

To simulate the effect of magnetic frustration and the alignment between the M-dimers and Ni-chains, I considered a model where they are randomly picked and flipped along the *c*-axis. I used the magnetic structure of $PbMn_2Ni_6Te_3O_{18}$ as

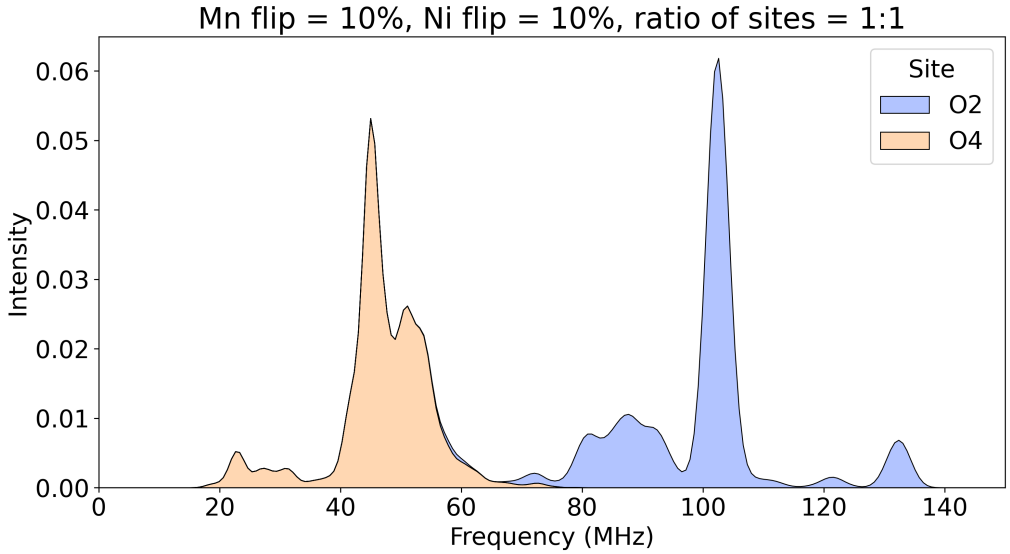

Figure 4.8: Simulated Fourier spectrum of the muon decay asymmetry $A(t)$ for $PbMn_2Ni_6Te_3O_{18}$ at the O2 and O4 muon site with a random 10% of spin-chain and Mn dimer undergone spin flipping. This simulation assumes that the muons are split 50-50 between the O2 and O4 sites (shown as shaded areas under the curve).

the base case and strictly kept the intrachain/intradimer AFM alignment given the strong J_1, J_2 and J_4 interactions. This chance of flipping can be tuned as a parameter from 0% (no flipping) to 50% (maximum randomness). The former is expected in the M = Mn case when the M moment is large, therefore stabilising nearby Ni-chains via J_5, and the latter is expected when the M moment is small as Ni interchain arrangements are decided by the frustrating J_3 pathways. The local dipolar fields were calculated to simulate the muons probing a range of magnetic environments and the results were compared against the Fourier spectra in Fig. 4.6.

From the simulations, it is clear that spin-flipping causes additional shoulder peaks near the main peaks as shown in Fig. 4.8 for M = Mn. In general, broadening in the frequency spectrum means that the muons are probing a range of diverse local magnetic environments, and is, therefore, an indication of a frustrated state. For the simulation to best describe the experimental outcome, I observed that the amount of flipping grows from 10% in M = Mn to 50% in M = Co & Zn, hence verifying the existence of growing frustration across this family of compounds.

The dipolar field at each muon site can be roughly accounted for by considering the nearest magnetic ions; for ν_1 at the O2 site, the two closest M^{2+} ions belong

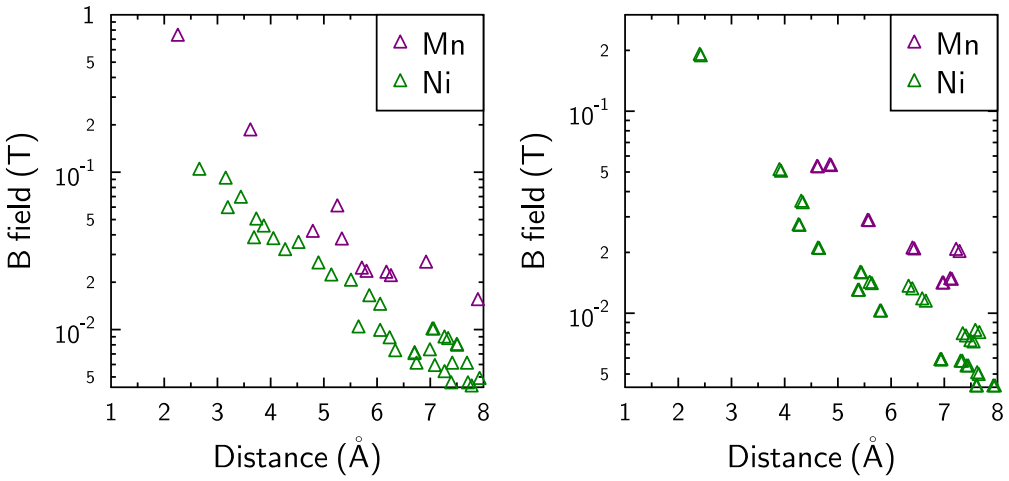

Figure 4.9: Magnitude of the dipolar field produced by each nearby atoms at the O2 (left) and O4 (right) sites in $PbMn_2Ni_6Te_3O_{18}$ and their distances from the muon, based on DFT+μ calculations.

to two separate dimers which makes the muon at the O2 site a direct probe of the M-dimer ordering – i.e. the relative strength of J_5 over J_3. If J_5 is strong enough, all M-dimers align ferromagnetically with the neighbouring Ni-chains, and this is supported by the simulation showing a very small amount of flipping among the Mn dimers. However when $J_5 \lesssim J_3$, the M-dimers could start to deviate from the usual alignment along $\hat{\mathbf{c}}$ and create more magnetic disorder. For ν_2 at the O4 site, most of its local field comes from the two nearest Ni^{2+} moments (see Fig. 4.9), therefore, it is minimally affected by the M substitutions. This is consistent with the dipolar field calculations and the observed frequency spectra for M = Mn and Fe in Fig. 4.6 which show that the peaks remain close to 41 MHz. These two nearest Ni^{2+} ions belong to the same AFM Ni-chain and hence they would always produce the same magnitude of local field regardless of spin-chain flipping. As a result, spin-flipping of the nearest M-dimers and next-nearest Ni-chains can be considered as a perturbation to the base case AFM magnetic structure. This could perhaps explain why the broadening effect is relatively small at this muon site and the frequency never exceeds the range between 30 and 60 MHz, whereas ν_1 at the O2 site ranges from 30 to 140 MHz for M = Mn & Fe. The complete smearing in frequency spectra for M = Co and Zn shows that the Ni-chains in these compounds are highly frustrated, where the diverse range of local environments washes out the sharp peaks at 41 MHz.

I also tested a case where the M-dimers flip if two of the nearest three Ni-chains have flipped. This is because the J_5 pathways are ferromagnetic and the system would ideally minimise energy by doing so (from $E_{J_5} = 2J_5 - J_5 = J_5$ to $-2J_5 + J_5 = -J_5$ per M ion). However, while this model agrees with the main features in the spectra, I noticed that it alone could not reproduce some smaller satellite peaks. For example, small peaks around 30 MHz and 110 - 120 MHz in the M = Fe case are evidence of some small fraction of AFM J_5 arrangement within the sample. This shows that J_5 is less effective in controlling the M-dimers' alignment with nearby Ni-chains when the system is increasingly frustrated.

In addition, dipolar field calculation for M = Zn with spin flipping of 50% shows two broad peaks at 20 - 30 (ν_1) and 40 - 60 MHz (ν_2). This may be why the muon asymmetry for the original batch of sample could be represented by Eq 4.7 where the fast relaxing component represents the static but broadened ν_1 frequencies. As for the other batch of samples measured at 1.8 K, the O4 site might have been preferred and therefore a more noticeable oscillation with ν_2 around 35-40 MHz was detected.

4.7 Conclusion

In this chapter, I showed that the pentanary oxides $PbM_2Ni_6Te_3O_{18}$, where M = Mn, Fe, Co, Zn, allow magnetic frustration to be tuned by changing the transition metal ion M. These compounds contain Ni^{2+} zigzag chains along the *c*-axis which order antiferromagnetically below T_N, in addition to a kagome-like interchain structure in the *a*-*b* plane which becomes geometrically frustrated when coupled ferromagnetically by the interchain exchange pathways J_3 and J_5. The competition between J_3 and J_5 is crucial to understanding the magnetic ground state. By direct comparison of muon-spin rotation (μSR) data on these four compounds, I demonstrated that

Table 4.2: The estimated percentages of spin flipping that best describe the spectral intensity.

	Mn	Fe	Co	Zn
M-dimers	∼10%	∼25%	50%	—
Ni-chains	∼10%	∼25%	50%	50%

when M = Mn, the larger M moment allows the M–Ni exchange J_5 to dominate over the interchain (Ni–Ni) exchange J_3 and suppress magnetic frustration. But as J_5 weakens (M = Fe, Co) and vanishes (M = Zn), J_3 becomes increasingly significant, giving rise to a strongly frustrated magnetic system within the kagome-like structure. These results show beautifully how the nature of the magnetic ground state, whether fully ordered or strongly frustrated, can be constructed by the choice of a single magnetic ion in an isostructural family of materials containing zigzag chains.

Dedicated to the Memory of Dr Pabitra Biswas

5

2D Honeycomb Lattices: α-RuI_3

Contents

In this chapter, I explore the magnetic state of the triangular-lattice material α-RuI_3. It is an isostructural compound to the widely-studied α-$RuCl_3$ which was identified as a potential Kitaev system but exhibits a magnetically ordered zig-zag ground state below 14 K instead of spin liquid behaviour. I present the μSR data which shows that the spins in α-RuI_3 remain dynamic down to at least 50 mK. In addition, I investigate the spin dynamics in a range of temperatures using the LF-μSR methods and determine the presence of the low-frequency fluctuations which are characteristic of a two-dimensional system, and hence demonstrate the potential for α-RuI_3 to realise a spin liquid ground state.

Stephen Blundell helped with the interpretation of the μSR results and Francis Pratt helped with the fitting of the spin diffusion models. Danrui Ni and Robert

Cava synthesised the α-RuI_3 powder samples. Ben Huddart, Francis Pratt and Stephen Blundell assisted with the μSR measurements which were carried out on the HIFI spectrometer at the ISIS Neutron and Muon Source, UK. All computational work was run on the SCARF cluster supported by the Scientific Computing Research Infrastructures Group at the Rutherford Appleton Laboratory and on the Redwood cluster hosted at the Department of Physics, University of Oxford.

5.1 Background

Materials with magnetic ions decorating layered triangular or honeycomb planes are of great interest due to the geometric frustration that is present when the magnetic ions are antiferromagnetically coupled [7]. The compound α-$RuCl_3$ has been widely studied as a candidate quantum spin liquid (QSL) material as the Ru^{3+} ions form a layered honeycomb structure [89] that could be a potential realisation of the exactly solvable Kitaev model, where the exchange interactions on each bond pick a specific spin component [90, 91]. For example, for the six spins that form a honeycomb geometry, each of the six nearest-neighbour bonds facilitates an Ising interaction either along x, y or z, and there is no arrangement that could possibly satisfy all bonds simultaneously. In addition, there exist many degenerate configurations where pairs of neighbouring spins can minimise energy in this model, and hence, when quantum tunneling between these states is considered, the system can form a highly-entangled QSL state [92]. In addition, the spin-orbit coupling in the Ru atoms' 4d orbitals allow a description of an effective $J = \frac{1}{2}$ spin which enhances the quantum fluctuations and the likelihood for the system to avoid magnetic ordering.

However, it was later found that α-$RuCl_3$ orders magnetically between 7 K to 14 K in zero-field depending on stacking faults [93–98], although it enters a possible spin liquid state under an applied magnetic field at 10 T [99, 100]. Studies reported on a similar compound α-$RuBr_3$ have also found a zigzag antiferromagnetic ground state with a higher transition temperature at 34 K [101, 102]. The magnetic ordering in both compounds has been attributed to non-Kitaev interactions in the

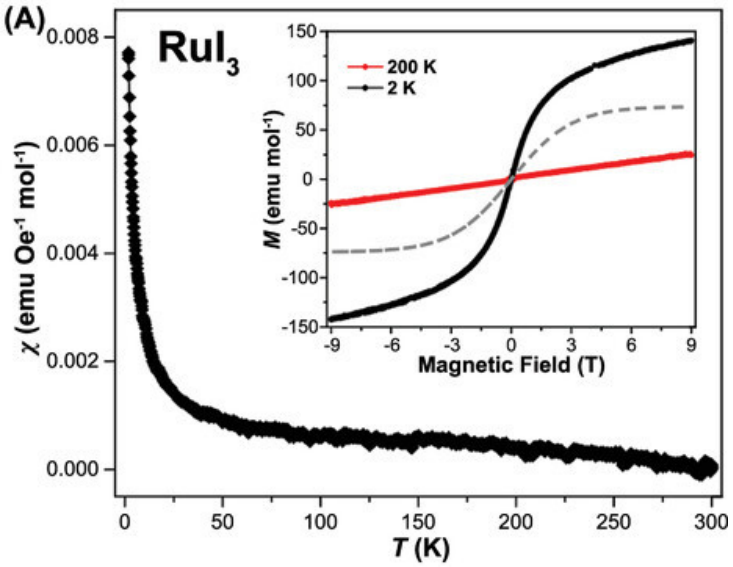

Figure 5.1: Magnetic susceptibility of α-RuI_3 between 1.8 K and 300 K. The inset shows the magnetisation curve at 2 K and at 200 K. This figure is extracted from [104].

Hamiltonian, and both compounds are now thought to realise the more general J-K-Γ model [103], the Hamiltonian for which is given by

$$H = \sum_{\langle i,j \rangle} J\mathbf{S}_i \cdot \mathbf{S}_j + KS_i^\gamma S_j^\gamma + \Gamma\left(S_i^\alpha S_j^\beta + S_i^\beta S_j^\alpha\right), \tag{5.1}$$

where J is the Heisenberg exchange, K is the Kitaev exchange, and Γ the off-diagonal interaction. On each bond, one spin direction is chosen as γ, with α and β denoting the remaining directions. Although both the chloride and bromide salts exhibit magnetic order, the magnetic order in α-$RuBr_3$ appears more robust. The larger ionic radius of the Br^- anion both expands the lattice and increases the covalency of the Ru–halide bond due to the up-floating of Br 4p bands compared with Cl 3p bands [101], both of which effects tend to enhance the Kitaev interaction.

The isostructural iodide α-RuI_3 has only been recently synthesized and has shown promising potential to become another candidate QSL [104]. Magnetic susceptibility measurements of polycrystalline samples found α-RuI_3 to be weakly paramagnetic and no magnetic ordering was observed down to 1.8 K, as shown in Fig. 5.1. The magnetisation data show a linear dependence on the external field at 200 K, but at low temperature (2 K) there is an S-shaped feature which cannot be completely explained by a Brillouin function [104].

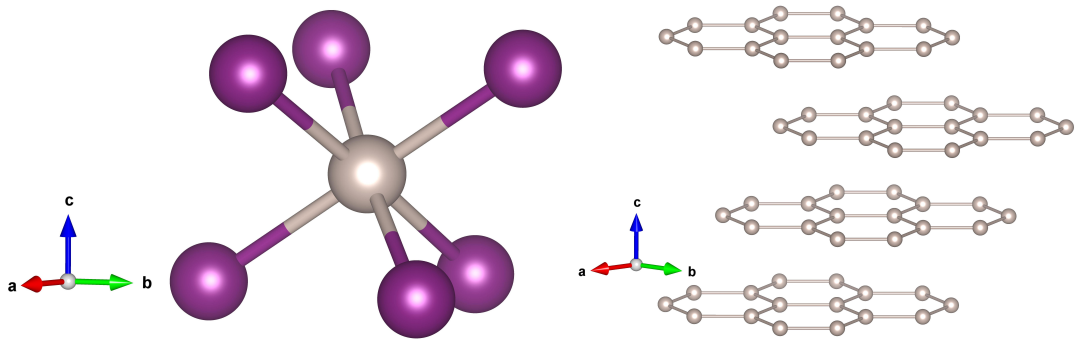

Figure 5.2: (Left) The octahedral crystal field of I^- ions (purple) around a Ru^{3+} ion (grey). (Right) The honeycomb layers of Ru^{3+} ions stack along the c-axis in an A-B-C stacking order.

Meanwhile, heat capacity (C_p) measurements also found no indication of a phase transition between 0.35 K and 10 K, but did identify a large T-linear term (29.3 mJ mol^{-1} K^{-2}, larger than other layered insulating metal trihalides such as CrI_3, 1.17 mJ mol^{-1} K^{-2}, and in contrast with α-$RuCl_3$ in which the γT term vanishes) [104]. In contrast with the insulating nature of α-$RuCl_3$, resistivity measurements revealed metallic behaviour [104, 105], which is consistent with DFT calculations that identify metallic states near the Fermi surface [104–106] and is supported by resonant inelastic x-ray scattering measurements that demonstrates bulk metallicity in α-RuI_3 [107].

5.2 Crystal Structure

α-RuI_3 crystallises in the $R\bar{3}$ space group in a three-layer centrosymmetric rhombohedral lattice structure, where the magnetic Ru^{3+} ions are located in the 6c Wykoff position $\left(\frac{2}{3}, \frac{1}{3}, 0\right)$ and the non-magnetic I^- ions occupy the 18f position (0.3510, 0.0014, 0.0796) [104]. The Ru^{3+} ions form honeycomb lattice layers within the ab-plane and the layers stack along the c-axis in an A-B-C fashion with a vertical separation of 6.29 Å and with a horizontal translation between layers. After three layers, the fourth layer returns to the same position vertically above the first as shown in Fig. 5.2. The in-plane Ru^{3+}-Ru^{3+} distance is 3.91 Å , which is much smaller than the vertical separation of Ru layers, allowing α-RuI_3 to be considered as a 2D layered material with honeycomb lattices. The magnetic Ru^{3+} ion is located in an

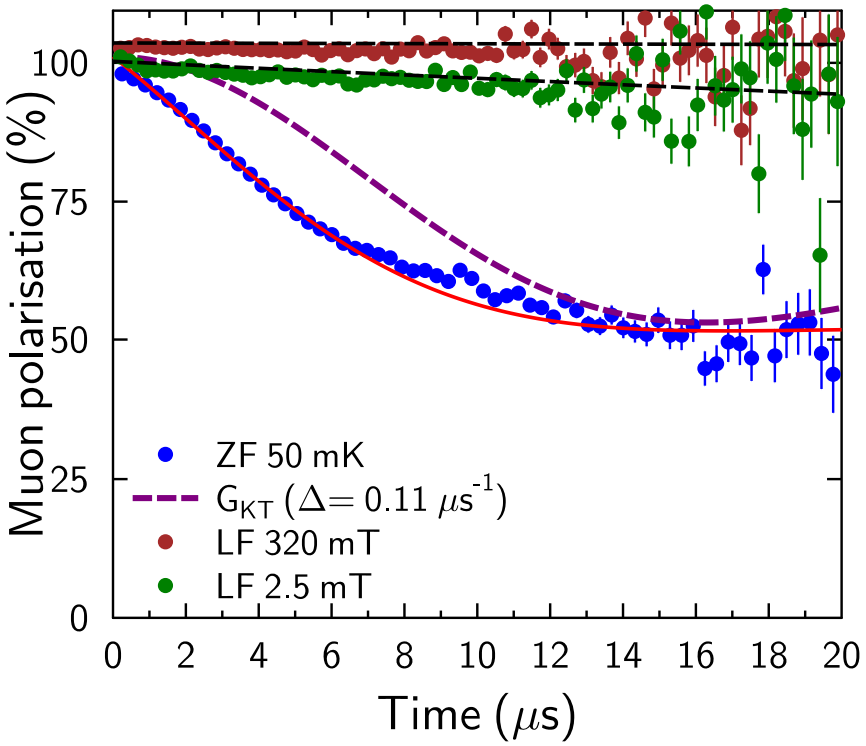

Figure 5.3: Blue: ZF-μSR polarisation measured at 50 mK with error and a fitted line (red) by Eqn 5.2. Purple: A Kubo-Toyabe relaxation with $\Delta \approx 0.11\ \mu s^{-1}$ as a comparison to a pure relaxation by nuclear moments. Green & Brown: LF-μSR polarisation with 2.5 mT and 320 mT applied at 50 mK, with black dashed lines indicating the fit to an exponential decay function $e^{-\lambda t}$.

octahedral crystal field of the six surrounding I^- ions, similar to that in α-$RuCl_3$ which has led to a low-spin configuration in the t_{2g} levels and, with spin-orbit coupling, an effective $J = \frac{1}{2}$ ground state that potentially realises the anisotropic interactions described by the Kitaev model [108, 109]. In addition, single crystal X-ray diffraction measurements reported in [104] found a very small occupancy of Ru ions at the 3a Wykoff position (0, 0, 0), and this has been attributed to the stacking faults of the Ru layers, which is a widely known phenomenon for α-$RuCl_3$ [93–98]. The polycrystalline sample used in our experiment was prepared using a self-flux method and has been characterised using X-ray diffraction (as described in [104]).

5.3 μSR Zero Field

Zero-field (ZF) μSR measurements have been performed with a total of $\approx$ 200 mg of powder samples contained in two silver packers and held onto the sample holding

silver plate with cryogenic vacuum grease, using the HiFi spectrometer at the ISIS Neutron and Muon Source, UK. The muon asymmetry at 50 mK, which is plotted in Fig. 5.3, shows a monotonic relaxation of the muon asymmetry, and the results across all temperatures between 50 mK and 160 K show no evidence of any precession signal that would indicate magnetic ordering. The asymmetry exhibits an initial Gaussian-like decay but becomes exponential at late times. This behavior can be crudely fitted by

$$P(t) = P_{\mathrm{r}} G_{\mathrm{KT}}(t, \Delta) e^{-\lambda t} + P_{\mathrm{bg}} \tag{5.2}$$

where P_{r} and P_{bg} are the normalised muon polarisation asymmetry relating to the relaxing component and background component (due to muons implanted in the silver packet and the silver plate). This can be interpreted by assigning the function $G_{\mathrm{KT}}(t, \Delta)$, a Kubo-Toyabe relaxation function, to a distribution of static, but randomly oriented, nuclear moments and assuming that the muon is simultaneously coupled to dynamical fields at the muon site which arises from fluctuations in the electronic Ru^{3+} moments, giving rise to the weak exponential decay term $e^{-\lambda t}$. To illustrate the effect of this exponential term, the pure Kubo-Toyabe function with a field distribution width $\Delta = 0.11\ \mu s^{-1}$ and no extra decay term is plotted as a dashed line in Fig. 5.3. I found no possible fit to the data using just the relaxation function G_{KT} which indicates that there is an additional relaxation process occurring along with the effect of static magnetic fields from nuclear moments. If the fitting is performed with a stretched exponential term $e^{-(\lambda t)^{\beta}}$ instead, we found β to be 1.22(1) which confirms the Lorenztian case for field distribution.

For this experiment, I loaded the powder samples into a silver packet made of 25 μm silver foil, placed it on a silver plate, and mounted it in a dilution refrigerator. Despite the large surface area, the packet is thin and therefore a significant fraction of the muons have stopped in the silver, which has a negligible relaxation rate and is therefore represented by the constant background P_{bg} in our ZF-μSR data.

To conclude, ZF-μSR results therefore provide strong evidence that the sample does not undergo magnetic ordering down to the lowest temperature 50 mK, in strong

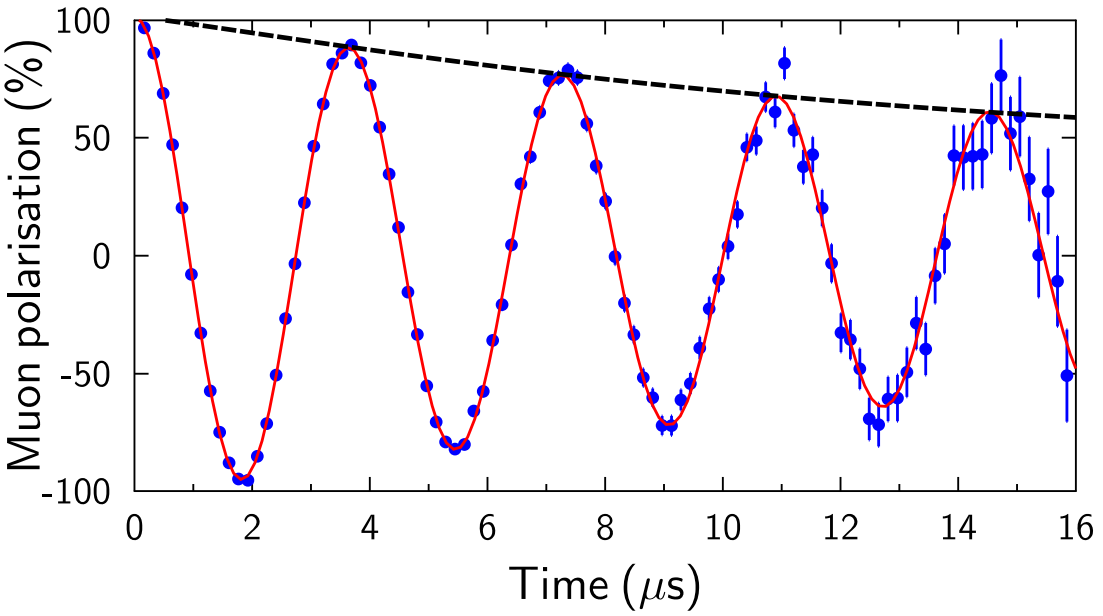

Figure 5.4: wTF muon asymmetry (blue) at 61 mK with a 2.0 mT transverse field, and the fitted line (red) using Eqn. 5.3. The dashed line (black) shows the relaxation envelope.

contrast to the spin precession signals that are obtained in ZF-μSR experiments on α-$RuCl_3$ [98] and α-$RuBr_3$ [110] below their ordering transitions temperatures.

5.4 μSR Weak Transverse Field

A weak transverse field (wTF) is normally applied in the paramagnetic state as a routine procedure to calibrate α in the muon asymmetry function $A(t) = A_0 P(t)$ and to find the initial asymmetry A_0 (see Chapter 3). However, when performed at low temperatures, it can help unveil the important magnetic state of the compound.

The wTF-μSR measurements with a 2.0 mT transverse field at 61 mK exhibit a clear oscillation with weak damping, as shown in Fig. 5.4, which rules out the presence of a strong local static field as that would have provided an asymmetry spectrum that is either heavily damped and/or oscillates at a different frequency. By fitting the wTF-μSR spectrum to a cosine function multiplied by a relaxation envelope, given by

$$P(t) = (P_{\mathrm{r}} e^{-\lambda t} + P_{\mathrm{bg}}) \cos(2\pi\nu t + \phi), \tag{5.3}$$

and using the same relaxing asymmetry P_r as in the ZF measurements (see Eqn 5.2), the precession frequency ν is consistent with the applied field, and λ is found to be 0.074(2) μs^{-1}. I also fitted the spectrum with a stretched exponential decay $e^{(-\lambda t)^{\beta}}$ and found $\beta = 1.17(4)$, which is consistent with a Lorentzian field distribution superimposed on top of the applied transverse field instead of a Gaussian distribution which would yield $\beta = 2$. This reflects persistent spin dynamics and a fluctuating local field at the muon site in α-RuI_3.

5.5 μSR Longitudinal Field

To verify the nature of the local field, we applied a longitudinal field (LF) at five temperatures from 100 mK up to 40 K. The purpose of applying a longitudinal field is to use a large, dominating field to quench the muon relaxation that originates from nearby nuclear moments. In materials without electronic magnetism, a small applied field of 2.5 mT is sufficient to decouple the muon from the field produced by surrounding nuclear moments. Our results show that there is a significant recovery of muon polarization at 2.5 mT, which confirms that the muon experiences a significant relaxation due to nuclear moments. However, a small fraction of the relaxation in the form of $e^{-\lambda t}$ remains, as shown in Fig. 5.3, which could be traced back to the small, fluctuating Ru^{3+} electronic moments.

The dynamical relaxation weakens with increasing longitudinal field, as shown in Fig. 5.3 for T = 100 mK. I extracted the muon relaxation rate λ for applied longitudinal fields between 2.5 mT and 1.25 T, which is plotted as a function of the field in Fig. 5.5.

To study the spin correlations in α-RuI_3, I fitted the relaxation rate $\lambda(B_{\mathrm{LT}})$ at five temperatures against both the Redfield model, which describes local spin fluctuation and spins do not correlate with any of its neighbours (see Chapter 3), and a 2D spin diffusion model shown in Fig. 5.5. The 2D model, which accounts for a field-dependent spin excitation term [55, 56], was consistently found to fit the LF data better than the Redfield model. This is because the Redfield model plateaus at low fields, but experimentally the relaxation rate is found to increase

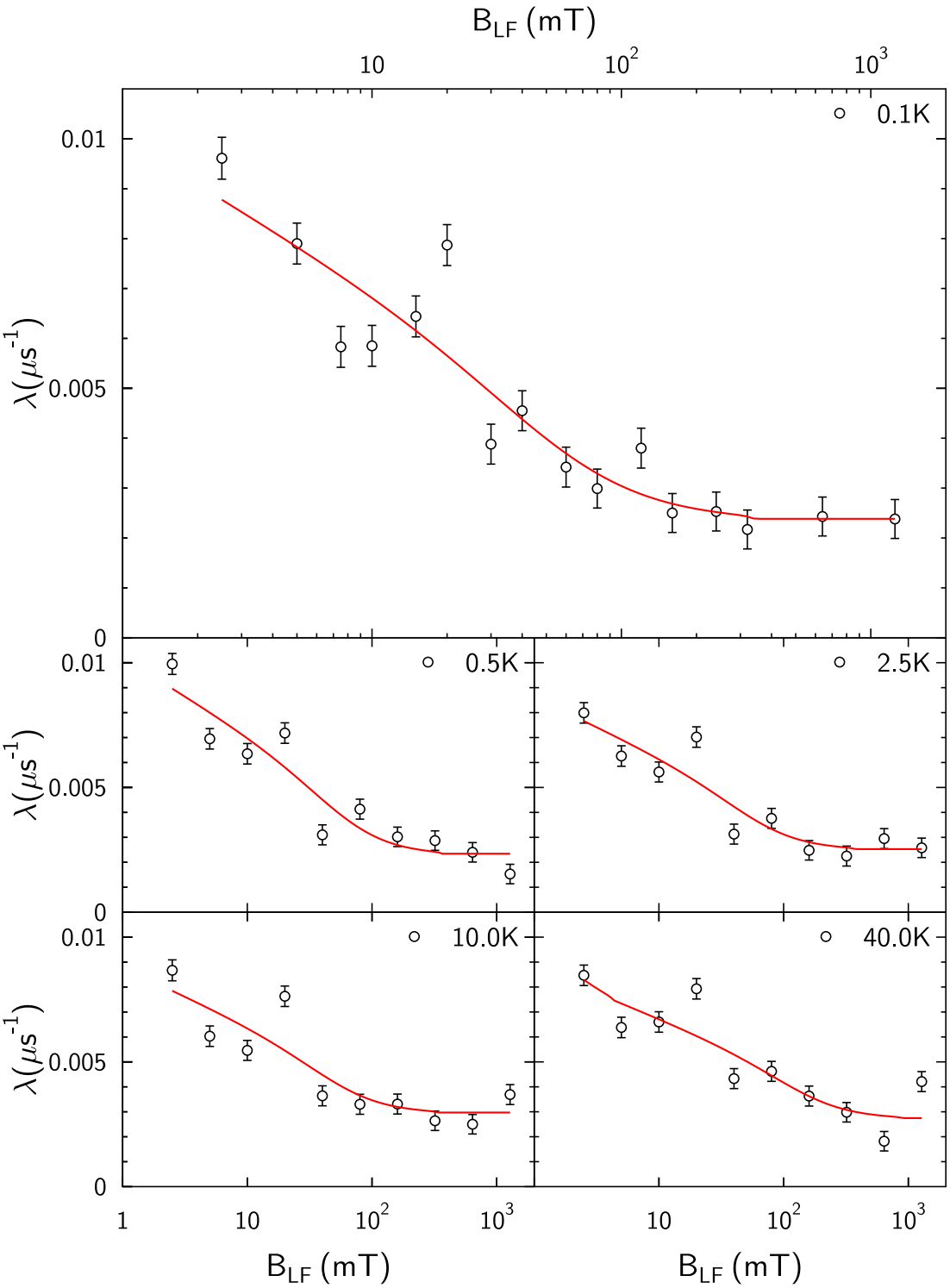

Figure 5.5: Dynamical relaxation rate λ as a function of the applied longitudinal field B_{LF} for α-RuI_3 between temperatures 50 mK and 40 K. The red line shows the fits to the 2D spin diffusion model.

continuously even at very low fields such as 2.5 mT, as shown in Fig. 5.5. The plot could be interpreted as a combination of a field-dependent term and a field-independent contribution such that

$$\lambda(B_{\mathrm{LF}}) = \lambda_{\mathrm{2D}}(B_{\mathrm{LF}}) + \lambda_0, \tag{5.4}$$

where the term $\lambda_{\mathrm{2D}}(B_{\mathrm{LF}})$ refers to the diffusion spin excitation and is proportional to the Fourier transform of the 2D random walk autocorrelation function given by

$$S_{\mathrm{2D}}(t) = \left(e^{-2D_{\mathrm{2D}}t} I_0(2D_{\mathrm{2D}}t)\right)^2 e^{-2D_\perp t} I_0(2D_\perp t), \tag{5.5}$$

where D_{2D} and $D_\perp$ are the fast and slow spin diffusion rates, respectively [56, 111]. The slow diffusion rate is usually much weaker, i.e. $D_{\mathrm{2D}} \gg D_\perp$, and hence one can safely ignore its presence in Eqn. 5.5. In addition, Fig. 5.5 also shows that a field of around 0.5 T is required to fully suppress the field-dependent spin diffusion in α-RuI_3, in which case the remaining relaxation is then due to the effect of the localised spin excitation λ_0.

The fast diffusion rate D_{2D}, extracted from the fits (red lines) in Fig. 5.5 and plotted as a function of temperature in Fig. 5.6, stays around 10 ns^{-1} between 0.1 K and 10 K, but shoots up to 26 ns^{-1} at 40 K. The rising diffusion rate corresponds to a falling entanglement length and is consistent with the scenario where in the high-T classical regime the Ru^{3+} moments are correlated to only their nearest neighbours, whereas at low-T (in the quantum regime) the QSL state has a longer entanglement range between spin pairs [56]. It is noted that the reported Curie-Weiss temperature (15.4 K [112]) lies within the crossover regime between 10 K and 40 K.

This LF-μSR analysis, therefore, demonstrates that the α-RuI_3 sample shows characteristic field dependence of a 2D spin diffusion model, which contains fast diffusion within the *ab* plane (deduced by the crystal symmetry) and slow diffusion along $\hat{c}$, making the case for the antiferromagnetic spin correlations among the weak Ru^{3+} moments beyond the nearest neighbours, and a cross-over transition from the quantum regime to the classical regime between 10 K and 40 K, based on the fitted spin diffusion rate D_{2D}.

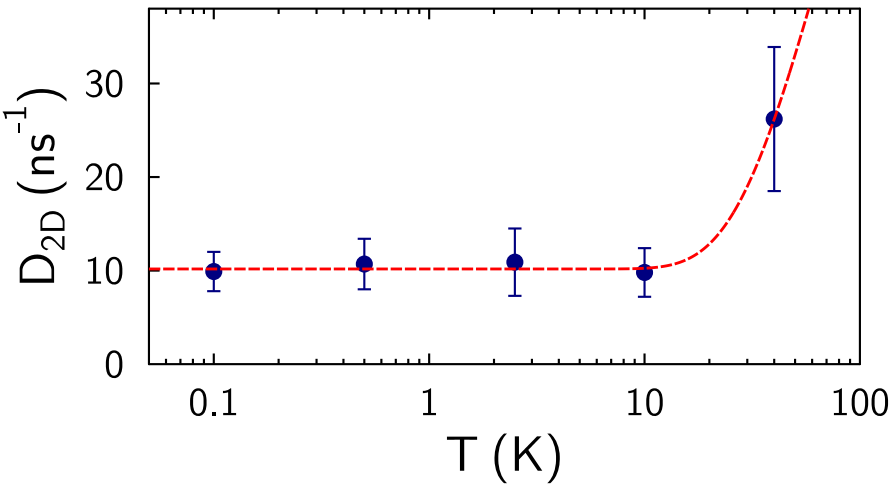

Figure 5.6: The fast diffusion rate D_{2D} of the 2D spin diffusion model extracted by fits in Fig. 5.5 at five temperatures from 0.1 K to 10 K. The red line is a guide to the eye, which assumes a temperature independent term and an activated temperature dependent process contributing in parallel.

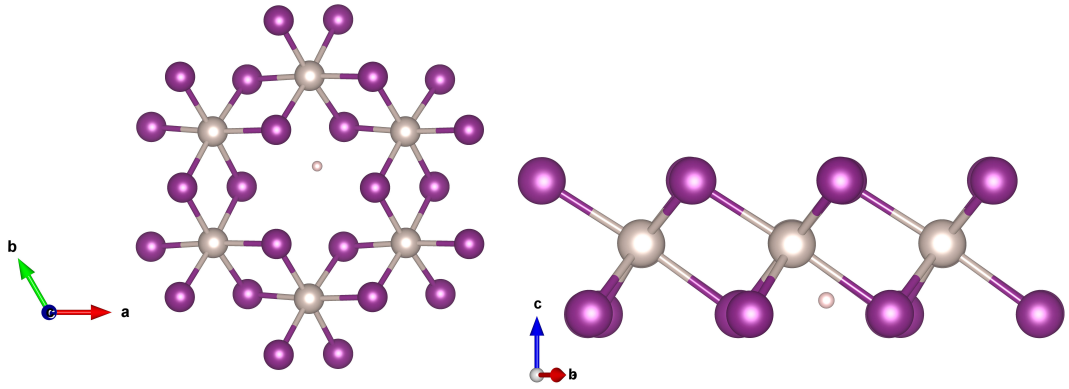

Figure 5.7: Muon site for α-RuI_3, (left) viewed along the *c*-axis and showing the structure of the layer, and (right) viewed along the *b*-axis, showing the layer edge-on. Colours: Ru (Silver), I (purple), μ (white)

5.6 Muon Site

Using the DFT+μ method (see Chapter 3), the muon site in α-RuI_3 is identified to be at [0.544, 0.180, 0.286], within a single RuI_3 layer and is close to the centre of a Ru-hexagon as shown in Fig. 5.7. The site is in close proximity to two I^- ions at distances of 1.91 Å and 2.03 Å with an I-μ-I angle of 156.84°. Because the compound consists of stacks of RuI_3 hexagonal layers, the location of this site implies that the muon will be particularly sensitive to the moments within a single layer.

Estimates of the relaxation caused by randomly oriented nuclear moments

calculated for this muon site and also for a couple of other more energetic sites show that nuclear moments could account for a relaxation rate between $\Delta = 0.03$ μs^{-1} to 0.08 μs^{-1} in the form of a Kubo-Toyabe relaxation as the shortest μ-I bond ranges from 1.67 Å, to 1.93 Å. This effect is mostly dominated by the distance to the nearest I^- ion(s) as the Van Vleck sum goes as $\sigma^2 \propto \sum_i \frac{\mu_{i,I}}{r_i^6}$ and that the iodine nuclear moments with spin $I = \frac{5}{2}$ are 7.5 times larger than that of Ru on average (accounting for various isotopes and abundances). Fitting the 50 mK ZF-μSR data to a Kubo-Toyabe function together with an exponential relaxation to account for fluctuating moments gives a fitted value of $\Delta = 0.11$ μs^{-1} (see Section 5.3), confirming the muon's proximity to the nearest I^- ion. I have also looked into the effect of a static field in the case of an AFM zig-zag order as observed in α-$RuCl_3$ and α-$RuBr_3$, and found that this should produce a dipolar field of at least 1.5 mT (or muon precession frequency of 0.2 MHz) at all potential muon sites if the Ru^{3+} moments are 0.1 μ_B each. This corresponds to an oscillation period of 5 μs^{-1} and is certainly greater than the relaxation observed in our ZF-μSR data (see Fig. 5.3). In addition, should there be a magnetic order the local static field would have damped the 2 mT wTF-μSR measurements at 61 mK very effectively (see Fig. 5.4). Therefore I can confidently rule out static order for α-RuI_3.

5.7 Discussion

RIXS spectra reported showed that the substitution of the halogen in α-RuX_3, from Cl to Br and to I, enhances the d-p hybridisation between the Ru's 4d orbitals and the halogen's p orbitals, which is linked to the more delocalised nature of the 4d orbitals in α-RuI_3 when compared to the sister compounds [107, 112, 113]. Meanwhile, it was also reported that while zigzag ordered state was calculated to be the energetically favourable state in α-$RuCl_3$ and α-$RuBr_3$, while the magnetic states found for α-RuI_3 were very similar in energy, which can lead to the possibility of a QSL state [112]. First principles LDA calculations have further confirmed this and other studies have estimated the magnitude of the Ru^{3+} moments to be very small, of the order of 0.1 μ_B [112, 114].

Recent studies on the solid solution α-Ru$(Br_{1-x}I_x)_3$ showed that a metal-insulator transition is induced at around $x = 0.8$ [115, 116], and hence the α-RuI_3 compound is in close proximity to such a transition. Through halide substitution, the system cross over from a strongly-correlated state that the α-$RuBr_3$ hosts to one that is weakly paramagnetic where the electronic orbitals become more delocalised. However, it is also reported that the Ru spins in the $RuBr_3$-RuI_3 solution are far from a purely paramagnetic case based on magnetisation measurements, so that they cannot be considered as isolated spins [115]. Furthermore, RIXS spectra confirmed that the low-temperature magnetism can be described by $J = \frac{1}{2}$ pseudospins even though the compound is metallic [107]. These are all consistent with the μSR results presented in this Chapter, and when combined, make the case for a QSL state in α-RuI_3 with small but fluctuating Ru^{3+} moments that do not magnetically order.

5.8 Conclusion

Through zero-field and weak transverse-field μSR measurements, I demonstrated the absence of magnetic order in α-RuI_3 down to 50 mK and that the local magnetism can be explained in terms of the effects of both the static nuclear moments and the fluctuating electronic moments. The zero-field μSR data shows that the spins remain dynamic at base temperature; these are very small fluctuating moments and their presence is only directly observable at late times, from $t = 6$ μs onwards, when the nuclear moments-led relaxation fades out. Even though these small Ru^{3+} moments are of the order of 0.1 μ_B, their fluctuating dynamics can be further verified by applying a weak transverse field and also by applying a longitudinal field in the μSR measurements which suppresses relaxation from nuclear moments. And finally, the analysis in this chapter has shown that the nature of spin correlations is consistent with a 2D spin diffusion model which has a cross-over between a quantum and a classical regime between 10 K and 40 K, which explains the departure of the reported magnetic susceptibility and magnetisation curve from calculated values for isolated Ru spins. These results therefore demonstrate the strong likelihood that α-RuI_3 contains highly-entangled Ru^{3+} spins needed to host a QSL state, and

have provided further insights to the exploration of a Kiteav QSL state that is in proximity to a metal-insulator transition.

Sometimes you just let life take you anywhere;
Relax, let it happen, and enjoy the moment.

6

2D Triangular Lattices: $DyTa_7O_{19}$

Contents

In this chapter, I start by presenting new results and evidence of persistent spin dynamics of a new spin liquid candidate $DyTa_7O_{19}$ which contains Dy^{3+} moments arranged in 2D triangular lattice layers that are well-separated along the c-axis. This compound has strong magnetic anisotropy and with antiferromagnetic exchange interaction, it could potentially realise the Triangular Ising Antiferromagnetism that was first proposed by G.Wannier in 1950 [117]. This material, apart from its synthesis and basic magnetic characterisation, has never been reported and therefore this is an

exciting avenue where we explore and contribute to the development of QSL studies.

In addition, I show some brief results on $DyNb_7O_{19}$ and $PrTa_7O_{19}$ where the quantum effect of Pr^{3+} ion is well-known in $Pr_2Sn_2O_7$ (see Chapter 7), and discuss the difference between these isostructural compounds. Finally, with measurements on a $Ba_3Tb(BO_3)_3$ sample, I discuss how a material can transition from a magnetic triangular lattice into a honeycomb one by exploiting the crystal field properties of 4f Kramers and non-Kramers ions, and how this opens up a new pathway towards chemically designing new highly frustrated quantum materials. By doing so, I hope to demonstrate how the interplay between crystal field energy levels, single-ion anisotropy, and the Kramers theorem can be important in the search for new spin liquid materials, and also how isostructural materials containing rare-earth ions can display very distinct low-tempearture magnetic states.

Stephen Blundell helped with the interpretation of the results. Dharmalingam Prabhakaran synthesised all the REM_7O_{19} (RE = Pr/Dy, M = Ta/Nb) samples and performed the powder XRD measurements. Benjamin Huddart, Tom Lancaster and Stephen Blundell assisted with the μSR measurements which were carried out on the GPS and FLAME spectrometers at the Paul Scherrer Institut, Switzerland together with the assistance of staff scientist Thomas Hickens and Chennan Wang. All computational work was run on the SCARF cluster supported by the Scientific Computing Research Infrastructures Group at the Rutherford Appleton Laboratory, and on the Redwood cluster hosted at the Department of Physics, University of Oxford.

6.1 Background

The triangular lattice was one of the earliest lattice structures that was studied in the field of frustrated magnetism. The underlying reason is visually simple; three $S = \frac{1}{2}$ spins at the corners of a triangle that are linked anti-ferromagnetically could never reach a state that fully satisfies all three bonds, and as a result, there exist many equivalent ground states in the planar triangular lattices. When these layers in a 3D material are well-separated along the c-axis, the magnetic structure becomes

a 2D one which strengthens the likelihood for the material to evade magnetic order due to the geometric frustration [16, 17].

Many 2D layered triangular lattice materials have been studied in the search for a quantum spin liquid state such as $YbMgGaO_4$ [118, 119], $Ba_3CuSb_2O_9$ [120], $KYbSe_2$ [121] etc. In particular, $YbMgGaO_4$ generated a substantial hype amongst these compounds due to the absence of magnetic transition and the continuum of excitations (spinons) that are consistent with theoretical predictions [122, 123]. The compound comprises a series of well-separated triangular plaquettes containing Yb^{3+} ions which usually have a large CEF gap of about 20-30 meV between the ground state doublet and the excited states, making it a perfect platform to study the effective $S = \frac{1}{2}$ state at low temperatures. However, it turns out that there is the possibility of site-mixing between the non-magnetic Mg^{2+} and Ga^{3+} ions which could have distorted the Yb-O bonds across the lattice and led to a range of CEF environments around the Yb^{3+} ions [124] (also see Chapter 7 for site-mixing in pyrochlores).

Recently, studies of $NdTa_7O_{19}$ have reported spin excitations down to 40 mK and an Ising-like effective $S = \frac{1}{2}$ state for the Nd^{3+} moments, and μSR measurements have shown spin fluctuations at 66 mK [125]. The crystal structure that $NdTa_7O_{19}$ hosts provides a new opportunity to investigate the effect of crystal fields and spin dynamics by replacing the magnetic A-site with other 4f rare-earth ions, an example being Dy^{3+} which has a much larger electronic moment than Nd^{3+}. This substitution could change the balance between the exchange interactions and the dipolar coupling, and hence, lead to different ground state dynamics.

6.2 Crystal Structure

$DyTa_7O_{19}$ crystallises in the $P\bar{6}c2$ space group in a hexagonal crystal structure, where the magnetic Dy^{3+} ions are located in the 2c Wykoff position and the non-magnetic Ta^{5+} ions occupy the 2e and 12l positions. The Dy^{3+} ions form 2D triangular lattice layers within the ab plane and are vertically stacked along the c-axis. The in-plane Dy^{3+}-Dy^{3+} distance is 6.199 Å which leads to a perfect triangular lattice geometry

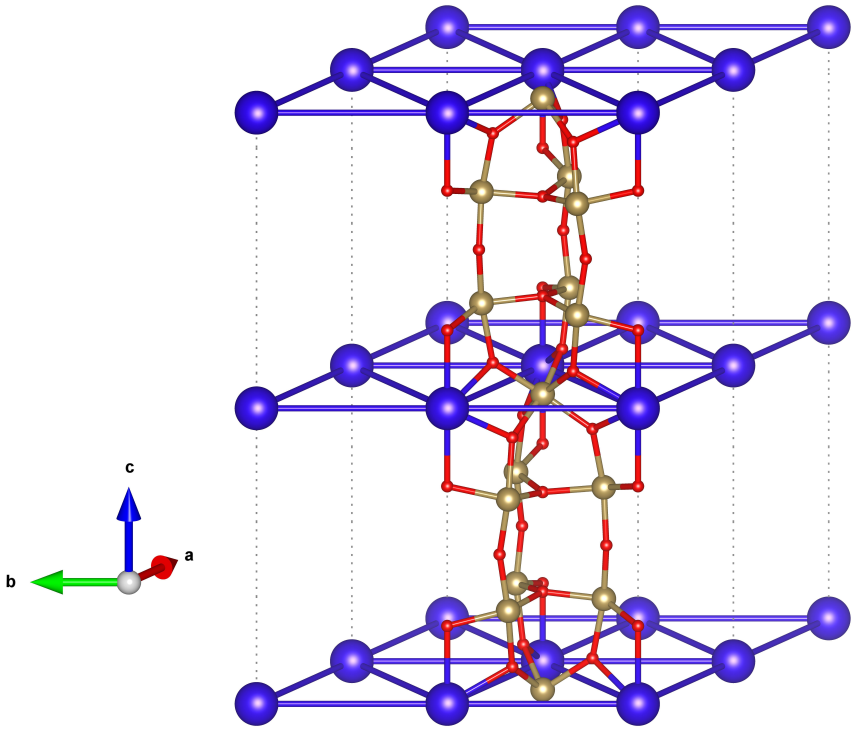

Figure 6.1: The crystal structure of the $DyTa_7O_{19}$ showing the Ta-O bonds that lead to the in-plane and out-of-plane exchange pathways between Dy^{3+} ions. The triangular lattice layers of Dy^{3+} ions are stacked along $\hat{\mathbf{c}}$. Colours: Dy (Blue), Ta (Gold), O (Red).

within the ab-plane. The vertical distance between the layers is 9.93 Å and they are well-separated by TaO_7 pentagonal bipyramidal double layers [126–128]. The ratio of the nearest-neighbour distances in-plane and out-of-plane is 9.93 Å/6.199 Å= 1.602, allowing $DyTa_7O_{19}$ to be considered as a 2D layered material.

The in-plane interactions between the magnetic Dy^{3+} ions are mediated by the exchange pathways -O-Ta-O- within the triangular plane, and the out-of-plane interactions are via the longer exchange pathway -O-Ta-O-Ta-O through the TaO_7 double layers as shown in Fig. 6.1.

Powder XRD measurements have been taken in order to verify the phase of the synthesised $DyTa_7O_{19}$ sample. A Rietveld refinement, completed using the software Profex5 [129], successfully fitted the data with a profile that contains 95.7(1)% of the $DyTa_7O_{19}$ phase and 4.3(1)% of the non-magnetic Ta_2O_5 phase (see Fig. 6.2). The χ^2 value of the refinement reaches 3.1 which represents a good agreement between composite phases and the sample.

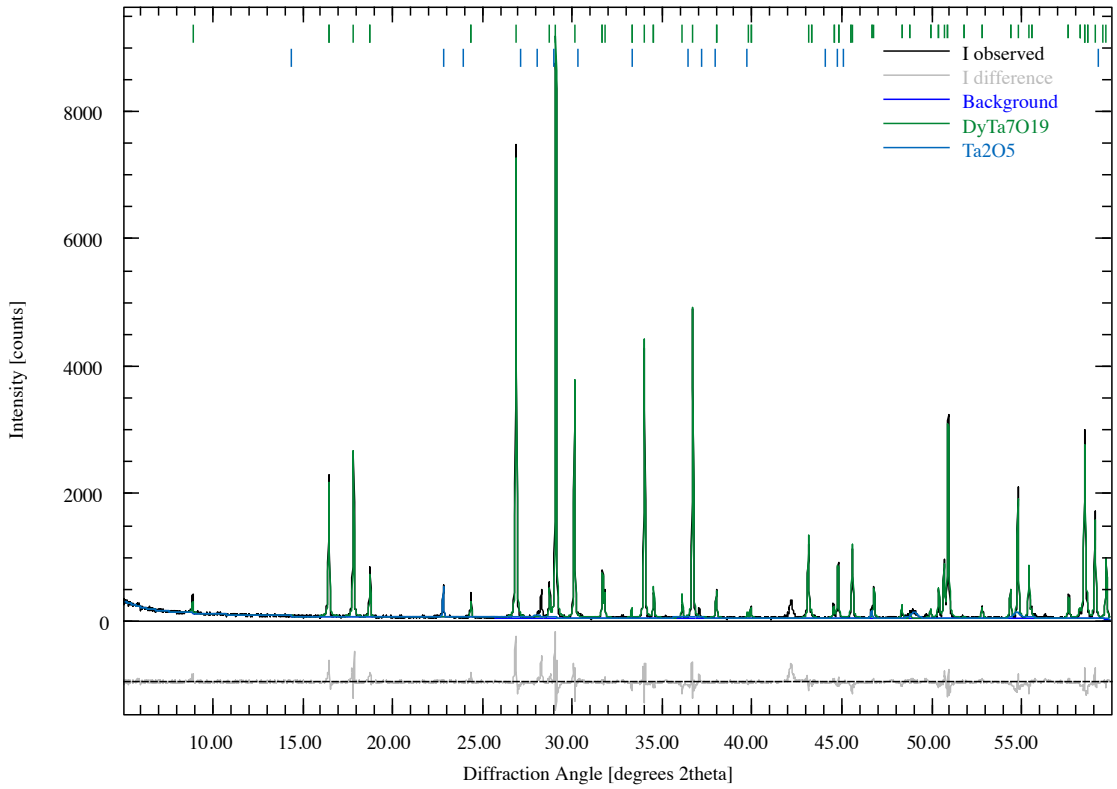

Figure 6.2: Powder XRD measurements and Rietveld refinement are performed to confirm the expected phase for the $DyTa_7O_{19}$.

6.2.1 Single-ion properties

In $DyTa_7O_{19}$, each Dy^{3+} ion is surrounded by 8 O^{2-} ions with two slightly longer Dy-O bonds along the c-axis (2.62 Å) and 6 other Dy-O bonds closer to the a-b plane (2.44 Å). The 8-coordinated Dy-O octahedron has point symmetry operations including a 3-fold axis (C_3) along $\hat{\mathbf{c}}$ and three 2-fold axes ($3C_2'$) perpendicular to $\hat{\mathbf{c}}$. Therefore each Dy^{3+} ion has a D_3 site symmetry. With a $4f^9$ electronic configuration, the ground state multiplet of a free Dy^{3+} ion has quantum numbers $S = \frac{5}{2}, L = 5, J = \frac{15}{2}$, term symbol ${}^6H_{\frac{15}{2}}$, with $2J + 1 = 15$ degenerate $|m_J\rangle$ states and a Landé g-factor g_J of $\frac{4}{3}$. Using PyCrystalField, I found the CEF doublet ground state to be approximately $|m_J\rangle = \left|\pm\frac{15}{2}\right\rangle$ (see Table 6.1) and the energy gap Δ_{CEF} to the first excited state is 6.08 meV and is mainly composed of $\left|\pm\frac{13}{2}\right\rangle$ states. Calculating the expectation values of the $\hat{\mathbf{J}}$ components, I found

$$\left\langle \hat{J}_x \right\rangle = \left\langle \hat{J}_y \right\rangle = 0 \text{ and } \left\langle \hat{J}_z \right\rangle = \pm 7.34 = \pm 0.98J, \tag{6.1}$$

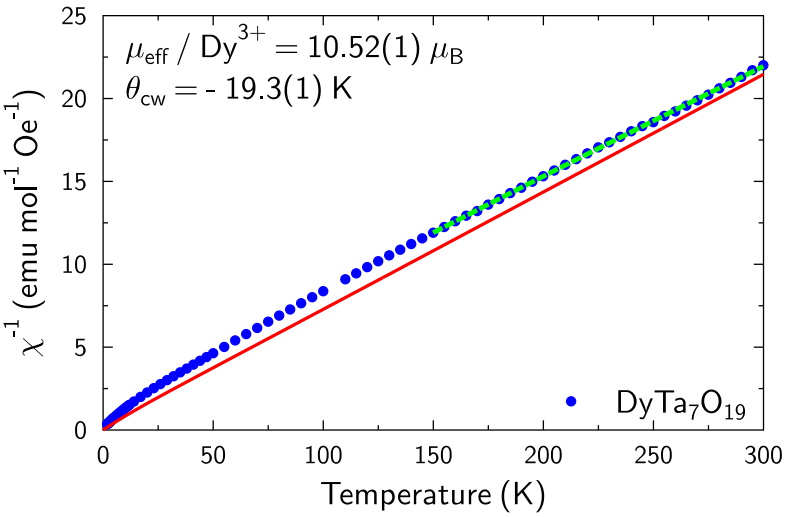

Figure 6.3: Inverse magnetic susceptibility of a powder sample of $DyTa_7O_{19}$ with a Curie-Weiss fit (lime dashed line) in the high temperature region between 150 K and 300 K. The red line shows the calculated values considering the CEF energy levels in the Dy ground state multiplet.

which demonstrates strong magnetic anisotropy along the crystallographic c-axis, resulting in the Dy^{3+} moments behaving like classical Ising spins. Therefore, $DyTa_7O_{19}$ is a candidate material that could potentially realise the Triangular Ising Antiferromagnet state which was first proposed by G. Wannier in 1950 [117].

6.3 Magnetic Susceptibility

Magnetic susceptibility of the powder sample of $DyTa_7O_{19}$ (5.90(5) mg sealed in a gelatin capsule) was taken using the MPMS3 system with an applied field of 10 mT at temperatures between 1.8 K and 300 K. As shown in Fig. 6.3, the susceptibility of $DyTa_7O_{19}$ increases monotonically when the sample is cooled and shows no sign of magnetic transition down to 1.8 K. This identifies $DyTa_7O_{19}$ as a spin

Table 6.1: The ground state and the first excited state of the Dy^{3+} moments in $DyTa_7O_{19}$ expressed as $|\Psi\rangle = \sum_{i=-J}^{J} c_i |m_i\rangle$. Only the four largest components are shown for $|\Psi_{ES}\rangle$.

E (meV)	$\lvert\Psi\rangle$	$\lvert\pm\frac{15}{2}\rangle$	$\lvert\pm\frac{13}{2}\rangle$	$\lvert\pm\frac{9}{2}\rangle$	$\lvert\pm\frac{7}{2}\rangle$	$\lvert\pm\frac{3}{2}\rangle$	$\lvert\pm\frac{1}{2}\rangle$	$\lvert\pm\frac{-3}{2}\rangle$	$\lvert\pm\frac{-5}{2}\rangle$
0	$\lvert\Psi_{GS}\rangle$	0.974		-0.221		0.044		0.001	
7.16	$\lvert\Psi_{ES}\rangle$		0.958		-0.281		0.046		0.008

liquid candidate for which spin dynamics may persist at very low temperatures. Fitting the inverse susceptibility χ^{-1} against the Curie-Weiss law in the high-temperature region (from 150 K up to 300 K) allows us to extract the effective moment per formula unit (i.e. per Dy^{3+} ion) μ_{eff} to be 10.52(1) μ_B, which is close to the free ion value of 10.6 μ_B, and the Curie-Weiss temperature is found to be $\theta_{CW} = -19.3(1)$ K, which demonstrates the presence of antiferromagnetic interactions between the Dy^{3+} moments.

Below 50 K, it can be seen in Fig. 6.3 that χ^{-1} data deviates from the linear Curie-Weiss law, a behaviour linked to the crystal electric field (CEF) splitting of the $J = \frac{15}{2}$ energy levels. A calculated inverse susceptibility curve is shown in the same figure (red line) by considering the lowest energy level in the Dy ion's ground state multiplet. While it is in good agreement with the experimental data, the latter deviates from the calculated values as temperature drops. At both the high and low temperature regions (T < 10 K), linear fits always provide a Curie-Weiss temperature that is more negative than that produced by the CEF-only curve, suggesting a small antiferromagnetic coupling between Dy^{3+} spins.

6.4 Magnetisation

Magnetisation measurements for $DyTa_7O_{19}$ show that the Dy^{3+} ions are approaching saturation at a field of 7 T and at temperature 2 K, with the moment per Dy^{3+} ion reaching almost 7.5 μ_B (see Fig. 6.4). This value is smaller than the full moment of a Dy^{3+} ion which is $g_J J \approx 10$ μ_B given a ground state mostly made up of the $\left|m_J = \pm\frac{15}{2}\right\rangle$ states. It is possible that this is only an intermediate regime where the magnetisation is gradually increasing due to the single ion anisotropy, and upon high field one might observe the full saturation [130–132]. This could be further investigated by applying a large magnetic field at high-field facilities [133] and also by using a single crystal to study the effect when the field is applied parallel and perpendicular to the crystalline c-axis. Attempts to fit the magnetisation curve using a Brillouin function has been carried out, as shown in Fig. 6.4. However, these fitting attempts produce unphysical values for g_J and J of the Brillouin function even when

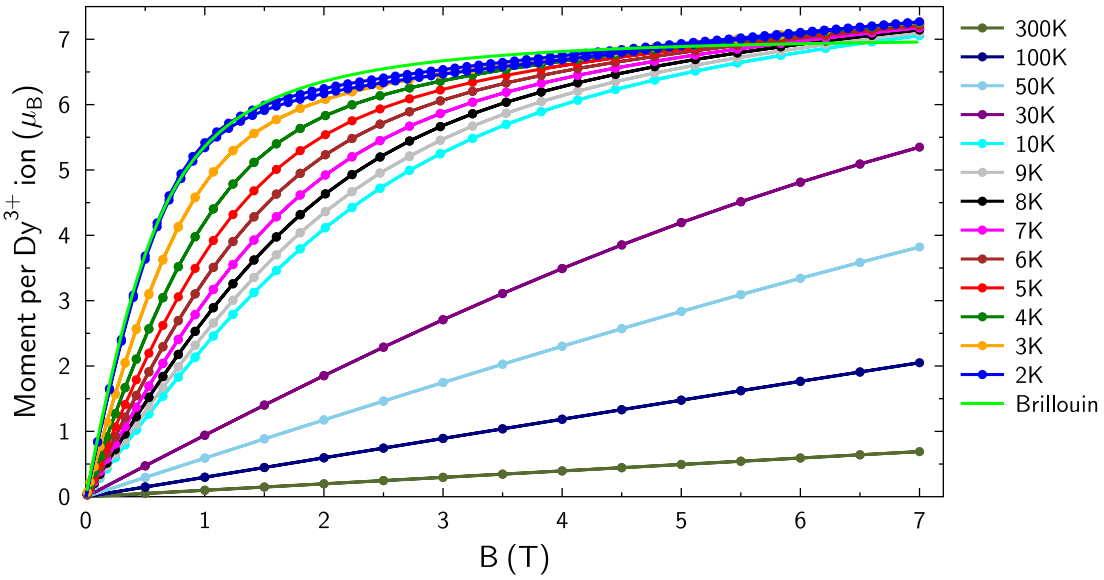

Figure 6.4: Magnetisation of $DyTa_7O_{19}$ at temperatures between 2 K and 300 K and with an applied field up to 7 T. A Brillouin function with $J = \frac{15}{2}, g_J = \frac{4}{3}$, and saturation moment of 7 μ_B at $T = 2$ K is also plotted as a guide for comparison.

the Van Vleck contribution is considered. The disagreement between the measured value and a Brillouin function indicates that there are additional interactions such as the anti-ferromagnetic dipolar couplings between the large Dy^{3+} moments, and therefore, the system could not be considered to be purely paramagnetic.

6.5 μSR Zero Field

A zero-field (ZF) μSR measurement of a powder sample of a mass of approximately 0.5 g is performed using both the FLAME (for 38 mK $\leq T \leq$ 2 K, mounted on a silver plate with N-grease) and GPS (for 1.6 K $\leq T \leq$ 300 K, with powder sample contained in a silver foil packet) spectrometers. The data show a monotonic decay of the muon asymmetry and no magnetic order was observed at all temperatures, as plotted in Fig. 6.5 for temperatures between 1.6 K and 300 K. The relaxation at 1.6 K can be fitted by a stretched exponential function

$$A(t) = A_{\text{relax}} e^{-(\lambda t)^{\beta}} + A_{\text{bg}}, \tag{6.2}$$

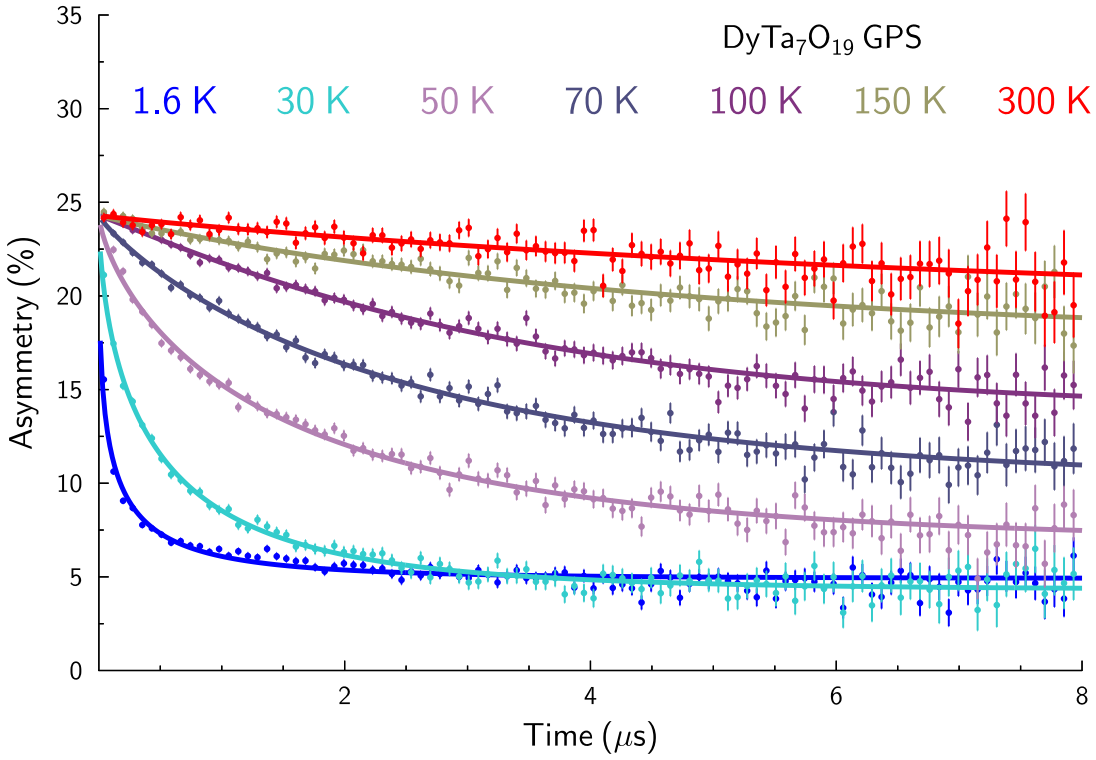

Figure 6.5: Muon asymmetry of $DyTa_7O_{19}$ at temperatures between 1.8 K and 300 K using the GPS spectrometer at PSI, showing relaxation of the muon asymmetry at all temperatures. The data are fitted according to Eqn. 6.2 and are shown as solid lines.

where A_{relax} and A_{bg} refer to the relaxing and background asymmetry respectively, λ is the muon relaxation rate, and β is the stretching exponent that is of the order of unity. To fit the ZF data from FLAME, one has to add an additional slow relaxation term $A_{\text{slow}}e^{-\lambda t}$ to account for muons that might have stopped in the Apiezon N grease (to enhance thermal contact across the polycrystalline sample) and other additional tools such as the silver sample plate. This additional asymmetry accounts for around 22.5% of the relaxing asymmetries and could be quenched by an applied field of 5 mT as shown later in Section 6.6.

A monotonic relaxation is observed down to the lowest temperature as shown in Fig. 6.5 indicates that the muons are experiencing dynamical magnetic environments. The change in the relaxation rate λ, plotted in Fig. 6.6, increases as the temperature falls which points towards slowing dynamics that become more and more effective in suppressing the muon asymmetry (hence rising λ values).

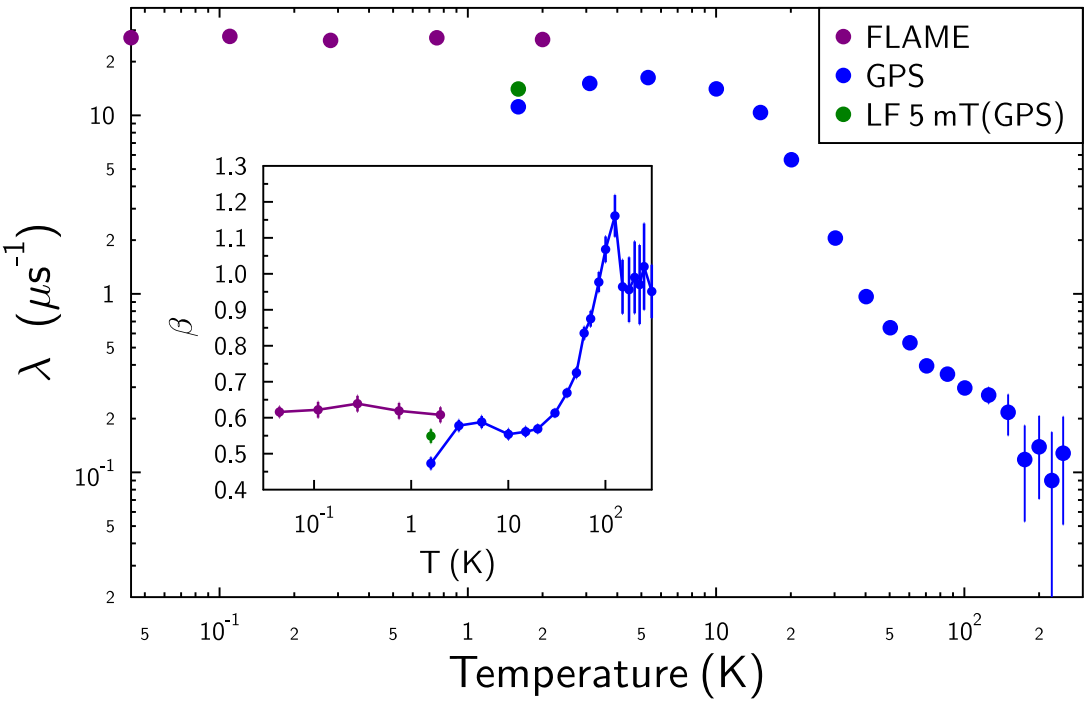

Figure 6.6: Muon relaxation rate λ and exponent β (inset) at temperatures between 38 mK and 300 K by fitting the ZF asymmetry with Eqn. 6.2, indicating a rise of λ below 100 K. A measurement with 5 mT of applied longitudinal field which quenches nuclear-induced relaxation is also plotted as a comparison.

Another possible case that could give rise to very similar μSR ZF asymmetry results is for the system to have a diverse range of static magnetic fields, which can produce a quick relaxation at very early times. This is observed in classical spin ice compounds such as $Dy_2Ti_2O_7$ where dynamic spin fluctuations slow down and become static. However, this would produce a constant one-third tail at larger t because one-third of the local field lies along the initial muon polarization on average so that the muon does not precess. However, by observing the muon asymmetries at low temperatures with zero or with a small 5 mT longitudinal field (LF) which quenches nuclear contributions, the flat tail was always found to be below two-thirds of the initial asymmetry (the maximum possible relaxing asymmetry), it is unlikely that the muons are probing a static magnetic field distribution but instead a dynamical one (or at least a mixture of both).

Further evidence that supports a dynamic case is found by looking at the muon asymmetry when a weak 5 mT transverse field is applied at low temperatures.

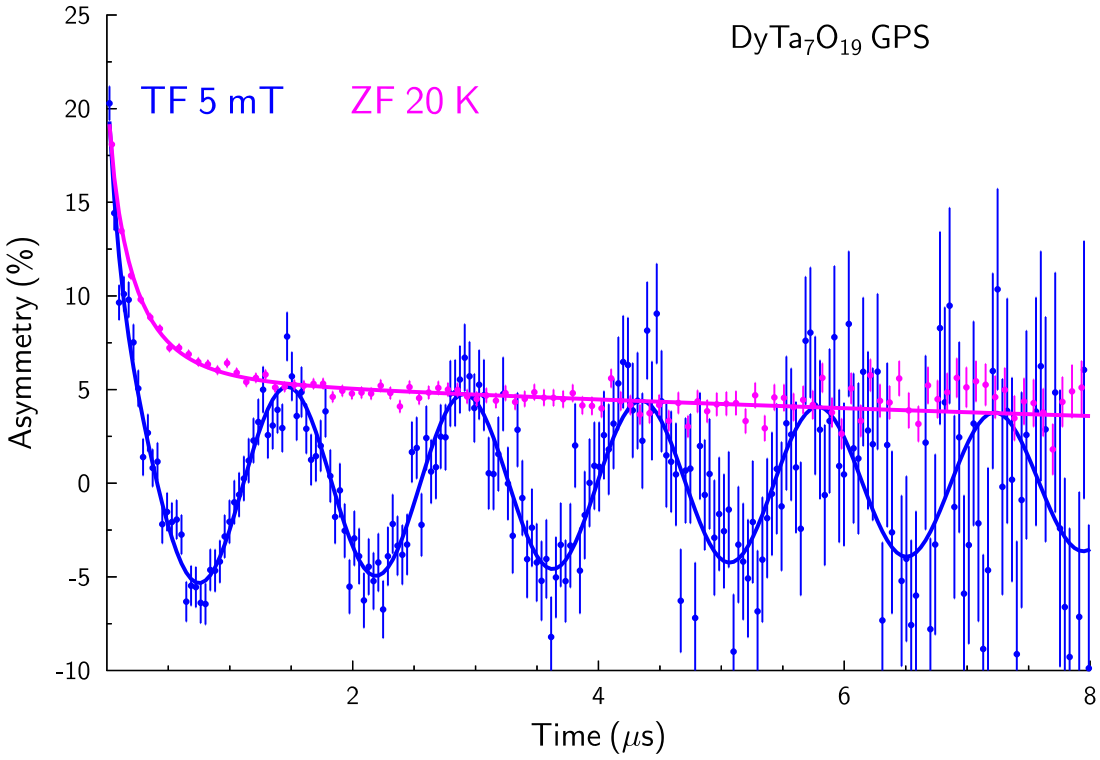

Figure 6.7: ZF asymmetry at 20 K (pink) and a TF50 run (blue) during the cooling of $DyTa_7O_{19}$. Data are taken using the GPS spectrometer at PSI.

Figure 6.7 shows the plot for a ZF run at 20 K and a trial transverse field 5 mT run during cooling from 130 K to 10 K. Despite the larger error bars due to the changing temperatures, the clear oscillation is sufficient to demonstrate that the non-relaxing asymmetries of the ZF-μSR measurements in fact represent muons implanted in other parts of the system (such as the silver foil or sample holder). Should this be a one-third tail of a frozen magnetic spin system the local field would be much stronger than the applied TF and therefore such a clear oscillation would not be observed at all. This provides firm evidence for the case of purely dynamical fields in $DyTa_7O_{19}$.

To find the temperature dependence of the spin dynamics, one could fit the μSR relaxation rate to extract the activation energy E_a [134], by

$$\lambda = Ae^{\frac{E_a}{k_B T}}, \tag{6.3}$$

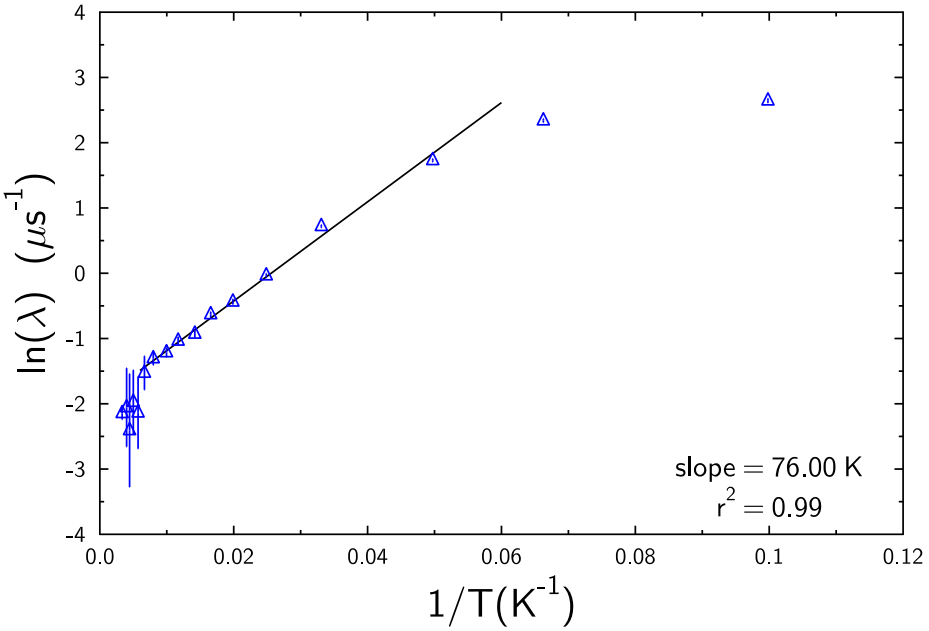

Figure 6.8: Fitting of $\ln\lambda$ against $\frac{1}{T}$ according to Eqn. 6.3 where the slope gives the activation energy E_a in unit of K. This shows that the rise in λ is likely a process linked to the crystal field levels of the Dy^{3+} ions.

such that,

$$\ln\lambda = \left(\frac{E_\mathrm{a}}{k_\mathrm{B}}\right)\frac{1}{T} + \underbrace{\ln A}_{\text{const.}}, \tag{6.4}$$

where the linear slope (also $E_\mathrm{a}/k_\mathrm{B}$) in Fig. 6.8 is found to be 76(4) K which is in close agreement to the theoretical value (Δ_CEF = 7.16 meV = 84 K) from the CEF calculations. At this temperature, the system starts to populate the first excited doublet state and hence the muon relaxation rate changes drastically.

6.6 μSR Longitudinal Field

To further understand the nature of the dynamics in $DyTa_7O_{19}$, we performed LF-μSR measurements at 40 mK and 1.6 K using the FLAME and GPS spectrometers respectively at the Paul Scherrer Institute. The reason is three-fold; First, if the relaxation mainly originates from the randomly oriented paramagnetic nuclear moments, which leads to a Kubo-Toyabe relaxation, a 5 mT of LF would be sufficient to quench it and produce a constant flat asymmetry. Second, if the magnetism of the system is created by electronic moments, one could check if the relaxation is from

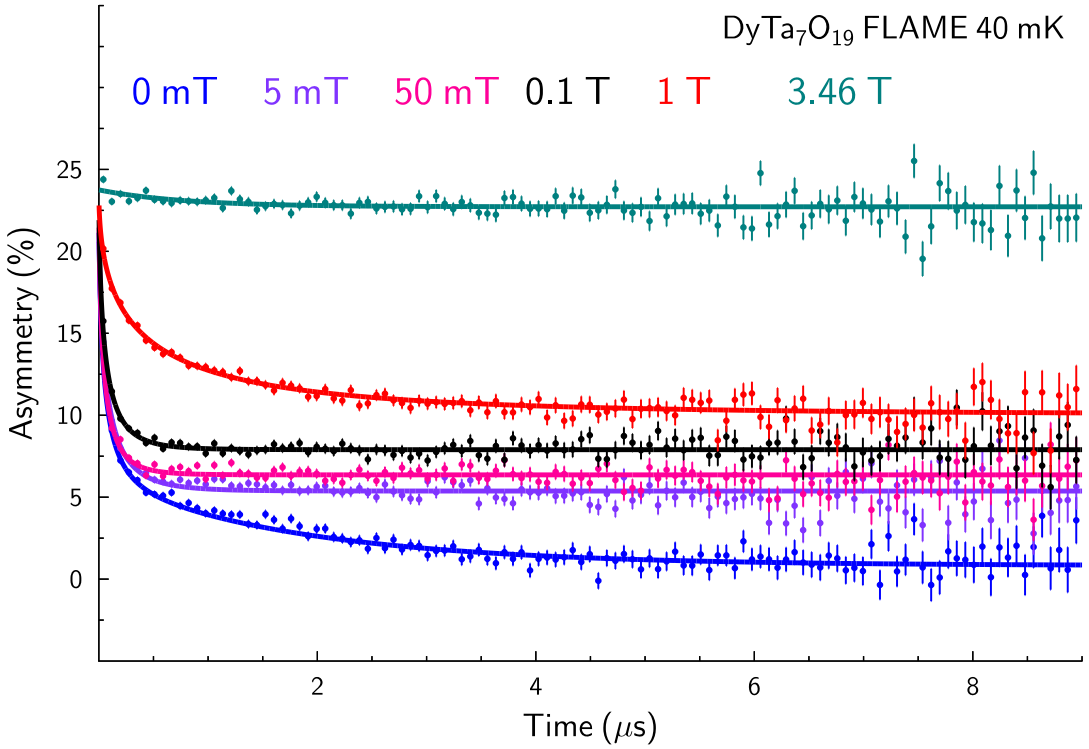

Figure 6.9: Muon asymmetry of $DyTa_7O_{19}$ at base temperature (38 mK) with an applied longitudinal field up to 3.46 T using the FLAME spectrometer at PSI. The data shows a muon relaxation even with an applied longitudinal field of 1 T, which indicates dynamical fields in the sample.

static moments by applying a large LF that dominates over the local static field. Last, if the ground state of the magnetic structure is indeed a dynamic one, extracting the key parameters (relaxation rate λ and the exponent β) and plotting them against the applied field B allows one to study the nature of dynamics and evaluate the fluctuation rate using the Redfield formula or different spin diffusion models [56].

Our results from LF-μSR at base temperature 40 mK (see Fig. 6.9) show that the rapid relaxation remains significant even at 1 T (which easily rules out nuclear-led relaxation) and only at a very high field at about 3.5 T could one fully decouple the muons from the local dynamical state. If the Dy^{3+} spins slow down and freeze at lower temperatures, one should expect to see an extremely fast muon relaxation, which would not normally be resolvable in μSR experiments apart from the constant 1/3-tail component. Considering data from all μSR measurements, there is strong case for persistent spin dynamics in $DyTa_7O_{19}$.

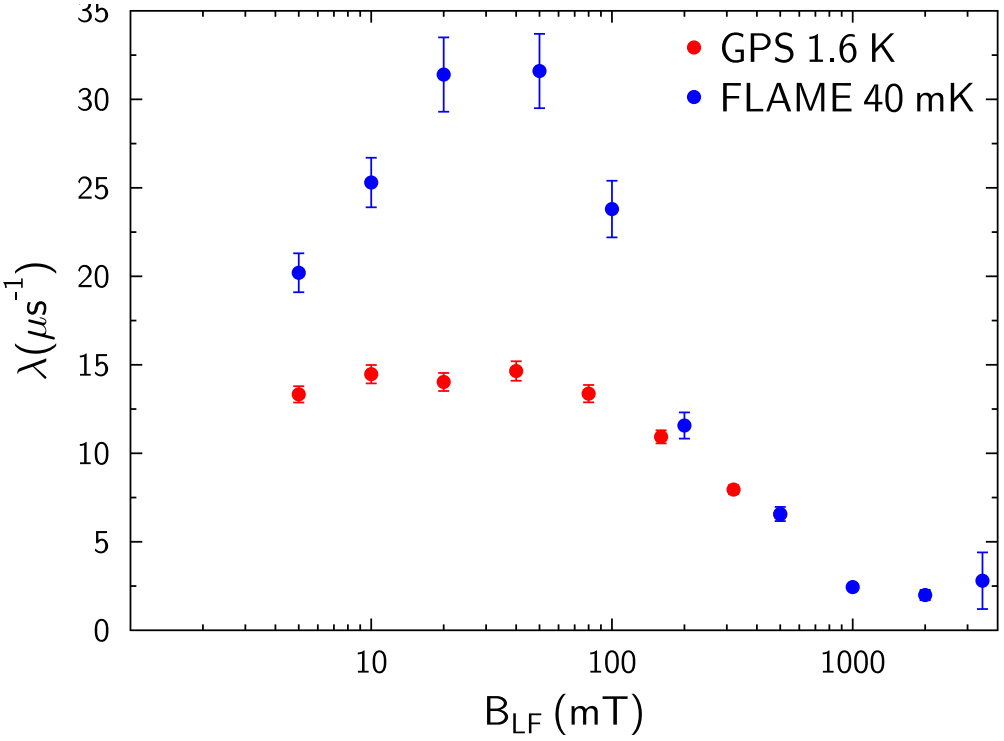

Figure 6.10: The muon relaxation rate with applied LF from 5 mT up to 3.46 T at base temperatures in both the GPS and FLAME spectrometers (38 mK and 1.6 K respectively). This shows that there is potentially a field-activated effect at between 10 mT and 200 mT.

The LF dependence of the relaxation rate $\lambda(t)$, with fixed β, is plotted in Fig. 6.10 which first rises at smaller applied fields and reaches a peak between 20 mT and 50 mT, then falls off as the field increases to 2 T. This effect has previously been reported in LF-μSR measurements of spin ice pyrochlore compounds $Tb_2Sn_2O_7$ [135], $Tb_2Ti_2O_7$ [136] and $Dy_2Zr_2O_7$ [137], and has been linked to the increased magnetic excitations induced by the applied field [135].

6.7 Muon Site Calculations

Muon site calculations using the DFT+μ method (see Chapter 3) were performed on a 2 x 2 x 1 supercell lattice which contains 217 atoms – 216 from the $DyTa_7O_{19}$ plus a muon. The site with the lowest energy was found at [0.19, 0.53, 0.25] and lies between two O3 atoms with 6k Wyckoff positions and is sandwiched by the two pentagonal bipyramidal TaO layers along **c**, as shown in Fig. 6.11. Therefore the site is also equidistant to two Dy^{3+} triangular lattice layers. It is at distances 1.04 Å

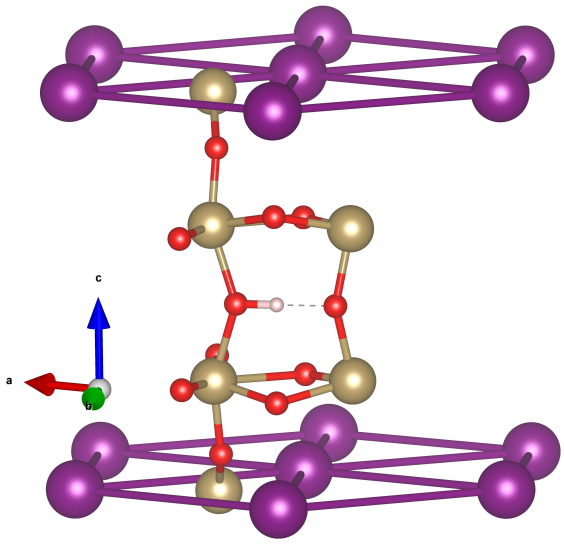

Figure 6.11: Most probable muon site for $DyTa_7O_{19}$. Colour scheme: Dy (purple), Ta (gold), O (red), and the muon (white).

and 1.51 Å to the two nearest O3 atoms. The muon site calculation therefore supports the case that the muon is located far from the magnetic Dy^{3+} triangular lattices, and therefore can resolve the dynamics of the Dy^{3+} moments despite their sizeable moments which often leads to a muon precession that is too fast to be resolved in μSR experiments. At this position, the muon is approximately 10 Å from the nearest Dy atoms, and hence, if the Dy moments are static, they would generate a dipolar field of the order of 10 mT at the muon site, which is about 1.4 MHz in terms of muon preccession frequency, but this has not been observed in our μSR data. To test the robustness of the results I have repeated the calculations using a different set of ultra-relativistic pseudopotential (PP) named PBE instead of PBESOL. First, I performed a structural relaxation allowing both atomic positions and lattice parameters (a, b, c, α, β, and γ) to vary. The results showed small changes to the original atomic positions and unit cell lengths (of the order of 0.5 %) but have retained the hexagonal symmetry. This shows that lattice parameters are susceptible to the choice of PP used. DFT+μ calculations with the new set of lattice parameters and PP files have resulted in an identical muon site position as found above and shown in Fig. 6.11.

More energetic muon sites were also found during the DFT+μ calculations,

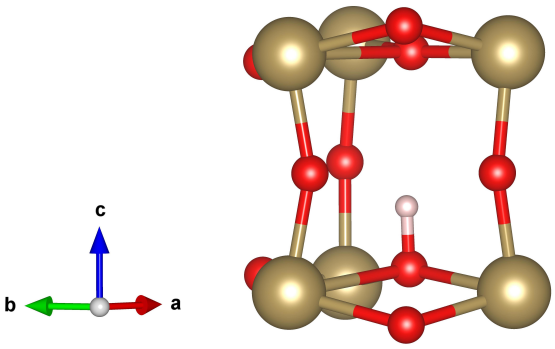

Figure 6.12: An alternative muon site for $DyTa_7O_{19}$ with a higher potential energy than that in Fig. 6.11.

one of which is at a similar position found above but instead linked to the 12l O1 atoms as shown in Fig. 6.12. However, given that both calculations use different pseudopotential files and slightly different lattice parameters, and yet have concluded with the same lowest energy muon site, I believe that this site is the most probable site for $DyTa_7O_{19}$.

6.8 Discussion

In this chapter, I have shown that $DyTa_7O_{19}$ remains paramagnetic-like down to low temperatures in the MPMS susceptibility measurements. With relaxation in our ZF-μSR and TF-μSR measurements, I have demonstrated the absence of magnetic ordering in $DyTa_7O_{19}$ down to 38 mK and that the nature of the spin system is a dynamic one. By LF-μSR, I showed that spin dynamics persist under an applied longitudinal field up to at least 1 T. I therefore believe that $DyTa_7O_{19}$ behaves as a classical spin liquid, and given the magnetic anisotropy calculated with its crystal field profile, it has the potential to realise a Triangular Antiferromagnetic Ising model which was first proposed by G. Wannier [117].

In our LF-μSR measurements, we observed the rise of muon relaxation rate λ at a small applied field between 0 mT to 50 mT, and this is an effect that has not been fully understood by the μSR community [135–137]. One possible aim of future experiments is to look into how the applied field changes the properties of fluctuation of Dy^{3+} moments and magnetic field at the muon site. Firstly, a LF-μSR

field scan at more temperatures would allow us to observe the development of this effect more thoroughly across T. Furthermore, AC susceptibility measurements could be used to explore the proposed increased magnetic excitation activities [135] by changing the DC field and the probe frequency ω. Preliminary results, which are included in Chapter 9, show signs of spin dynamics at 1.8 K with DC field of 50 mT and AC probe frequency of 1000 Hz. It is likely that higher frequencies are needed to fully probe the spin dynamics in $DyTa_7O_{19}$.

While we have not yet been able to determine the strength of the nearest-neighbour exchange interaction J_1 from the results reported in this Chapter, the dipolar interaction between each pair of Dy^{3+} spins, separated by about 6.2Å, has a magnitude of about 400 G (or equivalently 0.3 K). Furthermore, because of the Ising nature and the geometry of the triangular network of the Dy spins, each spin always produce an anti-aligning field on its neighbouring spins. Therefore, this interaction is anti-ferromagnetic and could be crucial to the understanding of the ground state dynamics of $DyTa_7O_{19}$ in addition to the nearest-neighbour exchange interactions.

6.9 Related Materials

6.9.1 $DyNb_7O_{19}$

When a new compound is found to host interesting physics, it is interesting to study the other members of the same family by chemical substitution. In most cases, such a substitution does not change the overall structural phase of the compound and only modifies the lattice parameters and atomic positions of the order of 1 %. However, this is different when one substitutes the Ta^{5+} ions in $DyTa_7O_{19}$ with Nb^{5+}. It turns out that the substitution between Ta^{5+} and Nb^{3+} ions has a significant effect on how the pentagonal bipyramidal NbO_7 (P) and octahedral REO_6 (O) layers are stacked along the c-axis [138], and this can change the out-of-plane interactions between the magnetic ions; In $DyTa_7O_{19}$, the magnetic O layers follow a -O-P-P-O stacking rule and hence they are always separated by two non-magnetic P layers. For $DyNb_7O_{19}$, the stacking order becomes -O-P-O-P-P-P-O- where the Dy^{3+} O layers are now separated by single or triple P layers.

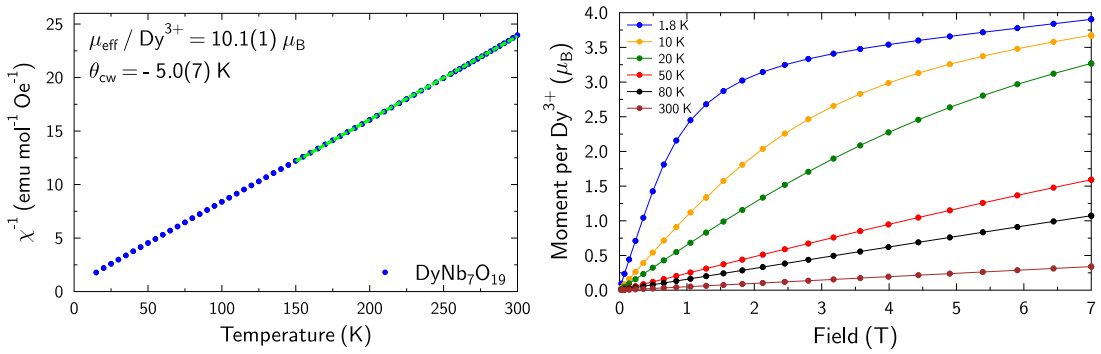

Figure 6.13: (Left) Curie Weiss fit of the magnetic susceptibility for $DyNb_7O_{19}$ between 1.8 K and 300 K with a fitted linear line. (Right) Magnetisation $M(B)$ curve for $DyNb_7O_{19}$ between 1.8 K and 300 K.

This means that every pair of magnetic Dy^{3+} layers becomes closer but each pair is well-separated from other pairs. The question now one should ask is how these closer triangular nets affect the spin liquid properties?

A powder sample of $DyNb_7O_{19}$ has been prepared by Dr. Dharmalingam Prabhakaran (Oxford). Our magnetic susceptibility measurements on $DyNb_7O_{19}$ (see Fig. 6.13) find no magnetic transition down to 1.8 K and there is no divergence between zero-field cooling and field cooling. By performing a Curie-Weiss fit in the high-temperature region we obtain an effective moment of $\mu_{\text{eff}} = 10.1(1)\ \mu_{\text{B}}$ and Curie-Weiss temperature of $\theta_{\text{CW}} = -5.0(7)$ K , which indicates a antiferromagnetic correlation between the Dy^{3+} ions. Using PyCrystalField, Dy^{3+} ions $\left(J = \frac{15}{2}\right)$ in $DyNb_7O_{19}$ were found to contain a low-lying ground state with an energy gap of ≈ 8 meV (90 K) to the first excited state, and therefore, the compound provides an ideal platform to explore the interaction between the muon and the effective $J = \frac{1}{2}$ ground state at low temperatures below 50 K.

Zero Field (ZF) μSR measurements between 1.8 K and 300 K were performed on the $DyNb_7O_{19}$ powder sample packed in a silver packet and the results are plotted in Fig. 6.14. The data showed a fast relaxation in the first 0.5 μs^{-1} which then slows down but continues to relax throughout the entire time window. The relaxation is certainly much slower than that observed for $DyTa_7O_{19}$ (Fig. 6.5) and is similar to a relaxation caused by randomly oriented nuclear moments. When a small longitudinal field of 5 mT is applied, the asymmetry has the same quick relaxation

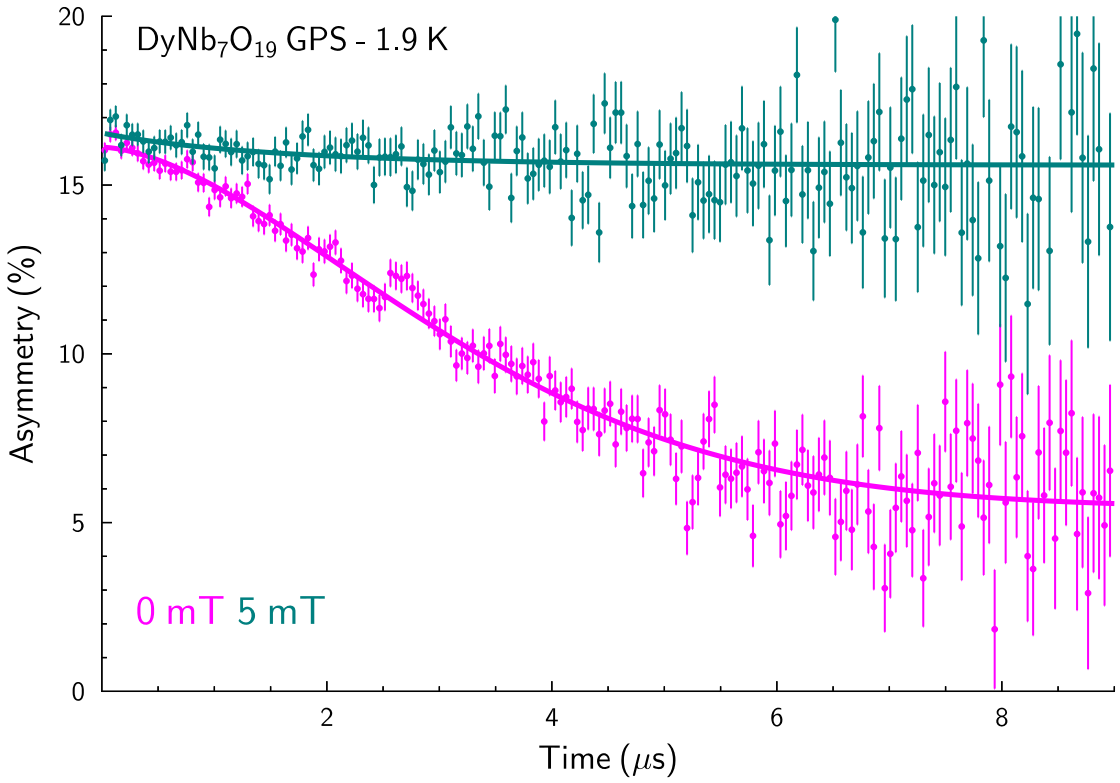

Figure 6.14: Muon asymmetry of $DyNb_7O_{19}$ at temperatures 1.9 K using the GPS spectrometer with (green) and without (pink) an applied longitudinal field of 5 mT.

feature in the first 0.5 μs^{-1} but the majority of the asymmetry is now fully recovered as shown in Fig. 6.14 which confirms that it is a nuclear moment-induced relaxation. This phenomenon suggests that a small fraction of the muons that relax at early times are subject to a dynamical field but a larger fraction sees no Dy^{3+} moments at all. The powder sample is placed in a silver packet which has a negligible relaxation rate and therefore it could not cause such a nuclear relaxation. If the muons are indeed implanted in the sample, where have the Dy^{3+} moments gone?

Dy^{3+} is a Kramers ion such that its doublet ground state is always protected from muon-induced distortion (see Chapter 2), and given its large $J = \frac{15}{2}$ moment it should produce very strong relaxation of the muon if the moment is static. An AC susceptibility measurement has been performed on $DyNb_7O_{19}$ but there is no observable frequency-dependent effect on the magnetic susceptibility. While this puzzling phenomenon needs further investigation, one plausible guess is that the

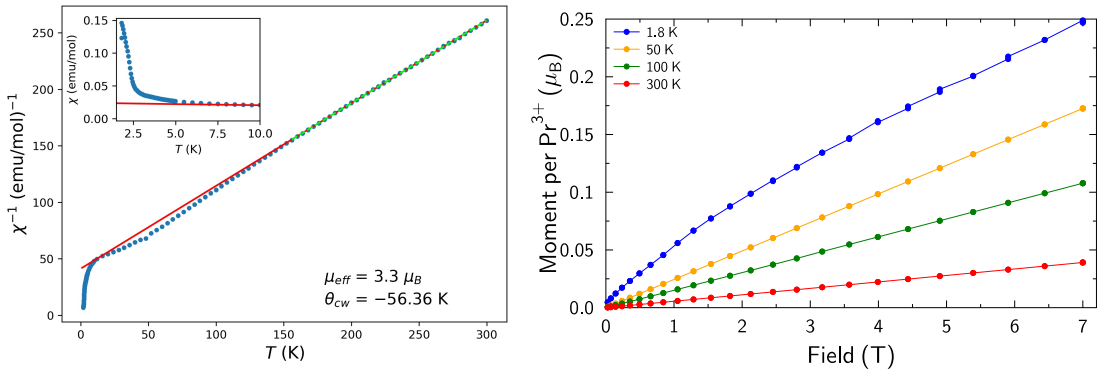

Figure 6.15: (Left) Curie-Weiss fit (red line) of the inverse susceptibility χ^{-1} (blue points) for $PrNb_7O_{19}$ in the high-temperature region (lime dotted line). Inset shows the magnetic susceptibility χ at temperatures below 10 K. (Right) Magnetisation of $PrNb_7O_{19}$ between 1.8 K and 300 K.

Dy^{3+} ions are undergoing extremely fast fluctuation and therefore the dynamics could not be resolved by any AC measurement, nor by μSR, but could perhaps be tested by neutron scattering which can probe much faster dynamics.

6.9.2 $PrNb_7O_{19}$

PrM_7O_{19} (M = Ta, Nb) are isotructural to the DyM_7O_{19} compounds that are discussed in this chapter. The Pr^{3+} ions have a $4f^2$ electronic configuration and therefore they contain a smaller moment than the Dy^{3+} ions, and this is one of the key factors to the differences between their magnetic ground states. Therefore, the aim of studying PrM_7O_{19} with μSR is to find out whether such a chemical substitution (Dy^{3+} to Pr^{3+}) on a 2D triangular-layered lattice material introduces changes to the ground state magnetism, or if they remain the same.

Magnetic susceptibility data of the powder sample of $PrNb_7O_{19}$ were taken using the MPMS3 system with a small applied field of 100 Oe between 1.8 K and 300 K and show no sign of any magnetic transition down to 1.8 K, as shown in Fig. 6.15. The Curie-Weiss fit of the inverse susceptibility χ^{-1} in the high-temperature region allows us to extract the effective moment μ_{eff} to be 3.3(1) μ_{B} per Pr^{3+} ion, which is close to the free ion value of 3.5 μ_{B}, and the Curie-Weiss temperature is $\theta_{\text{CW}} = -56(2)$ K, which demonstrates significant antiferromagnetic correlations between the Pr^{3+} moments. The lack of ordering and strong antiferromagnetic correlations on a

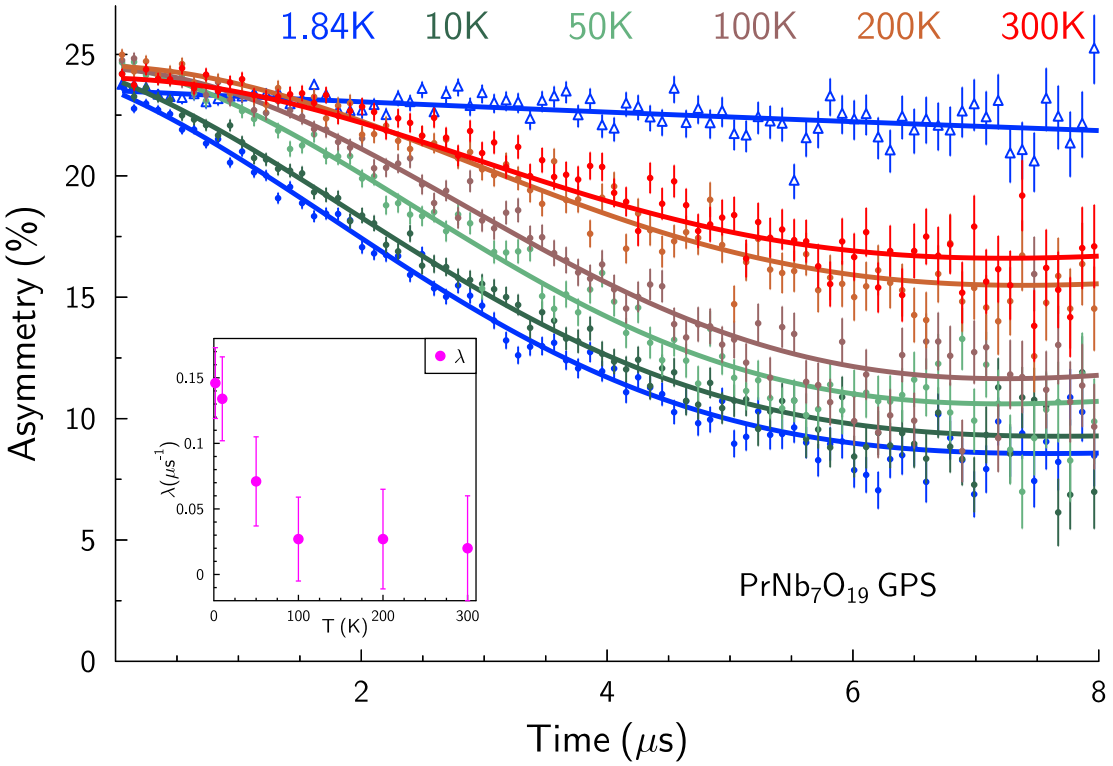

Figure 6.16: ZF asymmetry of $PrNb_7O_{19}$ between 1.8 K and 300 K using the GPS spectrometer at PSI. A LF 5 mT run at 1.84 K is plotted with white triangle markers. The inset shows the fitted relaxation rate λ as a function of T.

triangular lattice are typical signatures of a quantum spin liquid where spin dynamics persist at very low temperatures.

At around 100 K, it can be shown in Fig. 6.15 that χ^{-1} deviates from the linear Curie-Weiss law, a typical behaviour that is related to CEF splitting of the $J = 4$ energy levels, and that the system is populating only the lowest energy states. Since every energy level has its effective moment, depending on its composite $|m_J\rangle$ states, one can turn the O^{2-} ionic positions into the CEF Hamiltonian and energy states and perform a multi-level Curie-Weiss fit on $\chi(T)$. In addition, extending the base temperature of magnetic susceptibility measurement down to 380 mK would help reveal whether or not the system has an intrinsic singlet ground state which leads to a constant $\chi(T)$ at low T according to the Van Vleck susceptibility in Eqn. 7.3.

Zero Field (ZF) μSR measurements were performed on a $PrNb_7O_{19}$ powder sample in a silver packet between 1.8 K and 300 K and the results are plotted

in Fig. 6.16. The overall trend could be fitted by a Kubo-Toyabe function G_{KT} with a small exponential relaxation term such that

$$A(t) = A_0 G_{\mathrm{KT}}(\Delta) e^{-\lambda t} + A_{\mathrm{bg}}, \tag{6.5}$$

which shows that muons are likely to interact with nearby nuclear moments. The rise of the relaxation rate at low temperatures is very similar to that observed in the Pr-based pyrochlores which will be discussed in detail in Chapter 7 together with the Bleaney mechanism [139] which enhances the nuclear moments via hyperfine interactions between the muon and the nuclear spins.

When a small longitudinal field of 5 mT is applied to $PrNb_7O_{19}$, the asymmetry is immediately recovered as shown in Fig. 6.16 (blue line with white triangular markers) which confirms that the relaxation is caused by nuclear moments. While this is a similar behaviour to $DyNb_7O_{19}$ under a small LF field, it is an unsurprising outcome in this case because the doublet ground state of a non-Kramers ion Pr^{3+} is prone to muon-led local distortion which destroys the symmetry of the ion's CEF. I believe that the rise of relaxation rate λ around 50 K is linked to the CEF gap of the two singlet states which usually is around 1-5 meV and this could be checked with DFT+μ calculations.

Magnetisation measurements for $PrNb_7O_{19}$, see Fig. 6.15, show that the Pr moments are far from saturation, even at a field of 7 T, with an effective magnetisation per Pr^{3+} ion reaching only 0.25 μ_{B} at the lowest 1.8 K, much smaller than its effective moment at room temperature. However, this is consistent with the effective ground state moment (0.55 μ_{B}) estimated using a three CEF level fit of the magnetic susceptibility data. The magnetisation curve increased non-linearly and is very similar to that of $PrTa_7O_{19}$, which reaches 0.12 μ_{B} at 2 K and is also far from saturation.

Comparing the magnetisation of $PrNb_7O_{19}$ (Fig. 6.15) to that of $DyNb_7O_{19}$ (Fig. 6.13), we observe a clear contrast between the two isostructural compounds that contain different Rare Earth ions (preliminary data on $PrTa_7O_{19}$ also show the same trend when compared to $DyTa_7O_{19}$); The former with Pr^{3+} $\left(4f^2, J = 4\right)$ ions are

far from saturation and the latter with Dy^{3+} $\left(4f^9, J = \frac{15}{2}\right)$ saturates around 4.5 T. While the explanation for such behaviour is not fully known, one can reasonably explain it by considering the $|m_J\rangle$ states of these compounds; both ions with the D_3 point symmetry host doublet ground states that act as an effective $J = \frac{1}{2}$ state at low temperature. Therefore, without external influence (additional terms in the Hamiltonian), these geometrically frustrated compounds with antiferromagnetic nearest-neighbour interactions enter a phase where every moment is superposed in the spin-up $\left|m_J = \frac{1}{2}\right\rangle$ and spin-down $\left|m_J = -\frac{1}{2}\right\rangle$ state, where m_J refers to the magnetic quantum number of the effective $J_{\text{eff}} = \frac{1}{2}$ state. Note that this is only an effective state, which means that the actual m_J would be a larger value (e.g. $m_J = \pm 4$ for the ground state in Pr^{3+} ions in pyrochlore compounds).

With an external field applied, the Hamiltonian includes the CEF term $\mathbf{H} = V_{\text{CEF}}$, the exchange term $\mathbf{H} = \sum_{i,j} S_i J_{ij} S_j$ and the Zeeman term $\mathbf{H} = -\boldsymbol{\mu} \cdot \mathbf{B}$. When the field is small, the system remains approximately the same as the original state and is studied by magnetic susceptibility measurements with a field of 10 mT. However, as the magnetic field increases, the system could save energy by entering a (partially) polarised phase where the ground state contains more spin-up $\left|m_J = \frac{1}{2}\right\rangle$ and less spin-down state. Because the ground state of Dy^{3+} ions contains larger m_J states, the corresponding Zeeman energy induced by an applied field is stronger than that for Pr^{3+}. As a result, it is reasonable to expect that Dy^{3+} is more susceptible to externally applied fields and it is easier for it to transition from a QSL phase into a field-polarised one. Strictly speaking, one should also consider the relative magnitude of the CEF and exchange terms to the Zeeman term for both ions, which would be the fundamental principle in understanding the nature of the ground state magnetism and the behaviour of the material under an applied magnetic field.

6.9.3 $Ba_3Tb(BO_3)_3$

In this section, I show how the μSR measurements on the $Ba_3Tb(BO_3)_3$ compound and the temperature dependence of the data are potentially linked to the transition from a quasi-2D triangular lattice to honeycomb layers and the crystal field levels

of the Tb^{3+} ions. The samples used for μSR measurements were prepared by Sara Haravifard's group at Duke University, USA.

$Ba_3Tb(BO_3)_3$ is a hexagonal compound, with space group $P6_3cm$, that contains layers quasi-2D triangular lattice containing two species of Tb^{3+} ions that has a inter-layer separation of 8.86 Å along the c-axis which is much larger than the Tb-Tb distances within the layer (5.45 Å) as shown in Fig. 6.17. Magnetic susceptibility measurement has shown no sharp magnetic ordering transition down to 2 K, but a change in gradient at 10 K suggests the presence of a broad transition which is likely linked to the crystal field gap at the Tb1 site (1.2 meV) [140]. This compound, therefore, provides an ideal platform to explore effective $J_{\text{eff}} = \frac{1}{2}$ ground states at both the Tb1 and Tb2 ions as they are well-isolated from the higher excited levels when the system is at a low temperature.

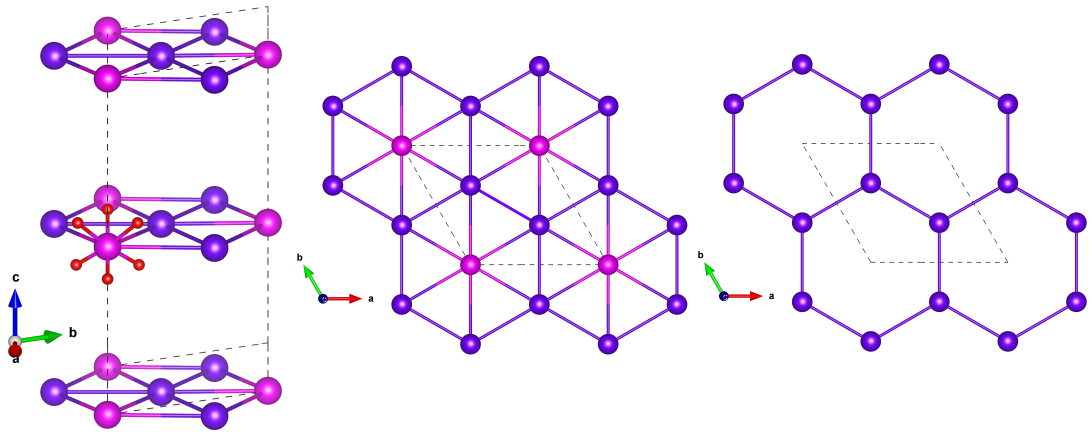

Figure 6.17: a) Tb layers in $Ba_3Tb(BO_3)_3$. b) View along $\hat{\mathbf{c}}$ showing the quasi-2D triangular lattice layers formed by Tb1 (violet) and Tb2 (magenta) ions. c.) View along $\hat{\mathbf{c}}$ showing the honeycomb lattice layers formed by only Tb2 ions at low temperature.

μSR

Our ZF-μSR data show a monotonic decay signal at all temperatures between 270 mK and 250 K and are plotted in Fig. 6.18. The data could be fitted using the following equation which contains a stretched exponential term and a background term

$$A(t) = A_{\text{R}} e^{-(\lambda t)^{\beta}} + A_{\text{Bg}}, \tag{6.6}$$

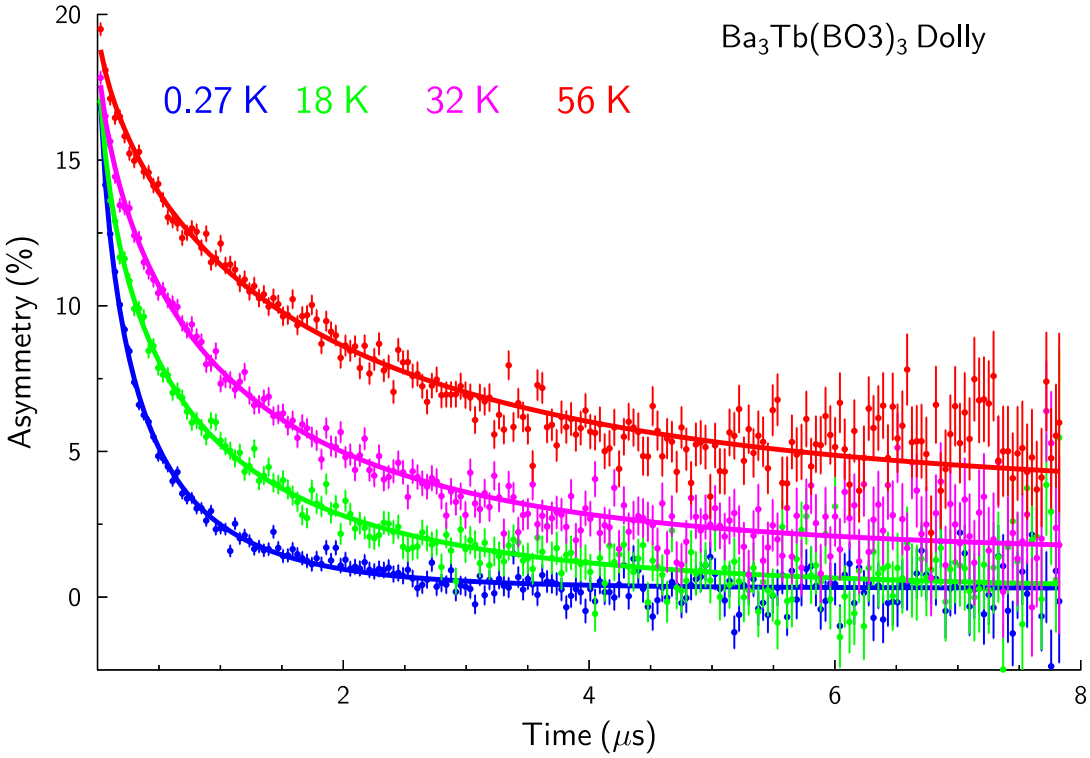

Figure 6.18: Zero-field μSR asymmetry measured between 0.27 K and 56 K measured on Dolly spectrometer at PSI.

where A_{R} and A_{Bg} refer to the amplitude of relaxing and background asymmetries, λ refers to the dynamical relaxation rate of the muon, and β is the stretching coefficient. The relaxation rates $\lambda(T)$ extracted from Eqn. 6.6 can be phenomenologically fitted to a two-delta model

$$\lambda = \lambda_0 + \eta_1 \tanh\left(\frac{\Delta_1}{T}\right) + \eta_2 \tanh\left(\frac{\Delta_2}{T}\right), \tag{6.7}$$

are plotted in Fig. 6.19 which shows the rise of λ upon cooling from 100 K and plateaus at 1 K. Two Δ terms in Eqn 6.7 physically represent the response of the muon against the crystal field gaps Δ_1 and Δ_2 at the Tb1 and Tb2 sites respectively.

Subsequently, we performed LF-μSR measurements to check the ground state dynamics and the relaxation asymmetry is plotted in Fig. 6.20. Our measurements show that the fast relaxation remains even with an applied field of 0.5 T which is a typical behaviour for muons in quantum spin liquid candidates. The relaxation rate

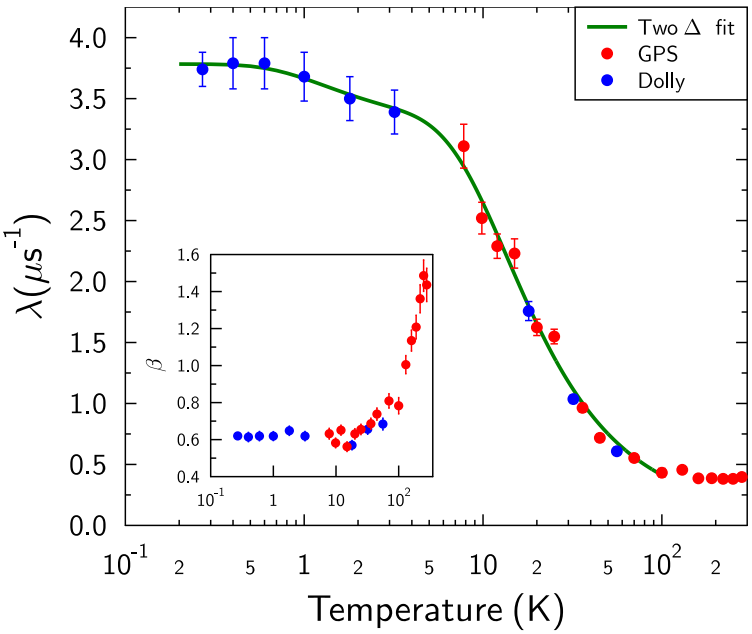

Figure 6.19: Zero-field μSR dynamical relaxation rate λ and β (inset). The green line is the fitted curve using the two-delta model in Eqn 6.7.

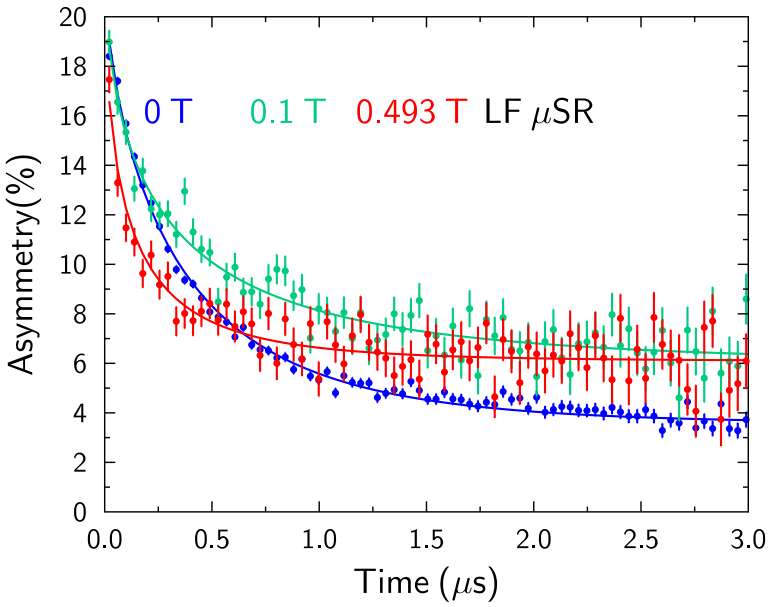

Figure 6.20: Longitudinal-field muon asymmetry relaxation measured at 0.27 K.

λ drops as the applied field increases but surges at 0.4 T, indicating the possibility of the compound entering another magnetic phase under an externally applied field.

Crystal Fields

The crystal field environment plays an important role in compounds containing 4f rare-earth atoms and $Ba_3Tb(BO_3)_3$ is no exception. The Tb^{3+} ions, which are surrounded by 6 oxygen atoms as shown in Fig. 6.17, have a C_{3v} point group symmetry that splits the lowest energy multiplet $^7F_6$. Despite the 3-fold symmetry, the Tb ions have unequal bond lengths towards the two oxygen species O_n and O_{nn} (see Table 6.2), preventing the formation of a doublet ground state.

As shown in Table 6.2, Tb1 ions have a bigger difference between the two sets of Tb-O bond lengths, whereas the Tb2 ions are very close to a perfect D_{3d} symmetry. The implication of this is reflected in the crystal field splitting where Tb^{3+} ions at the Tb1 sites have a slightly larger crystal field splitting (1.37 meV) than those at the Tb2 sites (0.57 meV), as shown in Fig. 6.21, using PyCrystalField.

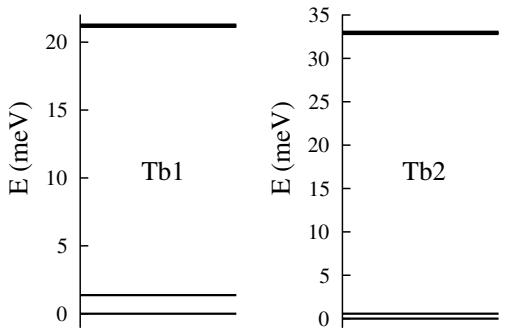

Figure 6.21: Energy levels at the Tb1 and Tb2 sites due to crystal field splitting. Thin and thick lines represent singlet and doublet states respectively.

Discussion

The μSR data have shown that the muon's relaxation rate is sensitive to the crystal field occupation levels of the Tb^{3+} ions from base temperature 270 mK to 250 K. When $\Delta_{Tb2} < \Delta_{Tb1} < k_BT$, effective $J_{eff} = \frac{1}{2}$ states exist in both Tb sites

Table 6.2: Bond lengths between Tb atoms to its closest six oxygen atoms.

	Tb1	Tb2
Tb-O_n (x3)	2.21 Å	2.23 Å
Tb-O_{nn} (x3)	2.31 Å	2.26 Å

and forming a quasi-2D triangular lattice as shown in Fig. 6.17. However, when $\Delta_{\mathrm{Tb2}} < k_{\mathrm{B}}T < \Delta_{\mathrm{Tb1}}$, the magnetic moment at the Tb1 site vanishes as it slowly depopulates the upper singlet state and becomes non-magnetic. The Tb lattice layers then transform into perfect 2D honeycomb layers due to the remaining Tb2 moments (dark violet atoms in Fig. 6.17) where the two lowest states are still occupied. This is similar to the behaviour reported in $TbInO_3$ which contains two species of Tb^{3+} ions, of which one becomes non-magnetic below 7.5 K due to its singlet ground state [141].

The relaxation rate with an applied field above 0.1 T is not well understood and could be linked to the sample entering another magnetic phase. Future work could look at this phenomenon by studying the material under an applied field.

In summary, $Ba_3Tb(BO_3)_3$ provides an elegant example of how one could cleverly manipulate the single-ion and structural properties in the pursuit of designing new quantum materials that contain rich and intricate physics.

6.10 Conclusion

Throughout this Chapter, I presented the studies and measurements on several new materials, with a focus on the new spin liquid candidate $DyTa_7O_{19}$. Using μSR techniques and magnetometric measurements, I showed the strong evidence of persistent spin fluctuations in $DyTa_7O_{19}$ down to 40 mK. The material's geometry, where Dy atoms are arranged in triangular planes slacked along the crystallographic c-axis, allows the intriguing physics of Triangular Ising antiferromagnet to be studied furtherexperimentally and theoretically; this include AC magnetic susceptibility and heat capacity measurements to study its spin dynamics and magnetic entropy at sub-Kelvin temperatures (also see Future Work in Chapter 9).

The studies of other related materials in this Chapter, such as $DyNb_7O_{19}$ and $PrTa_7O_{19}$, show that even when magnetometric measurements indicate a lack of magnetic ordering, one would still need to use a suite of additional spectroscopic techniques to probe the materials before making any conclusive statement about their ground state magnetism and behaviours.

Last but not least, this Chapter showed how the interplay between the crystal field environment, the doublet state protection, the single-ion anisotropy of rare-earth ions, and the inter-atomic interactions can all play an important role to the resulting magnetic states. It demonstrated how novel materials, magnetic or not, must be carefully designed to reach the right balance between each term, so that one can create a clean and ideal system for the pursuit of new physics.

7

3D Spin Ice: Pr-based Pyrochlores

Contents

In this chapter, I aim to address the response of muons in non-Kramers rare earth compounds where the doublet ground states are split by either intrinsic chemical or muon distortion. I start by reviewing the properties of a well-studied quantum spin ice compound $Pr_2Sn_2O_7$ as an example and explore the links between the Crystalline Electric Field (CEF) environment, single-ion properties and magnetic behaviour. I then present μSR results on a B-site substituted pyrochlore compound Pr_2ScTaO_7, high-field magnetisation measurements on Pr_2ScNbO_7. With this, I address the observations in μSR data by taking into account the muon-nuclei

hyperfine interactions which lead to enhanced nuclear moments.

Stephen Blundell helped with the interpretation of the μSR measurements and discussion on the hyperfine interaction. Paul Goddard helped with the analysis of the high-field magnetisation measurements. Dharmalingam Prabhakaran synthesised the Pr_2ScTaO_7 and Pr_2ScNbO_7 sample. As a result of COVID lockdown restrictions, the μSR measurements were performed remotely with Stephen Blundell, George Gill, and John Wilkinson on the GPS spectrometer at the Paul Scherrer Institut, Switzerland with the technical support provided by Chennan Wang. All computational work was run on the Advanced Research Computing (ARC) cluster hosted by the University of Oxford and on the Redwood cluster hosted at the Department of Physics, University of Oxford. High-field measurements were performed at the Nicholas Kurti High Magnetic Field Laboratory at the Department of Physics, University of Oxford in collaboration with Stephen Blundell, Paul Goddard, John Singleton and Johan Fopma.

7.1 Background

Over the last twenty years, scientists have intensely studied the pyrochlore oxide compounds, a class of material with the general formula of $A_2B_2O_7$. They are interesting because they contain a network of corner-sharing tetrahedra, each for the A-site and the B-site network, and when magnetic ions are placed at the A-sites, their geometry naturally frustrates the tendency for the moments to align, allowing physicists to study the complex yet fascinating phenomena in 3D frustrated magnetism.

In this family of materials, the full Hamiltonian H is given by the sum of the crystal electric field term H_{CEF}, the exchange interaction term H_{ex}, and the dipole-dipole magnetostatic term H_{dip}, so that

$$H = H_{\mathrm{CEF}} + H_{\mathrm{ex}} + H_{\mathrm{dip}}. \tag{7.1}$$

The CEF term is important because it decides the magnetic anisotropy of the rare-earth moments; based on the exact CEF parameters, the moment could either

be Ising-like along the local-[111] easy axis, or it could be in an easy plane that leads to the XY pyrochlores [142]. The exchange interaction and dipole-dipole term then decide, within the anisotropy determined by H_{CEF}, how moments align in the system. The interplay of these interactions has led to a large range of magnetic phases, including the all-in-all-out long-range order and the well-known 2-in-2-out spin ice order within the network of corner-sharing tetrahedra. [143, 144]

Amongst the pyrochlore oxides, the group of $RE_2Ti_2O_7$ (RE = Rare Earth) compounds has stolen the spotlight due to the countless intriguing properties they host [134, 145–151]. In particular, $Dy_2Ti_2O_7$ and $Ho_2Ti_2O_7$, which contain large Ising moments of the order of 10 μ_{B} at the A-sites, were discovered to host a classical spin ice state where the moments in each tetrahedron satisfy the 2-in-2-out ice rule along the local z-axis [152–154]. These spin ice compounds do not form long-range order, and because of their extensive degenerate ground states, they have a finite zero-point entropy [155–157]. Later on, the concept of 'magnetic monopoles' emerged for these classical spin ice compounds, referring to spin-flipping excitations that create sources and sinks of local magnetisation [158–162]. Lately, studies have extended to the monopole dynamics and measurements of magnetic noise [163, 164].

On the other hand, when the A-site moment reduces, the dipole-dipole term in the Hamiltonian weakens and the exchange interactions come into play. Pyrochlore compounds with effective $J = \frac{1}{2}$ moments in their ground states can lead to strong quantum fluctuations and hence they are known as 'quantum spin ice' [142, 165, 166]. Because Pr^{3+} has a free ion moment of 3.5 μ_{B}, Pr-based pyrochlores such as $Pr_2Sn_2O_7$ [53, 167], $Pr_2Zr_2O_7$ [168, 169], and $Pr_2Hf_2O_7$ [170, 171] have formed an ideal platform for scientists to test the theoretical predictions on the properties quantum spin ice.

Most recently, there have been several studies that look into the effect of chemical substitution at the non-magnetic B-sites, for example, RE_2ScNbO_7 and RE_2InSbO_7, they have reported intriguing disordered-induced magnetic behaviour although in some occasions the nature of the ground state is not completely known [11, 172–177]. Therefore, by reporting on the results on μSR and the pulsed field magnetisation

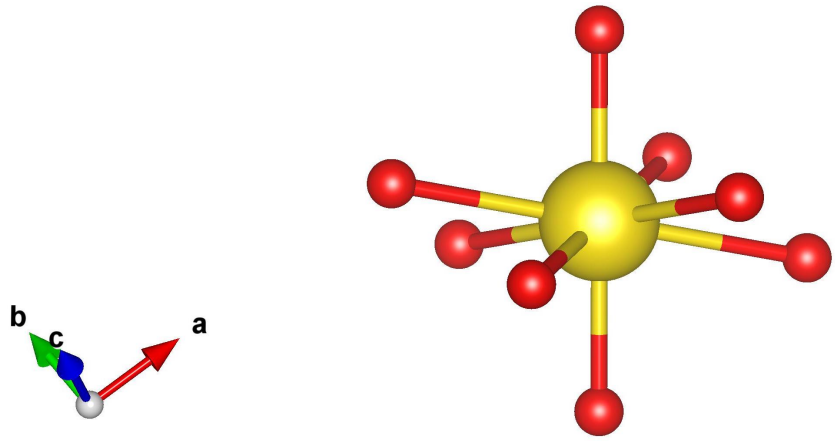

Figure 7.1: In a pyrochlore structure, each Pr atom is surrounded by 8 O atoms with a D_{3d} symmetry. Red: O, Yellow: Pr

experiments, and by considering the crystal fields and single-ion properties of the Pr^{3+}, the Chapter aims to understand the implications of the results and the effect of chemical disorder on the intrinsic magnetic behaviours of these materials.

7.2 $Pr_2Sn_2O_7$: Structure and Magnetic Properties

7.2.1 Crystal structure

The pyrochlore-structured compounds crystallise in the $Fd\bar{3}m$ space group and their chemical formula can be written as $A_2^{3+}B_2^{4+}O_7^{2-}$ (or more formally $A_2B_2O_6O'$) where the A and B atoms occupy 16d and 16c Wyckoff positions and the O and O' atoms are at the 48f and 8b sites. The A-site atoms are surrounded by eight electrons of which two lie along the local z-axis (the [111]-axis) and the other six are closer to the XY plane creating a D_{3d} point symmetry environment as shown in Fig. 7.1. The Pr-O' bond lengths along the local z-axis are 2.30 Å and are shorter than the Pr-O bonds which are 2.59 Å long. The B-site atoms have a similar D_{3d} point symmetry as the A-site but without the two electrons on the local z-axis and therefore they have a coordination number of 6 [144]. While the atomic positions in a pyrochlore compound are mostly well-determined, as shown in Table 7.1, the position of the 48f O atoms $\left(x, \frac{1}{8}, \frac{1}{8}\right)$ can vary depending on the exact composition of the compound but it is generally between values 0.320 and 0.345 to maintain the pyrochlore

Atoms	Wyckoff position	Point Symmetry	Coordinates	C.N.
A	16d	$\bar{3}m(D_{3d})$	$\frac{1}{2}, \frac{1}{2}, \frac{1}{2}$	8
B	16c	$\bar{3}m(D_{3d})$	0, 0, 0	6
O	48f	$mm(C_{2v})$	$x, \frac{1}{8}, \frac{1}{8}$	4
O'	8b	$\bar{4}3m(T_d)$	$\frac{3}{8}, \frac{3}{8}, \frac{3}{8}$	4
Space group	$Fd\bar{3}m$			
$\alpha = \beta = \gamma$	90°			

Table 7.1: Crystallographic properties of $A_2B_2O_6O'$ pyrochlore compound. C.N. refers to Coordination Number.

structure [144]. A small change in x could influence the CEF environments, and therefore, have an impact on energy levels and eigenstates of the Pr^{3+} multiplet.

7.2.2 Single-ion properties

A Pr^{3+} ion has an electronic configuration of $4f^2$ in the outermost orbital, and with spin-orbit (LS) coupling, the ground state has quantum numbers $S = 1$, $L = 5$, and $J = 4$ giving $2J + 1 = 9$ degenerate energy states as a free ion. When it is placed in a crystal, the CEF environments from the nearby ligands[1] act as a perturbation to the Hamiltonian of LS-coupling, i.e. $H_{\text{SO}} \gg H_{\text{CEF}}$, and split the $2J + 1$ levels of the ${}^3H_4$ ground state multiplet into a series of singlet and doublet levels. As discussed in Chapter 2, the CEF Hamiltonian can be written as

$$H_{\text{CEF}} = B_0^2 C_0^2 + B_0^4 O_0^4 + B_3^4 O_3^4 + B_0^6 O_0^6 + B_3^6 O_3^6 + B_6^6 O_6^6. \tag{7.2}$$

Crystal field calculations have been performed to solve for H_{CEF} in the basis of the total angular momentum eigenstates $|m_J\rangle$, using PyCrystalField [70], and the resulting energy levels and eigenstates are shown in Table 7.2, which shows that $Pr_2Sn_2O_2$ has a doublet ground state with a crystal field gap of 15 meV to the first excited singlet state.

[1] An ion or molecule that is attached to a central metal atom.

E (meV)	$\|m_J=-4\rangle$	$\|-3\rangle$	$\|-2\rangle$	$\|-1\rangle$	$\|0\rangle$	$\|1\rangle$	$\|2\rangle$	$\|3\rangle$	$\|4\rangle$
0.000			-0.078			-0.408			0.910
0.000	0.910			0.408			-0.078		
14.972		-0.161			-0.974			0.161	
60.121	0.214		-0.007	-0.477		0.778	-0.004		0.349
60.121	0.349		0.004	-0.778		-0.477	-0.007		-0.214
92.114		0.689			-0.228			-0.689	
104.878	0.066		-0.478	0.022		0.012	0.875		-0.036
104.878	-0.036		-0.875	-0.012		0.022	-0.478		-0.066
108.299		-0.707						-0.707	

Table 7.2: Eigenvalues and eigenvectors of the ground state multiplet of $Pr_2Sn_2O_7$. Listed in the table is the probability amplitude for each angular momentum eigenstate $|m_J\rangle$.

7.2.3 Magnetic susceptibility

The behaviour of magnetic susceptibility χ of a rare earth magnetic ion is usually more involved than the Curie-Weiss Law (see Chapter 3). The admixture of $|m_J\rangle$ states occupied can significantly affect the effective magnetic moment at temperature T, or in other words, each energy state has its magnetic moment depending on the composite m_J states. Therefore, the evaluation of the magnetic susceptibility for such a system is given by the Van Vleck susceptibility

$$\frac{\chi_\alpha}{N} = \mu_0 \sum_i c_i \left[\frac{|\langle i|\mu^\alpha|i\rangle|^2}{k_B T} - 2\sum_{j\neq i} \frac{|\langle i|\mu^\alpha|j\rangle|^2}{E_i - E_j} \right], \tag{7.3}$$

where $c_i = \frac{1}{Z} e^{-\beta E_i^0}$ is the probability of occupying the i-th state with energy E_i^0, and $\mu^\alpha = \mu_B J^\alpha$, the total angular momentum operator in the direction of the applied field $\alpha \in \{x, y, z\}$ [178, 179]. The full derivation of Equation 7.3 is provided in Appendix A.2.

With Eqn. 7.3, one can use the calculated energy eigenstates in Table 7.2 to work out the magnetic susceptibility of $Pr_2Sn_2O_7$, which has been plotted inversely in Fig. 7.2 and is in good agreement with the reported experimental values [53]. Calculations of the magnetic anisotropy have also been plotted in Fig. 7.2 which shows that $\chi_\perp/\chi_\parallel \approx 80$ at 10 K while the reported value is 60 [53]. This shows that the Pr^{3+} moments in $Pr_2Sn_2O_7$ have a strong magnetic anisotropy that favours the local (111) z-axis.

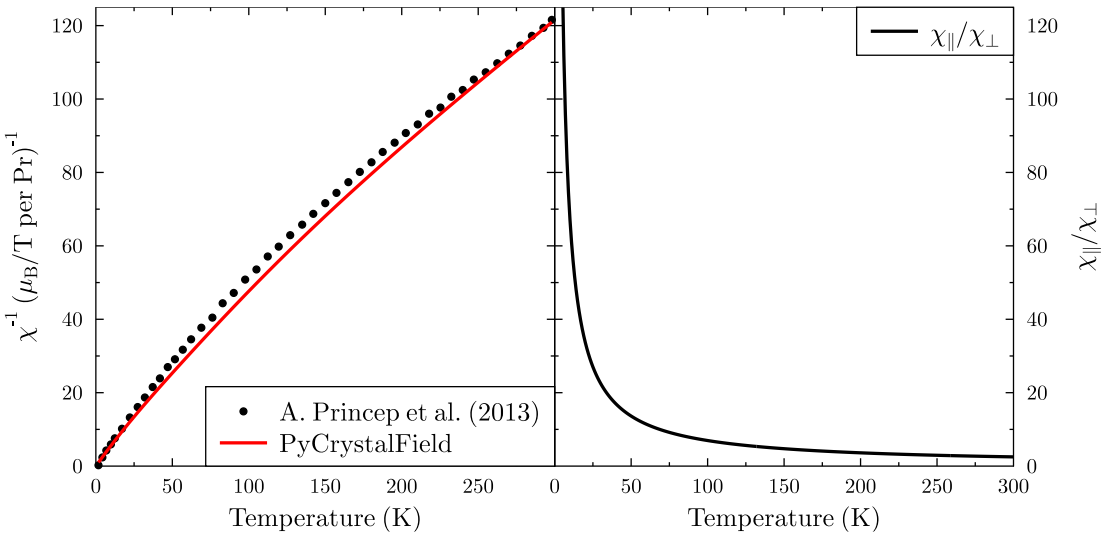

Figure 7.2: (Left) Magnetic susceptibility of $Pr_2Sn_2O_7$ calculated using PyCrystalField and from [53]. (Right) Anisotropy in susceptibility $\chi_\parallel/\chi_\perp$ calculated using PyCrystalField.

7.3 Pr_2ScTaO_7: Disorder in Pyrochlores

The formula $Pr_2B'B''O_7$ is describes a compound that contains two different B-site ions, B'^{3+} and B''^{5+}, instead of the two identical B^{4+} ions as found in a conventional $A_2B_2O_7$ pyrochlore lattice. The motivation for making such a replacement is to understand how the single-ion properties of the central Pr^{3+} ion can change by varying the non-magnetic B-atoms.

7.3.1 DFT structural relaxation

DFT structural relaxation calculations have been performed to study the effect on structural disorder by the B-site mixing of Sc^{3+} and Ta^{5+} ions. The exact ordering pattern of these two B-atoms is not known, and therefore, the relaxation calculations were repeated several times with random 1:1 allocation of Sc^{3+} and Ta^{5+} ions at the B-sites. The outcome of all calculations showed that chemical disorder has led to a small degree of structural distortion, with oxygen atoms being the most susceptible to position shift due to their smaller mass, and as a result, the D_{3d} point group symmetry around the A-site Pr^{3+} ions is broken. Because Pr^{3+} ions are non-Kramers ions, the doublet ground state is not protected and a perturbation of the CEF symmetry can easily split the ground state into two singlets.

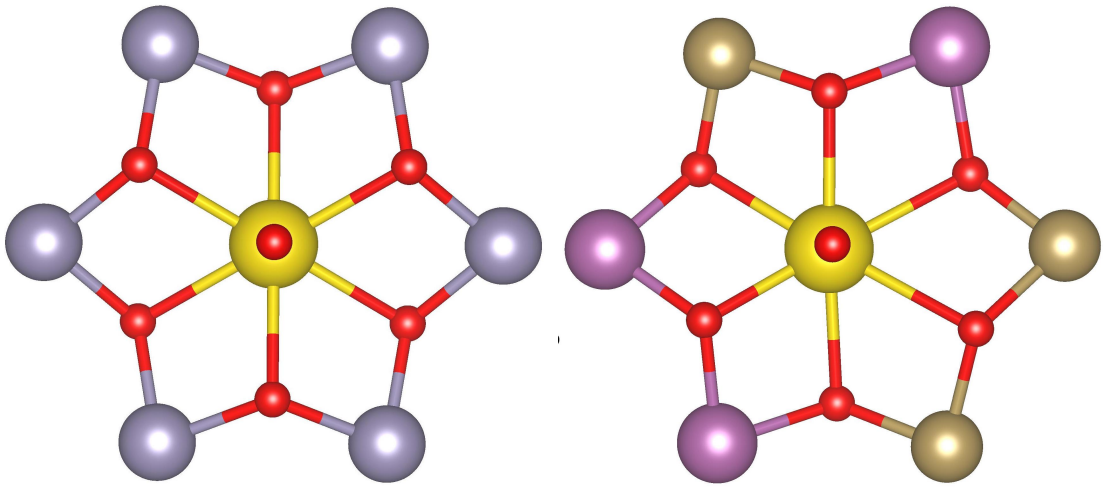

Figure 7.3: $Pr_2Sn_2O_7$ (left) and the B-site substituted Pr_2ScTaO_7 (right). In the latter, the Pr-O bond lengths vary based on which B atoms that the O atom is linked to.

48f O connected to	Before DFT (Å)	After DFT (Å)
Ta x 2	2.585	2.773
Sc x 2	2.585	2.405
Ta + Sc	2.585	2.549 – 2.644

Table 7.3: Bond lengths between B-site atom and oxygen before and after DFT structural relaxation in the Pr_2ScTaO_7 model. The former represents a perfect pyrochlore lattice and has been re-scaled to match the lattice parameter of Pr_2ScTaO_7 for a fair comparison.

Looking further into the structural disorder, I notice that each Pr^{3+} ion at the A-site is surrounded by six B-site atoms which form a hexagon ring perpendicular to the Pr^{3+} ion's local [111]-axis, as shown in Fig. 7.3. Using $Pr_2Sn_2O_7$ as a base case, where the hexagon rings have perfect symmetry, the hexagonal rings in Pr_2ScTaO_7 are slightly distorted because the two B-site ions have different ionic radii – Sc and Ta have ionic radii of 0.745 Å and 0.64 Å respectively. In other words – Ta attracts O more than Sc. In the DFT relaxation calculations, it has been found that the Pr-O bond length is shortened when the oxygen atom is connected to two Ta atoms and extended when it is connected to two Sc atoms, as shown in Fig. 7.3 (also see Table 7.3).

Because there are six B-atoms on a hexagon ring, each allowing either Sc or Ta, it is intuitive to think that there are $2^6 = 64$ ways to fill the ring. But in fact, these reduce to only 13 unique configurations which are shown in Fig. 7.4.

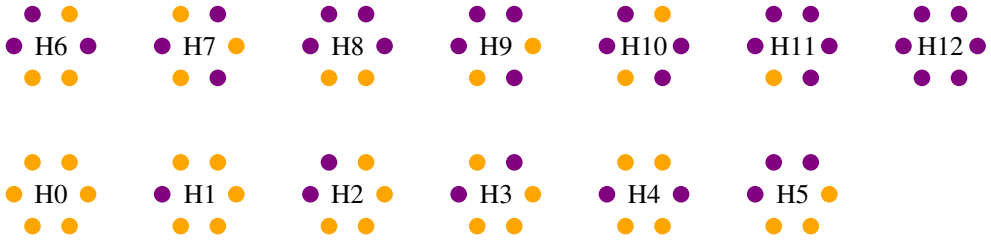

Figure 7.4: All 13 unique hexagon ring configurations that could be formed by the B-site atoms around each central Pr^{3+} ion. Yellow for Sc and Purple for Ta.

For H0 (all Sc), H12 (all Ta) and H7 (3 Sc & 3 Ta), the CEF symmetry is mostly retained and hence the splitting between the doublet ground state is minimal but non-zero (for H7, see Fig. 7.5); this is because H0 and H12 have not been affected by any substitution effect, (although the energy levels in the $^3H_4$ multiplet would change because the O^{2-} moved radially to/from the Pr^{3+} ion). The hexagon ring H7 has a Sc-Ta allocation has a 3-fold rotation symmetry, and therefore the crystal field gap is also relatively small (of 1.18 meV). However, even with symmetries in the nearest hexagon ring arrangement like H0, H12 and H7, the CEF gap is non-zero. This is supported by the observation that identical hexagon rings do not give identical CEF levels as the distortion beyond the nearest ring serves as a perturbation to the model that I have considered here.

DFT+μ

DFT+μ calculations were performed to find the muon-led distortion in Pr_2ScTaO_7 which found that the muon-stopping site is identical to that in $Pr_2Sn_2O_7$ regardless of the B-site Sc-Ta allocations. The muon site is 1 Å away from a 48f O atom.

Compound	Lattice Parameter	Pr1	Pr2	Pr2'	Pr3	Pr4	Pr4'
$Pr_2Sn_2O_7$*	10.6055 Å	2.74	3.20	3.20	4.10	4.74	4.74
Pr_2ScTaO_7	10.5828 Å	2.86	3.24	3.37	4.08	4.55	4.85
Pr_2ScNbO_7	10.5824 Å	2.86	3.24	3.34	4.07	4.66	4.78

Table 7.4: Distances, in the unit of Å , to the 6 nearest Pr atoms from the muon site according to DFT+μ relaxation calculations. *Results for $Pr_2Sn_2O_7$ are from [171].

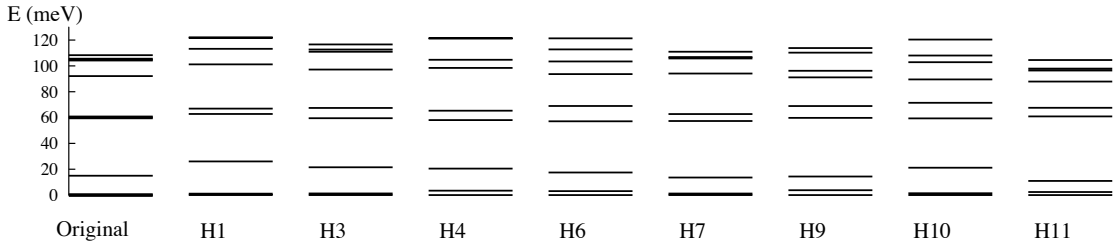

Figure 7.5: CEF levels of the $^3H_4$ multiplet for some hexagonal rings. Bold lines in the original structure represent doublet states. Note: Rings H0, H2, H5, H8, and H12 are not shown as they could not be constructed under the periodic lattice condition for one unit cell (see Discussion for charge ice structures).

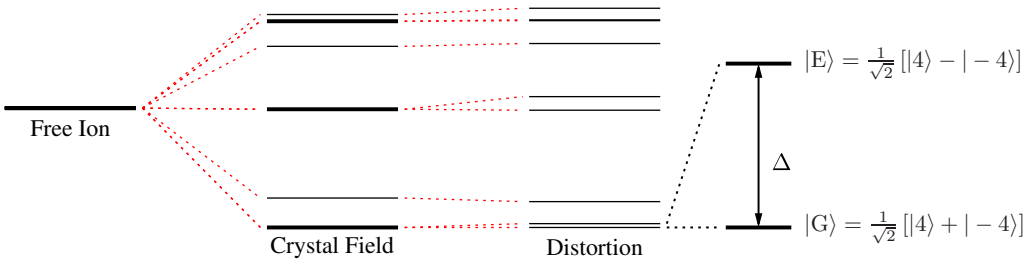

Figure 7.6: Schematic diagram of energy level splitting due to the CEF environment, chemical disorder and muon distortion. The CEF splits the $2J+1$ degenerate states, and the chemical and muon-induced distortion causes further splittings. The splitting of the ground doublet state produces a singlet ground state $|\mathrm{G}\rangle$ and a singlet excited state $|\mathrm{E}\rangle$ separated by an energy gap Δ (this is scaled up for better visualisation and the composite $|m_J\rangle$ states are included).

Although muon implantation generally causes local distortion of an insulating oxide compound, because of the intrinsic disorder in Pr_2ScTaO_7, the muon has a lesser role in this aspect. The distances to the nearest six Pr atoms from the muon are listed in Table 7.4, with comparison to the reported DFT+μ calculation in $Pr_2Sn_2O_7$ [171], which confirms that all Pr pyrochlores, whether or not the B-sites are mixed, share the same muon site.

7.3.2 Single-ion properties

Magnetic Susceptibility

The energy levels in Pr_2ScTaO_7 are singlet states, as shown in Fig. 7.5. Each singlet level contains equal magnitude coefficients in the opposite angular momentum eigenstates $|\pm m_J\rangle$, so that the matrix element $\langle i|\, J_\alpha \,|i\rangle$ always vanishes. Therefore,

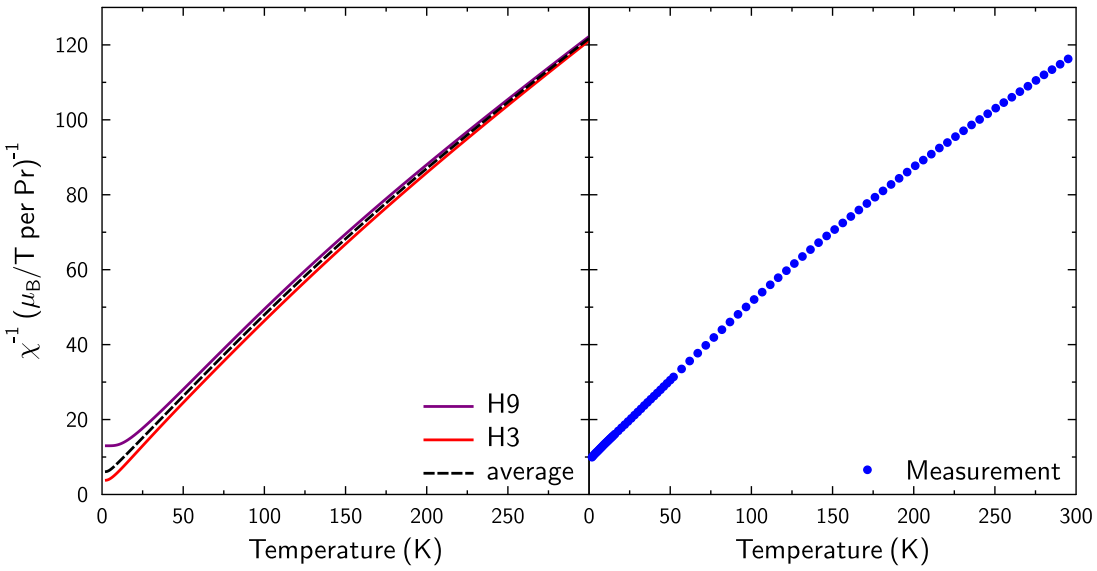

Figure 7.7: (Left) Calculated $\chi^{-1}(T)$ for selected hexagonal ring configurations H3 and H9, and their average. Calculations were performed using PyCrystalField. (Right) Inverse susceptibility measured using the MPMS2 system.

the expression for the magnetic susceptibility in Eqn. 7.3 can be simplified to give

$$\chi_\alpha = \sum_i 2P_i \sum_{j \neq i} \frac{|\langle i|\, \mu_\alpha \,|j\rangle|^2}{E_j - E_i}, \tag{7.4}$$

where $P_i = \frac{1}{Z} e^{-\beta E_i}$ is the probability of occupying the i-th state of energy E_i. From Eqn 7.4, one can infer that when the material is in its singlet ground state $|\mathrm{G}\rangle$ at low temperatures (i.e. excited states are not populated), $P_\mathrm{G} = 1$ and therefore, χ becomes a constant. One can also observe that the temperature dependence of $\chi(T)$ purely depends on the occupation of energy states. Figure 7.7 shows the inverse susceptibility of a single Pr^{3+} ion when it is surrounded by an H3 or H9 hexagonal ring, and also the average to simulate a sample that contains both H3 and H9 environments in equal proportion. This is only a guide because a real material would contain a collection of Pr^{3+} ions which have a range of single-ion properties due to inhomogeneous local disorder.

The measured inverse magnetic susceptibility has been plotted in Fig. 7.7 which shows a similar lineshape to the simulated value. However, it has a continuous downtrend at low temperatures, instead of levelling off to reach a plateau as predicted for a singlet state by Eqn 7.4. This downward trend normally occurs in cases where

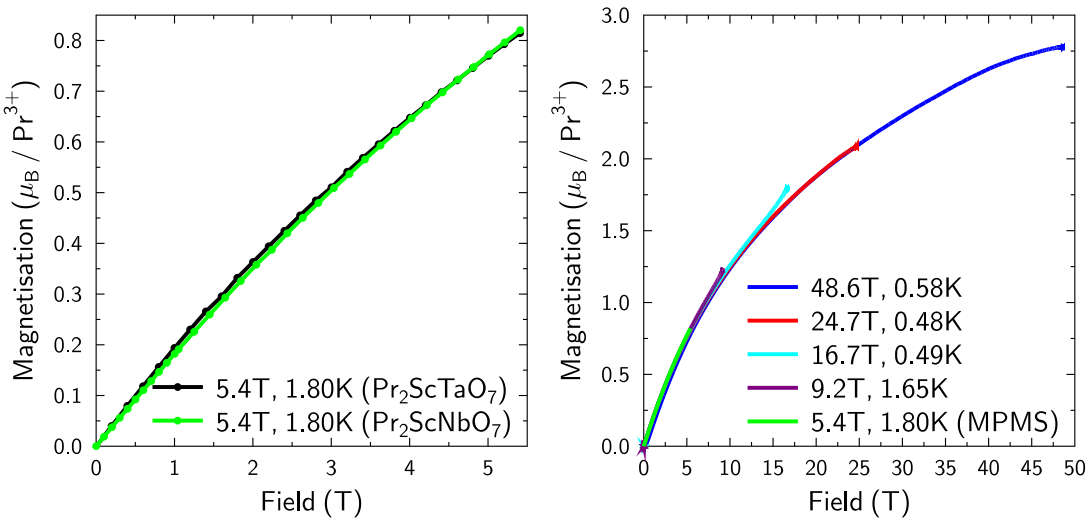

Figure 7.8: (Left) Magnetisation of Pr_2ScTaO_7 and Pr_2ScNbO_7. (Right) High-field magnetisation of Pr_2ScNbO_7 at low temperatures with an applied field up to 48.6 T showing that the system still has not reached saturation. Both Figures share the same neon green curve as it is used to calibrate the high-field magnetisation measurements.

there are doublet ground states, such as in the $Pr_2Sn_2O_7$ base case, in which the χ^{-1} curve reaches 0. In addition, the measurements show that χ^{-1} has a non-zero y-intercept. While this is not fully understood, one could reasonably suspect this is a signature of heterogeneous local environments that include the singlet states, which produce the non-zero y-intercept, but also part of the system could have retained the D_{3d} symmetry (or the observed behaviour could be contributions from paramagnetic orphan spins) and hence the giving the continuous downward trend.

Magnetic anisotropy

In terms of magnetic anisotropy, $\chi_\parallel/\chi_\perp$ of Pr_2ScTaO_7 is calculated to be within the range of 15 and 180 depending on the local hexagon ring configuration. High anisotropy is usually found in rings that contain more Ta atoms as they draw the 48f O atoms away from the central Pr ions so that the system gains anisotropy by having a sharper contrast between the Pr-O and Pr-O' bonds.

Magnetisation

Magnetisation measurements of the Pr_2ScTaO_7 and the Pr_2ScNbO_7 powder samples were carried out using the MPMS system and plotted in Fig. 7.8 which shows the

almost-linear responses up to 5.4 T. This behaviour is consistent with measurements reported for polycrystalline samples of Pr_2ScNbO_7 [177] and Pr_2InSbO_7 [11] which contain low-lying singlet states. However, not all pyrochlore compounds with non-Kramers rare earth ions show this phenomenon; Tb_2InSbO_7 and Ho_2InSbO_7 both show a saturation of around 5 μ_B per moment [11]. On the other hand, magnetisation curves of most mixed B-site pyrochlores with Kramers ion at the A-site appear to saturate below 8 T, this includes Nd_2ScNbO_7 [180], Dy_2InSbO_7, and Yb_2InSbO_7, with the exception of Sm_2InSbO_7 which showed a linear response like the disorder-less $Sm_2Ir_2O_7$ [181, 182]. It is not surprising as Sm^{3+} is known to be affected by Van Vleck paramagnetism, and could have the admixture of other J multiplets in the ground state [21].

High-field measurements, with applied fields up to 48.6 T and at temperatures between 0.48 K and 1.65 K, have been performed on a single crystal sample of Pr_2ScNbO_7 along the [111] direction at the Nicholas Kurti High Magnetic Field Laboratory in Oxford (see Fig. 7.8). To the best of my knowledge, this is the first attempt at a high-field experiment on any mixed B-site pyrochlore. The results of the high-field measurements show that, even at the highest field of 48.6 T, the Pr^{3+} moments have not reached the saturation point, although it is leaning towards the full value of $g_J J = 3.2$ μ_B per Pr^{3+} moment, assuming that the ground state is dominated by the $|m_J = +4\rangle$ eigenstate that gives the largest Zeeman energy.

7.3.3 μSR Zero Field

Zero field (ZF) μSR measurements between 1.55 K and 300 K have been performed at the Paul Scherrer Institute, Switzerland on a powder sample of Pr_2ScTaO_7 using the GPS spectrometer and the muon asymmetry is plotted in Fig. 7.9 for selected temperatures. The data are fitted with a phenomenological Kubo-Toyabe function that describes the static nuclear moments,

$$A(t) = A_f G_{KT} e^{-\lambda_f t} + A_s e^{-\lambda_s t} + A_{base}, \tag{7.5}$$

$$\text{and} \quad G_{KT} = \frac{1}{3} + \frac{2}{3}\left(1 - \sigma^2 t^2\right) e^{-\sigma^2 t^2/2}, \tag{7.6}$$

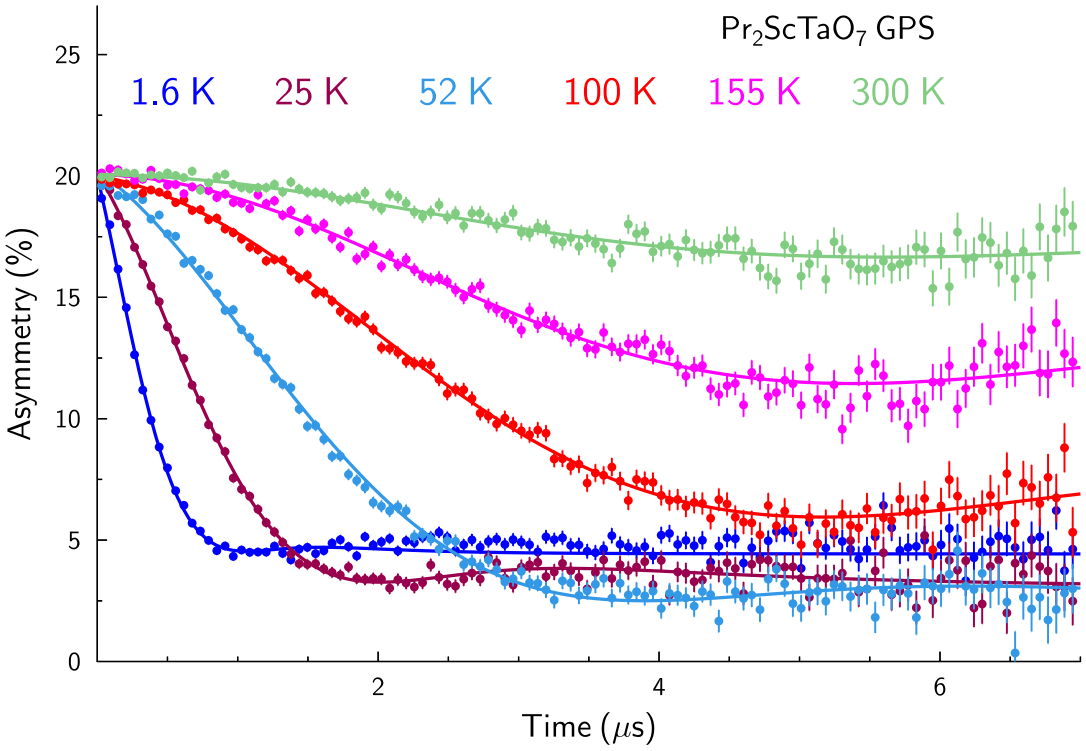

Figure 7.9: ZF-μSR Asymmetry plot $A(t)$ of Pr_2ScTaO_7 between 1.6 K to 300 K measured using the GPS spectrometer at PSI, Switzerland, with the fitted line shown.

where σ is the second moment of the nuclear spin distribution that gives the static relaxation rate, $e^{-\lambda_f t}$ and $e^{-\lambda_s t}$ are the dynamical relaxation terms of the fast and slow relaxation, and A_f (18.2%) and A_s (1.8%) are the initial asymmetries of the corresponding parts.

Fitted relaxation rates $\lambda_f(T)$ and $\sigma(T)$ are plotted in Fig. 7.10 which shows that both rates start to increase around 100 K upon cooling and plateau at about 5 K. This trend is consistent with the temperature-dependence observed for Pr-based pyrochlores $Pr_2B_2O_7$ (B = Sn, Hf, Zr) [171] and also in many other frustrated magnets [145, 183–186]. In the case of $Pr_2B_2O_7$, $\sigma(T)$ can be fitted by the model

$$\sigma = \sigma_0 + \frac{\eta}{\tilde{\epsilon}} \tanh\left(\beta\tilde{\Delta}\right), \tag{7.7}$$

where $\eta = g_J \mu_B \alpha^2 A_J I_z$, $\tilde{\Delta} = \sqrt{(\Delta/2)^2 + (\alpha A_J I_z)^2}$, and Δ is the CEF gap between the two low-lying singlet states [171]. Because of the perfect D_{3d} symmetry in $Pr_2B_2O_7$, all the Pr^{3+} ions have the same intrinsic CEF gap Δ, and the muon-led

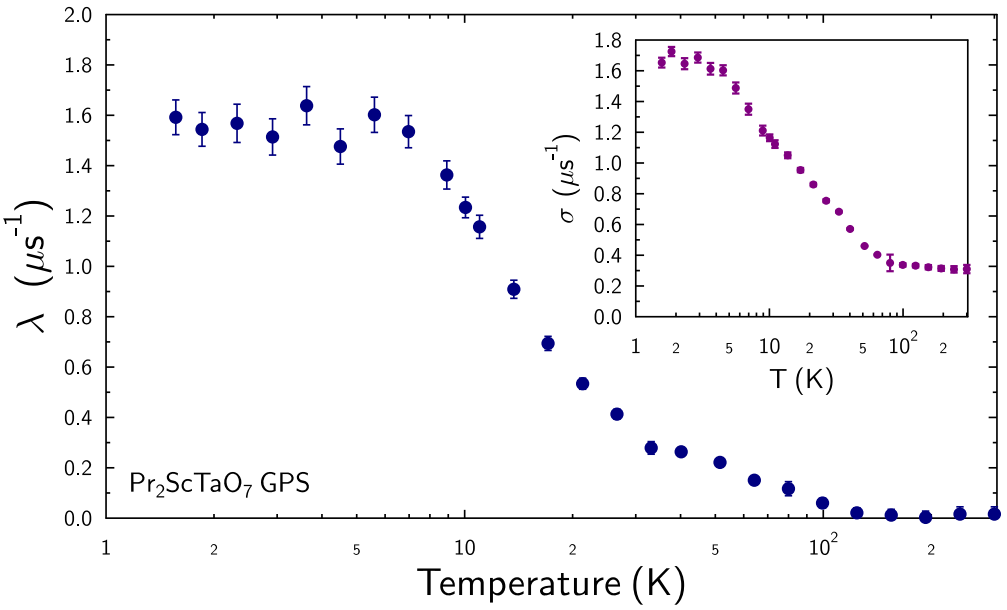

Figure 7.10: The dynamical relaxation rate λ as a function of temperature extracted from fitting the ZF-μSR data according to Eqn 7.5. This shows a λ value that increases from around 100 K as the sample is cooled and it plateaus at around 5 K.

distortion only causes broadening around this value. In contrast, the range of local structural disorder in the $Pr_2B'B''O_7$ mixed B-site pyrochlores, together with muon implantation, means that the Pr^{3+} ions have a wide range of CEF environments, and therefore, the trend in Fig. 7.10 could not be easily captured using Eqn. 7.7.

7.4 Hyperfine-enhanced Nuclear Magnetism

The ZF muon asymmetry of Pr_2ScTaO_7, plotted in Fig. 7.9, was analysed and fitted using a Kubo-Toyabe function to represent static but randomly oriented moments in the system. As the Pr^{3+} ions have singlet ground states they contain no moment at base temperature. However, the fitted relaxation rate $\sigma(T)$ is at the order of unity at this temperature (see Fig. 7.10) which is too large to be simply induced by nuclear moments as it is usually less than 0.1 μs^{-1} and is also temperature-independent.

One important observation is that both $\lambda(T)$ and $\sigma(T)$ begin to rise at temperatures equivalent to the crystal field gaps. To look into this, one can consider the interactions that exist in Pr_2ScTaO_7: with **J** and **I** representing the electronic and nuclear moments of the Pr^{3+} atom respectively, the Hamiltonian of the system

can be written as

$$H = H_\Delta + H_{\rm H}(\mathbf{J},\mathbf{I}) + H_{\rm Z}^J + H_{\rm Z}^I + H_{\rm D}(S_\mu,\mathbf{J}) + H_{\rm D}(S_\mu,\mathbf{I}), \tag{7.8}$$

which include the CEF energy gap Δ between the split states $|\mathrm{G}\rangle$ and $|\mathrm{E}\rangle$ (see Fig. 7.6), the hyperfine interaction $H_{\rm H}$ between $\mathbf{J}$ and $\mathbf{I}$, the Zeeman terms $H_{\rm Z}$, and the dipolar interactions term $H_{\rm D}$ between the muon's spin and each of the Pr^{3+} moments $\mathbf{J}$ and $\mathbf{I}$.

For a simple case, we consider Eqn. 7.8 without the dipolar interactions $H_{\rm D}$, i.e. only the intrinsic interactions in the sample, so that

$$H = H_\Delta + H_{\rm H}(\mathbf{J},\mathbf{I}) + H_{\rm Z}^J + H_{\rm Z}^I \tag{7.9}$$

$$= \begin{pmatrix} \mu_B g_J J B_z + AJI_z - g_I\mu_{\rm N} I_z B_z & -\Delta/2 \\ -\Delta/2 & -\mu_B g_J J B_z - AJI_z - g_I\mu_{\rm N} I_z B_z \end{pmatrix}, \tag{7.10}$$

in the basis of $\{|4\rangle, |-4\rangle\}$, and by assigning CEF energies of the ground and excited singlet states $|\mathrm{G}\rangle$ and $|\mathrm{E}\rangle$ to be $\frac{\Delta}{2}$ and $-\frac{\Delta}{2}$ respectively.

The zero-field ($B_z = 0$) energies are given by

$$E = \pm\sqrt{(AJI_z)^2 + \left(\frac{\Delta}{2}\right)^2} \approx \pm\left[\frac{\Delta}{2} + \frac{(2AJI_z)^2}{\Delta} + \ldots\right], \tag{7.11}$$

and the new eigenstates are given by

$$|\mathrm{G}'\rangle = |\mathrm{G}\rangle + \frac{AJI_z}{\Delta}|\mathrm{E}\rangle \quad \text{and} \quad |\mathrm{E}'\rangle = |\mathrm{E}\rangle - \frac{AJI_z}{\Delta}|\mathrm{G}\rangle. \tag{7.12}$$

This is a remarkable result because it shows that hyperfine interactions can cause mixing between the two singlet states $|G\rangle$ and $|E\rangle$.

From Eqn. 7.12, one calculates the expected ground state electronic moments to be

$$\langle\mu\rangle = -g_J\mu_B\langle G'|J_z|G'\rangle = g_J\mu_B J\underbrace{\frac{2AJI_z}{\Delta}}_{\sim 2\%}, \tag{7.13}$$

which is about 2% of a full electronic Pr^{3+} moment of $g_J\mu_{\rm B}J = 3.2\ \mu_{\rm B}$, but larger than that of its nuclear moment. This derivation provides a mechanism for the muon to interact with split singlet states in non-Kramers ions when one expects a vanishing electronic moment [187]. The resulting nuclear moment is enhanced by hyperfine coupling, and therefore, one observes a nuclear relaxation rate than is larger than expected in the ZF-muSR relaxation asymmetry.

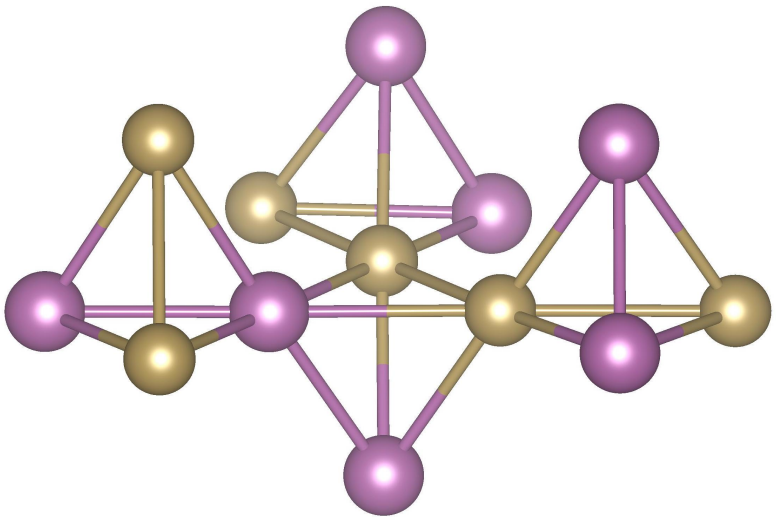

Figure 7.11: Network of corner-sharing tetrahedra of the B-site atoms obeying the 2-Sc-2-Ta charge ice rule. Colour: Sc (Gold), Ta (Purple).

7.5 Discussion

7.5.1 Charge ice order

Beyond magnetism, scientists are interested in how the two B-site elements are arranged. Because of the different charges that the Sc^{3+} and Ta^{5+} ions possess, the system should ideally avoid placing too many Ta^{5+} together and form a highly-charged cluster that leads to a larger Coulomb potential. One possible solution to suppress the formation of Ta clusters is to have a structure known as a 'charge ice', where each B-site corner-sharing tetrahedron contains two Sc^{3+} and two Ta^{5+} atoms [188, 189]. This is similar to the 'spin ice' magnetic structure which contains groups of four spins at each A-site tetrahedron that obey the 2-in-2-out rule [154, 155]. To visualise charge ice, one could map the 'in' and 'out' spins of a 2-in-2-out spin ice into Sc^{3+} and Ta^{5+}, therefore, giving a 2-Sc-2-Ta structure as shown in Fig. 7.11.

To calculate the intrinsic structural and muon-induced distortion, one has to provide QuantumEspresso with an input file that includes the well-defined positions of each constituent atom as the program is primarily designed for systems with integer site occupancy (i.e. 1). Therefore, it is necessary to work out the allocation of atoms at the B-sites. To find the charge ice configurations, I have written a Python script to allocate eight of each B-atom species into the sixteen B-sites in one

Group No.	Hexagon rings contained	Occurrence
I	H1 x 2 + H6 x 8 + H7 x 4 + H11 x 2	48
II	H3 x 4 + H4 x 4 + H9 x 4 + H10 x 4	24
III	H3 x 8 + H9 x 8	12
IV	H4 x 8 + H10 x 8	6

Table 7.5: Grouping of 90 possible charge ice configurations within a Pr_2ScTaO_7 unit cell. Each group shares an identical hexagon ring count.

unit cell and filter out the successful cases – the ones that fulfil the 2-Sc-2-Ta charge ice rule. The periodic boundary condition for a single unit cell has been assumed to limit the computational time for DFT relaxations, although this is unlikely to be realised in the real material (unless the charge ice order has a high symmetry such as a stripe order etc). From $\binom{16}{8}$ possible configurations, I found only 90 that satisfy the charge ice rule and many are related by symmetry operations. The method I used to categorise them into groups is to assess the composite B-site hexagon rings they contain within the unit cell (see Table 7.5).

With the charge ice configurations, I performed a structural relaxation to investigate how the local environment distorts and how the energy changes. Table 7.6 listed the results of the first ten configurations as an example, which shows that even though these are all charge ice configurations, some possess lower energy than others. For instance, configurations 1 and 6, which are in Group III in Table 7.5, are the most energetically favourable. This is not surprising because the charge ice rule, i.e. the 2-Sc-2-Ta restriction, is merely a minimisation of energy between nearest neighbour Coulomb interactions and it has not considered the next-nearest neighbours and beyond.

In a spin ice compound, an excitation of the magnetic ground state can be achieved by flipping one of the spins in the system which would turn two 2-in-2-out tetrahedra into a 1-in-3-out (source) and a 3-in-1-out (sink) tetrahedra. These excitations are free to propagate around the system and if the distance between the 'source' and the 'sink' is far enough, they become what are known as magnetic monopoles [158]. However, for a charge ice, the B-site atoms are spatially fixed and propagation is not possible. Table 7.6) shows that, in most cases, the charge ice

Configuration	Group No.	Energy $(E - E_0)$	Swap ΔE
1	III	0	+0.0198
2	I	0.0197	+0.0003
3	I	0.0197	+0.0180
4 & 5	I	0.0197	−0.0009
6	III	0	+0.0200
7	II	0.0366	+0.0185
8	I	0.0197	+0.0002
9	I	0.0197	+0.0354
10	II	0.0366	−0.0017

Table 7.6: Energies (Ry) of the first ten charge ice configurations, and the energy change for breaking the charge ice rule. E_0 is a constant value of −21203.1279 Ry which is the energy for configurations in Group III.

configurations are energetically more favourable and breaking the charge ice rule generally leads to a penalty in energy. This agrees with the reported Monte Carlo simulations that found charge ice to be the preferable state [180].

7.6 Conclusion

In summary, I introduced the effect of chemical disorder on the crystal fields and single-ion properties of a non-Kramers rare earth ion. I presented the high-field magnetisation measurements and the Zero-Field (ZF) μSR measurements on two Pr-based pyrochlore oxide compounds in which the B-sites contain two different non-magnetic atoms. I found that the trends observed in the ZF-μSR measurements are closely linked to crystal field gaps in the system, and I show that this is related to the enhancement of nuclear moments **I** (or reduction of electronic moments **J**) mediated by hyperfine interactions which cause the mixture of the two low-lying singlet states. It is noted that in these mixed B-site pyrochlore compounds, the inhomogeneity of the local environment has complicated the analysis of measurements by μSR. By reporting the results on these new measurements, this Chapter contributed better understanding of the effect of chemical disorder on local magnetism and crystal field-related effects. However, with the presence of such disorder, it can be difficult for simulations to be performed and there are still many aspects of the mixed B-site pyrochlore compounds that are yet to be explored, such as the charge

ice orders among the B-site corner-sharing tetrahedra, which could potentially be linked to other magnetic behaviours of these compounds.

8

3D Weyl Semimetals: REAlSi (RE = Ce, Nd)

Contents

In this chapter, I present the data of zero-field (ZF) and transverse-field (TF) μSR measurements on two Weyl semimetals compounds CeAlSi and NdAlSi. The measurements on the CeAlSi sample confirm the layered ferromagnetic order which agrees well with the ZF-μSR measurements. The data on the NdAlSi sample demonstrate magnetic phase transitions at 3.3 K and 7.2 K, and a broadened frequency spectrum across low temperatures that is potentially caused by the

formation of small domains and hence magnetic disorder. Meanwhile, the TF-μSR measurements give evidence for a link between the bulk magnetisation and the shift in muon precession frequency. Together with symmetry arguments, I propose a muon stopping site which is consistent with our μSR findings in both compounds.

Tillman Weinhold, Rajib Sarkar, Hans-Henning Klaus, and Stephen Blundell helped with the interpretation of the results. The Tafti group of Boston University synthesised the REAlSi (RE = Ce, Nd) samples. George Gill, Rajib Sarkar, Hans-Henning Klaus, and Stephen Blundell assisted with the μSR measurements which were carried out on the GPS and HAL-9500 spectrometers at the Paul Scherrer Institute (PSI), Switzerland with the technical support provided by Chennan Wang, Robert Scheuermann, and Zurab Guguchia. All computational work was run on the SCARF cluster supported by the Scientific Computing Research Infrastructures Group at the Rutherford Appleton Laboratory and on the Redwood cluster hosted at the Department of Physics, University of Oxford.

8.1 Background

Weyl semimetal compounds have become an increasingly popular research topic in recent years due to their interesting electronic properties and topological features. They contain electronic bands that disperse linearly and have a vanishing density of states at the Fermi energy, where the crossing points are called the Weyl nodes [190–192]. In particular, a family of Weyl semimetal compounds with chemical formula REAlSi (RE = Rare Earth) has attracted attention in recent years because of the link between their Weyl nodes and the magnetic properties [193–200]. For example, NdAlSi was found to host a mechanism of a Weyl fermion-driven magnetism where the nesting vector between two of its Fermi pockets is linked to the k-vector of the material's helical magnetic order at the Nd sites [199].

The REAlSi compounds crystallise in a tetragonal unit cell and have a non-centrosymmetric space group $I4_1md$ [201, 202]. The RE atoms are located at [0,0,0], the Al atoms at [0,0,0.5841], and the Si atoms at the [0,0,0.4182] position, as shown

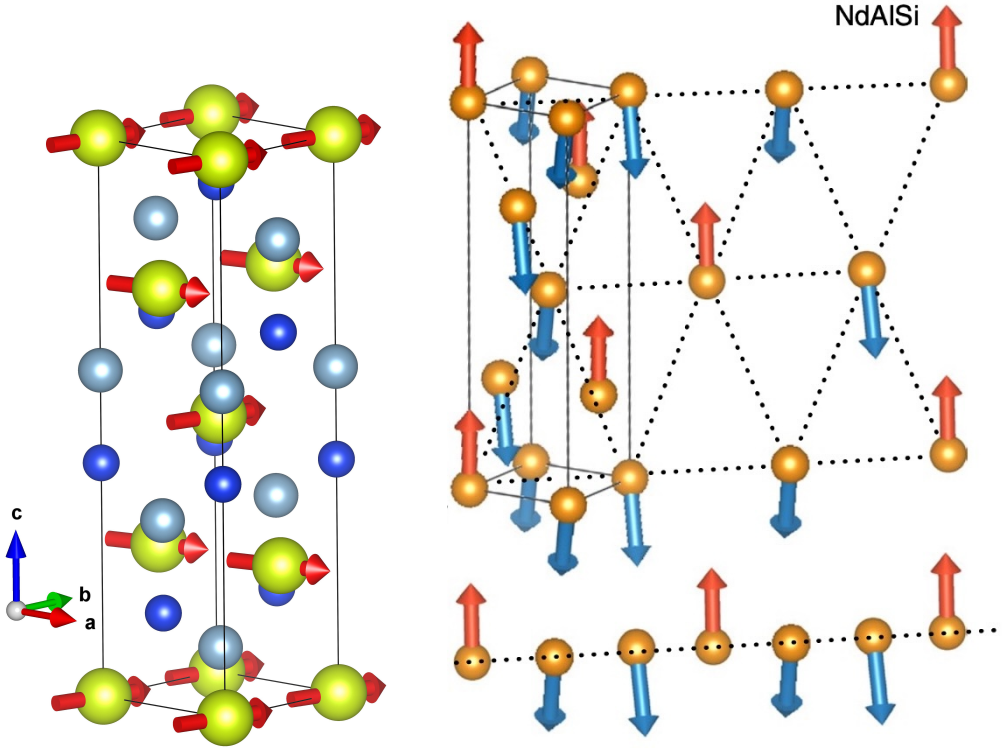

Figure 8.1: (Left) Magnetic structure of CeAlSi where the layers of Ce (lime) spins are aligned ferromagnetic along the *ab* planes and stacked along $\hat{c}$. Ce, Al, and Si atoms are in lime, light blue, and dark blue colours respectively. (Right) The unit cell of NdAlSi: $a = b = 4.1972$ Å and $c = 14.4915$ Å. The magnetic structure is one where the Nd (orange) spins are aligned mainly along **c** and they form an up-down-down order that extends along the [110]-axis. The Figure for NdAlSi is extracted from [199]. This shows that the two isostructural compounds contain contrasting magnetic structures.

in Fig. 8.1, and all atoms have Wyckoff multiplicity 4a. Further information on structural characterisation are reported in the supplementary information of [199].

The magnetic moments in this family of compounds are located at the RE^{3+} sites. For Ce^{3+}, the electronic configuration is $4f^1$; therefore, by Hund's rules, $S = \frac{1}{2}$, $L = 3$, and $J = \frac{5}{2}$. Similarly for $Nd^{3+}(4f^3)$, $S = \frac{3}{2}$, $L = 6$ and $J = \frac{9}{2}$. In the unit cell, each magnetic rare earth ion is surrounded by a number of Al and Si atoms, the CEF environment means that these Kramers RE^{3+} ion's $2J + 1$ degenerate states are split into protected doublet states.

8.2 CeAlSi

8.2.1 Magnetic structure

CeAlSi has an in-plane ferromagnetic structure where Ce spins $\mathbf{S}_1$ ($z = 0$ and $z = \frac{1}{2}$) and $\mathbf{S}_2$ ($z = \frac{1}{4}$ and $z = \frac{3}{4}$) are polarised at an angle of 11° to the **b** and **a** respectively, and the angle between the two layers is 68° with a magnetisation along [110] as shown in Fig. 8.1. All Ce^{3+} ions carry a moment of 1.1 μ_B [198]. In addition, CeAlSi is understood to form domains with magnetisation along the four equivalent directions [110],[1$\bar{1}$0],[$\bar{1}$10], and [$\bar{1}\bar{1}$0]. This is due to the crystal structure which contains mirror planes along the *ac* and *bc*, and when the material is cooled in zero-field, all four domains are equally likely to be formed, and they have been studied extensively in [196, 197, 200].

8.2.2 μSR Zero Field

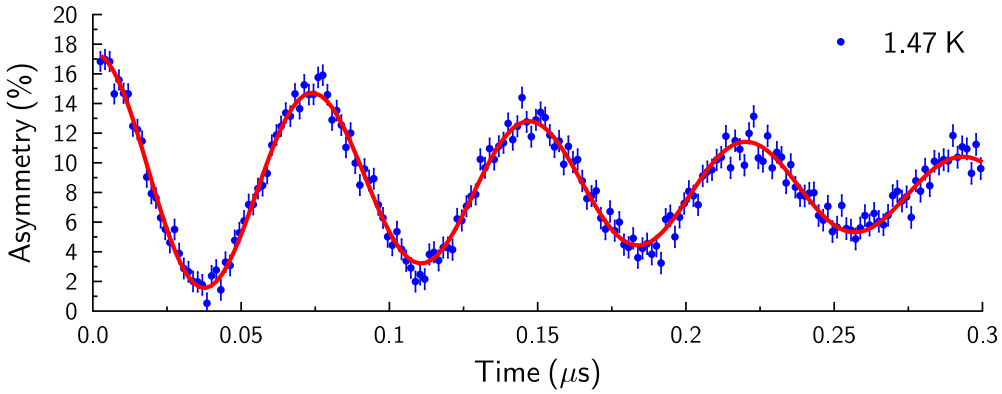

Figure 8.2: ZF-μSR asymmetry performed on multiple pieces of CeAlSi crystals at the base temperature 1.472(2) K shows one single oscillation frequency. The data with error bars are plotted in blue, and the fitted line (using Eqn 8.1) is in red.

Zero-field μSR measurements on CeAlSi were performed using multiple pieces of single crystal placed in a silver packet at temperatures between 1.53 K and 300 K using the GPS spectrometer at PSI, Switzerland. The muon asymmetry data shows a clear oscillating signal, as shown in Fig. 8.2, and the asymmetry can be modelled by a single cosine term with the addition of a small non-oscillaing relaxation

$$A(t) = A_{\mathrm{osc}} \cos(\nu t + \phi) e^{-\lambda_{\mathrm{osc}} t} + A_{\mathrm{n}} e^{-\lambda_{\mathrm{n}} t} + A_{\mathrm{bg}}, \tag{8.1}$$

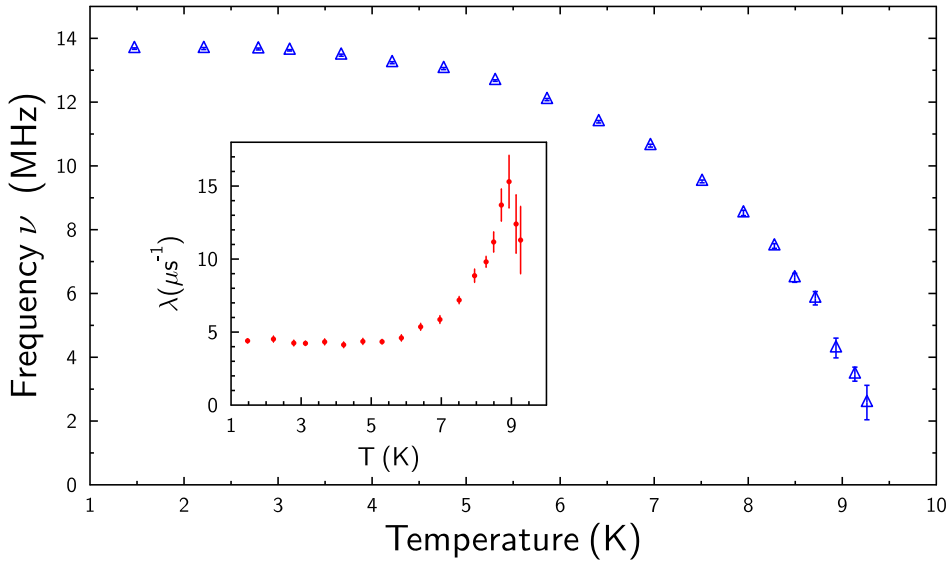

Figure 8.3: The fitted frequencies of ZF-μSR for CeAlSi according to Eqn. 8.1, with $T_N = 9.4(1)$ K. Inset: The fitted relaxation rate λ_{osc} as a function of temperature T.

where A_{osc} (8.6(2) %), A_n (1.54(2) %) and A_{bg} (7.22(5) %) refer to the oscillating, non-oscillating, and background components respectively, λ_{osc} (4.4(1) μs^{-1}) and λ_n (0.8(1) μs^{-1}) are the dynamical relaxation rates of the corresponding components, and ν (13.70(2) MHz) and ϕ (-8.26(9)°) are the oscillation frequency and phase respectively. The clear oscillating signal in the early-time window (from $t = 0$ to $t = 0.3$ μs) indicates that there exists only one unique crystallographic muon site where all equivalent positions produce the same magnitude of the local magnetic field. The oscillation has an exponential envelope and is fully damped at $t = 0.5$ μs, which implies that there is a small broadening of the local field distribution that could possibly be attributed to the formation of magnetic domains. Extracting the fit parameters at higher temperatures, one finds the transition temperature T_N of CeAlSi to be 9.4(1) K, above which the system turns paramagnetic (see Fig. 8.3).

The local field at the muon stopping site can be written as the sum $\mathbf{B}_{loc} = \mathbf{B}_{dip} + \mathbf{B}_{demag} + \mathbf{B}_L + \mathbf{B}_{con}$, where $\mathbf{B}_{con}$ is the contact hyperfine field caused by conduction electrons, $\mathbf{B}_L$ and $\mathbf{B}_{demag}$ are the Lorentz and demagnetising fields respectively which scale as the sample's bulk magnetisation, but we can deduce that their effect is certainly much weaker than $\mathbf{B}_{loc}$ on the basis of the observation

of clear oscillating data and the formation of domains in four [110]-equivalent directions suppressing bulk magnetisation.

8.2.3 Muon site

With the DFT+μ method, as discussed in Chapter 3, I identified the muon stopping site to be at the position (0, 0.38, 0.4214) which is close to the center of the three nearest Ce^{3+} ions and which has a Wyckoff position 8b. The dipolar field $\mathbf{B}_{\text{dip}}$ at this site, by imposing the magnetic structure reported in [198], was calculated to be 14.1 MHz which is consistent with the observed frequency in the ZF μSR measurements shown in Fig. 8.2. Considering the crystal and magnetic structure symmetries, had the muon been placed at a general Wyckoff 16c position one would have expected two distinct groups of muon frequency. The sharp frequency observed in the ZF-μSR therefore suggests that the muon stopped somewhere along a high symmetry line near the 4a and 8b positions and this is consistent with my muon site calculation.

8.3 NdAlSi

8.3.1 Magnetic structure

Despite the similarities in their structural properties, CeAlSi and NdAlSi host very distinct magnetic structures and the latter is reported to have two magnetic phases; at temperatures below $T_{\text{com}} = 3.3$ K, the Kramers Nd^{3+} moments $\left(4f^3, J = \frac{9}{2}\right)$ form a helical up-down-down commensurate order that propagates along the [110]-axis with a k-vector $\left(\frac{4\pi}{3}, \frac{4\pi}{3}, 0\right)$. The magnetic structure determined by neutron diffraction measurements can be written as

$$\mu_x = -0.11 \cos\left(\mathbf{k}\cdot\mathbf{r} + \frac{\pi}{2}\right), \tag{8.2}$$

$$\mu_y = 0.11 \cos\left(\mathbf{k}\cdot\mathbf{r} + \frac{\pi}{2}\right), \tag{8.3}$$

$$\mu_z = -0.965 + 3.87 \cos(\mathbf{k}\cdot\mathbf{r}), \tag{8.4}$$

in units of Bohr magneton μ_{B}, and each Nd^{3+} moment is found to have a size of 2.9 μ_{B}, as reported in [199]. Note that there is a ferromagnetic component along

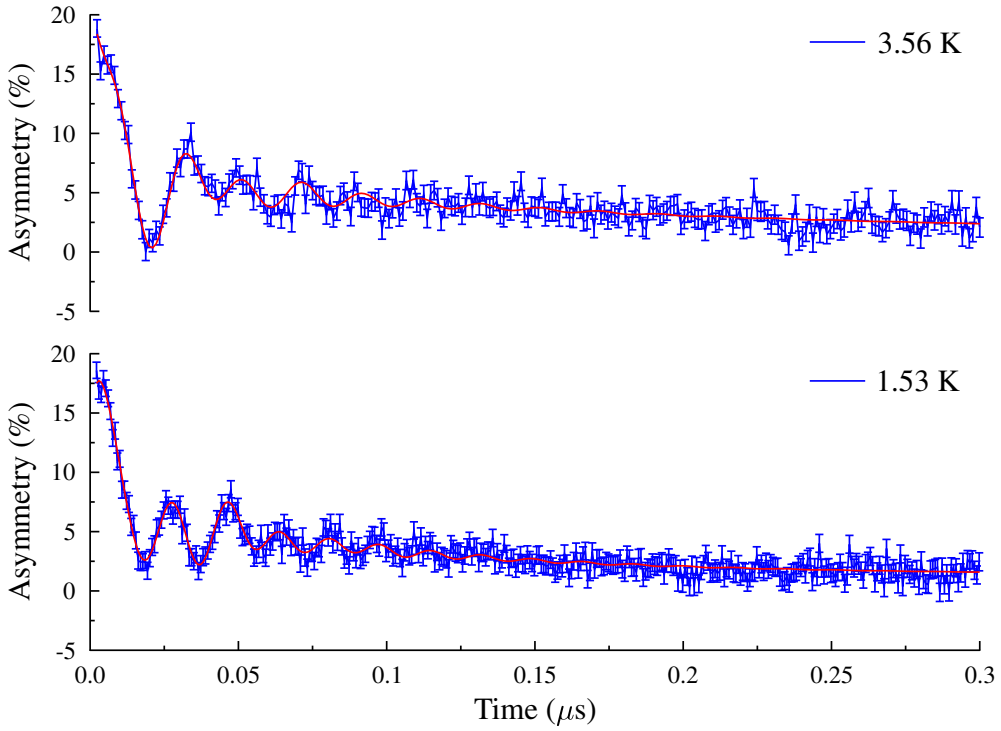

Figure 8.4: Zero-field muon decay asymmetry measured at 1.53 K (commensurate) and 3.56 K (incommensurate) for NdAlSi which show distinct patterns in the first 0.05 μs. Data points including errors are in blue and the fitted line is in red.

the c-axis (see Eqn. 8.4), but the bulk magnetisation is believed to be weakened by the formation of domains, which will be discussed in the following subsections.

At temperatures between 3.3 K and $T_{\text{incom}} = 7.2$ K, the system enters an incommensurate phase in which the magnetic order has a k-vector of $\left(\frac{4\pi}{3} + \delta, \frac{4\pi}{3} + \delta, 0\right)$, where δ is the incommensurability [199].

8.3.2 μSR Zero Field

The ZF-μSR data on several pieces of NdAlSi crystals, obtained using the GPS spectrometer at PSI and plotted in Fig. 8.4, has captured this magnetic phase transition which shows distinct oscillatory patterns in the two phases (at 1.53 K and 3.56 K). I fitted the muon data phenomenologically using Eqn. 8.5 which contains three components – a Bessel function, an oscillating term, and a background relaxation such that

$$A(t) = A_J J_0(\nu_J t) e^{-\lambda_J t} + A_c \cos(\nu_c t + \phi) e^{-\lambda_c t} + A_B e^{-\lambda_B t}, \tag{8.5}$$

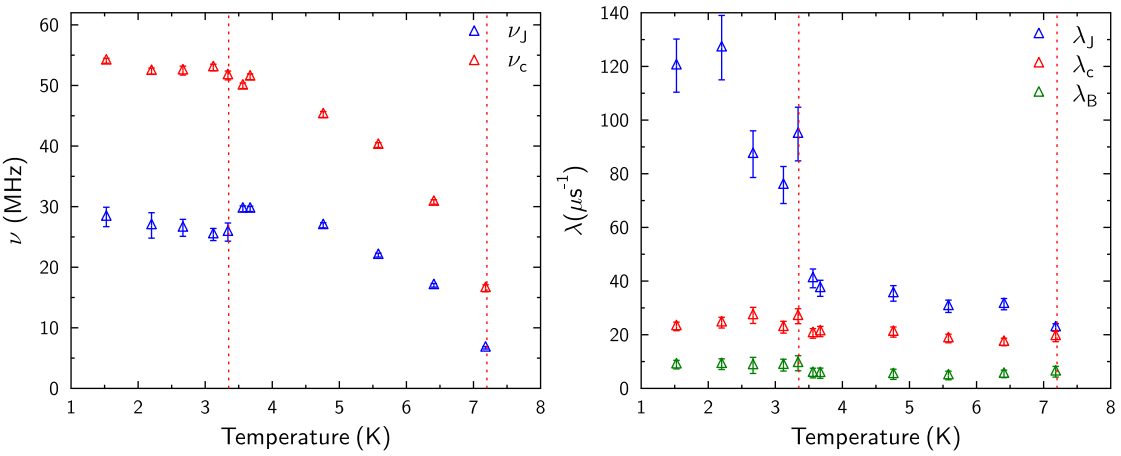

Figure 8.5: Fitted frequencies and relaxation rates of the NdAlSi zero-field asymmetry data, using Eqn. 8.5. The red dotted lines mark the transition temperatures T_{com} (3.3 K) and T_{incom} (7.2 K).

where A_i, λ_i refer to the initial asymmetry and dynamical relaxation rate of the i-th component, $J_0(\nu_J t)$ is the zeroth order Bessel function of the first kind, and $\cos(\nu_c t + \phi)$ is a simple cosine function with a phase ϕ. The fitted frequencies and relaxation rates for the two magnetic phases were plotted in Fig. 8.5. The asymmetry fitting reveals a slight drop in the Bessel function frequency ν_J as the system enters the commensurate phase, but the cosine function frequency ν_{c} crosses smoothly over the transition.

The Fourier spectrum of the ZF-μSR asymmetry across 1.5 K to 7.2 K is plotted in Fig. 8.6 which shows a wide spread of frequencies from 0 MHz to 60 MHz. The maximum frequency falls as temperature increases and follows the trend of ν_c.

8.3.3 μSR Transverse Field

Further measurements on multiple pieces of NdAlSi crystals were performed using the HAL-9500 spectrometer where external transverse fields of 3 T, 6.5 T, and 8 T were applied at temperatures between 1.5 K and 300 K.

The frequency spectrum with 8 T applied (see Fig. 8.7) shows the magnetic response of the field-polarised phase and contains two features as the sample is being cooled; First, there are two main peaks which shift into opposite directions. Second, the widths of the peaks are broadened. Note that only data with temperatures above

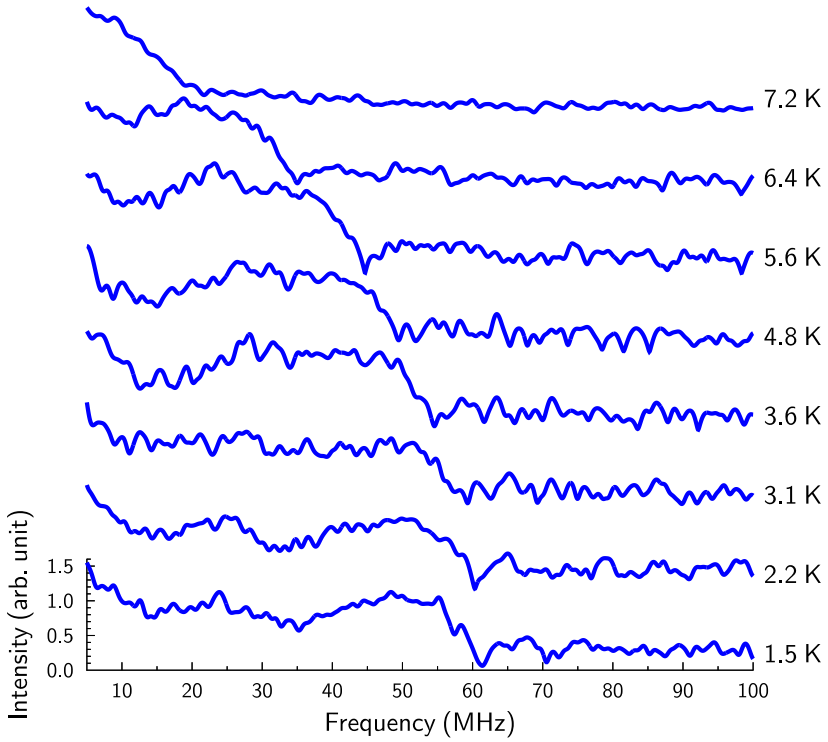

Figure 8.6: A waterfall plot of the Fourier spectra of ZF-μSR asymmetry $A(t)$ for NdAlSi from 1.5 K to 7.2 K showing a wide range of muon precession frequencies 60 MHz. The top end of the frequency range falls as the moment size decreases with rising temperature.

40 K are plotted but the trend follows down to the lowest available temperature of 2.2 K. The measurement at a lower field of 6.5 T has an identical spectrum as the system is in the same magnetic phase, based on reported magnetisation measurements [203]. However, the spectrum is very different at 3 T. Apart from the two shifting main peaks as before, there is also a stationary peak around 3 T across all temperatures. At this field, the peaks drift sideways when the sample is cooled from 300 K to 8 K but they stopped when the temperature reaches 6 K. This is consistent with the reported magnetisation measurements under an applied field of 3 T along $\hat{\mathbf{c}}$ as the sample transitions from a paramagnetic phase into a ferrimagnetic phase around 7 K [203].

The focusing effect of the muon beam is stronger at a higher field and hence fewer muons land on the silver plate. Therefore a much weaker central peak is expected at 6.5 T and 8 T. Given the same set-up, the stationary peak at 3 T demonstrated that significantly more muons have landed on the silver plate. The stray-field effect is

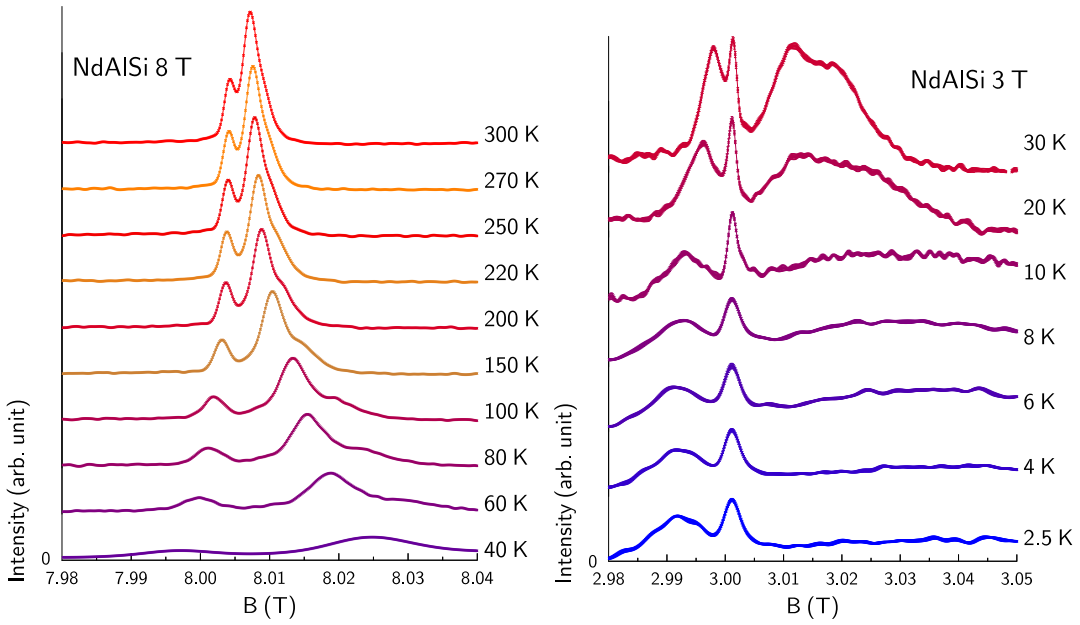

Figure 8.7: The muon precession frequency spectra (in units of Tesla) of the Transverse-Field (TF) μSR measurements on NdAlSi with an external field of 3 T and 8 T performed using the HAL spectrometer at PSI. Measured peaks that depart from the applied field value indicate a presence of additional magnetic field at the muon site. The 3 T data show a temperature-independent central peak which refers to muons landing on the silver plate.

expected to be tiny as the sample forms domains which suppress bulk magnetisation.

The non-magnetic sister compound LaAlSi was subsequently measured as a comparison to NdAlSi, and the results show an identical frequency spectrum across all temperatures, i.e. one stationary peak at B_{ext}. In contrast, for NdAlSi, there were already two peaks at 300 K that are close to the applied field value, but they are expected because of the small but non-negligible magnetisation of the polarised Nd moments at this temperature.

8.3.4 Muon site

Calculations performed on a NdAlSi supercell using the DFT+μ method have identified the same muon site as CeAlSi and it is located at the position (0, 0, 0.4218), the centre of the three nearest Nd atoms. This is a reasonable finding because compounds of the same family often have very similar electronic potential profiles, and hence the same muon site. The three Nd^{3+} moments form a triangle plane which lays either in the *ac*-plane or the *bc*-plane (Fig. 8.1). Knowing the

muon site allows the calculations of the local dipolar field, which will be discussed in the next subsection, by imposing the proposed magnetic structure for the zero-field and the field-polarised case.

8.4 Discussion

CeAlSi is known to form domains with magnetisation along [110], [1$\bar{1}$0], [$\bar{1}$10] or [$\bar{1}\bar{1}$0]. However, the stacking order between Ce moments $\mathbf{S}_1$ and $\mathbf{S}_2$ (at $z = 0$ and $z = \frac{1}{4}$ respectively) was not resolved by neutron scattering [200]. Dipolar field calculations, together with the muon stopping site identified, show that the spin structure $\mathbf{S}_1 = [\cos 79°, \sin 79°, 0]$, $\mathbf{S}_2 = [\cos 11°, \sin 11°, 0]$ in the $\mathbf{M} \parallel [110]$ domain has a precession frequency of 14 MHz, which is consistent with the experimental value 13.68(2) MHz. The calculated precession frequency remain the same in all other magnetic domains, where the magnetic structure transform according to the crystalline symmetry, hence only one peak is found in μSR frequency spectrum.

For NdAlSi, there is a broad frequency spectrum in the ZF-μSR data at the base temperature of 1.53 K in the commensurate phase that spans continuously from 0 to 60 MHz (Fig. 8.6). Further measurements with only one piece of single crystal found an identical spectrum and therefore ruled out the occurrence of weak stray fields from adjacent (magnetised) crystals. I suspect that the broadening is caused by the formation of small magnetic domains. Because of the symmetry between $\hat{\mathbf{c}}$ and $-\hat{\mathbf{c}}$, when one cools NdAlSi in zero-field, local clusters of magnetic moments will have to spontaneously pick one of the two directions hence forming domain walls between clusters. For muons stopping near the domain walls, they are subject to a range of local magnetic environments which results in a broadened frequency spectrum. Stripe domains have been found in the isostructural compound NdAlGe, which was reported to have a similar magnetic structure, and small angle neutron scattering (SANS) measurements showed distinct results between the zero-field and field-cooled measurements as the field applied in $\hat{\mathbf{c}}$ breaks the crystal symmetry along $\hat{\mathbf{c}}$ and $-\hat{\mathbf{c}}$ [204].

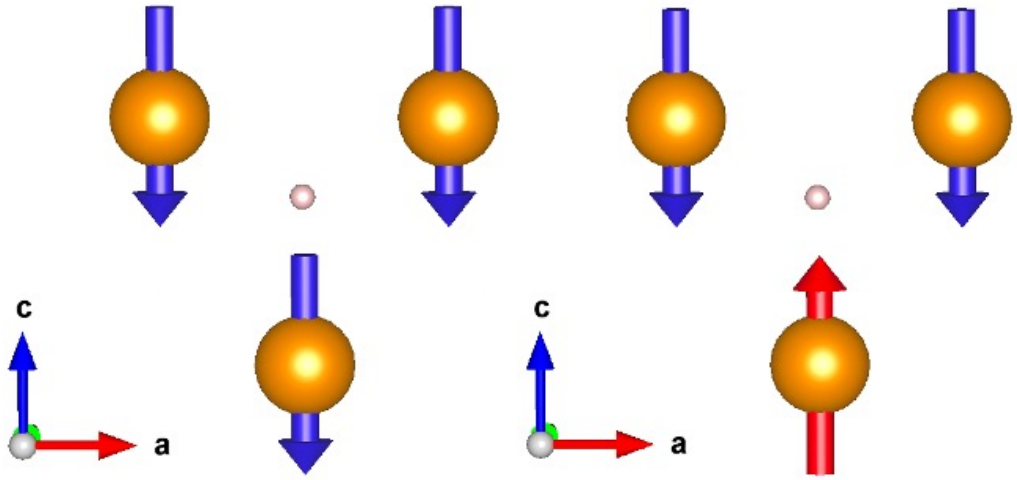

Figure 8.8: (Left) Departure from the up-down-down order in NdAlSi leads to a lower range of the muon precession frequencies between 20 MHz and 45 MHz. (Right) When the nearest three Nd^{3+} moments obey the up-down-down order, the frequency ranges between 50 MHz and 80 MHz. The frequency ranges quoted here include the contribution by Nd atoms beyond the three shown in the Figure.

In a commensurate phase, one normally expects a finite number of muon precession frequencies that represent all possible local magnetic environments at crystallographically equivalent sites. In the case of NdAlSi, the domain formation, i.e. local magnetic disorder, might have caused a broadening effect in the frequency spectrum. To look into this, I considered a case where all the Nd spins are randomly allocated: Each with a moment of 2.9 μ_B and the probability of it pointing up (down) is $\frac{1}{3}$ ($\frac{2}{3}$). Physically this refers to the extreme case where the disorder is so strong that the Nd moments are no longer magnetically correlated. Using the muon site identified, which is located close to the centroid of the nearest three Nd atoms, our dipolar field calculations found two main groups of frequencies. The first group lies in the range from 50 MHz to 80 MHz and was found to occur when the nearby Nd moments follow the standard up-down-down configuration. The second group is between 20 MHz and 45 MHz where the three closest Nd moments are all aligned in the same direction, along $\hat{\mathbf{c}}$ or $-\hat{\mathbf{c}}$, allowing the dipolar fields to partially cancel out each other at the muon site. The further broadening is caused by the addition of further Nd spins beyond the nearest three which gives rise to a large number of magnetic environments. This calculation shows that the broadened spectrum is a

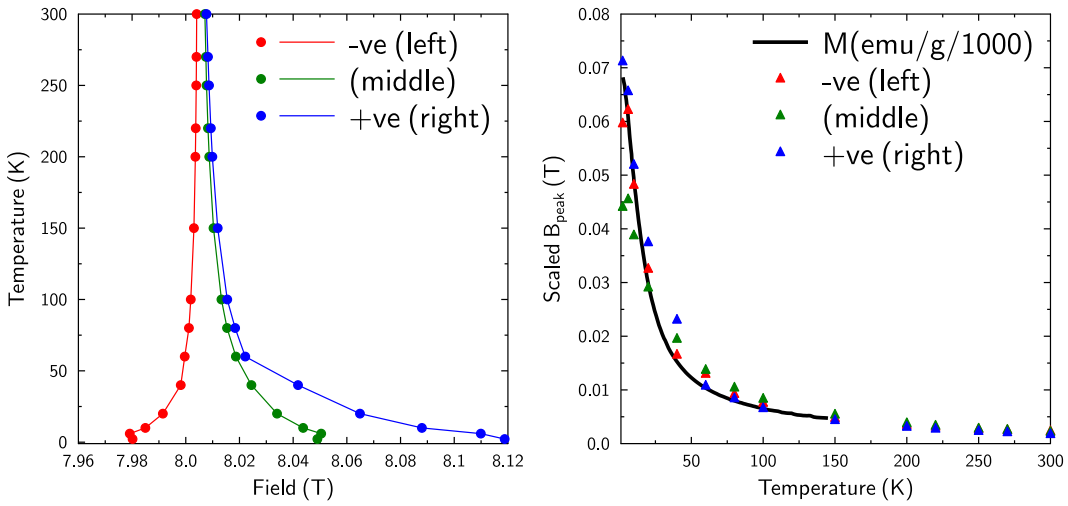

Figure 8.9: For an applied transverse field of 8 T: (Left) The shifting Fourier peaks as a function of temperature. (Right) The magnitude of the shift mapped to the magnetisation $M(T)$. This shows that the origin of the shifts in the Fourier spectra is directly linked to the Nd^{3+} moments.

direct result of the magnetic disorder, and the lower frequency range (20 MHz to 45 MHz) in our measured frequency spectrum appears when the up-down-down rule of the magnetic order is violated (see Fig. 8.8). Because of domains, one can consider the sample to have no bulk magnetisation. The field experienced by muons can now be simplified to $\mathbf{B} = \mathbf{B}_{\text{dip}} + \mathbf{B}_{\text{con}}$, where the contact hyperfine term $\mathbf{B}_{\text{con}}$ remains due to a non-zero local magnetisation at the muon site.

8.4.1 Contact hyperfine interaction

The contact hyperfine interaction $\mathbf{B}_{\text{con}}$ is observed in many metallic compounds (e.g. in MnSi [205]) and is very often studied using transverse field muon spectroscopy. This interaction originates from overlapping wavefunctions between the muon and the conduction electrons, of which the electron's spin interacts with the muon's spin and causes spin-flipping interactions between the two (represented by the $S_\mu^+ S_e^-$ and $S_\mu^- S_e^+$ terms). In the context of TF-μSR, the hyperfine field $\mathbf{B}_{\text{con}}$ is significantly smaller than the external applied field $\mathbf{B}_{\text{ext}} \gg \mathbf{B}_{\text{con}}$, so only the parallel component of $\mathbf{B}_{\text{con}}$ along $\mathbf{B}_{\text{ext}}$ plays a role. In general, $\mathbf{B}_{\text{con}}$ is considered isotropic and is proportional to the local magnetisation $\mathbf{M}_{\text{loc}}$ around the muon site [206–208].

8.4.2 Transverse field

In transverse field measurements, the muon is exposed to a superposition of five fields $\mathbf{B} = \mathbf{B}_{\text{ext}}(8\text{T}) + \mathbf{B}_{\text{L}} + \mathbf{B}_{\text{demag}} + \mathbf{B}_{\text{dip}} + \mathbf{B}_{\text{con}}$. Among these fields, $\mathbf{B}_{\text{demag}}$ and $\mathbf{B}_{\text{L}}$ are approximately constant across all crystal-equivalent muon sites and are linearly proportional to the bulk magnetisation $\mathbf{M}_{\text{bulk}}$. Strictly speaking, $\mathbf{B}_{\text{demag}}(r) = -\tilde{N}(r)\mu_0\mathbf{M}_{\text{bulk}}$ and I expect $\tilde{N}(r)$ to vary as position r across the sample. However, this should only lead to continuous broadening instead of two larger peaks in the frequency spectrum (see Fig. 8.7). The last two terms $\mathbf{B}_{\text{dip}}$ and $\mathbf{B}_{\text{con}}$ scale linearly with the Nd moments and local magnetisation $\mathbf{M}_{\text{loc}}$ respectively.

Using the field-polarised phase at 8 T as an example: as the temperature lowers, the bulk magnetisation increases [209]. All Nd spins lie along $+\hat{\mathbf{c}}$ and therefore $\mathbf{M}_{\text{loc}} = \mathbf{M}_{\text{bulk}}$. I expect the dipolar and contact fields ($\mathbf{B}_{\text{dip}}$ and $\mathbf{B}_{\text{con}}$) to scale as $\mathbf{M}_{\text{bulk}}$. Using symmetry arguments, the z-component of $\mathbf{B}_{\text{dip}}$ and $\mathbf{B}_{\text{con}}$ are identical at all equivalent sites in this field-polarised phase, therefore, each peak in the frequency spectrum could only be attributed to one muon site when the external field is applied along $\hat{\mathbf{c}}$.

At 8 T, as shown in Fig. 8.9, all the peaks shift progressively away from the central position as the sample is cooled. To look into this, I mapped the movements of the peaks to the magnetisation $M(T)$ data [209] and I found that the magnitude of the shifts scales as the bulk magnetisation $M(T)$ (see the right panel of Fig. 8.9) by a relationship $B_{\text{peak}} = 8.005\ \text{T} + \alpha M_{\text{bulk}}$, where all additional field contributions are represented by α and the peaks shift as a function of M_{bulk}. Therefore, to account for the two main peaks in Fig. 8.7, one explanation is that there exist two muon sites, where the area under the curve represents their relative intensities. This however contradicts the single frequency observed for CeAlSi which rules out the possibility of two muon sites, and therefore a future investigation would be to perform TF-μSR measurements on CeAlSi to assess to what extent it agrees with that from NdAlSi, and perhaps from this one could fully understand the muon sites, the properties of this family of Weyl semimetal compounds, and the effect of the contact hyperfine interactions $\mathbf{B}_{\text{con}}$.

The focusing effect of the muon beam (as discussed in Section 8.3.3) plays an important role in the appearance of the silver peaks; None was observed at 8 T but a temperature-independent peak is seen at 3 T. At an intermediate field of 6.5 T, there is a very small silver peak signal that shifts slightly to the left as the temperature drops. One plausible explanation for this is that a small fraction of muons landed on the silver plate and experienced both the applied field (6.5 T) and the weak stray fields from nearby magnetised samples, which increases with magnetisation as the temperature drops [209]. This could be written as $B_z = B_{\text{ext}} + \mathbf{B}_{\text{stray}} \cdot \hat{\mathbf{z}} = 6.5\ \text{T} - \beta M_{\text{bulk}}$, where $|\mathbf{B}_{\text{stray}}| \ll 6.5$ T and β is a proportionality constant.

8.5 Conclusion

In this chapter, I presented the Zero-Field (ZF) and Transverse-Field (TF) μSR measurements on two Weyl semimetal compounds CeAlSi and NdAlSi. The ZF-μSR asymmetry on CeAlSi which showed a clear oscillating feature agrees well with the dipolar field calculations across all magnetic domains. As for NdAlSi, I suspected that the formation of small domains has caused the broadening of the ZF-μSR frequency spectrum in the commensurate phase below $T_{\text{com}} = 3.3$ K. I found that, with TF-μSR measurements in an applied field up to 8 T, the shifts of the frequency peaks and broadening follow closely to the sample's magnetisation. I suspect that this is a consequence of contact hyperfine interaction, and I believe that this is crucial to the understanding of μSR responses in a wider range of Weyl semimetals where similar phenomena have been observed [210].

9 Conclusion

Through this thesis, I explored the fascinating field of frustrated magnetism by showcasing a wide range of systems; From the 1D spin-chain compounds with kagome arrangements, to the 2D honeycomb and triangular lattice materials, and finally, the 3D pyrochlore spin ice and also the (non-frustrated) Weyl semimetals. I unveiled several aspects of the local dynamics and magnetism of new materials that have not previously been known, including new candidate spin liquid materials with persistent spin dynamics at temperatures down to the order of 40 mK.

Studying a quantum material requires a suite of experimental and computational techniques that complement each other; these include magnetometry (D.C. and A.C.measurements), μSR, DFT and crystal field calculations as discussed in Chapter 3, but also heat capacity measurements, neutron diffraction, inelastic neutron scattering, and Raman scattering [211] which I have not touched on in this thesis. Chapters 4 and 8 demonstrated the importance of the muon site determination using DFT+μ and how, together with dipolar field calculations and the magnetic structures determined via neutron diffraction, one could shed light on the local magnetism and expand our understanding of these new materials.

In particular, the work in Chapters 5 and 6 has shown that μSR can be a rather informative tool in the studies of many novel frustrated magnets. By presenting the zero-field, longitudinal-field, and weak transverse-field measurements on several

frustrated magnets, this thesis has standardised the μSR protocol for gathering firm evidence and extracting key information about the local spin dynamics over a range of temperatures. Furthermore, studying the longitudinal field dependence of the relaxation rate allows researchers to establish the mode of spin diffusion in potential quantum spin liquid materials.

Throughout the thesis, I emphasised the importance of the crystalline electric fields (CEF) on spin dynamics, muon relaxation rates, and other magnetic properties. The CEF sets the framework in which the magnetic moments are allowed to vary – for example, creating the magnetic easy-axis anisotropy along the local z-axis as shown in Chapters 6 and 7. For many rare earth oxides, the CEF potential splits the $2J + 1$ degenerate levels and the transverse components of the exchange interactions, outlined in Chapter 3, cause spin-flipping through transitions between the effective $J = \frac{1}{2}$ doublet ground state, which can be linked to the fast spin dynamics observed in many frustrated spin liquid materials. However, as shown in Chapter 7, the presence of chemical disorder can lead to inhomogeneous local properties and hinder our abilities to understand the intrinsic mechanism.

By employing various spectroscopic techniques, we gain newfound insights into the remarkable properties exhibited by new quantum materials which empower us to better position ourselves for the challenges we face. As we continue to unravel the secrets in these materials, we are poised to enter a new era of revolutionary advancements, shaping a brighter future for the next generations.

Future Work

- **$DyTa_7O_{19}$ – A.C.susceptibility and heat capacity**

  In Chapter 6, I presented the $DyTa_7O_{19}$ compound that exhibits persistent spin dynamics at base temperature. To fully understand the dynamics, one could perform A.C. magnetic susceptibility measurements using the MPMS or the PPMS (Physical Property Measurement Systems). Preliminary measurements at 1.8 K with a D.C. applied field of 2000 G, plotted in Fig. 9.1, have shown a frequency-dependent response in the $DyTa_7O_{19}$ sample and a

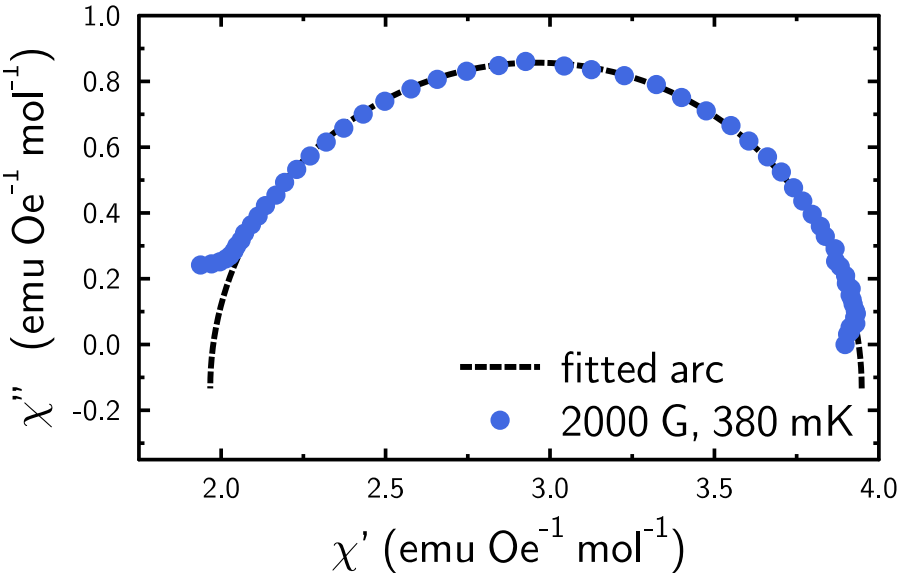

Figure 9.1: The Cole-Cole plot of the real and imaginary part of A.C.susceptibility measurements on $DyTa_7O_{19}$ with D.C. field of 2000 G applied and fitted against a semi-circular arc. This measurement is taken at the Materials Characterisation Laboratory at ISIS, Rutherford Appleton Laboratory, UK.

single relaxation time by fitting the data against a semi-circular arc. However, the data suggest that even with 1000 MHz, which is the highest possible frequency in an MPMS3 system, it is not sufficient to probe the spin dynamics fully at higher temperatures and a wider frequency range is needed. This should be possible with a PPMS system which can apply an A.C. driving field with frequencies up to 10 kHz.

In addition, one could perform Monte-Carlo simulations to calculate the A.C. magnetic susceptibility for a system of Ising spins decorating a triangular lattice. Similar work has been done on the classical spin ice $Dy_2Ti_2O_7$ compound which shows the slowing down of spin dynamics, and the real and imaginary parts of the A.C. susceptibility can be calculated by

$$\chi'(\omega) = \frac{1}{N_{\mathrm{MC}} H_{\mathrm{a.c.}}} \sum_{t_i} M(t_i) \sin(\omega t_i), \tag{9.1}$$

$$\chi''(\omega) = \frac{1}{N_{\mathrm{MC}} H_{\mathrm{a.c.}}} \sum_{t_i} M(t_i) \cos(\omega t_i) \tag{9.2}$$

summed over all Monte-Carlo time steps t_i, as described in [212], where N_{MC} is the number of steps taken, $H_{\mathrm{a.c.}}$ is the amplitude of the driving a.c. field

with frequency ω, and $M(t_i)$ is the magnetisation at time t_i. The results can be used to check against the experimental data obtained from the SQUID measurements.

Furthermore, heat capacity $C(T)$ measurements allow one to study the entropy of a magnetic spin system at temperature T by

$$\Delta S(T) = \int_{T_0}^{T} \frac{C(T)}{T} \mathrm{d}T + S_0, \tag{9.3}$$

where S_0 is the magnetic entropy at the lowest achievable temperature T_0. For an effective spin-$\frac{1}{2}$ system at high temperature, spins are free to pick between the spin-up and spin-down state and the entropy of the system reaches $R \ln 2$, assuming that the higher excited states are not occupied. As temperature drops, ordering between magnetic spins starts to play a role and hence entropy falls accordingly. For most materials, the residual entropy at $T = 0$ reaches zero except in cases such as a pyrochlore spin ice compound $A_2B_2O_7$, where a robust degenerate ground state configuration could exist [155, 213]. For a Triangular Ising Antiferromagnet, a zero-point residual entropy of 0.323 R was predicted to exist because of the possible degenerate ground states if only the nearest-neighbour interactions J_1 are considered [117]. It is also predicted that this plateau in $S(T)$ would collapse and fall to zero even if a small $\frac{J_2}{J_1}$ ratio of the next nearest-neighbour interaction J_2 is present [214]. Therefore, it would be advantageous to perform heat capacity measurements and to evaluate the zero-point entropy of $DyTa_7O_{19}$.

- **$PbMNi_6Te_3O_{18}$ (M = Fe, Co, Zn) – Magnetic structure determination**

  The $PbMNi_6Te_3O_{18}$ family of isostructural compounds in Chatpter 4 showed intriguing features in the μSR data and also the magnetometry results. Further work on these compounds could include determination of the exchange interactions J_1 to J_5 in the M = Fe, Co and Zn cases with inelastic neutron scattering measurements of the magnetic excitations, ideally on single crystal samples. Such measurements can potentially reveal the properties these

exchange interactions at a range of temperatures, especially at around 25 K and 50 K where interesting features are found in the magnetic susceptibility curves, and allow a better understanding of the ground state magnetic structure of these compounds.

- **Pr-based Pyrochlore – Solving the full Hamiltonian**

  Chapter 7 sets out the Hamiltonian of a pyrochlore system and suggests that there is a link between the static relaxation rate σ and the crystal field in the system by solving a simplified version of Eqn. 7.8. However, to calculate the muon asymmetry one needs to solve the Hamiltonian fully with the dipolar coupling between the muon and each of the Pr^{3+} moment **J** and **I**. The muon asymmetry can be calculated by

$$\left\langle \sigma_\mu^z(t) \right\rangle \propto \mathrm{Tr}\left[U^{-1}(t)\rho(0)U(t)\sigma_\mu^z \right], \tag{9.4}$$

  where the information of the time-evolution operator $U(t)$ is given by the eigenstates of the full Hamiltonian. Figure 9.2 shows preliminary results on the resulting muon asymmetry by considering the three nearest Pr atoms (therefore, a system of seven spins including the muon with a Hamiltonian of size 3456^2) and shows a reasonable relaxation rate that lies between the electronic and nuclear-only rates. The ongoing challenge for this work is to shorten the computational time required to include more Pr atoms which should theoretically average the oscillations and produce an asymmetry observed in the ZF-μSR measurements.

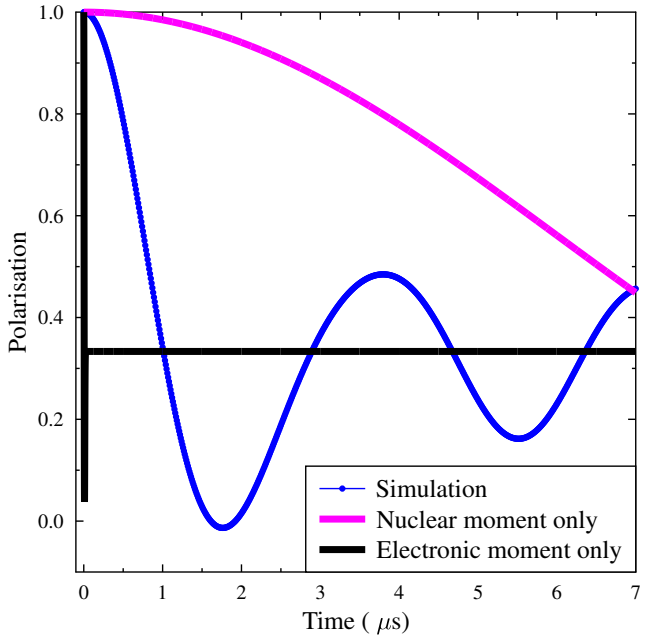

Figure 9.2: Calculation of the muon asymmetry by solving the full Hamiltonian in Eqn. 7.8. The expected asymmetry from static electronic moments and static nuclear moments are also plotted for comparison.

Appendices

A

A number of important formulae

Contents

A.1 Larmor diamagnetism

In Chapter 2, the first-order energy correction of an atom with Z electrons in an applied field contains a diamagnetic term

$$\Delta E^{(1)}_{\text{dia}} = \frac{e^2}{8m_e} \sum_{i=1}^{Z} \left\langle \Psi_0 \middle| (\mathbf{B} \times \mathbf{r}_i)^2 \middle| \Psi_0 \right\rangle , \tag{A.1}$$

assuming that $\mathbf{B}$ is applied along the z-axis so that $\mathbf{B} = (0, 0, B)$,

$$\Delta E^{(1)}_{\text{dia}} = \frac{e^2 B^2}{8m_e} \sum_{i=1}^{Z} \left\langle \Psi_0 \middle| x_i^2 + y_i^2 \middle| \Psi_0 \right\rangle \tag{A.2}$$

$$= \frac{e^2 B^2}{12m_e} \sum_{i=1}^{Z} \left\langle r_i^2 \right\rangle . \tag{A.3}$$

where $\sum_{i=1}^{Z} \langle x_i^2 + y_i^2 \rangle = \frac{2}{3} \langle r_i^2 \rangle$ is used and is a reasonable assumption for a spherical wavefunction.

To obtain the contribution to susceptibility χ_{dia}, we consider

$$\chi_{\text{dia}} = \lim_{H\to 0} \frac{\partial M}{\partial H} \tag{A.4}$$

$$= \lim_{B\to 0} \mu_0 \frac{\partial M}{\partial B} \tag{A.5}$$

$$= \lim_{B\to 0} -\mu_0 \frac{\partial^2 F}{\partial B^2} \tag{A.6}$$

$$= -n\mu_0 \frac{\partial^2}{\partial B^2} \left(\Delta E^{(1)}_{\text{dia}}\right) \tag{A.7}$$

$$= -\frac{\mu_0 n e^2}{6m_e} \sum_{i=1}^{Z} \left\langle r_i^2 \right\rangle, \tag{A.8}$$

which sums over all Z electrons of the atom and is always negative.

A.2 Van Vleck paramagnetism

The treatment to find the contribution of Van Vleck paramagnetism to the magnetic susceptibility is similar to that of Larmor Diamagnetism as discussed in Section A.1. The second-order energy correction due to the Van Vleck paramagnetism, as shown in Chapter 2, is given by

$$\Delta E^{(2)}_{\text{VV}} = \mu_{\text{B}}^2 \sum_{j>0} \frac{\left|\left\langle \Psi_j \right| \left(\hat{\mathbf{L}} + g_S \hat{\mathbf{S}}\right) \cdot \mathbf{B} \left| \Psi_0 \right\rangle\right|^2}{E_0 - E_j}. \tag{A.9}$$

With $\mathbf{B} = (0, 0, B)$, we have

$$\chi_{\text{VV}} = -n\mu_0 \frac{\partial^2}{\partial B^2} \left(\Delta E^{(2)}_{\text{VV}}\right) \tag{A.10}$$

$$= 2n\mu_0\mu_{\text{B}}^2 \sum_{j>0} \frac{\left|\left\langle \Psi_j \right| \left(\hat{L}_z + g_S \hat{S}_z\right) \left| \Psi_0 \right\rangle\right|^2}{E_j - E_0}, \tag{A.11}$$

which is always positive for the ground state, unlike the diamagnetic susceptibility χ_{dia}.

A.3 Van Vleck susceptibility

For many 4f rare earth ions, the magnetic susceptibility curve does not always behave like a paramagnet; the latter has a constant magnetic moment that follows the Curie-Weiss Law, but for the lanthanides, it depends on the occupation of

each energy state in the ground state multiplet. To start with, we could write the magnetisation $M(T,B)$ at temperature T and applied field B as

$$\langle M(T,B)\rangle = \frac{1}{Z}\sum_j M_j e^{-\beta E_j}, \tag{A.12}$$

which sums over the magnetisation of the j-th state with a probability of occupation $e^{-\beta E_j}/Z$, where $Z = \sum_i e^{-\beta E_i}$ is the partition function.

Using $M_j = -\frac{dE_j(B)}{dB}$ and that $E_j(B) = E_j^{(0)} + \Delta E_j^{(1)} + \Delta E_j^{(2)} + \ldots$ as outlined in Section 2.1, we have

$$\frac{\partial \langle M(T,B)\rangle}{\partial B} = \frac{1}{Z}\sum_j e^{-\beta E_j}\left[\frac{1}{k_{\mathrm{B}}T}\left(\frac{dE_j}{dB}\right)^2 - \frac{d^2E_j}{dB^2}\right], \tag{A.13}$$

$$\therefore \chi = \mu_0 \left.\frac{\partial M}{\partial B}\right|_{B\to 0} = \mu_0 \frac{1}{Z}\sum_j e^{-\beta E_j(0)}\left[\frac{\left(W_j'\right)^2_{B=0}}{k_{\mathrm{B}}T} - \left(W_j''\right)_{B=0}\right], \tag{A.14}$$

where

$$W_j'\Big|_{B=0} = \left.\frac{dE_j}{dB}\right|_{B=0} = \mu_{\mathrm{B}}\left\langle j\middle|\hat{L}_z + g_S\hat{S}_z\middle|j\right\rangle \tag{A.15}$$

and

$$W_j''\Big|_{B=0} = \left.\frac{d^2E_j}{dB^2}\right|_{B=0} = 2\mu_{\mathrm{B}}^2\sum_{k\neq j}\frac{\left|\left\langle k\middle|\hat{L}_z + g_S\hat{S}_z\middle|j\right\rangle\right|^2}{E_j - E_k}. \tag{A.16}$$

This shows that, as though the paramagnetic part remains important, the matrix elements in W_j'' which connects energy levels can play a significant role when one considers a singlet state in which $W_j'\Big|_{B=0} = 0$ [178, 179].

B

Landé g-factor

Contents

B.1 Landé g-factor

For orbital angular moment $\mathbf{L}$ and spin angular moment $\mathbf{S}$ we have magnetic moments μ_L and μ_S given as

$$\boldsymbol{\mu}_L = g_L \mu_{\mathrm{B}} \mathbf{L} \quad \text{and} \quad \boldsymbol{\mu}_S = g_S \mu_{\mathrm{B}} \mathbf{S}. \tag{B.1}$$

In the case where $\mathbf{L}$ and $\mathbf{S}$ are combined to give total angular momentum $\mathbf{J}$, so that $\mathbf{J} = \mathbf{L} + \mathbf{S}$, one looks to express the magnetic moment as

$$\boldsymbol{\mu}_J = g_J \mu_{\mathrm{B}} \mathbf{J}. \tag{B.2}$$

We can combine the magnetic moments so that

$$
\begin{aligned}
\boldsymbol{\mu}_J &= \boldsymbol{\mu}_L + \boldsymbol{\mu}_S \\
g_J \mu_{\mathrm{B}} \mathbf{J} &= g_L \mu_{\mathrm{B}} \mathbf{L} + g_S \mu_{\mathrm{B}} \mathbf{S} \\
g_J \mathbf{J} \cdot \mathbf{J} &= g_L \mathbf{L} \cdot \mathbf{J} + g_S \mathbf{S} \cdot \mathbf{J}, \quad \text{using } \mathbf{J} = \mathbf{L} + \mathbf{S}, \\
g_J \mathbf{J}^2 &= g_L (\mathbf{L}^2 + \mathbf{L} \cdot \mathbf{S}) + g_S (\mathbf{S}^2 + \mathbf{S} \cdot \mathbf{L}) \\
g_J \mathbf{J}^2 &= g_L \left(\mathbf{L}^2 + \frac{\mathbf{J}^2 - \mathbf{L}^2 - \mathbf{S}^2}{2} \right) + g_S \left(\mathbf{S}^2 + \frac{\mathbf{J}^2 - \mathbf{L}^2 - \mathbf{S}^2}{2} \right) \\
g_J \mathbf{J}^2 &= \left(\frac{\mathbf{J}^2 + \mathbf{L}^2 - \mathbf{S}^2}{2} \right) + 2 \left(\frac{\mathbf{J}^2 - \mathbf{L}^2 + \mathbf{S}^2}{2} \right) \\
g_J \mathbf{J}^2 &= \frac{3\mathbf{J}^2 - \mathbf{L}^2 + \mathbf{S}^2}{2} \\
g_J J(J+1) &= \frac{3J(J+1) - L(L+1) + S(S+1)}{2} \\
g_J &= \frac{3}{2} + \frac{S(S+1) - L(L+1)}{2J(J+1)},
\end{aligned}
$$

where $g_L = 1$ and $g_S = 2$ have been used. This gives the Landé g-factor g_J which is important for rare earth ions when the crystal field levels are expressed in the basis of the total angular momentum eigenstates $|J, m_J\rangle$.

References

1. Cava, R., de Leon, N. & Xie, W., Introduction: Quantum Materials, *Chem. Rev.* **121,** 2777 (2021).
2. Keimer, B. & Moore, J. E., The physics of quantum materials, *Nat. Phys.* **13,** 1045 (2017).
3. Clark, L. & Lightfoot, P., All in a spin, *Nat. Chem.* **8,** 402 (2016).
4. Kumar, N., Guin, S. N., Manna, K., Shekhar, C. & Felser, C., Topological Quantum Materials from the Viewpoint of Chemistry, *Chem. Rev.* **121,** 2780 (2021).
5. Mühlbauer, S., Binz, B., Jonietz, F., Pfleiderer, C., Rosch, A., Neubauer, A., Georgii, R. & Böni, P., Skyrmion Lattice in a Chiral Magnet, *Science* **323,** 915 (2009).
6. Anderson, P., Resonating valence bonds: A new kind of insulator?, *Mater. Res. Bull.* **8,** 153 (1973).
7. Balents, L., Spin liquids in frustrated magnets, *Nature* **464,** 199 (2010).
8. Savary, L. & Balents, L., Quantum spin liquids: a review, *Rep. Prog. Phys.* **80,** 016502 (2016).
9. Shikano, M., Delmas, C. & Darriet, J., $NaRuO_2$ and $Na_xRuO_2 \cdot yH_2O$: New Oxide and Oxyhydrate with Two Dimensional RuO_2 Layers, *Inorg. Chem.* **43,** 1214 (2004).
10. Bordelon, M. M., Kenney, E., Liu, C., Hogan, T., Posthuma, L., Kavand, M., Lyu, Y., Sherwin, M., Butch, N. P., Brown, C., Graf, M. J., Balents, L. & Wilson, S. D., Field-tunable quantum disordered ground state in the triangular-lattice antiferromagnet $NaYbO_2$, *Nat. Phys.* **15,** 1058 (2019).
11. Ortiz, B. R., Sarte, P. M., Pokharel, G., Garcia, M., Marmolejo, M. & Wilson, S. D., Traversing the pyrochlore stability diagram: Microwave-assisted synthesis and discovery of mixed B-site Ln_2InSbO_7 family, *Phys. Rev. Mater.* **6,** 094403 (2022).
12. Han, T.-H., Helton, J. S., Chu, S., Nocera, D. G., Rodriguez-Rivera, J. A., Broholm, C. & Lee, Y. S., Fractionalized excitations in the spin-liquid state of a kagome-lattice antiferromagnet, *Nature* **492,** 406 (2012).
13. Khuntia, P., Velazquez, M., Barthélemy, Q., Bert, F., Kermarrec, E., Legros, A., Bernu, B., Messio, L., Zorko, A. & Mendels, P., Gapless ground state in the archetypal quantum kagome antiferromagnet $ZnCu_3(OH)_6Cl_2$, *Nat. Phys.* **16,** 469 (2020).
14. Ramirez, A. P., Strongly Geometrically Frustrated Magnets, *Annu. Rev. Mater. Sci.* **24,** 453 (1994).

15. Norman, M. R., Colloquium: Herbertsmithite and the search for the quantum spin liquid, *Rev. Mod. Phys.* **88,** 041002 (2016).

16. Chamorro, J. R., McQueen, T. M. & Tran, T. T., Chemistry of Quantum Spin Liquids, *Chem. Rev.* **121,** 2898 (2021).

17. Clark, L. & Abdeldaim, A. H., Quantum Spin Liquids from a Materials Perspective, *Annu. Rev. Mater. Res.* **51,** 495 (2021).

18. Blundell, S. J., Magnetism in Condensed Matter (Oxford University Press, 2001).

19. Blundell, S. J., Spin-polarized muons in condensed matter physics, *Contemp. Phys.* **40,** 175 (1999).

20. Stevens, K. W. H., Matrix Elements and Operator Equivalents Connected with the Magnetic Properties of Rare Earth Ions, *Proc. Phys. Soc. A* **65,** 209 (1952).

21. Mugiraneza, S. & Hallas, A. M., Tutorial: a beginner's guide to interpreting magnetic susceptibility data with the Curie-Weiss law, *Commun. Phys.* **5,** 95 (2022).

22. Kramers, H. A., Théorie générale de la rotation paramagnétique dans les cristaux, in *Proceedings of the Royal Netherlands Academy of Arts and Sciences* (1930), 959.

23. Klein, M. J., On a Degeneracy Theorem of Kramers, *Am. J. Phys.* **20,** 65 (1952).

24. Orbach, R. & Bleaney, B., Spin-lattice relaxation in rare-earth salts, *Proc. R. Soc. A* **264,** 458 (1961).

25. Fagaly, R. L., Superconducting quantum interference device instruments and applications, *Rev. Sci. Instrum.* **77,** 101101 (2006).

26. Buchner, M., Höfler, K., Henne, B., Ney, V. & Ney, A., Tutorial: Basic principles, limits of detection, and pitfalls of highly sensitive SQUID magnetometry for nanomagnetism and spintronics, *J. Appl. Phys.* **124,** 161101 (2018).

27. Anderson, C. D. & Neddermeyer, S. H., Cloud Chamber Observations of Cosmic Rays at 4300 Meters Elevation and Near Sea-Level, *Phys. Rev.* **50,** 263 (1936).

28. Cecchini, S. & Spurio, M., Atmospheric muons: experimental aspects, *Geosci. Instrum. Method. Data Syst.* **1,** 185 (2012).

29. Hillier, A. D., Blundell, S. J., McKenzie, I., Umegaki, I., Shu, L., Wright, J. A., Prokscha, T., Bert, F., Shimomura, K., Berlie, A., Alberto, H. & Watanabe, I., Muon spin spectroscopy, *Nat. Rev. Methods Primers* **2,** 4 (2022).

30. Brewer, J. H., μSR HOWTO, *Hyperfine Interact.* **230,** 35 (2015).

31. Senba, M., Arseneau, D. J., Pan, J. J. & Fleming, D. G., Slowing-down times and stopping powers for $\sim 2-$MeV μ^+ in low-pressure gases, *Phys. Rev. A* **74,** 042708 (2006).

32. Wu, C. S., Ambler, E., Hayward, R. W., Hoppes, D. D. & Hudson, R. P., Experimental Test of Parity Conservation in Beta Decay, *Phys. Rev.* **105,** 1413 (1957).

33. Garwin, R. L., Lederman, L. M. & Weinrich, M., Observations of the Failure of Conservation of Parity and Charge Conjugation in Meson Decays: the Magnetic Moment of the Free Muon, *Phys. Rev.* **105,** 1415 (1957).

34. Nuccio, L., Schulz, L. & Drew, A. J., Muon spin spectroscopy: magnetism, soft matter and the bridge between the two, *J. Phys. D: Appl. Phys.* **47,** 473001 (2014).

35. Cooley, J. W. & Tukey, J. W., An algorithm for the machine calculation of complex Fourier series, *Math. Comput.* **19,** 297 (1965).

36. Sonier, J. E., Brewer, J. H. & Kiefl, R. F., μSR studies of the vortex state in type-II superconductors, *Rev. Mod. Phys.* **72,** 769 (2000).

37. Lancaster, T., Blundell, S. J., Baker, P. J., Hayes, W., Giblin, S. R., McLain, S. E., Pratt, F. L., Salman, Z., Jacobs, E. A., Turner, J. F. C. & Barnes, T., Intrinsic magnetic order in Cs_2AgF_4 detected by muon-spin relaxation, *Phys. Rev. B* **75,** 220408 (2007).

38. Pratt, F., WIMDA: a muon data analysis program for the Windows PC, *Phys. B* **289-290,** 710 (2000).

39. Kreitzman, S. R., Williams, D. L., Kaplan, N., Kempton, J. R. & Brewer, J. H., Spin Echoes for μ^+-Spin Spectroscopy, *Phys. Rev. Lett.* **61,** 2890 (1988).

40. Kreitzman, S. R., Hitti, B., Lichti, R. L., Estle, T. L. & Chow, K. H., Muon-spin-resonance study of muonium dynamics in Si and its relevance to hydrogen, *Phys. Rev. B* **51,** 13117 (1995).

41. Storchak, V., Brewer, J. H., Morris, G. D., Arseneau, D. J. & Senba, M., Muonium formation via electron transport in solid nitrogen, *Phys. Rev. B* **59,** 10559 (1999).

42. Blundell, S. J., De Renzi, R., Lancaster, T. & Pratt, F. L., Muon Spectroscopy: An Introduction (Oxford University Press, 2021).

43. Kubo, R. & Toyabe, T., Magnetic resonance and relaxation, in *Proceedings of the XIVth Colloque Ampère* (1967), 810.

44. Yaouanc, A. & de Réotier, P., Muon Spin Rotation, Relaxation, and Resonance: Applications to Condensed Matter (Oxford University Press, 2011).

45. Le, L. P., Keren, A., Luke, G. M., Sternlieb, B. J., Wu, W. D., Uemura, Y. J., Brewer, J. H., Riseman, T. M., Upasani, R. V., Chiang, L. Y., Kang, W., Chaikin, P. M., Csiba, T. & Grüner, G., Muon-spin-rotation and relaxation studies in $(TMTSF_2)$-X compounds, *Phys. Rev. B* **48,** 7284 (1993).

46. Le, L. P., Heffner, R. H., Thompson, J. D., Nieuwenhuys, G. J., Maclaughlin, D. E., Canfield, P. C., Cho, B. K., Amato, A., Feyerherm, R., Gygax, F. N. & Schenck, A., μSR studies of borocarbides, *Hyperfine Interact.* **104,** 49 (1997).

47. Savici, A. T., Fudamoto, Y., Gat, I. M., Ito, T., Larkin, M. I., Uemura, Y. J., Luke, G. M., Kojima, K. M., Lee, Y. S., Kastner, M. A., Birgeneau, R. J. & Yamada, K., Muon spin relaxation studies of incommensurate magnetism and superconductivity in stage-4 $La_2CuO_{4.11}$ and $La_{1.88}Sr_{0.12}CuO_4$, *Phys. Rev. B* **66,** 014524 (2002).

48. Abragam, A., The Principles of Nuclear Magnetism (Clarendon Press, 1961).

49. Kehr, K. W., Honig, G. & Richter, D., Stochastic theory of spin depolarization of muons diffusing in the presence of traps, *Z. Phys. B: Condens. Matter* **32,** 49 (1978).

50. Bloembergen, N., Purcell, E. M. & Pound, R. V., Relaxation Effects in Nuclear Magnetic Resonance Absorption, *Phys. Rev.* **73,** 679 (1948).

51. Brewer, J. H., Kreitzman, S. R., Noakes, D. R., Ansaldo, E. J., Harshman, D. R. & Keitel, R., Observation of muon-fluorine "hydrogen bonding" in ionic crystals, *Phys. Rev. B* **33,** 7813 (1986).

52. Luke, G. M., Brewer, J. H., Kreitzman, S. R., Noakes, D. R., Celio, M., Kadono, R. & Ansaldo, E. J., Muon diffusion and spin dynamics in copper, *Phys. Rev. B* **43,** 3284 (1991).

53. Princep, A. J., Prabhakaran, D., Boothroyd, A. T. & Adroja, D. T., Crystal-field states of Pr^{3+} in the candidate quantum spin ice $Pr_2Sn_2O_7$, *Phys. Rev. B* **88,** 104421 (2013).

54. Blundell, S. J. & Lancaster, T., DFT+μ: Density functional theory for muon site determination, *Appl. Phys. Rev.* **10,** 021316 (2023).

55. Pratt, F. L., Lang, F., Steinhardt, W., Haravifard, S. & Blundell, S. J., Spin dynamics, entanglement, and the nature of the spin liquid state in $YbZnGaO_4$, *Phys. Rev. B* **106,** L060401 (2022).

56. Pratt, F. L., Lang, F., Blundell, S. J., Steinhardt, W., Haravifard, S., Mañas-Valero, S., Coronado, E., Huddart, B. M. & Lancaster, T., Studying spin diffusion and quantum entanglement with LF-μSR, *J. Phys. Conf. Ser.* **2462,** 012038 (2023).

57. Keren, A., Generalization of the Abragam relaxation function to a longitudinal field, *Phys. Rev. B* **50,** 10039 (1994).

58. Giannozzi, P. *et al.,* QUANTUM ESPRESSO: a modular and open-source software project for quantum simulations of materials, *J. Phys. Condens. Matter* **21,** 395502 (2009).

59. Giannozzi, P. *et al.,* Advanced capabilities for materials modelling with QUANTUM ESPRESSO, *J. Phys. Condens. Matter* **29,** 465901 (2017).

60. Giustino, F., Materials Modelling using Density Functional Theory (Oxford Unversity Press, Oxford, 2014).

61. Pribram-Jones, A., Gross, D. A. & Burke, K., DFT: A Theory Full of Holes?, *Annu. Rev. Phys. Chem.* **66,** 283 (2015).

62. Kohn, W. & Sham, L. J., Self-Consistent Equations Including Exchange and Correlation Effects, *Phys. Rev.* **140,** A1133 (1965).

63. Kohn, W., Nobel Lecture: Electronic structure of matter—wave functions and density functionals, *Rev. Mod. Phys.* **71,** 1253 (1999).

64. Perdew, J. P., Burke, K. & Ernzerhof, M., Generalized Gradient Approximation Made Simple, *Phys. Rev. Lett.* **77,** 3865 (1996).

65. Perdew, J. P. & Zunger, A., Self-interaction correction to density-functional approximations for many-electron systems, *Phys. Rev. B* **23,** 5048 (1981).

66. Perdew, J. P. & Wang, Y., Accurate and simple analytic representation of the electron-gas correlation energy, *Phys. Rev. B* **45,** 13244 (1992).

67. Feynman, R. P., Forces in Molecules, *Phys. Rev.* **56,** 340 (1939).

68. Möller, J. S., Ceresoli, D., Lancaster, T., Marzari, N. & Blundell, S. J., Quantum states of muons in fluorides, *Phys. Rev. B* **87,** 121108 (2013).

69. Möller, J. S., Bonfà, P., Ceresoli, D., Bernardini, F., Blundell, S. J., Lancaster, T., Renzi, R. D., Marzari, N., Watanabe, I., Sulaiman, S. & Mohamed-Ibrahim, M. I., Playing quantum hide-and-seek with the muon: localizing muon stopping sites, *Phys. Scr.* **88,** 068510 (2013).

70. Scheie, A., *PyCrystalField*: Software for calculation, analysis and fitting of crystal electric field Hamiltonians, *J. Appl. Crystallogr.* **54,** 356 (2021).

71. McMahon, B. & Hall, S. R., International Tables for Crystallography, Definition and Exchange of Crystallographic Data (Springer Netherlands, 2005).

72. Hutchings, M., Point-Charge Calculations of Energy Levels of Magnetic Ions in Crystalline Electric Fields, *Solid State Phys.* **16,** 227 (1964).

73. Baldoví, J. J., Cardona-Serra, S., Clemente-Juan, J. M., Coronado, E., Gaita-Ariño, A. & Palii, A., SIMPRE: A software package to calculate crystal field parameters, energy levels, and magnetic properties on mononuclear lanthanoid complexes based on charge distributions, *J. Comput. Chem.* **34,** 1961 (2013).

74. Boothroyd, A., Spectre — a program for calculating spectroscopic properties of rare earth ions in crystals, 1999.

75. Peierls, R., On Ising's model of ferromagnetism, *Math. Proc. Camb. Philos. Soc.* **32,** 477 (1936).

76. Affleck, I., Quantum spin chains and the Haldane gap, *J. Phys. Condens. Matter* **1,** 3047 (1989).

77. Bethe, H., Zur Theorie der Metalle, *Zeitschrift für Physik* **71,** 205 (1931).

78. Anderson, P. W., An Approximate Quantum Theory of the Antiferromagnetic Ground State, *Phys. Rev.* **86,** 694 (1952).

79. Kubo, R., The Spin-Wave Theory of Antiferromagnetics, *Phys. Rev.* **87,** 568 (1952).

80. Coldea, R., Tennant, D. A., Wheeler, E. M., Wawrzynska, E., Prabhakaran, D., Telling, M., Habicht, K., Smeibidl, P. & Kiefer, K., Quantum Criticality in an Ising Chain: Experimental Evidence for Emergent E_8 Symmetry, *Science* **327,** 177 (2010).

81. Haldane, F. D. M., Nonlinear Field Theory of Large-Spin Heisenberg Antiferromagnets: Semiclassically Quantized Solitons of the One-Dimensional Easy-Axis Néel State, *Phys. Rev. Lett.* **50,** 1153 (1983).

82. Affleck, I., Kennedy, T., Lieb, E. H. & Tasaki, H., Rigorous results on valence-bond ground states in antiferromagnets, *Phys. Rev. Lett.* **59,** 799 (1987).

83. Katsumata, K., Hori, H., Takeuchi, T., Date, M., Yamagishi, A. & Renard, J. P., Magnetization process of an $S = 1$ linear-chain Heisenberg antiferromagnet, *Phys. Rev. Lett.* **63,** 86 (1989).

84. Uchiyama, Y., Sasago, Y., Tsukada, I., Uchinokura, K., Zheludev, A., Hayashi, T., Miura, N. & Böni, P., Spin-Vacancy-Induced Long-Range Order in a New Haldane-Gap Antiferromagnet, *Phys. Rev. Lett.* **83,** 632 (1999).

85. Wedel, B., Sugiyama, K., Hiraga, K. & Itagaki, K., On a lead nickel manganese tellurium oxide $PbM_2Ni_6Te_3O_{18}$ containing Mn^{2+} in trigonal prismatic oxygen coordination, *Mater. Res. Bull.* **34,** 2193 (1999).

86. Doi, Y., Suzuki, R., Hinatsu, Y., Kodama, K. & Igawa, N., Crystal Structures and Magnetic Properties of Nickel Chain Compounds $PbM_2Ni_6Te_3O_{18}$ (M = Mn, Cd), *Inorg. Chem.* **54,** 10725 (2015).

87. Sivakumar, G., Mazumder, M., Lahiri, A., Sundaresan, A., Pati, S. K., Maesato, M., Kitagawa, H., Gopalakrishnan, J. & Natarajan, S., New Series of Pentanary Oxides, $AM_2C_6Te_3O_{18}$ (A = Pb, Sr; M = Mn, Cd; C = Ni, Co): Synthesis, Structure, and Magnetic and Optical Properties, *J. Phys. Chem. C* **124,** 25071 (2020).

88. Panneer Muthuselvam, I., Saranya, K., Büscher, F., Wulferding, D., Lemmens, P., Chen, W.-T. & Sankar, R., High magnetic anisotropy and magnon excitations in single crystals of the double spin chain compound $PbMn_2Ni_6Te_3O_{18}$, *Phys. Rev. B* **103,** 064401 (2021).

89. Plumb, K. W., Clancy, J. P., Sandilands, L. J., Shankar, V. V., Hu, Y. F., Burch, K. S., Kee, H.-Y. & Kim, Y.-J., α-$RuCl_3$: A spin-orbit assisted Mott insulator on a honeycomb lattice, *Phys. Rev. B* **90,** 041112 (2014).

90. Kitaev, A., Anyons in an exactly solved model and beyond, *Ann. Phys.* **321,** January Special Issue, 2 (2006).

91. Chaloupka, J., Jackeli, G. & Khaliullin, G., Kitaev-Heisenberg Model on a Honeycomb Lattice: Possible Exotic Phases in Iridium Oxides A_2IrO_3, *Phys. Rev. Lett.* **105,** 027204 (2010).

92. Takagi, H., Takayama, T., Jackeli, G., Khaliullin, G. & Nagler, S. E., Concept and realization of Kitaev quantum spin liquids, *Nat. Rev. Phys.* **1,** 264 (2019).

93. Fletcher, J. M., Gardner, W. E., Fox, A. C. & Topping, G., X-Ray, infrared, and magnetic studies of α- and β-ruthenium trichloride, *J. Chem. Soc. A,* 1038–1045 (1967).

94. Kobayashi, Y., Okada, T., Asai, K., Katada, M., Sano, H. & Ambe, F., Moessbauer spectroscopy and magnetization studies of α- and β-ruthenium trichloride, *Inorg. Chem.* **31,** 4570 (1992).

95. Johnson, R. D., Williams, S. C., Haghighirad, A. A., Singleton, J., Zapf, V., Manuel, P., Mazin, I. I., Li, Y., Jeschke, H. O., Valentí, R. & Coldea, R., Monoclinic crystal structure of α-$RuCl_3$ and the zigzag antiferromagnetic ground state, *Phys. Rev. B* **92,** 235119 (2015).

96. Majumder, M., Schmidt, M., Rosner, H., Tsirlin, A. A., Yasuoka, H. & Baenitz, M., Anisotropic $Ru^{3+}4d^5$ magnetism in the α-$RuCl_3$ honeycomb system: Susceptibility, specific heat, and zero-field NMR, *Phys. Rev. B* **91,** 180401 (2015).

97. Sears, J. A., Songvilay, M., Plumb, K. W., Clancy, J. P., Qiu, Y., Zhao, Y., Parshall, D. & Kim, Y.-J., Magnetic order in α-$RuCl_3$: A honeycomb-lattice quantum magnet with strong spin-orbit coupling, *Phys. Rev. B* **91,** 144420 (2015).

98. Lang, F., Baker, P. J., Haghighirad, A. A., Li, Y., Prabhakaran, D., Valentí, R. & Blundell, S. J., Unconventional magnetism on a honeycomb lattice in α-$RuCl_3$ studied by muon spin rotation, *Phys. Rev. B* **94,** 020407(R) (2016).

99. Baek, S.-H., Do, S.-H., Choi, K.-Y., Kwon, Y. S., Wolter, A. U. B., Nishimoto, S., van den Brink, J. & Büchner, B., Evidence for a Field-Induced Quantum Spin Liquid in α-$RuCl_3$, *Phys. Rev. Lett.* **119,** 037201 (2017).

100. Banerjee, A., Lampen-Kelley, P., Knolle, J., Balz, C., Aczel, A. A., Winn, B., Liu, Y., Pajerowski, D., Yan, J., Bridges, C. A., Savici, A. T., Chakoumakos, B. C., Lumsden, M. D., Tennant, D. A., Moessner, R., Mandrus, D. G. & Nagler, S. E., Excitations in the field-induced quantum spin liquid state of α-$RuCl_3$, *npj Quantum Mater.* **3,** 8 (2018).

101. Imai, Y., Nawa, K., Shimizu, Y., Yamada, W., Fujihara, H., Aoyama, T., Takahashi, R., Okuyama, D., Ohashi, T., Hagihala, M., Torii, S., Morikawa, D., Terauchi, M., Kawamata, T., Kato, M., Gotou, H., Itoh, M., Sato, T. J. & Ohgushi, K., Zigzag magnetic order in the Kitaev spin-liquid candidate material $RuBr_3$ with a honeycomb lattice, *Phys. Rev. B* **105,** L041112 (2022).

102. Choi, Y., Lee, J.-H., Lee, S., Wulferding, D., Fujihara, H., Sato, F., Imai, Y., Ohgushi, K., Seong, M.-J. & Choi, K.-Y., Magnetic and spin-orbit exciton excitations in the honeycomb lattice compound $RuBr_3$, *Phys. Rev. B* **106,** 174430 (2022).

103. Rau, J. G., Lee, E. K.-H. & Kee, H.-Y., Generic Spin Model for the Honeycomb Iridates beyond the Kitaev Limit, *Phys. Rev. Lett.* **112,** 077204 (2014).

104. Ni, D., Gui, X., Powderly, K. M. & Cava, R. J., Honeycomb-Structure RuI_3, A New Quantum Material Related to α-$RuCl_3$, *Adv. Mater.* **34,** 2106831 (2022).

105. Nawa, K., Imai, Y., Yamaji, Y., Fujihara, H., Yamada, W., Takahashi, R., Hiraoka, T., Hagihala, M., Torii, S., Aoyama, T., Ohashi, T., Shimizu, Y., Gotou, H., Itoh, M., Ohgushi, K. & Sato, T. J., Strongly Electron-Correlated Semimetal RuI_3 with a Layered Honeycomb Structure, *J. Phys. Soc. Jpn* **90,** 123703 (2021).

106. Zhang, Y., Lin, L.-F., Moreo, A. & Dagotto, E., Theoretical study of the crystal and electronic properties of α-RuI_3, *Phys. Rev. B* **105,** 085107 (2022).

107. Gretarsson, H., Fujihara, H., Sato, F., Gotou, H., Imai, Y., Ohgushi, K., Keimer, B. & Suzuki, H., $J{=}\frac{1}{2}$ pseudospins and $d{-}p$ hybridization in the Kitaev spin liquid candidates RuX_3 (X=Cl, Br, I), *Phys. Rev. B* **109,** L180413 (2024).

108. Banerjee, A., Bridges, C. A., Yan, J.-Q., Aczel, A. A., Li, L., Stone, M. B., Granroth, G. E., Lumsden, M. D., Yiu, Y., Knolle, J., Bhattacharjee, S., Kovrizhin, D. L., Moessner, R., Tennant, D. A., Mandrus, D. G. & Nagler, S. E., Proximate Kitaev quantum spin liquid behaviour in a honeycomb magnet, *Nat. Mater.* **15,** 733 (2016).

109. Banerjee, A., Yan, J., Knolle, J., Bridges, C. A., Stone, M. B., Lumsden, M. D., Mandrus, D. G., Tennant, D. A., Moessner, R. & Nagler, S. E., Neutron scattering in the proximate quantum spin liquid α-$RuCl_3$, *Science* **356,** 1055 (2017).

110. Weinhold, T., Wang, C., Seewald, F., Grinenko, V., Imai, Y., Sato, F., Ohgushi, K., Klauss, H.-H. & Sarkar, R., Magnetism in the Kitaev quantum spin liquid candidate $RuBr_3$, *Phys. Rev. B* **109,** 014440 (2024).

111. Butler, M. A., Walker, L. R. & Soos, Z. G., Dimensionality of spin fluctuations in highly anisotropic TCNQ salts, *J. Chem. Phys.* **64,** 3592 (1976).

112. Kaib, D. A. S., Riedl, K., Razpopov, A., Li, Y., Backes, S., Mazin, I. I. & Valentí, R., Electronic and magnetic properties of the RuX_3 (X = Cl, Br, I) family: two siblings—and a cousin?, *npj Quantum Mater.* **7,** 75 (2022).

113. Kim, H.-S., Spin-Orbit-Entangled Nature of Magnetic Moments and Kitaev Magnetism in Layered Halides, *Appl. Sci. Converg. Technol.* **30,** 191 (2021).

114. Liu, L., Yang, K., Wang, G., Lu, D., Ma, Y. & Wu, H., Contrasting electronic states of RuI_3 and $RuCl_3$, *Phys. Rev. B* **107,** 165134 (2023).

115. Ni, D., Xu, X. & Cava, R. J., The layered $RuBr_3$–RuI_3 honeycomb system, *J. Mater. Chem. C* **12,** 4897 (2024).

116. Sato, F., Fujihara, H., Gotou, H., Aoyama, T., Imai, Y. & Ohgushi, K., Insulator-metal transition in $Ru(Br_{1-x}I_x)_3$ with honeycomb structure, *Phys. Rev. B* **109,** 035154 (2024).

117. Wannier, G. H., Antiferromagnetism. The Triangular Ising Net, *Phys. Rev.* **79,** 357 (1950).

118. Li, Y., Chen, G., Tong, W., Pi, L., Liu, J., Yang, Z., Wang, X. & Zhang, Q., Rare-Earth Triangular Lattice Spin Liquid: A Single-Crystal Study of $YbMgGaO_4$, *Phys. Rev. Lett.* **115,** 167203 (2015).

119. Paddison, J. A. M., Daum, M., Dun, Z., Ehlers, G., Liu, Y., Stone, M. B., Zhou, H. & Mourigal, M., Continuous excitations of the triangular-lattice quantum spin liquid $YbMgGaO_4$, *Nat. Phys.* **13,** 117 (2017).

120. Zhou, H. D., Choi, E. S., Li, G., Balicas, L., Wiebe, C. R., Qiu, Y., Copley, J. R. D. & Gardner, J. S., Spin Liquid State in the $S = 1/2$ Triangular Lattice $Ba_3CuSb_2O_9$, *Phys. Rev. Lett.* **106,** 147204 (2011).

121. Scheie, A. O., Ghioldi, E. A., Xing, J., Paddison, J. A. M., Sherman, N. E., Dupont, M., Sanjeewa, L. D., Lee, S., Woods, A. J., Abernathy, D., Pajerowski, D. M., Williams, T. J., Zhang, S.-S., Manuel, L. O., Trumper, A. E., Pemmaraju, C. D., Sefat, A. S., Parker, D. S., Devereaux, T. P., Movshovich, R., Moore, J. E., Batista, C. D. & Tennant, D. A., Proximate spin liquid and fractionalization in the triangular antiferromagnet $KYbSe_2$, *Nat. Phys.* **20,** 74 (2024).

122. Shen, Y., Li, Y.-D., Wo, H., Li, Y., Shen, S., Pan, B., Wang, Q., Walker, H. C., Steffens, P., Boehm, M., Hao, Y., Quintero-Castro, D. L., Harriger, L. W., Frontzek, M. D., Hao, L., Meng, S., Zhang, Q., Chen, G. & Zhao, J., Evidence for a spinon Fermi surface in a triangular-lattice quantum-spin-liquid candidate, *Nature* **540,** 559 (2016).

123. Balents, L., Quantum mechanics in a spin, *Nature* **540,** 534 (2016).

124. Zhu, Z., Maksimov, P. A., White, S. R. & Chernyshev, A. L., Disorder-Induced Mimicry of a Spin Liquid in $YbMgGaO_4$, *Phys. Rev. Lett.* **119,** 157201 (2017).

125. Arh, T., Sana, B., Pregelj, M., Khuntia, P., Jagličić, Z., Le, M. D., Biswas, P. K., Manuel, P., Mangin-Thro, L., Ozarowski, A. & Zorko, A., The Ising triangular-lattice antiferromagnet neodymium heptatantalate as a quantum spin liquid candidate, *Nat. Mater.* **21,** 416 (2022).

126. Guo, G.-C., Zhuang, J.-N., Wang, Y.-G., Chen, J.-T., Zhuang, H.-H., Huang, J.-S. & Zhang, Q.-E., Dysprosium Tantalum Oxide, $DyTa_7O_{19}$, *Acta Crystallogr. C* **52,** 5 (1996).

127. Wang, L., Ouyang, Z., Xiao, T., Li, Z. & Tian, Z., Synthesis, structure and magnetism of RTa_7O_{19} (R = Pr, Sm, Eu, Gd, Dy, Ho) with perfect triangular lattice, *J. Alloys Compd.* **937,** 168390 (2023).

128. King, N., Boltersdorf, J., Maggard, P. A. & Wong-Ng, W., Polymorphism and Structural Distortions of Mixed-Metal Oxide Photocatalysts Constructed with α-U_3O_8 Types of Layers, *Crystals* **7** (2017).

129. Doebelin, N. & Kleeberg, R., *Profex*: a graphical user interface for the Rietveld refinement program *BGMN*, *J. Appl. Crystallogr.* **48,** 1573–1580 (2015).

130. Ono, T., Tanaka, H., Kolomiyets, O., Mitamura, H., Goto, T., Nakajima, K., Oosawa, A., Koike, Y., Kakurai, K., Klenke, J., Smeibidle, P. & Meißner, M., Magnetization plateaux of the $S = 1/2$ two-dimensional frustrated antiferromagnet Cs_2CuBr_4, *J. Phys. Condens. Matter* **16,** S773 (2004).

131. Soto, R., Martínez, G., Baibich, M. N., Florez, J. M. & Vargas, P., Metastable states in the triangular-lattice Ising model studied by Monte Carlo simulations: Application to the spin-chain compound $Ca_3Co_2O_6$, *Phys. Rev. B* **79,** 184422 (2009).

132. Kamiya, Y., Ge, L., Hong, T., Qiu, Y., Quintero-Castro, D. L., Lu, Z., Cao, H. B., Matsuda, M., Choi, E. S., Batista, C. D., Mourigal, M., Zhou, H. D. & Ma, J., The nature of spin excitations in the one-third magnetization plateau phase of $Ba_3CoSb_2O_9$, *Nat. Commun.* **9,** 2666 (2018).

133. Sebastian, S. E., Harrison, N., Sengupta, P., Batista, C. D., Francoual, S., Palm, E., Murphy, T., Marcano, N., Dabkowska, H. A. & Gaulin, B. D., Fractalization drives crystalline states in a frustrated spin system, *Proc. Natl. Acad. Sci. U.S.A.* **105,** 20157 (2008).

134. Hodges, J. A., Bonville, P., Forget, A., Yaouanc, A., Dalmas de Réotier, P., André, G., Rams, M., Królas, K., Ritter, C., Gubbens, P. C. M., Kaiser, C. T., King, P. J. C. & Baines, C., First-Order Transition in the Spin Dynamics of Geometrically Frustrated $Yb_2Ti_2O_7$, *Phys. Rev. Lett.* **88,** 077204 (2002).

135. Dalmas de Réotier, P., Yaouanc, A., Keller, L., Cervellino, A., Roessli, B., Baines, C., Forget, A., Vaju, C., Gubbens, P. C. M., Amato, A. & King, P. J. C., Spin Dynamics and Magnetic Order in Magnetically Frustrated $Tb_2Sn_2O_7$, *Phys. Rev. Lett.* **96,** 127202 (2006).

136. Baker, P. J., Matthews, M. J., Giblin, S. R., Schiffer, P., Baines, C. & Prabhakaran, D., Unusual field dependence of spin fluctuations on different timescales in $Tb_2Ti_2O_7$, *Phys. Rev. B* **86,** 094424 (2012).

137. Sheetal, Biswas, P. K., Yokoyama, K., Adroja, D. T. & Yadav, C. S., Muon spin relaxation and emergence of disorder-induced unconventional dynamic magnetic fluctuations in $Dy_2Zr_2O_7$, 2023, arXiv: `2303.14426 [cond-mat.str-el]`.

138. Hofmann, R. & Gruehn, R., Zur Darstellung und Struktur neuer Niobate $LnNb_7O_{19}$ (Ln = La, Ce), *Z. Anorg. Allg. Chem.* **602,** 105 (1991).

139. Bleaney, B., Enhanced nuclear magnetism, *Physica* **69,** 317 (1973).

140. Kelly, N. D., Liu, C. & Dutton, S. E., Structure and magnetism of a new hexagonal polymorph of $Ba_3Tb(BO_3)_3$ with a quasi-2D triangular lattice, *J. Solid State Chem.* **292,** 121640 (2020).

141. Clark, L., Sala, G., Maharaj, D. D., Stone, M. B., Knight, K. S., Telling, M. T. F., Wang, X., Xu, X., Kim, J., Li, Y., Cheong, S.-W. & Gaulin, B. D., Two-dimensional spin liquid behaviour in the triangular-honeycomb antiferromagnet $TbInO_3$, *Nat. Phys.* **15,** 262 (2019).

142. Hallas, A. M., Gaudet, J. & Gaulin, B. D., Experimental Insights into Ground-State Selection of Quantum XY Pyrochlores, *Annu. Rev. Condens. Matter Phys.* **9,** 105 (2018).

143. Rau, J. G. & Gingras, M. J., Frustrated Quantum Rare-Earth Pyrochlores, *Annu. Rev. Condens. Matter Phys.* **10,** 357 (2019).

144. Gardner, J. S., Gingras, M. J. P. & Greedan, J. E., Magnetic pyrochlore oxides, *Rev. Mod. Phys.* **82,** 53 (2010).

145. Keren, A., Gardner, J. S., Ehlers, G., Fukaya, A., Segal, E. & Uemura, Y. J., Dynamic Properties of a Diluted Pyrochlore Cooperative Paramagnet $(Tb_pY_{1-p})_2Ti_2O_7$, *Phys. Rev. Lett.* **92,** 107204 (2004).

146. Snyder, J., Slusky, J. S., Cava, R. J. & Schiffer, P., Dirty spin ice: The effect of dilution on spin freezing in $Dy_2Ti_2O_7$, *Phys. Rev. B* **66,** 064432 (2002).

147. Snyder, J., Ueland, B. G., Slusky, J. S., Karunadasa, H., Cava, R. J. & Schiffer, P., Low-temperature spin freezing in the $Dy_2Ti_2O_7$ spin ice, *Phys. Rev. B* **69,** 064414 (2004).

148. Snyder, J., Ueland, B. G., Mizel, A., Slusky, J. S., Karunadasa, H., Cava, R. J. & Schiffer, P., Quantum and thermal spin relaxation in the diluted spin ice $Dy_{2-x}M_xTi_2O_7$ ($M = \mathrm{Lu}, \mathrm{Y}$), *Phys. Rev. B* **70,** 184431 (2004).

149. Ehlers, G., Gardner, J. S., Booth, C. H., Daniel, M., Kam, K. C., Cheetham, A. K., Antonio, D., Brooks, H. E., Cornelius, A. L., Bramwell, S. T., Lago, J., Häussler, W. & Rosov, N., Dynamics of diluted Ho spin ice $Ho_{2-x}Y_xTi_2O_7$ studied by neutron spin echo spectroscopy and ac susceptibility, *Phys. Rev. B* **73,** 174429 (2006).

150. Tomasello, B., Castelnovo, C., Moessner, R. & Quintanilla, J., Single-ion anisotropy and magnetic field response in the spin-ice materials $Ho_2Ti_2O_7$ and $Dy_2Ti_2O_7$, *Phys. Rev. B* **92,** 155120 (2015).

151. Borzi, R. A., Gómez Albarracín, F. A., Rosales, H. D., Rossini, G. L., Steppke, A., Prabhakaran, D., Mackenzie, A. P., Cabra, D. C. & Grigera, S. A., Intermediate magnetization state and competing orders in $Dy_2Ti_2O_7$ and $Ho_2Ti_2O_7$, *Nat. Commun.* **7,** 12592 (2016).

152. Harris, M. J., Bramwell, S. T., McMorrow, D. F., Zeiske, T. & Godfrey, K. W., Geometrical Frustration in the Ferromagnetic Pyrochlore $Ho_2Ti_2O_7$, *Phys. Rev. Lett.* **79,** 2554 (1997).

153. Harris, M. J., Bramwell, S. T., Holdsworth, P. C. W. & Champion, J. D. M., Liquid-Gas Critical Behavior in a Frustrated Pyrochlore Ferromagnet, *Phys. Rev. Lett.* **81,** 4496 (1998).

154. Bramwell, S. T. & Gingras, M. J. P., Spin Ice State in Frustrated Magnetic Pyrochlore Materials, *Science* **294,** 1495 (2001).

155. Ramirez, A. P., Hayashi, A., Cava, R. J., Siddharthan, R. & Shastry, B. S., Zero-point entropy in 'spin ice', *Nature* **399,** 333 (1999).

156. Cornelius, A. L. & Gardner, J. S., Short-range magnetic interactions in the spin-ice compound $Ho_2Ti_2O_7$, *Phys. Rev. B* **64,** 060406 (2001).

157. Lau, G. C., Freitas, R. S., Ueland, B. G., Muegge, B. D., Duncan, E. L., Schiffer, P. & Cava, R. J., Zero-point entropy in stuffed spin-ice, *Nat. Phys.* **2,** 249 (2006).

158. Castelnovo, C., Moessner, R. & Sondhi, S. L., Magnetic monopoles in spin ice, *Nature* **451,** 42 (2008).

159. Morris, D. J. P., Tennant, D. A., Grigera, S. A., Klemke, B., Castelnovo, C., Moessner, R., Czternasty, C., Meissner, M., Rule, K. C., Hoffmann, J.-U., Kiefer, K., Gerischer, S., Slobinsky, D. & Perry, R. S., Dirac Strings and Magnetic Monopoles in the Spin Ice $Dy_2Ti_2O_7$, *Science* **326,** 411 (2009).

160. Kadowaki, H., Doi, N., Aoki, Y., Tabata, Y., J. Sato, T., W. Lynn, J., Matsuhira, K. & Hiroi, Z., Observation of Magnetic Monopoles in Spin Ice, *J. Phys. Soc. Jpn.* **78,** 103706 (2009).

161. Jaubert, L. D. C. & Holdsworth, P. C. W., Magnetic monopole dynamics in spin ice, *J. Phys. Condens. Matter* **23,** 164222 (2011).

162. Castelnovo, C., Moessner, R. & Sondhi, S., Spin Ice, Fractionalization, and Topological Order, *Annu. Rev. Condens. Matter Phys.* **3,** 35 (2012).

163. Dusad, R., Kirschner, F. K. K., Hoke, J. C., Roberts, B. R., Eyal, A., Flicker, F., Luke, G. M., Blundell, S. J. & Davis, J. C. S., Magnetic monopole noise, *Nature* **571,** 234 (2019).

164. Hallén, J. N., Grigera, S. A., Tennant, D. A., Castelnovo, C. & Moessner, R., Dynamical fractal and anomalous noise in a clean magnetic crystal, *Science* **378,** 1218 (2022).

165. Ross, K. A., Savary, L., Gaulin, B. D. & Balents, L., Quantum Excitations in Quantum Spin Ice, *Phys. Rev. X* **1,** 021002 (2011).

166. Molavian, H. R., Gingras, M. J. P. & Canals, B., Dynamically Induced Frustration as a Route to a Quantum Spin Ice State in $Tb_2Ti_2O_7$ via Virtual Crystal Field Excitations and Quantum Many-Body Effects, *Phys. Rev. Lett.* **98,** 157204 (2007).

167. Zhou, H. D., Wiebe, C. R., Janik, J. A., Balicas, L., Yo, Y. J., Qiu, Y., Copley, J. R. D. & Gardner, J. S., Dynamic Spin Ice: $Pr_2Sn_2O_7$, *Phys. Rev. Lett.* **101,** 227204 (2008).

168. Matsuhira, K., Sekine, C., Paulsen, C., Wakeshima, M., Hinatsu, Y., Kitazawa, T., Kiuchi, Y., Hiroi, Z. & Takagi, S., Spin freezing in the pyrochlore antiferromagnet $Pr_2Zr_2O_7$, *J. Phys. Conf. Ser.* **145,** 012031 (2009).

169. Kimura, K., Nakatsuji, S., Wen, J.-J., Broholm, C., Stone, M. B., Nishibori, E. & Sawa, H., Quantum fluctuations in spin-ice-like $Pr_2Zr_2O_7$, *Nat. Commun.* **4,** 1934 (2013).

170. Sibille, R., Lhotel, E., Hatnean, M. C., Balakrishnan, G., Fåk, B., Gauthier, N., Fennell, T. & Kenzelmann, M., Candidate quantum spin ice in the pyrochlore $Pr_2Hf_2O_7$, *Phys. Rev. B* **94,** 024436 (2016).

171. Foronda, F. R., Lang, F., Möller, J. S., Lancaster, T., Boothroyd, A. T., Pratt, F. L., Giblin, S. R., Prabhakaran, D. & Blundell, S. J., Anisotropic Local Modification of Crystal Field Levels in Pr-Based Pyrochlores: A Muon-Induced Effect Modeled Using Density Functional Theory, *Phys. Rev. Lett.* **114,** 017602 (2015).

172. Mauws, C., Hiebert, N., Rutherford, M. L., Zhou, H. D., Huang, Q., Stone, M. B., Butch, N. P., Su, Y., Choi, E. S., Yamani, Z. & Wiebe, C. R., Magnetic ordering in the Ising antiferromagnetic pyrochlore Nd_2ScNbO_7, *J. Phys. Condens. Matter* **33,** 245802 (2021).

173. Gomez, S. J., Sarte, P. M., Zelensky, M., Hallas, A. M., Gonzalez, B. A., Hong, K. H., Pace, E. J., Calder, S., Stone, M. B., Su, Y., Feng, E., Le, M. D., Stock, C., Attfield, J. P., Wilson, S. D., Wiebe, C. R. & Aczel, A. A., Absence of moment fragmentation in the mixed B-site pyrochlore Nd_2GaSbO_7, *Phys. Rev. B* **103,** 214419 (2021).

174. Sarte, P. M., Cruz-Kan, K., Ortiz, B. R., Hong, K. H., Bordelon, M. M., Reig-i-Plessis, D., Lee, M., Choi, E. S., Stone, M. B., Calder, S., Pajerowski, D. M., Mangin-Thro, L., Qiu, Y., Attfield, J. P., Wilson, S. D., Stock, C., Zhou, H. D., Hallas, A. M., Paddison, J. A. M., Aczel, A. A. & Wiebe, C. R., Dynamical ground state in the XY pyrochlore Yb_2GaSbO_7, *npj Quantum Mater.* **6,** 42 (2021).

175. Léger, M., Lhotel, E., Ressouche, E., Beauvois, K., Damay, F., Paulsen, C., Al-Mawla, A., Suard, E., Ciomaga Hatnean, M., Balakrishnan, G. & Petit, S., Field-temperature phase diagram of the enigmatic $Nd_2(Zr_{1-x}Ti_x)_2O_7$ pyrochlore magnets, *Phys. Rev. B* **103,** 214449 (2021).

176. Jana, Y., Ghosal, A., Nandi, S., Alam, J., Bag, P., Islam, S. & Nath, R., Spin-ice behavior of mixed pyrochlore Dy_2GaSbO_7 exhibiting enhanced Pauling zero-point entropy, *J. Magn. Magn. Mater.* **562,** 169814 (2022).

177. Alexanian, Y., Lhotel, E., Ballou, R., Colin, C. V., Klein, H., Le Priol, A., Museur, F., Robert, J., Pachoud, E., Lejay, P., Hadj-Azzem, A., Fåk, B., Berrod, Q., Zanotti, J.-M., Suard, E., Dejoie, C., de Brion, S. & Simonet, V., Collective magnetic state induced by charge disorder in the non-Kramers rare-earth pyrochlore Tb_2ScNbO_7, *Phys. Rev. Mater.* **7,** 094403 (2023).

178. Van Vleck, J. H., The theory of electric and magnetic susceptibilities (The Clarendon Press, Oxford, 1932).

179. Van Vleck, J. H., Quantum mechanics-The key to understanding magnetism, *Rev. Mod. Phys.* **50,** 181 (1978).

180. Scheie, A., Sanders, M., Gui, X., Qiu, Y., Prisk, T. R., Cava, R. J. & Broholm, C., Beyond magnons in Nd_2ScNbO_7: An Ising pyrochlore antiferromagnet with all-in–all-out order and random fields, *Phys. Rev. B* **104,** 134418 (2021).

181. Taira, N., Wakeshima, M. & Hinatsu, Y., Magnetic properties of iridium pyrochlores $R_2Ir_2O_7$ (R = Y, Sm, Eu and Lu), *J. Phys. Condens. Matter* **13,** 5527 (2001).

182. Coak, M. J., Götze, K., Northam De La Fuente, T., Castelnovo, C., Tidey, J. P., Singleton, J., Boothroyd, A. T., Prabhakaran, D. & Goddard, P. A., Magnetotransport of $Sm_2Ir_2O_7$ across the pressure-induced quantum-critical phase boundary, *npj Quantum Mater.* **9,** 17 (2024).

183. Uemura, Y. J., Keren, A., Kojima, K., Le, L. P., Luke, G. M., Wu, W. D., Ajiro, Y., Asano, T., Kuriyama, Y., Mekata, M., Kikuchi, H. & Kakurai, K., Spin Fluctuations in Frustrated Kagomé Lattice System $SrCr_8Ga_4O_{19}$ Studied by Muon Spin Relaxation, *Phys. Rev. Lett.* **73,** 3306 (1994).

184. Kojima, K., Keren, A., Le, L. P., Luke, G. M., Nachumi, B., Wu, W. D., Uemura, Y. J., Kiyono, K., Miyasaka, S., Takagi, H. & Uchida, S., Muon Spin Relaxation and Magnetic Susceptibility Measurements in the Haldane System $(Y_{2-x}Ca_x)Ba(Ni_{1-y}Mg_y)O_5$, *Phys. Rev. Lett.* **74,** 3471 (1995).

185. Keren, A., Uemura, Y. J., Luke, G., Mendels, P., Mekata, M. & Asano, T., Magnetic Dilution in the Geometrically Frustrated $SrCr_{9p}Ga_{12-9p}O_{19}$ and the Role of Local Dynamics: A Muon Spin Relaxation Study, *Phys. Rev. Lett.* **84,** 3450 (2000).

186. Li, Y., Adroja, D., Biswas, P. K., Baker, P. J., Zhang, Q., Liu, J., Tsirlin, A. A., Gegenwart, P. & Zhang, Q., Muon Spin Relaxation Evidence for the U(1) Quantum Spin-Liquid Ground State in the Triangular Antiferromagnet $YbMgGaO_4$, *Phys. Rev. Lett.* **117,** 097201 (2016).

187. Blundell, S. J., The quantum muon, *J. Phys. Conf. Ser.* **2462,** 012001 (2023).

188. McClarty, P. A., O'Brien, A. & Pollmann, F., Coulombic charge ice, *Phys. Rev. B* **89,** 195123 (2014).

189. Fennell, T., Harris, M. J., Calder, S., Ruminy, M., Boehm, M., Steffens, P., Lemée-Cailleau, M.-H., Zaharko, O., Cervellino, A. & Bramwell, S. T., Multiple Coulomb phase in the fluoride pyrochlore $CsNiCrF_6$, *Nat. Phys.* **15,** 60 (2019).

190. Soluyanov, A. A., Gresch, D., Wang, Z., Wu, Q., Troyer, M., Dai, X. & Bernevig, B. A., Type-II Weyl semimetals, *Nature* **527,** 495 (2015).

191. Yan, B. & Felser, C., Topological Materials: Weyl Semimetals, *Annu. Rev. Condens. Matter Phys.* **8,** 337 (2017).

192. Boothroyd, A. T., Topological electronic bands in crystalline solids, *Contemp. Phys.* **63,** 305 (2022).

193. Lyu, M., Xiang, J., Mi, Z., Zhao, H., Wang, Z., Liu, E., Chen, G., Ren, Z., Li, G. & Sun, P., Nonsaturating magnetoresistance, anomalous Hall effect, and magnetic quantum oscillations in the ferromagnetic semimetal PrAlSi, *Phys. Rev. B* **102,** 085143 (2020).

194. Wu, L., Chi, S., Zuo, H., Xu, G., Zhao, L., Luo, Y. & Zhu, Z., Field-induced Lifshitz transition in the magnetic Weyl semimetal candidate PrAlSi, *npj Quantum Mater.* **8,** 4 (2023).

195. Zhang, Y., Gao, Y., Gao, X.-J., Lei, S., Ni, Z., Oh, J. S., Huang, J., Yue, Z., Zonno, M., Gorovikov, S., Hashimoto, M., Lu, D., Denlinger, J. D., Birgeneau, R. J., Kono, J., Wu, L., Law, K. T., Morosan, E. & Yi, M., Kramers nodal lines and Weyl fermions in SmAlSi, *Commun. Phys.* **6,** 134 (2023).

196. Sun, Y., Lee, C., Yang, H.-Y., Torchinsky, D. H., Tafti, F. & Orenstein, J., Mapping domain-wall topology in the magnetic Weyl semimetal CeAlSi, *Phys. Rev. B* **104,** 235119 (2021).

197. Piva, M. M., Souza, J. C., Brousseau-Couture, V., Sorn, S., Pakuszewski, K. R., John, J. K., Adriano, C., Côté, M., Pagliuso, P. G., Paramekanti, A. & Nicklas, M., Topological features in the ferromagnetic Weyl semimetal CeAlSi: Role of domain walls, *Phys. Rev. Res.* **5,** 013068 (2023).

198. Yang, H.-Y., Singh, B., Gaudet, J., Lu, B., Huang, C.-Y., Chiu, W.-C., Huang, S.-M., Wang, B., Bahrami, F., Xu, B., Franklin, J., Sochnikov, I., Graf, D. E., Xu, G., Zhao, Y., Hoffman, C. M., Lin, H., Torchinsky, D. H., Broholm, C. L., Bansil, A. & Tafti, F., Noncollinear ferromagnetic Weyl semimetal with anisotropic anomalous Hall effect, *Phys. Rev. B* **103,** 115143 (2021).

199. Gaudet, J., Yang, H.-Y., Baidya, S., Lu, B., Xu, G., Zhao, Y., Rodriguez-Rivera, J. A., Hoffmann, C. M., Graf, D. E., Torchinsky, D. H., Nikolić, P., Vanderbilt, D., Tafti, F. & Broholm, C. L., Weyl-mediated helical magnetism in NdAlSi, *Nat. Mater.* **20,** 1650 (2021).

200. Xu, B., Franklin, J., Jayakody, A., Yang, H.-Y., Tafti, F. & Sochnikov, I., Picoscale Magnetoelasticity Governs Heterogeneous Magnetic Domains in a Noncentrosymmetric Ferromagnetic Weyl Semimetal, *Adv. Quantum Technol.* **4,** 2000101 (2021).

201. Yang, H.-Y., Singh, B., Lu, B., Huang, C.-Y., Bahrami, F., Chiu, W.-C., Graf, D., Huang, S.-M., Wang, B., Lin, H., Torchinsky, D., Bansil, A. & Tafti, F., Transition from intrinsic to extrinsic anomalous Hall effect in the ferromagnetic Weyl semimetal $PrAlGe_{1-x}Si_x$, *APL Mater.* **8,** 011111 (2020).

202. Wang, T., Guo, Y. & Wang, C., Structure and magnetic properties of RAlSi (R = light rare earth), *Chin. Phys. B* **30,** 075102 (2021).

203. Wang, J.-F., Dong, Q.-X., Guo, Z.-P., Lv, M., Huang, Y.-F., Xiang, J.-S., Ren, Z.-A., Wang, Z.-J., Sun, P.-J., Li, G. & Chen, G.-F., NdAlSi: A magnetic Weyl semimetal candidate with rich magnetic phases and atypical transport properties, *Phys. Rev. B* **105,** 144435 (2022).

204. Yang, H.-Y., Gaudet, J., Verma, R., Baidya, S., Bahrami, F., Yao, X., Huang, C.-Y., DeBeer-Schmitt, L., Aczel, A. A., Xu, G., Lin, H., Bansil, A., Singh, B. & Tafti, F., Stripe helical magnetism and two regimes of anomalous Hall effect in NdAlGe, *Phys. Rev. Mater.* **7,** 034202 (2023).

205. Dalmas de Réotier, P., Yaouanc, A., Amato, A., Maisuradze, A., Andreica, D., Roessli, B., Goko, T., Scheuermann, R. & Lapertot, G., On the Robustness of the MnSi Magnetic Structure Determined by Muon Spin Rotation, *Quantum Beam Sci.* **2** (2018).

206. Amato, A., Heavy-fermion systems studied by μSR technique, *Rev. Mod. Phys.* **69,** 1119 (1997).

207. Amato, A., Feyerherm, R., Gygax, F. N. & Schenck, A., μ^+-site in heavy-fermion compounds, *Hyperfine Interact.* **104,** 115 (1997).

208. Amato, A., Dalmas de Réotier, P., Andreica, D., Yaouanc, A., Suter, A., Lapertot, G., Pop, I. M., Morenzoni, E., Bonfà, P., Bernardini, F. & De Renzi, R., Understanding the μSR spectra of MnSi without magnetic polarons, *Phys. Rev. B* **89,** 184425 (2014).

209. Wang, J.-F., Dong, Q.-X., Huang, Y.-F., Wang, Z.-S., Guo, Z.-P., Wang, Z.-J., Ren, Z.-A., Li, G., Sun, P.-J., Dai, X. & Chen, G.-F., New Type of Quantum Oscillations Stemmed From the Strong Weyl Fermions - 4f Electrons Exchange Interaction, 2022, arXiv: `2201.06412 [cond-mat.mtrl-sci]`.

210. Guguchia, Z., Verezhak, J. A. T., Gawryluk, D. J., Tsirkin, S. S., Yin, J. X., Belopolski, I., Zhou, H., Simutis, G., Zhang, S. S., Cochran, T. A., Chang, G., Pomjakushina, E., Keller, L., Skrzeczkowska, Z., Wang, Q., Lei, H. C., Khasanov, R., Amato, A., Jia, S., Neupert, T., Luetkens, H. & Hasan, M. Z., Tunable anomalous Hall conductivity through volume-wise magnetic competition in a topological kagome magnet, *Nat. Commun.* **11,** 559 (2020).

211. Zhang, Z., Ma, X., Li, J., Wang, G., Adroja, D. T., Perring, T. P., Liu, W., Jin, F., Ji, J., Wang, Y., Kamiya, Y., Wang, X., Ma, J. & Zhang, Q., Crystalline electric field excitations in the quantum spin liquid candidate $NaYbSe_2$, *Phys. Rev. B* **103,** 035144 (2021).

212. Takatsu, H., Goto, K., Otsuka, H., Higashinaka, R., Matsubayashi, K., Uwatoko, Y. & Kadowaki, H., AC Susceptibility of the Dipolar Spin Ice $Dy_2Ti_2O_7$: Experiments and Monte Carlo Simulations, *J. Phys. Soc. Jpn* **82,** 104710 (2013).

213. Pomaranski, D., Yaraskavitch, L. R., Meng, S., Ross, K. A., Noad, H. M. L., Dabkowska, H. A., Gaulin, B. D. & Kycia, J. B., Absence of Pauling's residual entropy in thermally equilibrated $Dy_2Ti_2O_7$, *Nat. Phys.* **9,** 353 (2013).

214. Bradley, O., Feng, C., Scalettar, R. T. & Singh, R. R. P., Robustness of entropy plateaus: A case study of triangular Ising antiferromagnets, *Phys. Rev. B* **100,** 064414 (2019).